THE
PHYSICAL REVIEW

A journal of experimental and theoretical physics established by E. L. Nichols in 1893

SECOND SERIES, VOL. 73, No. 11 JUNE 1, 1948

Neutron Polarization*

D. J. HUGHES, J. R. WALLACE, AND R. H. HOLTZMAN
Argonne National Laboratory, Chicago, Illinois

(Received February 17, 1948)

The production of polarized neutrons in magnetized iron has been studied, using the intense neutron beams available at the Argonne heavy water pile. The theoretical work of Halpern *et al.*, used as a guide in the experiments, has been checked in many respects, with the exception that the polarization cross section p has a measured value of 3.15 barns compared to the theoretical 1 barn. The application of neutron polarization to the measurement of the approach to saturation in ferromagnets is described and preliminary results are reported.

I. INTRODUCTION

THE possibility of polarizing the neutrons in a beam was first suggested by Bloch[1] who showed that the scattering cross section for neutrons by magnetized iron should be different for the two possible orientations of the neutron spin relative to the magnetic field. The difference in cross sections implies that a neutron beam, after passing through magnetized iron, should have a preponderance of neutrons with spins orientated in the same direction. In this way almost complete polarization could be produced in a very thick block of magnetized iron. The difference in cross section was shown by Bloch to arise from the term in the intensity caused by the interference of the neutron wave scattered by the magnetic field of the iron atom with the wave scattered by the nucleus. It was suggested that neutron polarization experiments would give valuable information on the interaction of neutrons with electrons and on the nature of ferromagnetism.

The earliest experiments to demonstrate the production of neutron polarization by passage through magnetized iron were performed by Hoffman, Livingston and Bethe,[2] by Frisch, von Halban and Koch,[3] and by Powers *et al.*[4] These experiments showed very small effects which indicated the polarization of neutrons but the results were such that quantitative interpretation was very difficult. Some later experiments of Powers[5] showed qualitative agreements with the theory but again the effects were so small that any detailed comparison was impossible. In 1939 Alvarez and Bloch[6] used the polarization of neutrons to determine the value of the neutron magnetic moment. In this work they were able to obtain effects somewhat larger than in the earlier experiments. Later, Bloch, Hammermesh, and Staub[7] made the first investigation of the

* Declassified (in sections) 4/24/47, 3/7/47, 12/22/47.

[1] F. Bloch, Phys. Rev. **50**, 259 (1936); **51**, 994 (1937).

[2] Hoffman, Livingston, and Bethe, Phys. Rev. **51**, 214 (1937).

[3] Frisch, von Halban, and Koch, Nature **139**, 756 (1937); Nature **140**, 360 (1937); Phys. Rev. **53**, 719 (1938).

[4] Powers, Carroll, and Dunning, Phys. Rev. **51**, 371, 1112 (1937); Dunning, Powers, and Beyer, Phys. Rev. **51**, 382 (1937).

[5] P. N. Powers, Phys. Rev. **54**, 827 (1938).

[6] L. Alvarez and F. Bloch, Phys. Rev. **57**, 111 (1939).

[7] Bloch, Hammermesh, and Staub, Phys. Rev. **64**, 47 (1943).

process of polarization in which results were obtained which were large enough to permit careful comparison with theory. Although the polarization effects obtained were somewhat larger than the theory predicted, the qualitative theoretical results could be verified quite well.

On the theoretical side, the initial suggestion of Bloch was followed by more detailed analysis of Schwinger[8] and especially of Halpern and co-workers.[9] The complete theoretical calculation of the polarization is quite complicated, as it requires detailed knowledge of the distribution of the magnetic scattering caused by the orbital electrons (form factor), as well as the calculation of the somewhat complicated crystalline effects in the iron. A short review of the main results will be given here but the reader is referred to the excellent papers of Halpern *et al.* for the complete theory.

The scattering in iron is caused not only by the usual nuclear scattering, which is isotropic, but also by the orbital electrons because of the interaction of the electron spins with the neutron magnetic moment. The magnetic scattering shows a marked angular dependence and a reversal of sign for the two possible orientations of the neutron spin relative to the magnetic moment of the atom (parallel or antiparallel). The coherent scattering in a microcrystalline substance (which is the major part of the scattering as will be seen later) is obtained by adding the amplitude of the scattered waves, both nuclear and magnetic, and squaring the resultant amplitude. In the summation, of course, contributions are obtained only for microcrystals orientated at such angles that the Bragg conditions of scattering obtain.

If the iron is unmagnetized, that is, if the magnetizations of the various domains are at random, then there is no preferential scattering depending on orientation of neutron spin in the incident beam. If, however, the iron is completely saturated, the scattering cross section can be written in the following way for the two spin orientations:

$$\sigma = \sigma_0 \pm p. \tag{1}$$

The total cross section σ, the cross section σ_0 for unmagnetized iron, and the polarization cross section, p, all depend on neutron velocity in a complex way because of the crystal effects. Because all the cross sections of Eq. (1) are made up of the coherent scattering only, they will disappear completely for neutrons of wave-length great enough so that no Bragg reflections are possible. This critical wave-length is 4.04A for iron.

The polarization effects are thus calculated only for the coherent part of the iron scattering. It is true that some of the iron scattering is incoherent; this incoherent scattering is caused by (a) presence of isotopes, (b) spin dependent scattering, (c) inelastic scattering, and (d) crystal irregularities. If the incoherent scattering in iron is the result of (a) and (b) only, then no additional polarization will be caused by the incoherent scattering. However, if the incoherent scattering is caused by (c) and (d), then polarization effects will be present in the incoherent scattering as well. Because of the possible polarization effects in the incoherent scattering it would be necessary to understand the nature of the incoherent scattering to present a complete picture of neutron polarization. However, the fact that only a small part of the scattering is incoherent means that the limitation of the theory to coherent scattering is not a serious inadequacy.[10]

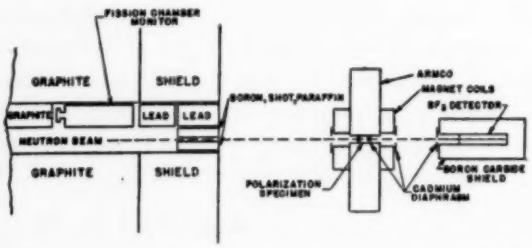

FIG. 1. Apparatus for measurement of single transmission effect, E.

[8] J. Schwinger, Phys. Rev. **51**, 544 (1937).

[9] O. Halpern and M. Johnson, Phys. Rev. **55**, 898 (1939); O. Halpern and T. Holstein, Phys. Rev. **59**, 960 (1941); Proc. Nat. Acad. Sci. **28**, 112 (1942); O. Halpern, M. Hammermesh, and M. Johnson, Phys. Rev. **59**, 981 (1941); M. Hammermesh, Phys. Rev. **61**, 17 (1942).

[10] O. Halpern, Phys. Rev. **72**, 261 (1947), has recently suggested the incoherent polarization as a method of study of the inelastic scattering. His suggestion was based on the finding of Shull and Wollan, Phys. Rev. **72**, 168A (1947), that inelastic scattering in crystals was surprisingly large. Although the inelastic scattering is certainly not large in iron (as shown in Section II) it is still possible that the experiment suggested by Halpern is feasible and it is planned to do work along that line.

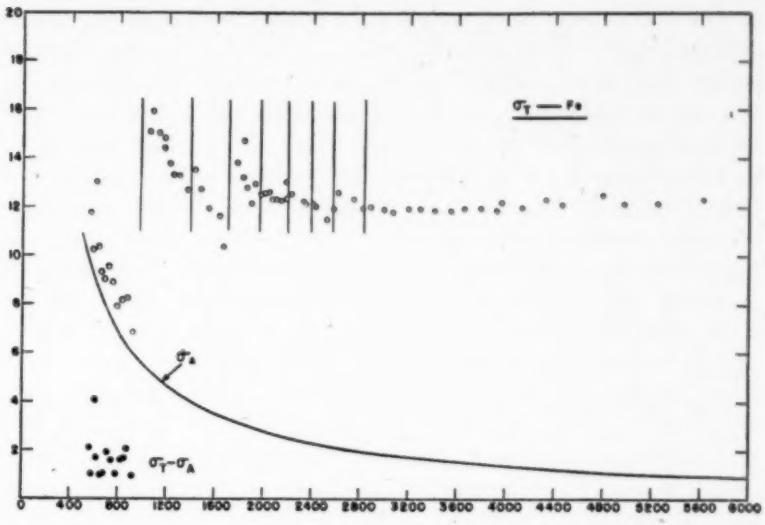

FIG. 2. Total cross section of iron as a function of neutron velocity (in meters/sec.). The points marked $\sigma_T - \sigma_A$ show the amount of incoherent scattering.

Halpern *et al.* have calculated the polarization cross section p as a function of neutron velocity, obtaining a value of about $1b$ averaged over the thermal velocity spectrum, and have shown the relationship between p and the amount of polarization produced in a block of magnetized iron. The most direct way to detect the polarization is by means of the relative increase in transmission of an iron block upon magnetization. This relative increase is called the single transmission effect E_s, and it depends on the polarization cross section p according to the equation

$$E_s = \cosh Npd - 1 \approx \tfrac{1}{2}(Npd)^2, \qquad (2)$$

where N is the number of iron nuclei/cm^3, and d the thickness of iron in cm. The quantity E_s of Eq. (2) refers to the transmission effect that would be obtained if the iron were completely saturated. If the iron is not quite saturated, as is always the case experimentally, then the small regions whose magnetizations are not in line with the applied field will have a serious effect in depolarizing the neutron beam. The result of depolarization is that the actual effect observed is related to E_s in the following way:

$$E = E_s f(x); \quad x = \lambda/\epsilon d. \qquad (3)$$

$f(x)$ is a saturation function (shown in Figs. 3 and 5) which depends on the degree of magnetization (ϵ is the fractional departure from saturation), the grain size of the iron (λ is a length related to the grain size), and the thickness of the iron block, d. Actually, Eq. (3) is a close approximation to the exact formula** given by Halpern and Holstein (their Eq. (9.4a)).

The general objectives of measurements with neutron polarization are (1) a measurement of the polarization cross section p to see how it compares with the theoretical expectation, (2) a study of the polarization phenomenon as a function of material, grain size, magnetization, etc., and (3) the use of polarized neutrons for the determination of magnetic properties as well as nuclear properties which depend on spin orientation. The earlier experiments had been hampered greatly by the lack of intense neutron beams, and it was felt that with the availability of much stronger beams at the Argonne chain reacting pile a detailed investigation of the production of polarized neutrons would be of value. Some measurements involving polarized neutrons had already been made at Argonne in the summer of 1946 by Arnold and Roberts[11] in connection with the redetermination of the neutron magnetic moment by the method of Alvarez and Bloch.

II. SCATTERING IN UNMAGNETIZED IRON

A fundamental problem in the study of neutron polarization is the measurement of the polarization cross section, p. If complete saturation of

** Equations (9.4a) and (9.4b) of Halpern and Holstein contain a slight misprint. The factor e^{-ps} should be written $e^{-ps/2}$ in each case.

[11] W. Arnold and A. Roberts, Phys. Rev. **71**, 878 (1947).

the iron block could be obtained, then p could be measured very easily by the use of Eq. (2). However, because complete saturation is never obtained it is necessary to extrapolate from the actual E to E_s in order to get the value of p. Also the value of p which results is actually an average over the distribution of neutron velocities used because intensities are usually low enough so that monoenergetic neutron beams cannot be used. In making the extrapolation to E_s it is necessary to know the shape of the neutron distribution and the change in this shape as the neutron beam passes through the iron blocks. For this reason and because it is important to know how much of the scattering in iron is coherent, it was felt important to study in some detail the scattering in unmagnetized iron before attempting a complete analysis of the production of polarized neutrons in magnetized iron.

The neutron beam used in the present experiments is one obtained from the thermal column of the Argonne deuterium moderated chain reacting pile (Fig. 1). The neutrons in the beam are those moderated by collisions with graphite of sufficient thickness so that they are in approximate thermal equilibrium. If the neutron distribution is Maxwellian, then the number of neutrons of velocity v will be proportional to $v^2 \exp(-v^2/v_0^2)$, where v_0 is the most probable velocity, and the flux (nv) will be proportional to $v^3 \exp(-v^2/v_0^2)$. The detector is a BF_3 proportional counter and such a detector, if very thin, has a sensitivity proportional to $1/v$. Thus the neutron intensity detected by the counter in such a case will again be proportional to the Maxwell distribution, $v^2 \exp(-v^2/v_0^2)$.

The neutron distribution in the beam was measured first using a mechanical velocity selector[12] ("chopper") and a B^{10} enriched BF_3 counter. The neutron distribution was shown by the chopper measurements to be approximately Maxwellian with a most probable velocity, v_0, about 2250 meters per sec. (The standard value of v_0 for room temperature neutrons is 2200 m/sec.) However, because of the finite resolution of the chopper it is difficult to infer the actual neutron distribution from the measured distribution. Because of the difficulty of determining the neutron distribution accurately with the chopper and because a distortion in the distribution is caused by the fact that the detector used was not thin enough to be an ideal $1/v$ detector, additional experiments were performed to determine the actual distribution and the effective distribution used in the experiments.

The most probable velocity of the neutron distribution as measured by a thin detector was determined by measuring the transmission of the beam through a piece of calibrated Pyrex using a thin $1/v$ detector. The transmission of this Pyrex plate as a function of neutron velocity had already been determined with the "chopper." Assuming a Maxwell distribution, it is possible to calculate v_0 from such a transmission experiment using the correction for hardening of the beam in the Pyrex as calculated by Bethe.[13] The transmission measured in this way gave the most probable velocity for the incident neutron beam as 2180 meters per sec., in excellent agreement with the theoretical value for room temperature of 2200 m/s.

The actual detector used for the polarization work (the enriched counter mentioned above) is less sensitive for low neutron velocities because it is not thin and hence, in effect, shifts the spectrum to somewhat higher energies. The effective neutron distribution as detected by the counter was calculated from the pressure of BF_3 gas in the counter and the cross section of boron, and it was found that the resulting distribution was very closely a Maxwellian again with a most probable velocity of 2250 instead of 2180 m/s. The value of 2250 thus checks the value obtained with the chopper. The transmission of the Pyrex plate was then calculated for this modified Maxwell distribution (as seen by the counter), the transmission through Pyrex again measured using the actual counter and it was found to be the same within the small experimental error as the calculated value. The results thus showed quite conclusively that the neutron distribution as used in the experiments could be taken to be very nearly a Maxwell distribution with a most probable velocity of 2250 m/s while

[12] The design of the rotating shutter velocity selector is given by T. Brill and H. Lichtenberger, Phys. Rev. 72, 585 (1947).

[13] H. A. Bethe, Rev. Mod. Phys. 9, 136 (1937).

the true neutron distribution in the beam had a most probable velocity of 2180 m/s.

In order to determine the change in the neutron spectrum with transmission through iron and also to determine how much of the scattering was coherent, a set of experiments was carried out on the iron cross section as a function of velocity. These experiments were performed using the chopper in the standard manner for the determination of total cross section as a function of velocity by transmission. The total cross section for a sample of Armco iron thus measured is shown in Fig. 2. It is seen that the total cross section is about 12 barns for high neutron velocities and with lower neutron velocities the cross section becomes irregular, as is to be expected from crystal effects. Below 1000 m/s there is a sudden drop in total cross section, then a rapid rise as the velocity becomes even lower. The short vertical lines represent the velocities at which discontinuities in the iron cross section are to be expected when the neutron wave-length exceeds twice the lattice spacing for a particular set of Miller planes. The last discontinuity is expected at 980 m/s (4.04A) as calculated from the lattice spacing for iron.

For neutron velocities less than the last cut-off value of 980 m/s, the cross section is caused only by incoherent scattering and capture. The neutron capture cross section was measured for the same iron sample by observing its effect on the reactivity of the graphite pile (danger coefficient method of measuring absorption cross sections) with the result that the absorption cross section is 2.5 b at 2200 m/s. Knowing the value of the absorption at 2200 meters per second and assuming a $1/v$ dependence, the solid line labeled σ_A can then be drawn. When the absorption is subtracted the points $\sigma_T - \sigma_A$ are obtained. These points show that the incoherent scattering in the region 400 to 1000 meters per sec. is about 1.5 barns and is roughly constant with velocity. If it is assumed that the incoherent scattering is 1.5 b at thermal energy also, it is possible to calculate the amount of coherent scattering at thermal energies. The coherent scattering at 2200 m/s is thus 12 b minus 2.5 b for absorption and 1.5 b for incoherent scattering giving 8 b for the coherent scattering cross section. The value of 1.5 b for the incoherent scattering is much less than that found by Whitaker[14] (3.5 b) which was used by Halpern in his theoretical calculation of neutron polarization. However, the present analysis is in good agreement with the value of 8.1 b for the coherent scattering cross section found by Fermi[15] in his work on the total reflection of neutrons from an iron mirror. The small value of the incoherent scattering means that it is unnecessary to assume that the scattering amplitudes for the different iron isotopes are of opposite sign as was assumed by Halpern. The fact that the incoherent scattering is small is also relevant to the discussion of reference 10 of the present paper.

The scattering cross section curve of Fig. 2 was used to calculate the change in shape of the neutron spectrum with penetration through iron. In this way the spectrum was calculated for various values of the iron thickness up to 6 cm. Knowing the shape of the spectrum at each d value, it was then possible to calculate the average value of the polarization cross section p which was appropriate for each particular iron thickness used in the polarization experiments. The effect of the change in shape, on "hardening" of the spectrum is to lower the average value of p as d increases.

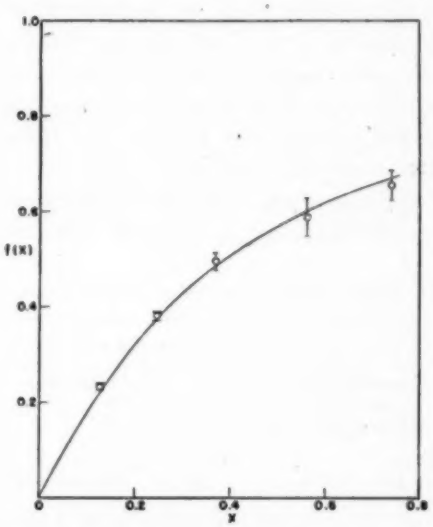

FIG. 3. The single transmission effect as measured in Armco iron. The function $f(x)$, which is the ratio of the observed to the saturated effect for a cross section of 3 barns, is shown for blocks of different thicknesses.

[14] M. D. Whitaker and H. G. Beyer, Phys. Rev. 55, 1101 (1939).
[15] E. Fermi and L. Marshall, Phys. Rev. 71, 666 (1947).

TABLE I. $H=7000$ oersteds, Armco.

d, cm	E(percent)
1.0	2.0±0.1
1.3	3.1±0.2
2.0	5.9±0.2
3.0	10.1±0.2
6.0	25.4±0.3

III. SINGLE TRANSMISSION EFFECT IN ARMCO IRON

In order to determine E_s it is necessary to measure E and then extrapolate to the saturated value by means of $f(x)$. If E is measured for different values of x, then the results can be fitted to the $f(x)$ curve of Fig. 3, assuming various values of p. In this way the extrapolated value E_s and hence p, can be determined. As x is equal to $\lambda/\epsilon d$, the value of x can be changed by changing λ, ϵ, or d. Bloch, Hammermesh, and Staub kept λ and d constant (using only a single block) and varied ϵ by changing the magnetic field H. In fitting their results to the $f(x)$ curve they had thus two adjustable constants, λ and p. They found that their results could be made to fit the $f(x)$ curve with a p value of 2.0 barns.† The difficulty in this procedure is that it is extremely hard to measure ϵ accurately, especially for high values of H. In the present work it was decided to vary d and keep ϵ constant by using the same value of the magnetizing field H for the different d values. In fitting the $f(x)$ curve there would then be the two disposable constants p and the ratio λ/ϵ.

The apparatus used for the measurements is shown schematically in Fig. 1. The neutron beam emerges from a 4-in.×4-in. hole in the thermal column of the pile. The electromagnet has exciting coils which operate at 2000 volts; the current is supplied by electronically regulated power supplies fed by 110 a.c. The total power dissipation is 3 kilowatts and at this power sufficient cooling is obtained by several fans placed near the magnet. The iron blocks are 1.2 cm high, 2 cm wide, and d cm in length while diaphragms of cadmium delineate a beam 1 cm square at the iron blocks. The neutron detector is an 8-in. long BF_3 proportional counter filled to a 20-cm pressure with enriched boron and placed so that the neutron beam passes down the axis of the counter. Even though the intensity in the beam is quite steady it was found necessary to monitor the beam to secure the desired accuracy. The monitor used was a fission ionization chamber placed just inside the graphite of the thermal column and counting rates were always recorded in terms of counts per monitor count. Careful checks were made to insure that the drop in voltage caused by the magnet current did not affect the counting rate of the BF_3 counter or the monitor counter. In order to determine whether the magnet caused any change in the counting rate aside from the polarization effect, a zero check was made by using a brass block instead of an iron block with all other conditions unchanged. With such an arrangement it was found that there was no change in the transmission with application of the magnetic field.

TABLE II. Single transmission effect for different materials.

$d=3$ cm	$H=11{,}000$ oersteds	
Swedish iron	9.8 percent	
Armco iron	13.0	
Hot-rolled	16.6	
Cold-rolled:		
H direction	E	(Neutron direction)
A	22.7 percent (B)	22.2 percent (C)
B	19.6 (A)	18.8 (C)
C	16.3 (A)	17.1 (B)
45° to A and B	19.1 (C)	

Measurements of the single transmission effect were made for the various block thicknesses d, keeping the magnetic field H equal to 7000 oersteds for each block by adjusting the magnet current; the field was measured at the surface of the block by a small search coil and flux meter. The values of the single transmission effect obtained are shown in Table I, with standard errors computed from the number of counts.

In order to compare the experimental values with the $f(x)$ curve it is necessary to consider the changing shape of the neutron distribution with d. In order to make this correction, the average value of p was calculated for the appropriate neutron distribution determined by the method described in Section II. In calculating the average p it was assumed that p varied with

† The p value was raised to about 2.2 b in some later work: F. Bloch, R. I. Condit, and H. H. Staub, Phys. Rev. 70, 972 (1946).

neutron velocity as shown by the theoretical curve calculated by Halpern. The effect of the hardening is that the average p decreases with d and that the saturated effect for a certain d is less than would be expected if the Maxwell distribution remained unchanged through the iron block. The expected saturated effect corrected for this "hardening" of the neutron distribution is called $E_{S,H}$ and it was calculated for different values of p for the various d's used. The ratio of the experimental E to $E_{S,H}$ is the experimental $f(x)$ and the values were fitted to the $f(x)$ curve, assuming different p values and adjusting the constant λ/ϵ for each particular p. The best fit was obtained for a p of 3.0 ± 0.2 b and a λ/ϵ of 0.74 cm as shown in Fig. 3. The value of p is surprisingly high when compared with the expected value of 1.1 b from Halpern's calculation and with Bloch's experimental value of 2.0 b.

In fitting the experimental points to the $f(x)$ curve it is assumed that x values are inversely proportional to d. This is actually correct only if all velocities in the distribution have the same x value. If the x is different for various velocities, then it would be necessary to calculate an average x for the neutron distribution, and as this average x would be different for different d's (because of hardening of the beam) it would no longer be correct to assume that x would be simply proportional to $1/d$. Because λ depends on velocity if the grain size is below a certain critical size (about 0.5×10^{-3} cm, see Section VII) but is independent of velocity above the critical size, the correctness of Fig. 3 depends on the grain size in Armco. Bloch assumed that the grain size in his experiments was less than the critical size but the assumption is made here that the grain size is above the critical size. A direct determination of the grain size for the Armco blocks was made for us by Mr. H. Paine, of the Argonne Laboratory, and by Dr. J. Berger, of the University of Pittsburgh, with a resulting average grain size of 7×10^{-3} cm which is well above the critical size. If it is assumed that the grain size is small and Fig. 3 changed accordingly, the resulting p value would be about 0.2 b higher.

It is noteworthy that the values of $f(x)$ for all the blocks are distinctly less than unity and the possibility suggests itself that the high p value might be due to a misinterpretation, that is, that the $f(x)$ values are really much closer to unity and hence p much smaller than 3.0 barns. The work to be described in the next section was designed in order to eliminate this possibility by obtaining higher values of $f(x)$ and lessening the amount of extrapolation involved in obtaining E, and p.

TABLE III. $H=12{,}000$ oersteds, cold-rolled steel.

d, cm	E, percent
0.7	1.5 ± 0.2
1.0	2.9 ± 0.2
1.7	7.7 ± 0.3
3.0	20.1 ± 0.4
6.0	59.9 ± 0.6

IV. MEASUREMENT OF p FOR COLD-ROLLED STEEL

Because the values of $f(x)$ obtained for Armco were substantially less than unity, it was decided to attempt to get higher values of x by obtaining an increase in the ratio λ/ϵ. It is very difficult to estimate in advance what materials will give high values for this ratio because of the complicated dependence of both λ and ϵ on material. As far as grain size is concerned, it is to be expected that going to either very large or very small grains would give an increase in x (see Section VII). In fact the grain size for Armco happened to be such that λ was quite small. However, using materials of larger grain size could result in smaller values of x because the ϵ obtained for a given field might be much larger.

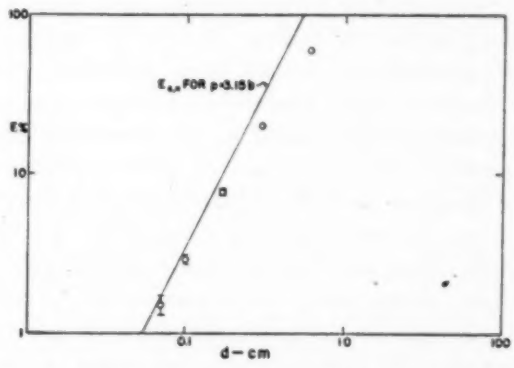

FIG. 4. The single transmission effect, E, for cold-rolled steel as a function of block thickness. The solid line shows the theoretical value for saturated iron for a p of 3.15 barns.

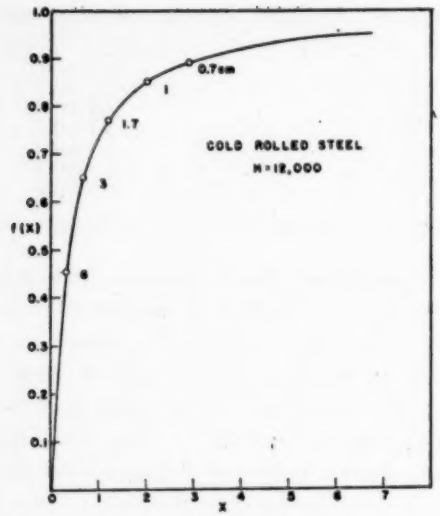

FIG. 5. The saturation function $f(x)$, and the experimental values for cold-rolled steel which lead to a p value of 3.15 barns.

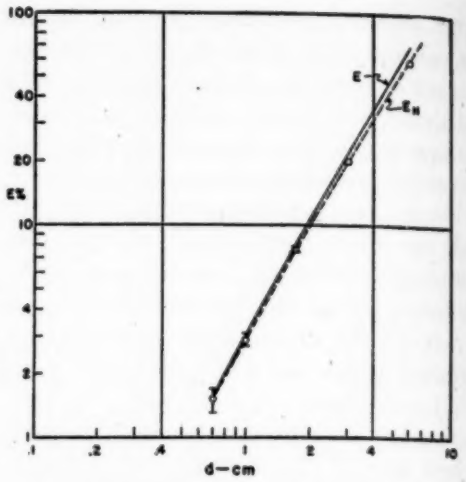

FIG. 6. Experimental values of E compared to the exact calculations for a p of 3.15 barns. E_H is the calculated curve corrected for hardening of the neutron beam.

In order to make a rapid survey of materials, various samples of iron and steel were selected and the single transmission effect was measured for each material using a d of 3 cm and an H of 11,000 oersteds (a substantial increase over the field of Section III). The values of E obtained for the different materials are listed in Table II. It is obvious from Table II that Armco is by no means the best material for production of polarized neutrons and that, of the samples tried, cold-rolled steel is the best. Several blocks of cold-rolled steel were cut to investigate the directional properties of the polarization and the results of these tests are shown in the second part of Table II. The blocks were cut so that the magnetic field was in the direction of rolling (A), perpendicular to the direction of rolling but in the plane of the rolling (B), and in the direction perpendicular to the plane of rolling (C). For each of these directions of magnetization, the neutrons were passed in two directions also. The data in Table II show that the largest effects were obtained with H in the direction of rolling with no evident variation depending on the neutron direction. The direction B gave intermediate results and C the lowest values; neither of these cases shows any variation with neutron direction. All these results are most simply interpreted as being caused by variation in ϵ, this quantity being the smallest when the magnetization is in the direction of rolling. Apparently any difference in effective grain size depending on the direction of neutron propagation is not very important.

In order to determine the value of p for cold-rolled steel, a series of blocks were cut of different d values such that H would always be in the direction of rolling. The single transmission effects measured for these blocks with a magnetic field of 12,000 oersteds are listed in Table III and are plotted against d in Fig. 4. In Fig. 4 the values for small d's show a slope of nearly 2 which means that the effect is proportional to d^2 at small thicknesses. The fact that proportionality to d^2 is obtained means that $f(x)$ must be very close to 1, for it is only when $f(x)$ does not change with d (that is with x) that a proportionality to d^2 would be observed. The solid line in Fig. 4 is the expected saturated effect corrected for hardening (as described in Section III), assuming a p value of 3.15 b. The points for small d fall very close to the solid line, showing that high values of $f(x)$ were obtained for these thicknesses. The decreasing values of $f(x)$ with increasing d are shown by the dropping off of the points below the solid line. The same results are shown in Fig. 5 where the data are plotted in terms of $f(x)$, again for a p of 3.15 b. Here, as for Armco, x is taken as inversely proportional to d; in other words, it is assumed that the grains are above the critical size. However,

metallographic examination (Section VI) as well as direct experiments with polarized neutrons (Section VII) show that the grain size is large for cold-rolled steel. The experimental $f(x)$ values fit the theoretical curve very well and the resulting λ/ϵ is 2.03 cm, much higher than for Armco. The error in p, estimated by varying p for the $f(x)$ curve, is 0.1 b.

As was stated in Section I, Eq. (3) which was used for Fig. 5 is not quite exact, so the exact values of E were calculated from Halpern and Holstein's formulas. The solid line of Fig. 6 shows the exact values of E for $p=3.15$ and $\lambda/\epsilon=2.03$ while the dotted line includes the correction for hardening. The experimental points agree extremely closely with the latter curve. In conclusion, the work with cold-rolled steel substantiates the high p value obtained from Armco and makes it much more certain because $f(x)$ values were obtained which were much closer to unity. There is very little doubt that the magnetic interaction between neutrons and iron atoms and the resulting polarization are much greater than would be expected from theory.

V. POLARIZATION AS A FUNCTION OF NEUTRON VELOCITY

As discussed in Section I, the polarization cross section p is a complicated function of neutron velocity, changing discontinuously as different Miller planes become effective and decreasing suddenly for neutron wave-lengths for which no Bragg reflections are possible. The work already described had shown that the actual value of p, averaged over the Maxwell distribution, was much larger than expected theoretically, and it was felt important to investigate the values of p for monoenergetic neutrons as well.

In order to study p as a function of velocity, the experimental set-up was modified by addition to the chopper velocity selector. All the velocity selector measurements were made with a single piece of iron, a sample of cold-rolled steel of the same type used for the measurements of Section IV, with a d of 1.3 cm. The method of using the chopper to obtain narrow velocity bands of neutrons will not be described here because it is discussed in the paper of Brill and Lichtenberger. The instrument was first used with low resolution in order to make a rapid survey of a large velocity range. This survey showed that the single transmission effect increased with decreasing neutron velocity as expected, then decreased suddenly to extremely low or zero values at velocities below about 1000 m/sec. These results indicated that the theoretical curve for the variation of p with velocity was qualitatively correct and could be used as a guide in more detailed investigations.

As the region just above the cut-off is of particular importance from the theoretical standpoint (only one set of planes is involved and the form factor is constant), the region from 980 to 1380 m/sec. (the 110 planes) was studied with high resolution. The values of E measured are shown in Fig. 7 where the solid line is the E that would be expected for a d of 1.3 cm based on the theoretical curve of Halpern, assuming $f(x)=1$. It is obvious that the experimental curve behaves qualitatively according to theory, but is very much greater in magnitude. In order to

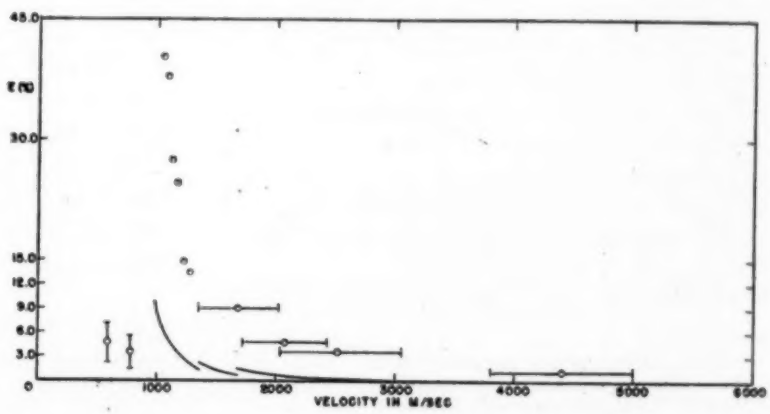

FIG. 7. The single transmission effect for a 1.32-cm block of cold-rolled steel as a function of neutron velocity. The solid curve is Halpern's theoretical curve.

see if the results for monoenergetic neutrons were consistent with those for the thermal distribution, the curve of Fig. 7 was integrated over the Maxwell distribution (of $v_0 = 2250$) with a resulting E of 5 percent. From Fig. 6 it is seen that 5 percent of a d of 1.3 cm agrees with the earlier thermal distribution measurements.

It is obviously of great interest to investigate whether any change in the theoretical treatment can account for the large quantitative difference between theory and experiment for the values of Fig. 7. Any changes in form factor of the iron atom would have to be quite large in order to explain the discrepancy. While it is not intended at present to attempt the determination of the magnetic form factor experimentally, it is worth pointing out that an increase in the theoretical factor would be relatively larger at high velocities. There is some evidence from Fig. 7 that the ratio of the experimental to the theoretical values is larger at high velocities in line with the behavior to be expected from a larger form factor. However, Sachs[16] has shown that a decrease in the size of the iron atom by a factor of 4 would be necessary to give p values as large as those actually observed. Halpern[17] has stated recently that some assumptions made in the theory are no longer true for such high p values as the experimental ones and correction to the theory for these assumptions might change the theoretical predictions by a sizeable amount. Wick[18] has pointed out that the assumption of randomly orientated crystal grains of the Halpern theory might not be correct for rolled steel and that a favorable distribution of grain orientation might cause a marked increase in magnetic scattering.††

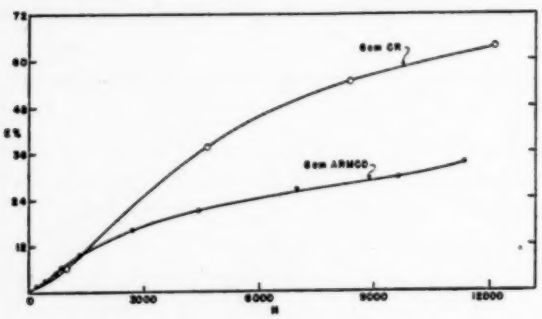

FIG. 8. The single transmission effect for different values of the magnetizing field, H.

As the theoretical curve is based only on coherent scattering it is zero below 980 m/sec. The experimental points on the other hand show a small single transmission effect at velocities below the cut-off. The existence of polarization for velocities below the cut-off means that there must exist scattering caused by crystal irregularities or inelastic scattering. This follows from the fact discussed in Section I that of the possible causes for scattering below the cut-off ("residual" scattering) only the above two possibilities would result in production of polarization. The question of the existence of polarization below the cut-off velocity is of interest[10] because of the fact that it reveals something of the nature of the incoherent scattering in iron, but it is difficult to investigate because the intensity of such slow neutrons is very low. Additional measurements were made at low velocity using BeO and graphite filters to produce slow neutron beams instead of the chopper. The filters can produce low velocity neutrons of moderate intensity even though the neutron distributions are not truly monoenergetic. Thus the BeO filter produces a neutron group of velocity about 700 m/sec., and the graphite filter a group of about 500 m/sec. The filtered neutrons showed a single transmission effect of about the same magnitude as the velocity selected neutrons but it could not be measured accurately. Recently Fryer[19] has published results of polarization measurements with cyclotron velocity selected neutrons down to 1300 m/s in velocity. He finds about a threefold increase over the thermal E for this range but his p values are much less than the present ones.

VI. THE APPROACH TO MAGNETIC SATURATION

When the polarization cross section p is known, then it is possible to obtain $f(x)$, and x, values by measuring the single transmission effect. In this way variations of the quantities entering into x, that is λ and ϵ, can be studied. The quantity ϵ shows the fraction of the magn[illegible]

[16] R. G. Sachs, private communication.
[17] O. Halpern, private communication.
[18] G. C. Wick, private communication.

†† J. Steinberger and G. C. Wick have recently made a series of corrections to the theoretical p value with the result that agreement with the present experiments is obtained (Bull. Am. Phys. Soc. **23**, 9 (1948).

[19] E. M. Fryer, Phys. Rev. **70**, 235 (1946).

ization in the iron which is not lined up with the magnetizing field H. Thus, measurements of x can be used to determine the departure of the magnetization from the saturation value. In ordinary magnetic measurements the departure from saturation is never measured directly but only the increase in magnetization as H is increased. In the ordinary measurements, therefore, it is always necessary to assume some law for ϵ as a function of H in order to extrapolate to infinite H in obtaining the saturated value of the magnetization. Because the quantity ϵ as measured by the neutron polarization shows directly how much of the magnetization is still not aligned, the method should give valuable information on the law of approach to magnetic saturation with increasing H.

As x is very sensitive to small changes in $f(x)$ when the latter is near unity (that is for small d values) it is much better to work with small $f(x)$ values (large d's) in order to measure x from observed changes in $f(x)$. Hence, for the measurements made to study the law of approach to magnetic saturation, 6-cm blocks of iron were used and values of E were measured as a function of magnetizing field H. Figure 8 shows the data for Armco and cold-rolled steel in the most obvious manner, E as a function of H. The values of $f(x)$ as a function of H were calculated directly from the ratio of E to E_s and x obtained from the analytical form of $f(x)$. The reciprocals of the x values thus determined are strictly proportional to ϵ, the constant of proportionality being just the ratio d/λ, and Fig. 9 shows $1/x$ for Armco iron plotted against $1/H$. According to ferromagnetic theory[20] it is expected that ϵ should vary as $1/H^2$. Magnetic measurements[20] have shown the $1/H^2$ dependence for moderate values of H (2000 to 6000 oersteds), but a departure from this law in the direction of a smaller exponent of H for higher magnetizing fields. Figure 9 shows a very good $1/H$ dependence for fields ranging from 3000 to 12,000 oersteds and it is only for fields as low as 1000 that the variation becomes more nearly like $1/H^2$. An additional fact of interest is that the straight line does not extrapolate to zero as H becomes infinite. This fact is probably to be interpreted

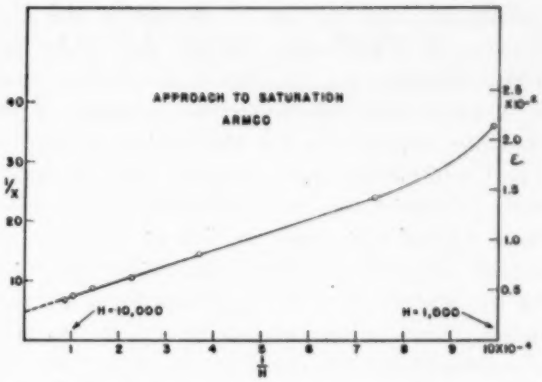

FIG. 9. The directly measured quantity, $1/x$, and the departure from magnetic saturation, ϵ, which is proportional to it, as a function of H.

in terms of a change in the exponent of H to even lower values as H is increased, such as to a $1/H^{\frac{1}{2}}$ behavior. Figure 10 is a similar plot of the measurements made with the 6-cm block of cold-rolled steel and it shows the same dependence on $1/H$ and also the same behavior at very high fields; that is, there is again evidence for a change in the $1/H$ law for high fields. W. F. Brown[21] has given a theoretical basis for laws of approach to saturation other than $1/H^2$ in terms of dislocations.

In the work of Bloch, Hammermesh, and Staub described above, the values of ϵ were determined by measuring changes in the magnetization by standard magnetic methods, which gave only changes in ϵ with changes in H rather than the actual values of ϵ. Values of ϵ were obtained by assuming that the data, which fitted a $1/H^2$ law for the region in which the magnetic measurements were made, continued to obey this law to saturation. If the findings of the present work are correct, it can be concluded that Bloch's method of getting the actual values of ϵ would be subject to error, and in a direction such that his assumed values of ϵ would be too small. The effect of such an error in ϵ would be that the resulting p value would be too small.

In order to use the polarization measurements as a basis for the determination of the actual magnitude of ϵ it is, of course, necessary to know λ. Values of λ (half the grain size) have been determined by metallographic examination of the blocks by Mr. H. Paine of the Argonne

[20] R. Becker and W. Doring, *Ferromagnetismus* (Verlag Julius Springer, Berlin, Germany, 1939) p. 167.

[21] W. F. Brown, Phys. Rev. 60, 139 (1941).

Laboratory and by Dr. J. Berger of the University of Pittsburgh. While the grain size determinations are necessarily somewhat rough in nature, they do allow an estimate of the absolute values of ϵ for the materials studied. The λ's obtained were 3.55×10^{-3} cm for Armco and 1.7×10^{-3} cm for cold-rolled steel. From these values it is then possible to calculate the actual values of λ which is done for Figs. 9 and 10 by placing a scale of values for ϵ on each figure. Thus, within the accuracy of the grain size determinations, these figures show the actual values of the departure from magnetic saturation as a function of applied field. The superiority of cold-rolled steel over Armco in producing polarized is shown in Figs. 9 and 10 to be caused by the much smaller ϵ for the former, which more than compensates for the larger grain size of the Armco.

VII. GRAIN SIZE

The quantity λ in the expression for $f(x)$ is related to the grain size of the iron blocks. However, the relationship is not unique for a given value of λ may correspond to either of two values of the actual grain size δ. The relationship between λ and δ changes when the grain size passes a critical size, l, which is twice the distance traversed by a neutron in one radian of the Larmor precession. The critical grain size, l, is about 7×10^{-4} cm for thermal neutrons. If δ is larger than l, then $\lambda\cong\delta/2$. If δ is much less than l then $\lambda\cong l^2/\delta$, and near the critical size λ is about equal to δ. These relationships show that λ increases as δ departs from the critical size in either direction and an ambiguity results when it is attempted to estimate the grain size from a value of λ. Bloch, Hammermesh, and Staub obtained an experimental value of λ and, assuming that δ was less than the critical size, calculated δ as 1.4×10^{-4} cm.

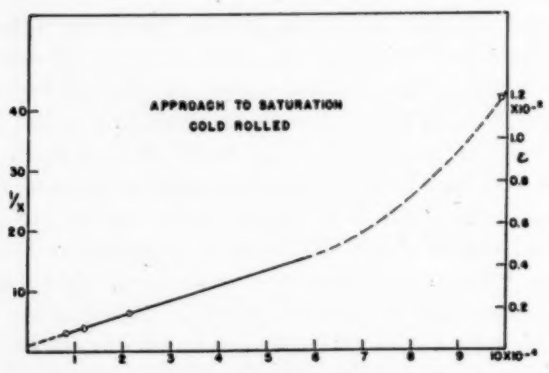

FIG. 10. The same material as Fig. 9, for cold-rolled steel.

The quantity δ considered here is the average length of the regions in the iron in which the magnetization is constant. For highly magnetized iron δ is not the size of the usual magnetic domain but is to be interpreted as the grain size. The magnetization in the polarization experiments is so nearly complete that the region of the B-H curve in which the usual magnetic domains are evident (the region of the Barkhausen effect) has been passed, and further increase of the magnetization is caused only by rotation of the magnetic vector (uniform throughout each crystal grain), toward the direction of the applied field. If this view is correct, then it should be possible to relate the values of δ as determined in the polarization experiments with the grain size as determined metallurgically. With the object of correlating the two methods of grain size investigation, several experiments with polarized neutrons were performed and the results compared with standard grain size determinations.

Preliminary grain size determinations based on the polarization experiments gave results that were above the critical grain size, in disagreement with the findings of Bloch. In order to clear up this discrepancy it was decided to perform an experiment designed to discriminate between the small and large grain size possibilities. Use was made of the fact already discussed that for large grain sizes λ is independent of velocity, while for small grain sizes λ is proportional to the square of the velocity. It follows from the shape of the $f(x)$ curve that if ϵ is changed by a certain amount for two velocity groups, then the fractional change in $f(x)$ will be much greater for the group of lower velocity if the grain size is small. If the grain size is large, then the fractional change in $f(x)$ will, of course, be independent of velocity.

The two velocity groups used were the Maxwell distribution (about 2250 m/sec.) and a group on the last Debye-Scherrer ring (about 1140 m/sec.) obtained with the chopper. These two groups differ by a factor of four in v^2. The single

transmission effect for a 1.3-cm block of cold-rolled steel was measured for both groups at a high H value (13,000 oersteds), then H was changed by a sufficient amount (to 4000 oersteds) to give a factor of 2.58 in x. Under such conditions the expected change in $f(x)$ or in the single transmission effect, for the high velocity group, is a decrease to 76 percent of the high field value (calculated from the curves of Figs. 5 and 10) whereas the expected change for the low velocity group would be to 41 percent if the grains are small, and again to 76 percent if the grains are large. The resulting values of the single transmission effect for the low velocity group are shown in Fig. 11. The average change for the points shown is a reduction to 77 percent of the high field value while the change for the thermal group is to 76.5 percent (both results good to about 8 percent). This agreement shows that the grain size is above the critical size because the change for the low velocity group is much less then would have been expected if the grain size were small.

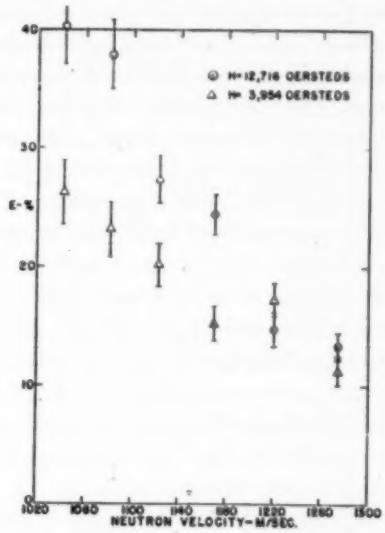

FIG. 11. The single transmission effect for two values of H at velocities just above the cut-off.

As described in Section VI the grain sizes of the Armco as well as the cold-rolled blocks were measured metallographically by Mr. Paine and Dr. Berger. These direct measurements also show that the grain sizes are above the critical size. As the polarization gives only the ratio λ/ϵ it would be necessary to obtain ϵ by a separate magnetic measurement in order to use neutrons for determination of grain size. No measurements of ϵ have been made in this work and it is not possible to say at present whether the single transmission effect alone will be a useful tool for the determination of grain size in ferromagnetic materials. Preliminary attempts to investigate changes in grain size with metallurgical operations such as rolling and annealing have been difficult to interpret because of the fact that both ϵ and λ change with metallurgical treatment.

VIII. CONCLUSION

In view of the fact that the best polarizer of neutrons turned out to be a material which was selected by chance, a survey of various types of iron was made in an attempt to obtain still better polarizers. A variety of irons and steels was tested for polarization, but it was found that none of these was better than the sample of cold-rolled steel which was tried early in the experiments (1020 steel). The efficacy of a material in neutron polarization is determined by the ratio λ/ϵ, and because of the rather complicated dependence of ϵ on mechanical or heat treatment, it is very difficult to estimate in advance what type of treatment will give the maximum polarization. Thus increasing the grain size when it is above the maximum will certainly increase λ, but if in the process the value of ϵ for a given H is increased, then the advantage of the larger grain size might be overcompensated. The determination of the best polarizing material is, of course, intimately related to the study of the approach to saturation of Section VI, and it is intended to extend that study at a later date.

It was found possible to obtain single transmission effects in nickel and the values lead to an estimated p for nickel of about 1 b. This value of p is roughly consistant with the fact that the saturated magnetization of nickel is about $\frac{1}{3}$ the value in iron. Various samples of Permalloy showed single transmission effects which were intermediate to those of nickel and steel. Although the single transmission effects were smaller than those for steel, it was found that E_s could be obtained with very small values of magnetizing field, H, as would be expected from the magnetic properties of Permalloy.

During the course of the work described here a new effect was discovered which interfered with measurements of single transmission for some time. The new effect, which causes large single transmission results when extremely good geometry prevails, is now known to be a small angle scattering (extending to about 1°) which exists for unmagnetized iron, but which disappears when the iron is magnetized. In other words, it is some kind of small angle, magnetic scattering which disappears when the domains (not grains in this case) disappear by alignment. For the present investigation the scattering was investigated sufficiently to insure that it did not affect the results. A much more complete investigation is of course now under way.

Some of the topics investigated in the course of these measurements are worthy of much more extensive effort and it is intended to pursue them further as time permits. At the present time the "double transmission" effect (use of polarizer and analyzer magnets) is being studied, as well as the depolarization of neutron beams by passage through magnetic fields and through thin sheets of unmagnetized iron.

It is a pleasure to acknowledge our indebtedness to the many persons who have been of assistance during these experiments. Professors Bloch, Fermi, Halpern, Sachs, Teller, and Wick have contributed many invaluable discussions. Mr. T. Brill is responsible for the design and construction of all the electronic equipment we have used. Mr. H. Paine and Dr. J. A. Berger have helped greatly in the preparation and metallographic study of specimens. The cross-section curve for iron was obtained with the assistance of Mr. G. Arnold, and Mr. M. Burgy has aided in the later stages of the work.

PHYSICAL REVIEW VOLUME 73, NUMBER 11 JUNE 1, 1948

Proton-Proton Scattering at 7 Mev*

I. H. DEARNLEY,** C. L. OXLEY, AND J. E. PERRY, JR.***
Department of Physics, University of Rochester, Rochester, New York

(Received February 27, 1948)

Scattering experiments have been performed with protons from the cyclotron scattered in hydrogen gas. Photographic plates were used in a camera which recorded simultaneously individual protons scattered at angles from 10.5° to 45°. 5000 tracks were counted in each of nine narrow angular ranges to give good statistical accuracy. An experimentally determined correction was necessary due to proton penetration of the edges of the slits which admitted scattered protons to the photographic plates. The energy of the protons was determined by magnetic deflection and from ionization ranges. Analysis of the results shows an s phase shift somewhat lower than that predicted by extrapolation of the earlier low energy data as analyzed in terms of square well, Gauss, and meson potentials. On the assumption of central p wave scattering the results are fitted by a p phase shift of $-0.22°$ which corresponds to scattering from a repulsive square well with interior Coulomb potential, range e^2/mc^2 and height 2.2 Mev. Extending the Rarita-Schwinger neutron-proton interactions to the proton-proton system for a prediction of tensor ${}^1P$ wave scattering, we find that the experimental results are reconcilable with the "symmetrical" theory and with the "charged" theory as formally constructed by them. The "neutral" theory gives ${}^1P$ scattering in definite disagreement with the experimental results.

I. INTRODUCTION

EXPERIMENTS on the anomalous scattering of protons by protons have been reported in the energy range from 200 to 2400 kev[1–3] with results consistent with nuclear distortion of Mott

* Parts of this work were presented by each author in partial fulfillment of the requirements for the Ph.D. at the University of Rochester.

** Now at General Electric Research Laboratory, Schenectady, New York.

*** Now at California Institute of Technology, Pasadena, California.

[1] N. P. Heydenburg, L. R. Hafstad, and M. A. Tuve, Phys. Rev. 56, 1048 (1939).

[2] Herb, Kerst, Parkinson, and Plain, Phys. Rev. 55, 998 (1939).

[3] G. L. Ragan, W. R. Kanne, and R. F. Taschek, Phys. Rev. 60, 628 (1941).

scattering in the s wave alone.[4] Experiments at 7 Mev should yield information concerning the ^3P state in addition to providing further information concerning the ^1S state. Wilson and co-workers[5] have recently reported on scattering experiments at 8, 10, and 14.5 Mev. Their results give some indication of repulsive p wave effects. The present experiments, which yielded results in substantial agreement with Wilson's, were carried out at a lower energy and by a completely different method.

II. APPARATUS

The photograph of Fig. 1 shows the scattering apparatus in place at the cyclotron. The proton beam was collimated and its energy spread limited[6] by three circular beam defining holes which were 2 mm in diameter and were located as marked in Fig. 1. The first hole located at the cyclotron exit port was covered with aluminum foil to separate the gas atmospheres of the cyclotron and the scattering apparatus. Because of the remaining fringing field, the last beam-defining hole, located at the chamber entry, was offset from the chamber axis so that the beam travel through the part of the chamber effective for scattering recorded protons was closely axial. Because of the fringing field, the beam assumed an elliptical cross section after passing through the last defining hole. In the chamber the collimated beam showed a maximum half-angle spread of 0.36° in the horizontal and 0.17° in the vertical plane. Magnetic effects on the scattered protons were small and were calculated to have negligible effects on the determination of the differential cross sections.

With beam-defining holes aligned for maximum visually observed beam at the last defining hole, a beam current of about 3×10^{-9} ampere entered the scattering chamber. During all experimental operations the cyclotron magnet current was adjusted so that the beam current to the brass surrounding the second beam defining hole was a maximum.

At the left of the chamber, as shown in Fig. 1, a removable back plate held vacuum and gas leads and the Faraday cage. This back plate was replaced by one bearing a glass window in order to align visually for axial travel of the beam through the scattering chamber.

Figure 2 shows a schematic view of the scattering chamber. The beam entered the chamber through the last of the three beam-defining holes and proceeded through the hydrogen, which filled the chamber, into the Faraday cage. Protons scattered by hydrogen passed through the small rectangular "scattering slits" above and below the main beam and entered the photographic plates, as indicated by Fig. 2. The position at which the proton entered the plate determined the angle at which it had been scattered. In the direction perpendicular to the plane of Fig. 2 scattered protons were limited to the central portion of the photographic plates by the slits.

Not shown in Fig. 2 are two plate holders, one above and one below the beam. They were designed to take 1-in.×3-in. photographic plates and to position them accurately with respect to the scattering slits. To define "swath" areas in the photographic plates for track counting, the

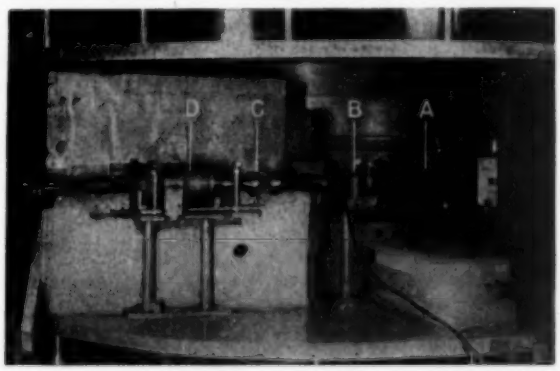

FIG. 1. Scattering apparatus at cyclotron. *A*, *B*, and *C* show the locations of the beam defining holes, respectively, at the cyclotron exit port, in the flexible beam tube, and at the entry to the scattering chamber. The glass sections in the beam tube near the defining holes allowed for observation of the beam on fluourescent materials surrounding the holes, thus simplifying the adjustment of hole position. *D* indicates the scattering chamber proper which is shown in schematic cross section in Fig. 2. The adjustable mounts for the chamber and beam tube are shown, as is part of the paraffin shield used around the chamber.

[4] G. Breit, H. M. Thaxton, and L. Eisenbud, Phys. Rev. **55**, 1018 (1939).
[5] R. R. Wilson and E. C. Creutz, Phys. Rev. **71**, 339 (1947); R. R. Wilson, Phys. Rev. **71**, 384 (1947); Wilson, Lofgren, Richardson, Wright, and Shankland, Phys. Rev. **72**, 1131 (1947).
[6] E. C. Creutz and R. R. Wilson, Rev. Sci. Inst. **17**, 385 (1946).

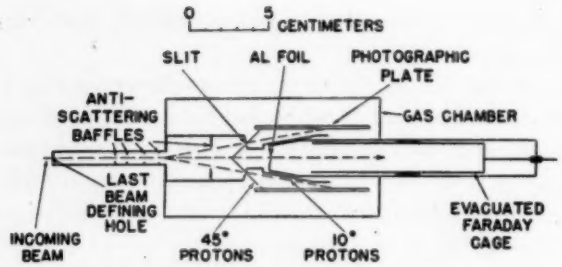

FIG. 2. Schematic drawing of scattering chamber in vertical cross section. All parts are of brass except as indicated and for the four small antiscattering baffles which are aluminum. The first antiscattering baffle at the left shielded the succeeding ones in the neck of the chamber from scattering by the edges of the last beam defining hole. The other neck baffles then prevented the useful part of the photographic plate from seeing any of the wall exposed to scattering from the edge of the first antiscattering baffle. The baffle in the large part of the chamber prevented protons from the last beam defining hole from striking the slits admitting scattered particles to the photographic plates.

plates were exposed before use to light through a grating ruled with lines every 0.25 mm. The lines were parallel to the one-inch edge of the plate. Exposure with an argon glow lamp made developable only the top grains of the emulsion so that during microscopic examination the proton tracks could be followed through these swath defining lines. Identical means of positioning the plates were used in the proton camera, the swath line camera, and the viewing microscope stage.

Difficulty was originally encountered with metallic scattering from baffles and chamber walls. The final baffle design, whose action is explained by the legend of Fig. 2, reduced metallic scattering to a very low level.

The details of the scattering slits are shown in Fig. 3. The plane of the slits was set at 10° to the vertical to favor the 10° scattering, since the number of protons per swath observed in our geometry is considerably higher for larger scattering angles. The form of the scattering slit edges constituted a special problem in the particular method used in these experiments. In conventional scattering experiments counters are normally used which record the scattering at any angle, after rotation to the correct angular position. The analyzer on the counter then has to accept scattering over only a small angular range. In the present experiments information at all angles from 10° to 45° was obtained simultaneously so the scattering slits were designed to present full aperture over this angular range. This accounts for the tapers of the slit jaws shown in Fig. 3. Such tapers had a very distinct disadvantage because they presented a penetrable area to protons. The extent of this area depended on their energy or scattering angle. In order to correct for this penetration, two additional rectangular slits were designed, one narrowed in the vertical direction and the other narrowed horizontally, as shown in Fig. 3. These were mounted at right angles to the "open slits" and were rotated into the active position before the plates for making the "closed slit" runs. Scattering experiments with both types of slits permitted calculation of the penetration effect.

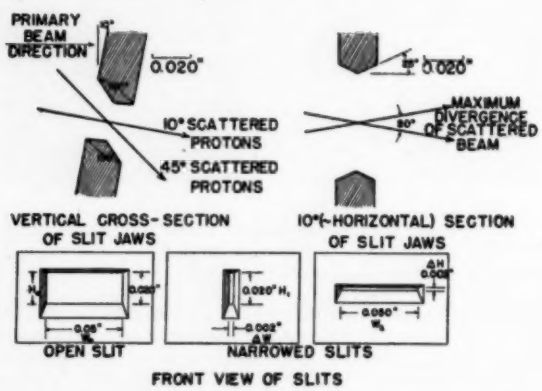

FIG. 3. Details of slits which admit scattered protons to the photographic plates. Dimensions shown are nominal.

The number of protons scattered through an angle Θ into a solid angle $\Delta\omega(\Theta)$ is given by the expression

$$N(\Theta)=\sigma(\Theta)n_t n_i 1(\Theta)\Delta\omega(\Theta), \qquad (1)$$

where $\sigma(\Theta)$ is the laboratory differential cross section per unit solid angle in units of cm², n_t is the number of target hydrogen atoms per cm², n_i is the number of incident protons in the beam, and $1(\Theta)$ is the effective target thickness or scattering length.

Under the assumption that hydrogen obeys the perfect gas law,[7] $n_t=1.4202\times10^{19}s\rho/T$ atoms/cc, where s is the difference in height of the oil levels in the manometer used to measure the hydrogen pressure, ρ is the density of the

[7] The numerical constants of these equations are derived with the values of the atomic constants given by R. T. Birge, Rev. Mod. Phys. 13, 233 (1941), and with the value $g=980.4$ cm/sec.² at Rochester.

manometer oil in grams per cm³, and T is the absolute temperature of the scattering gas. The number of incident protons is given by[7] $n_i = Q/e = 6.242 \times 10^{12} Q$, where Q is the charge in microcoulombs collected during the run and e is the proton charge in microcoulombs. Therefore[7]

$$N(\Theta) = 8.865 \times 10^{31} \sigma(\Theta) 1(\Theta) \Delta\omega(\Theta) R, \quad (2)$$

where $R = s\rho Q/T$ is called the run constant.

The scattering length is defined by a point on the photographic plate, and the height of the scattering slit as is shown in Fig. 4. In terms of the geometry of this figure the scattering length is calculated to be

$$1(\Theta) = hH \cos(\Theta - 10°) / f\{1 - (H/2f)^2 \cos^2 10°\} \sin\Theta. \quad (3)$$

Since in the actual apparatus the plate holders were found to be not exactly parallel, h and f are functions of the scattering angle.

The solid angle effective for recorded protons in a swath and subtended at a scattering center of the beam is determined by the width, W, of the scattering slit and the swath width, Δb, on the plate. The solid angle geometry, assuming a beam with cross-section dimensions shrunk to form a line, is shown in Fig. 5. The solid angle for this case is given by

$$\Delta\omega(\Theta) = W \Delta b \sin^2(\Theta) \sin(\Theta - \delta\phi)/hg, \quad (4)$$

where again h is a function of Θ and the plate is assumed inclined at an angle $\delta\phi$ with the horizontal.

The product $1(\Theta)\Delta\omega(\Theta)$, as defined above, must be corrected slightly in order to account for the finite dimensions of the beam, scattering slits, and swath width. These corrections are considered later.

The complete equation for the number of tracks per swath is then[7]

$$N(\Theta) = 8.865 \times 10^{31} \sigma(\Theta) R \times \frac{WH\Delta b \sin\Theta \cos(\Theta - 10°) \sin(\Theta - \delta\phi)}{gf\{1 - (H/2f)^2 \cos^2 10°\}}. \quad (5)$$

III. DIMENSIONAL MEASUREMENTS

Most of the critical measurements were made by three independent observers with the aid of a Bausch and Lomb toolmakers' microscope and a Gaertner comparator. The instruments were checked against each other and against gauge blocks, errors apparently being less than 0.1 percent for nearly all distances measured.

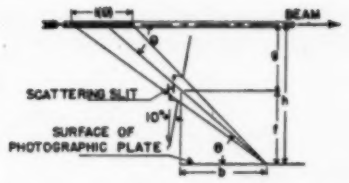

FIG. 4. Scattering length geometry.

The smallest distances, i.e., slit dimensions and swath width, could be measured directly, while the larger dimensions were found through a combination of two or more different measurements. Measurements were made at several places along the height and width of the slits. The swath width was measured on the swath line camera grating for those particular swaths counted in the final runs.

The vertical distance from the center of the beam to the center of a scattering slit was assumed to be the same for both upper and lower slits, since it was not possible to locate accurately the center of the beam. It can be shown that a slight vertical displacement in angle or position of the beam causes a negligible error in cross section, provided the cross section is computed from both upper and lower plates. Actually the cross section derived from the upper plates differed only slightly from that of the lower plates, so that the beam displacements were indeed small.

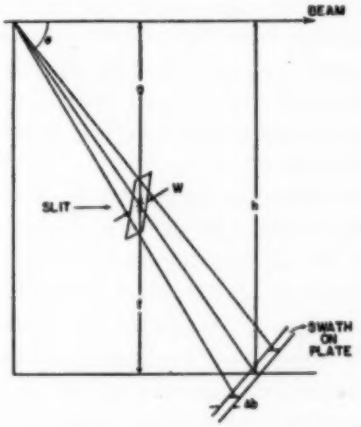

FIG. 5. Solid angle geometry.

TABLE I. Estimated uncertainty in dimensions.

Dimension	Nominal length	Uncertainty	Percent uncertainty	Percent uncertainty in cross section at 20°
Δb (10.5° to 20°)	250μ	0.5μ	0.2	0.2
Δb (25° to 45°)	250μ	0.75μ	0.3	
H (individual value)	20 mil	0.08 mil	0.4	0.3
W (individual value)	49 mil	0.05 mil	0.1	0.07
ΔH	2.05 mil	0.05 mil	2.5	0.3
ΔW	2.12 mil	0.05 mil	2.5	0.13
b	0.39" to 2.2"	2.0 mil	0.5 to 0.1	0.32
f	0.392"	0.8 mil	0.2	0.14
ε	0.395"	0.4 mil	0.1	0.1

The slit plate angle was checked to be 10° ±0.1°. $\delta\phi$ was found from measurements of the slight warp of the plate holders.

Individual uncertainties estimated from the checks of the instruments and the consistency of independent measurements are given in Table I.

Uncertainties in scattering angle computed from errors in b and f, amounted to ±0.15° at 45° decreasing to ±0.02° at 10.5°. The total uncertainty in cross section from all geometrical factors is about ±0.7 percent for all angles. The extent to which this error is increased by the correction for slit jaw penetration is discussed later.

IV. HYDROGEN SUPPLY AND PRESSURE MEASUREMENTS

Hydrogen was admitted to the scattering chamber through heated palladium tubes and was exhausted through a needle valve. With fixed hydrogen reservoir pressure and fixed heating current, the exhaust valve could be set to establish a practically constant hydrogen pressure of about 1.1-cm Hg in the scattering system. This pressure was chosen after calculations (following Breit, Thaxton, and Eisenbud[4]) showed multiple scattering would cause completely negligible effects.

The pressure was measured by a manometer containing octoil. The density of the octoil was measured in the temperature range 16°C to 36°C and was found to be 0.9803±0.0006 g/cc at 25°C with a temperature coefficient of −0.00075 g/cc per °C. The manometer was constructed of ½-in. i.d. tubing about 5 ft. long. To reduce the effects of outgassing of the manometer oil and possible small stopcock leakage during periods of use, the closed side was provided with a 1-liter ballast flask. Oil levels were measured with a cathetometer.

V. VACUUM SYSTEM

The vacuum system consisted of two branches exhausted by the same diffusion pump. One branch led to the Faraday cage, while the other evacuated the scattering chamber through a large "main" valve. There were two traps cooled with dry ice and acetone, one in the forepump line leading to the hydrogen exhaust valve, and one in the main pumping lead to the scattering chamber. Typical vacuums were 3×10^{-5} mm Hg in the whole system with photographic plates present, 1.2×10^{-5} mm Hg with no plates, and 5×10^{-6} mm Hg in the Faraday cage with the main valve closed.

VI. EXPERIMENTAL PROCEDURE

Hydrogen scattering runs were made in the following way. The camera was loaded with two plates and the system evacuated for about twelve hours, at which time the pressure was measured. No runs were started with a pressure greater than 4×10^{-5} mm Hg. After thorough outgassing of the palladium tubes, the rate of rise of pressure in the scattering chamber was measured after closing the main valve. The cathetometer alignment was checked, the main valve closed, and the hydrogen flow started. During the next hour the charge measurement system was calibrated and the cyclotron turned on. From about 20 minutes before run time until the end of the run the manometer levels and the thermometers waxed to the manometer and scattering chamber were read at 5- or 10-minute intervals. At the end of the run the hydrogen flushing rate was measured. The scattering chamber was then put on the diffusion pump for about 30 minutes, during which time the charge apparatus calibration was repeated and final readings were taken to determine the small amount of manometer "leakage."

The hydrogen pressure varied smoothly during the hour-long runs, total variations being between ½ mm and 5 mm (octoil) out of a total pressure of 16 cm of octoil. A constant rate of manometer leakage was assumed, and the consequent correction, amounting to at most 0.4

percent, was applied linearly with time. The sum of both manometer heights reflected very closely the change in manometer temperature, and indicated that the oil temperature was known to ± 0.3°C. Uncertainties in the manometer readings, cathetometer scale, oil temperature, and scattering chamber temperature combine to give an error of ± 0.2 percent in the term $s\rho/T$.

The charge was collected in forty small measured amounts, ΔQ, at recorded times throughout the run by the automatic current integrator to be described later. In computing the run constant, large scale plots of $s\rho/T$ *vs.* time were used. The value of $s\rho/T$ at the center of each charge interval was multiplied by the corrected charge ΔQ collected during that interval. The sum of these products, i.e., the run constant, is considered good to ± 0.7 percent in view of errors of 0.2 percent in $s\rho/T$, 0.5 percent in Q, and 0.1 percent from imperfect synchronization of charge and pressure readings.

VII. CONTAMINATION

An estimate of the amount of impurity gas present during the scattering runs was obtained from the relative magnitudes of the hydrogen flushing rate and the rate of rise of pressure in the closed-off evacuated system. The average flow of hydrogen during the final open-slit scattering runs was 0.51 liter/sec. at the pressure of 11.4-mm Hg. For the same runs the average evolution of foreign gas was 1.6×10^{-5} liter-mm Hg/sec. Under the assumption of constant evolution with either hydrogen or vacuum, the equilibrium pressure of "air" was 3.2×10^{-4} mm Hg.

Evidence from terminal vacuums with and without photographic plates in the chamber indicated that at least half of the foreign gas was water vapor from the plates. The remainder was probably water vapor from the walls of the chamber and air entering through minute leaks. It is believed that the presence of 1 cm of hydrogen would not increase the evolution of water vapor, and might decrease it somewhat, relative to the rate in vacuum.

A calculation assuming Rutherford scattering with $Z=7$ gives the ratio of impurity tracks to hydrogen tracks to be 0.6 percent at 10.5°. This ratio decreases rapidly as the scattering angle increases. The uncertainty in the composition of the gas and in the calibration of the ion gauge used for the rate of rise measurements makes this estimate somewhat uncertain. A correction for contamination was therefore not applied to the cross section, but the contamination was considered in estimating the accuracy of the cross section at low angles.

VIII. CHARGE MEASUREMENT

The number of individual protons passing through the scattering chamber during a run was measured by collecting the charge of the unscattered beam in a Faraday cage, which was separated from the scattering chamber by a 1-mil aluminum foil and evacuated by the diffusion pump. The charge was stored on a special dry air condenser. When the condenser potential reached about twelve volts, an automaton discharged the condenser and recorded the collection of a unit of charge.

The location and dimensions of the Faraday cage are shown in Fig. 2. During the series of runs the maximum observed ion gauge pressure in the Faraday cage system was 6×10^{-6} mm Hg. Estimates of the ionization from the currents observed in a similar cage by Herb, Kerst, Parkinson, and Plain[2] indicate that ionization currents were at the most about 0.1 percent of the proton current.

The entrance to the Faraday cage was in a magnetic field of about 2000 gauss because of the fringing field of the cyclotron. Calculation of electron paths in the magnetic field and extrapolation of the measurements of Herb, Kerst, Parkinson, and Plain[2] with a similar Faraday cage indicated that the field present was several times that necessary to prevent electrons from the 1-mil entrance foil from reaching the cage in appreciable numbers and to prevent secondary electrons in the interior of the cage from escaping. Neutralization of the proton charge in the foil is presumably negligible at this energy.

The entrance to the Faraday cage ($1\frac{5}{32}$-in. diameter) allowed ample clearance for the beam ($\frac{1}{8}$ in.$\times\frac{3}{16}$ in.) to enter the cage. After the apparatus had been aligned in the usual manner, the centering of the beam on the Faraday cage entrance was tested by observing the darkening caused by the proton beam on a microscope cover glass placed over the cage entrance foil.

The Faraday cage was connected by a fifty-foot length of coaxial cable (capacitance about 0.002 μf) to the special air dielectric condenser in the cyclotron control room. The special condenser was required to overcome the soakage effects characteristic of mica condensers. The condenser and cable were found to have negligible soakage and leakage and to have a capacitance of about 0.021 μf. The potential of the condenser was measured with a Cenco-Dershman electrometer whose fixed quadrant voltages were supplied by small radio "B" batteries. The sharp light spot of the electrometer was arranged to pass through a slit to a photo-multiplier. When the condenser reached a potential of about twelve volts, the amplified photo-cell response closed a double-pole relay which discharged the condenser and made a chronograph record of the collection of a measured amount of charge. The discharge of the condenser passed through a ballistic galvanometer providing a convenient measure of charge for checking the performance of the automatic current integrator. During each scattering run a total of 40 condenser charges or about ten microcoulombs was collected.

The amount of charge required to trip the circuit was found to be closely constant over a series of chargings from an artificial source. (The average deviation from the mean charge was found to be 0.15 percent when observed by noting the ballistic galvanometer deflection for twenty five discharges.) The amount of charge necessary to trip the integrator was determined before and after each scattering run by measuring the time needed for a known current to trip the integrator. This current was supplied by a 500-volt regulated power supply through a high resistance and galvanometer. The galvanometer was calibrated in the normal fashion with a standard cell, recently certified by the Bureau of Standards, and laboratory standard resistors. Several weeks after the conclusion of the experiment this method of charge calibration as used was checked against a capacitance-potential measurement of the charge. The two methods agreed within about 0.15 percent.

A correction was found necessary because the electrometer spot lagged appreciably behind the condenser voltage, making the amount of charge necessary to trip the circuit dependent upon the rate of collection of charge. In actual operation the dependence of charge per integrator count upon charging rate was determined after each run by observing the ballistic galvanometer deflection for different charging rates. A correction to the calibration charge could then be made by comparing the rate of charging used for calibration with the rate of charging for each unit of charge collected during the run. This correction amounted to about 3 percent. The cyclotron conditions were sufficiently constant so that the time between discharges could be used in the correction to indicate the charging rate. Considering known random errors in measurement and correction, and the accuracy of the standards involved, the accuracy of the charge measurement is estimated to be about 0.5 percent.

IX. DETECTION OF SCATTERED PROTONS

The use of the photographic plate as a detector in scattering experiments has been made practical by the development of improved fine grain emulsions which record a dense proton track against a low background of single developed grains even in the presence of considerable gamma-ray background. Although the counting of a large number of individual tracks is tedious, the method compares well with counter methods in convenience for the numbers of counts necessary to achieve an accuracy of one or two percent in the cross section. The observation of track length and direction provides high selectivity for the scattered protons against backgrounds of neutron recoils. The recording of all angles simultaneously makes changes in beam strength and hydrogen pressure affect all angles in the same way. Much data may be recorded on a few photographic plates, which are then available for subsequent re-examination.

The photographic plates used were Eastman Kodak alpha-particle plates with emulsions 25 microns thick. To prevent peeling of the emulsion in vacuum the edges of the plates were secured with cellulose tape. The plates exposed under the conditions of our experiments and processed according to the recommendations of the manufacturer showed easily identifiable proton tracks

and a low background of individual grains. The plates were dried slowly to minimize gelatin shifts. Any shift or contraction of the emulsion did not, however, effect the results, since plate positions and areas were fixed before proton exposure and processing by photographing the grid of swath lines in the emulsion.

After several preliminary runs which revealed correctable deficiencies in the apparatus, the following numbers of plates were exposed, as described, in the final runs:

(a) Four pairs of plates from four runs with the chamber evacuated and with the normal open slits.

(b) Four pairs of plates from runs with the hydrogen-filled chamber with normal open slits.

(c) Two pairs of plates from runs with a hydrogen-filled chamber but with one slit of each closed type.

(d) Two pairs of plates from runs as in (c) but with the positions of the slits before upper and lower plates reversed.

The proton tracks were observed by use of a binocular microscope at about 450× with dark field illumination supplied by a cardioid substage condenser. About 5000 tracks were counted for each of nine angles from 10.5 to 45 degrees. Because of the intensity distribution only one swath was counted at 45° on each plate, whereas at 10.5° five swaths were counted: increased resolution per swath at lower angles, however, maintained about the same angular resolution throughout the whole range of angles.

The tracks were counted by three observers, all swaths corresponding to a given angle being counted by one observer. Three weeks were consumed in the counting. The tracks counted were selected to eliminate tracks much shorter than the desired gas scattered proton tracks and those which proceeded in wrong directions. The individual observer's judgment sometimes determined whether a track should be eliminated. However, the criteria established for direction and length were such that no bona fide scattering track was eliminated and the correction procedure for spurious tracks should remove any effect of an observer's bias from the corrected results. Independent cross check counting by the three observers indicated that the ~5000 tracks at each angle could be counted to better than 0.5 percent. This uncertainty raises the statistical uncertainty in 5000 tracks from 1.4 to 1.5 percent.

X. TREATMENT OF EXPERIMENTAL DATA

Background Correction

At the pressures observed, the tracks found in the vacuum runs were due to scattering from metallic surfaces rather than from the residual gas in the chamber. In our calculations we assume that the number of these tracks is not changed appreciably by the presence of hydrogen in the chamber. This is reasonable, since these tracks originated largely from scattering by slit jaws and baffles, and with the design of the chamber used the small calculated beam spreading in hydrogen should effect this scattering little. The observed number of vacuum tracks was normalized to the charge of the open slit tracks and subtracted directly from the number of open slit tracks. This correction amounted to about 3 percent at 10.5 degrees and less than 1 percent at all other angles.

The closed slit runs were also corrected for vacuum scattering upon the assumption that the ratio of vacuum background tracks to total tracks is a constant independent of slit shape for a given angle. This seems to be justifiable, since the closed and open slits occupy closely the same position when in use and are therefore in the same spatial location relative to any sources of metallic scattering.

Penetration Correction

We consider N_0, the number of open slit gas tracks per swath with the "vacuum" tracks subtracted out, to be composed of three components: protons that came through (a) the scattering slit opening, (b) the side slit jaws, and (c) the top and bottom slit jaws. The number of tracks per swath resulting from protons which came through the opening can be written as

$$N=\frac{WH\sin\Theta\cos(\Theta-10^\circ)\sin(\Theta-\delta\phi)}{gf[1-(H/2f)^2\cos^2 10^\circ]}$$

$$R_0\Delta b\sigma(\Theta)\times 8.865\times 10^{31}=K_0R_0\Delta b\alpha(\Theta), \quad (6)$$

where $R_0\Delta b$ is the run constant times the swath width averaged over the runs from which N_0 was obtained and

$$\alpha(\Theta)=\sigma(\Theta)\times 8.865\times 10^{31}. \quad (7)$$

The number of tracks caused by protons penetrating the side slit jaws is taken as proportional to the length of those jaws. This number of tracks per swath is given by

$$R_0\Delta b H_0\beta(\Theta), \tag{8}$$

where H_0 is the slit height and where $\beta(\Theta)$ is some function to be determined. The number of tracks caused by the protons passing through the top and bottom jaws of the scattering slit is taken proportional to the slit width W_0 and is given by

$$R_0\Delta b W_0\gamma(\Theta). \tag{9}$$

These expressions so far do not take into account penetration of the corners of the slits. On the assumption that the correction for the corners may be expressed as an increased effective width δW and an increased effective height δH of the slit, the equation for the total number of tracks per swath with open slits is

$$\frac{N_0}{R_0\Delta b}=\alpha K_0+\beta(H_0+\delta H)+\gamma(W_0+\delta W). \tag{10a}$$

Similar equations may be written for the narrow vertical slit (subscript 1) and narrow horizontal slit (subscript 2):

$$\frac{N_1}{R_1\Delta b}=\alpha K_1+\beta(H_1+\delta H)+\gamma(\Delta W+\delta W), \tag{10b}$$

$$\frac{N_2}{R_2\Delta b}=\alpha K_2+\beta(\Delta H+\delta H)+\gamma(W_2+\delta W), \tag{10c}$$

where the various symbols are defined in the same way as for the open slits.

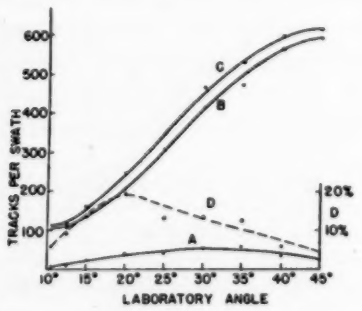

FIG. 6. Sources of tracks with open slits. *A* shows the number of tracks which penetrated the slit jaws, *B* shows the number of tracks which came through the slit opening proper, and *C* shows the total number of tracks being equal to the sum of the numbers shown by *A* and *B*. Curve *D* read with the scale at the right shows the ratio of penetration tracks to tracks from the slit opening.

The corner corrections, δH and δW, whose effect on the cross section is at most 0.8 percent, were calculated as follows. The maximum amount of energy lost in the brass slit jaws by *counted* protons was computed from the lengths of the shortest tracks counted at each angle and the stopping power of the emulsion. The extent of the penetration region was then derived from the maximum path length in brass and the slit jaw angles. δH and δW were obtained from the area of the corners of the penetration region.

In the three simultaneous Eqs. (10) only the functions α, β, and γ are unknown. Solving simultaneously for them at each angle we obtained (a) the actual number of protons which have come through the slit opening and through the different slit jaws, and (b) the desired cross sections for proton-proton scattering. The distribution of proton tracks from various sources is shown in Fig. 6. From the first of the three equations one can determine what percentage of the total number of tracks are so-called penetration tracks. This ratio checks closely with that from a theoretical estimate of the translucent area of the slit jaws, which was made as in the corner corrections. This demonstrates that our method of taking care of the penetration effect for corner corrections is satisfactory.

The values of $\sigma(\Theta)$ derived from Eqs. (7) and (10) are given in column 2 of Table II for the corrected laboratory scattering angles. In columns 3 and 4 are the final laboratory and center of mass cross sections with certain small corrections described in the next section.

Table II lists two values for the 35-degree region, one for the average of both upper and lower plates, the other for the lower plates alone. These are listed because the cross section from the upper plates deviates a large amount (10 percent) from the smoothed cross-section curve. Physical causes for this deviation were sought in a re-examination of the upper plates. The deviation was largely due to one plate. The tracks were, however, dense and of good quality; there were no physical imperfections in the emulsion, no evidence of shadowing by superfluous material was found, and the number of tracks on the one plate were normal at other angles. The large deviation from the smoothed cross section (10 percent compared to a r.m.s. value of 1.9 per-

cent for all points) curve indicates that this point would possess undue influence in fitting the curve by least squares methods. In analysis of the data, we have preferred to make the calculations discarding the upper plates at thirty-five degrees, however, in the summary of the analysis values with the upper plate value at thirty-five degrees are included in parentheses.

XI. SMALL CORRECTIONS

The scattered protons observed in any swath area on the photographic plate have been scattered through a range of angles about the nominal scattering angle at the center of the swath due to cross fire in the beam and to finite dimensions of the proton beam, slit, and swath. Because of the asymmetry of the distribution of angles in this small range the true average scattering angle differed from the nominal angle. The nominal angle was corrected by assuming an elliptical beam cross section of constant density and of extent determined from the size of the last defining hole and the visually observed dimensions of the beam spot at the rear of the scattering chamber. This assumption concerning the beam structure was born out by the observed track density across the swaths on the photographic plate. With this assumption the correction to the nominal angle was determined by averaging the angle over the finite dimensions and amounted to 2.3′ at 10° and 8.5′ at 45°. The corrected angles are given in Table II.

In addition to the change in average angle, the finite angular range and the second derivative of the cross section as a function of angle necessitated a small correction. This correction was calculated by finding the mean square angular deviation at the angles counted by use of the above assumptions concerning the beam structure, the cross fire in the beam estimated from its spreading, and the dimensions of the slit and swaths, and using the second derivative estimated from a theoretical s wave cross section. This correction to the cross section varied from -0.20 percent at ten degrees to $+0.01$ percent at forty-five degrees.

The size of the beam, slits, and area in which tracks were counted on the photographic plates also make necessary corrections to the cross section calculated with the elementary considerations of geometry used thus far. A correction is necessary in the product of the "solid angle" and "scattering length" because of the finiteness of the dimensions noted. These corrections have been estimated by integrating over the dimensions of the slit and plate area and over the beam. The corresponding total correction to the cross section varies from -0.46 percent at 10.5° to $+0.33$ percent at 45°. This correction along with the one of the preceding paragraph has been included in the corrected cross sections of Table II.

TABLE II. Experimental proton-proton cross section at 7.03 ± 0.06 Mev.

Average lab. angle	Average lab. cross section	Corrected* lab. cross section	Center of mass cross section*
10.51°	40.56 cm²×10⁻²⁶	40.28	10.24 cm²×10⁻²⁶
12.59°	29.38	29.21	7.48
15.06°	25.48	25.36	6.56
19.95°	23.29	23.21	6.17
24.99°	23.03	22.98	6.34
30.00°	22.60	22.56	6.51
34.83°**	21.51**	21.52**	6.55**
34.94°***	20.38***	20.40***	6.22***
39.87°	20.34	20.38	6.64
44.62°	18.75	18.81	6.61

* Corrected for small effects to be discussed in the next section.
** Lower plates only.
*** Lower and upper plates. See text for discussion of these two values.

XII. ACCURACY OF RESULTS

The errors in most of the factors of Eq. (10) enter the cross section directly, unaltered by the correction for slit jaw penetration. On the other hand, the errors caused by slit dimensions and tracks counted are magnified considerably by the penetration correction process. Thus if there were no penetration, the error caused by counting 5000 tracks would be 1.5 percent, with an additional error of 0.3 percent from the slit dimensions. At 20°, for example, the correction process increases these errors to 2.5 percent and 0.5 percent, respectively. Similar magnification of these particular errors occurs at all angles, being largest at 20° where the penetration is relatively the greatest. The increase is of course due to the necessity of solving the simultaneous Eqs. (10) rather than the single Eq. (5).

The r.m.s. errors of all individual factors have been estimated. For convenience these are separated into two groups: the random errors of

individual points and "absolute" errors that affect the cross-section curve as a whole.

1. The total random error varies from ±2.2 percent at 10.5° to ±2.5 percent at 20° and down to ±2.1 percent at 45°. The sources are counting (about 2.3 percent) and uncertainty in scattering angle (about 0.25 percent).

2. The total "absolute" error is ±1.8 percent at 10.5 degrees and about ±1.4 percent for angles above 20°. The sources are (a) geometry, charge, pressure (1 percent for all angles), (b) hydrogen contamination (±0.6 percent at 10.5°, ±0.34 percent at 12.5°), and (c) effective uncertainty in cross section due to uncertainty in energy of incident protons (±1.4 percent at 10.5°, ±0.9 percent for 20° and above).

XIII. MEASUREMENT OF PROTON ENERGY

The energy of the protons was determined from their range in air and their deflection in a magnetic field. In both types of experiments the beam was allowed to traverse the beam tube and scattering chamber in their normal positions, and, as in the scattering runs, the beam was monitored by maximizing the current to the second beam-defining hole.

Range Experiments

Bragg curves of the protons in air were obtained by means of a "range" ionization chamber and a "monitor" ionization chamber, of the types described by Wilson.[8] Plots of the ratio of ionization currents (range/monitor) against the air distance to the center of the range ion chamber constituted the final Bragg curves. The observed air distance was corrected for the air temperature and pressure, for estimated effects of water vapor in the air, and for the Al foils at the scattering chamber and ionization chamber entry. The latter correction was measured by interposing, adjacent to the regular foils, two additional foils cut from the same sheets as the regular foils, and noting the consequent decrease in range.

The relationship between the extrapolated ionization range and the mean range is not known experimentally for protons of this energy. The necessary relationships were found by constructing Bragg curves by numerical integration of the specific ionizations of a single proton. The specific ionization of a single proton was taken to be proportional to the air atomic stopping cross section, as given by Livingston and Bethe[9] and modified at low energies in accordance with the revised Cornell Range-Energy Relation.[10] For these integrations we assumed Gaussian number-range distributions of the form

$$N(R)dR=\frac{dR}{(2\pi)^{\frac{1}{2}}\sigma_R}\exp\{-(R-R_M)^2/2\sigma_R^2\}. \quad (11)$$

Values of $\sigma_R=0.5$, 1.0, 1.5, and 2.0 cm were used.

The resulting relationships, of the type considered by Holloway and Livingston,[11] and Rado,[12] are

$$y=2.05\sigma_R, \quad (12a)$$

and

$$x=1.63\sigma_R-0.04, \quad (12b)$$

where x, y, and σ_R are in cm and $0.5<\sigma_R<2.0$. The steep descent of the Bragg curve is extrapolated in both directions to intersect the range axis (at the extrap. ion. range) and a horizontal line through the maximum of the Bragg curve. y is defined to be the range distance between these two intersections, while x is the distance from mean range to extrapolated ionization range. Values of x and y are probably good to better than 10 percent. Other derived relations are (a) for a constant number of protons in a beam the maximum ordinate of a Bragg curve is proportional to $\sigma_R^{-0.424}$, and (b) the ratio of Bragg ordinate at the mean range to maximum Bragg ordinate is 0.775 ± 0.005 for $0.8<\sigma_R<2$ cm.

Bragg curves were taken after each of the four final open-slit hydrogen scattering runs, and after alternate narrow-slit runs. All curves gave the same extrapolated range within ±0.5 mm, but all showed the presence of two energy components in the beam. The relative intensity

[8] R. R. Wilson, Phys. Rev. 60, 749 (1941).

[9] M. S. Livingston and H. A. Bethe, Rev. Mod. Phys. 9, 245 (1937).

[10] Revised Cornell Range-Energy Relation, unpublished (1937).

[11] M. G. Holloway and M. S. Livingston, Phys. Rev. 54, 18 (1938).

[12] G. T. Rado, Thesis, Massachusetts Institute of Technology (1939).

and mean range of both components were found by subtracting two simple Bragg curves for the high energy component from our (average) compound Bragg curve. One of these was a theoretical curve with $\sigma_R = 1.27$ cm: the other, an experimental curve with, apparently, a very small amount of low energy component. (The latter curve was taken with a four-slit beam collimating system and with slightly different cyclotron conditions.) The compound, simple, and difference curves are shown in Fig. 7.

From these Bragg curves and the above theoretical relations the two energies were found to be 7.02±0.036 Mev and 6.73±0.05 Mev, with an intensity ratio of 8.4±1.4. Uncertainty in the relative intensity arises from uncertainty as to which curve best represents the Bragg curve of the high energy component alone. The average from both subtraction processes is given above.

The average beam energy from the range experiments was 6.99±0.04 Mev. This uncertainty includes the errors of temperature, pressure, and water vapor content of the air, position of the range ion chamber on the track, theoretical relations, air equivalence of Al foils, ±30 kv in the 1937 Cornell Range-Energy Relation, and the inaccuracy of the component intensity ratio.

Magnetic Deflection Experiments

The auxiliary magnet used for the deflection experiments could not quite produce 90° focusing of 7-Mev protons. To measure the beam deflection a 4 in.×10 in. spectrographic plate was placed in the field at a slight angle to the median plane of the gap. The beam through a narrow slit at the edge of the field hit this plate at nearly grazing incidence and left a curved trace of about 50° of arc. The radius of curvature was found from three points at the beginning, middle, and end of the trace, each point located transversely in the center of the trace. Energy and angular spreads in the high energy component made the trace rather broad even with a narrow slit, so that the three points could not be located very accurately.

The magnetic field was measured by means of a flip coil wound on a fused quartz form and calibrated at reduced fields by means of a proton nuclear induction experiment.[13] The values of $B = 13{,}480$ gauss and $\rho = 28.68 \pm 0.2$ cm yielded an energy of 7.11±0.1 Mev for the high energy component of the beam. This is an average from five final plates exposed about two weeks after the final scattering runs. The size and unwieldiness of the magnet precluded making magnetic deflection and scattering runs concurrently. Range runs preceding and following the deflection runs showed no change in the beam since the scattering runs.

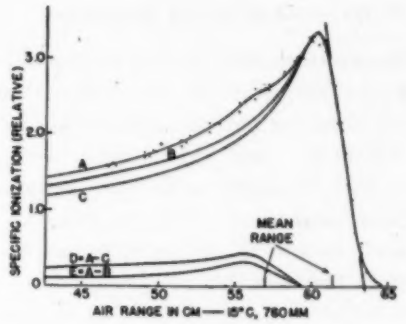

FIG. 7. Range ionization data. *A* is the experimental curve for the conditions of the scattering experiments. It shows the presence of two energy components. *B* is an experimental curve containing little low energy component. *C* is the theoretical curve fitted to the high energy component. *D* and *E* are the residual ionization due to the low energy component after the high energy component, as represented by *B* or *C*, respectively, is subtracted from *A*.

Average Energy

The deflection experiments were considered less accurate than the range experiments and gave no usable information on the relative strengths of the beam components. Consequently, the final mean energy was calculated by averaging range and magnetic deflection values of the high energy and subtracting from this the 0.03 Mev found necessary in the range experiments to account for the low energy component. All energy experiments were done with fore vacuum in the beam tube and scattering chamber. When corrected for energy loss caused by hydrogen, the average beam energy at the scattering region was 7.03 Mev±0.06 Mev.

[13] F. Bloch, Phys. Rev. **70**, 460 (1946); F. Bloch, W. W. Hansen, and M. Packard, Phys. Rev. **70**, 474 (1946); W. R. Arnold and A. Roberts, Phys. Rev. **71**, 878 (1947).

XIV. ANALYSIS OF RESULTS[14]

The theory of proton-proton scattering is well established. Formulas for the differential cross section in terms of the phase shift are given by Breit, Thaxton, and Eisenbud,[4] and Breit, Condon, and Present[15] who give references to other theoretical work. The treatment of scattering with tensor ^3P forces is given by Breit, Kittel, and Thaxton.[16]

S Wave Analysis

The low energy proton-proton scattering experiments of Herb, Kerst, Parkinson, and Plain[2] and Heydenburg, Hafsted, and Tuve[1] in the range from 860 to 2400 kev were found by Breit, Thaxton, and Eisenbud[4] to be well represented by nuclear s wave scattering from a square well of depth 10.5 Mev, radius e^2/mc^2. (Inclusion of Coulomb potential within the square well requires a depth of 11.3 Mev.) They were also fitted by a Gauss error well $A\exp(-\alpha r^2)$ with $A=51.44mc^2$ and $\alpha=21.59$ with a unit of length 9×10^{-13} cm and with interior Coulomb potential. The experiments of Ragan, Kanne, and Taschek[3] in the range 200 to 300 kev were found to be in agreement with the s wave scattering from the above square well. The phase shifts to be expected with these potentials at 7.03 Mev are given by Thaxton and Hoisington[17] as 53.8° for the square well and 54.0° for the Gauss error potential. The cross section for the square well is shown in Fig. 8 in comparison with the experimental results. It is seen that the experimental cross sections at higher scattering angles lie below the square well cross sections by about six percent.

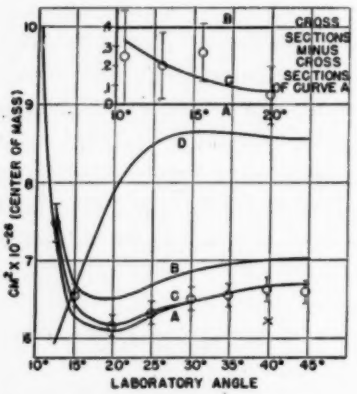

FIG. 8. Experimental 7-Mev differential cross sections in comparison with theory. The experimental points $\bar{Y}$ show the estimated random uncertainty of each point. X is the thirty-five degree value, including the upper plates (see text). A represents s wave scattering alone as fitted to the experimental cross sections at high scattering angles. B is the s wave scattering expected from the 10.5 Mev, e^2/mc^2 square well which fits experiments in the range from 200 to 2400 kev. C is fitted to the experimental points and includes s and p wave scattering on the basis of either central p scattering or of "symmetrical" or "charged" tensor theories fitted by modification as described in the text. D represents B plus the p wave scattering calculated from the Rarita-Schwinger "neutral" tensor interaction. The plot in the upper corner shows at low angles the differences of B, C, and experimental cross sections from the fitted s wave curve, A. This plot best shows the experimental evidence for p wave scattering.

Although central p wave scattering is zero at forty-five degrees in the laboratory system, Breit, Kittel, and Thaxton[16] have shown that tensor p wave scattering introduces an additional term in the cross section not zero at forty-five degrees. For small p phase shifts, as may be expected, this term increases the cross section at forty-five degrees, so that presence of tensor p wave scattering in addition to the square well scattering would increase the difference between our results and those predicted by extrapolating the low energy analysis with a square well. Assuming central p wave scattering, the s phase shift which best fits our results is $52.0°\pm0.6°$ $(51.6°\pm0.6°)$.[18] This may be considered an upper limit to the actual s phase shift since the presence of tensor p wave scattering would require a smaller s phase shift. Using the data of Thaxton and Hoisington,[17] we find that a square well with adjusted depth may be fitted to our experimental data and that at 1.4 Mev if the range of the square well is increased by 11 ± 4 percent. The accuracy of the e^2/mc^2 range assignment is given by Breit, Thaxton, and Eisenbud[4] as about 5 percent. The gauss error well would require similar adjustment in range to fit our experiments.

Hoisington, Share, and Breit[19] have also found

[14] One of us (C.L.O.) is responsible for the analysis.
[15] G. Breit, E. U. Condon, and R. D. Present, Phys. Rev. **50**, 825 (1936).
[16] G. Breit, C. Kittel, and H. M. Thaxton, Phys. Rev. **57**, 255 (1940).
[17] H. M. Thaxton and L. E. Hoisington, Phys. Rev. **56**, 1194 (1939).
[18] These values in parenthesis result from inclusion of the upper plate values at 35°.
[19] L. E. Hoisington, S. S. Share, and G. Breit, Phys. Rev. **56**, 884 (1939).

that the low energy scattering experiments may be fitted with a meson potential $Ce^{-r/a}\div r/a$ with $C=89.65mc^2$, $a=0.42e^2/mc^2$ and with interior Coulomb potential. Professor G. Breit and W. G. Bouricius have kindly calculated for us the phase shift expected with this potential. They find an s phase shift 55.6 degrees, in even poorer agreement with our experimental phase shift than either the square well or gauss well values. This potential would require a larger increase in range to fit our experiments and a lowering of the meson mass from the value 326-electron masses which corresponds to this range.

The above discrepancy between our experiments and the extrapolated predictions with gauss error or square wells is not far outside the accuracies of the experiments and predictions. The discrepancy with the meson well is larger. Some of the apparent increase in range may be due to velocity dependence. More experiments which provide accurate absolute cross sections in this energy range would be valuable.

Central p Wave Analysis

The experimental results were analyzed by a least squares method for the s and central p phase shifts which best fit the data. The p wave scattering observed is repulsive corresponding to a phase shift of $-0.22°\pm0.1°(0.28°\pm0.1°)$.[18] The fitted scattering with this phase shift is shown in Fig. 8, curve C, in comparison with the experimental cross sections. The r.m.s. deviation of the experimental points is 0.9 percent (1.9 percent)[18] from the fitted curve. The p phase shift $-0.22°$ corresponds to a repulsive square well of range e^2/mc^2, height 2.2 Mev, and with interior Coulomb potential. This interaction is considerably weaker than the ^1S interaction which has a depth of 11.3 Mev[4] for the same range. The marked sensitivity of the p phase shift to range has been noted in an exchange of letters by Peierls and Preston, and Foldy[20] in regard to the analysis of the experiments of Wilson *et al.*[5] Since tensor forces are probably present in the ^3P state, there is no need for further discussion of the central p wave analysis here.

[20] R. E. Peierls and M. A. Preston, Phys. Rev. **72**, 250 (1947); L. L. Foldy, Phys. Rev. **72**, 731 (1947).

TABLE III. ^3P phase shifts for 7-Mev proton-proton scattering with Rarita-Schwinger interactions.

Interaction	State $^3P_0$	$^3P_1$	$^3P_2$
(I) "Symmetrical"	1°16′	−1°0′	−19′
(II) "Charged"	7°57′	−2°0′	−50′
(III) "Neutral"	−1°55′	14°53′	1°15′

Calculation of Tensor p Wave Scattering with the Rarita-Schwinger Interactions

Rarita and Schwinger[21] have constructed tensor neutron-proton interactions to agree with the observed quadrupole moment and binding energy of the deuteron and low energy neutron-proton scattering. For states of odd parity they have used three types of exchange relations suggested by meson theories and labeled (I) "Symmetrical," (II) "Charged," and (III) "Neutral." Their interactions are of square well type with range e^2/mc^2 as determined from the low energy proton-proton scattering experiments. It is of interest to adapt their interaction to the ^3P proton-proton scattering to indicate the nature of possible tensor effects.

The equality except for Coulomb interaction of neutron-proton and proton-proton interaction in like states is formally assumed. This equality has been found to hold closely in the ^1S state.[4] The neutron-proton interactions are then used with addition of the interior Coulomb potential to calculate the ^3P proton-proton scattering.[22] Of the three triplet states with $J=0$, 1, 2, $^3P_0$ and $^3P_1$ are not coupled to any other states, but $^3P_2$ is coupled to $^3F_2$. This coupling is small for the energy under consideration and is neglected in the calculation. The potentials as given by Rarita and Schwinger are for the "neutral" theory (III) $^3P_0$: 29.16 Mev, $^3P_1$: −35.41 Mev, $^3P_2$: −9.58 Mev. The potentials of the "charged"

[21] W. Rarita and J. Schwinger, Phys. Rev. **59**, 436 (1941); Phys. Rev. **59**, 550 (1941).

[22] The "symmetrical" potential is

$$V=\tfrac{1}{4}(\tau_1\cdot\tau_2)(\sigma_1\cdot\sigma_2)\{1-\tfrac{1}{2}g+\tfrac{1}{2}g\sigma_1\cdot\sigma_2+\gamma S_{12}\}J(r),$$

where g, γ, and the depth of the square well potential, $J(r)$, have been determined by Rarita and Schwinger from the neutron-proton system. The "charged" or "exchange" potential as formally assumed here may be written

$$V=\tfrac{1}{4}(1+\tau_1\cdot\tau_2)(1+\sigma_1\cdot\sigma_2)\{1-\tfrac{1}{2}g+\tfrac{1}{2}g\sigma_1\cdot\sigma_2+\gamma S_{12}\}J(r).$$

This potential is not to be confused with the potential given by the first-order charged meson theory which gives no force between like particles.

theory (II) have the same magnitude but are opposite in sign, and those of the "symmetrical" theory (I) are one-third those of the "charged" (II). The phase shifts were found using the series expansions of Yost, Wheeler, and Breit[23] for the interior regular Coulomb functions and their derivatives and for the exterior regular and irregular Coulomb functions and their derivatives. The values of the phase shifts given by Thaxton and Hoisington[17] for the 10.5 Mev, e^2/mc^2 attractive and repulsive square wells were checked with our values of the exterior functions. Values of the phase shifts for the ^3P states are given in Table III for 7-Mev scattering.

The differential cross sections for each of the theories is shown in Fig. 9 as calculated by the formula of Breit, Kittel, and Thaxton.[16] The p wave scattering is added to the s wave scattering from the 10.5 Mev, e^2/mc^2 square well. Shown in Fig. 10 are the p wave effects in ratio to the s wave scattering from the aforementioned square well. Also shown in Fig. 10 are the p wave effects due to 10.5 Mev, e^2/mc^2 attractive and repulsive square wells as calculated by Eisenbud[24] from the phase shifts of Thaxton and Hoisington.[17] The theoretical p wave effects are relatively most important near ten degrees at the end of the experimental range of angles.

The presence of the non-vanishing p wave

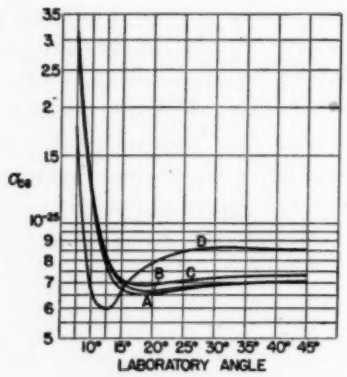

FIG. 9. Theoretical 7-Mev proton-proton scattering with Rarita-Schwinger tensor interactions. Shown is the differential cross section in cm² in the center of mass system. A is s wave scattering, due to the 10.5-Mev, e^2/mc^2 square well, to which the p wave effects in B, C, and D are added. B includes p wave scattering calculated with the "symmetrical" theory, C with the "charged" theory, and D with the "neutral" theory.

[23] F. L. Yost, J. A. Wheeler, and G. Breit, Phys. Rev. 49, 174 (1936).
[24] L. B. Eisenbud, private communication.

scattering at 45 degrees is peculiar to tensor force scattering. This term is negligibly small with the "symmetrical" theory, but appreciable with both "charged" and "neutral" theories. Scattering widely divergent from s wave scattering, such as is predicted by the "neutral" theory, should be easily distinguishable.

The rather small difference between scattering with the "symmetrical" and "charged" theories may be understood from examination of the terms in the formula of Breit, Kittel, and Thaxton.[16] The cross-section expression contains three terms. The first contains the phase shifts as

$$\sum_{i=0}^{2} g_i \sin\delta_i \cos\delta_i,$$

where the g_i's are the statistical weights and the δ_i's the phase shifts for the states ^1P_i; the second term contains

$$\sum_{i=0}^{2} g_i \sin^2\delta_i,$$

and the third term, present only with tensor forces, depends on the differences of the phase shifts. The first term is the only appreciable one with central force scattering fitted to our experiments. It also predominates in the "symmetrical" theory, where the cancellation of effects of phase shifts of opposite signs leaves predominately repulsive scattering. The "symmetrical" scattering contains very little of the third or tensor term. In the charged theory, however, both second and third terms are appreciable and add,

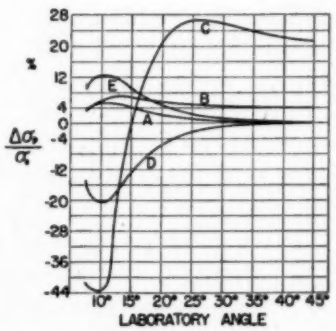

FIG. 10. Ratio at 7 Mev of theoretical nuclear p wave scattering to s wave scattering from a 10.5, e^2/mc^2 square well. A, B, and C are calculated with the "symmetrical," "charged," and "neutral" tensor interactions of Rarita and Schwinger, respectively. D and E are due, respectively, to central p wave scattering from attractive and repulsive 10.5-Mev, e^2/mc^2 square wells.

TABLE IV.

Theory	s phase shift		Root mean square percent deviation of experiment from fitted curves
"Symmetrical"	51.8°±0.6	c {0.60±0.3	0.8
"Charged"	50.8°±0.6	c {1.10±0.5	0.9
Central	52.0°±0.6	Central phase shift: −0.22°±0.1	0.9
If the value of cross section from the upper plates is included at 35 degrees the analysis becomes			
"Symmetrical"	51.6°	c {0.79	1.9
"Charged"	49.5°	c {1.46	1.9
Central	51.6°	Central phase shift: −0.28°	1.9

in the angular range under study, to give a constant addition to the center of mass cross section. The constant addition might also be closely represented by scattering caused by an increase in s phase shift. The first term of the "charged" theory is smaller than in the "symmetrical" theory. The interactions, which are three times as intense in the "charged" theory, increase the attractive phase shifts more strongly to give a total first term still predominately repulsive but smaller in magnitude.

The symmetrical theory is then very similar in ^3P scattering to a central theory, and the "charged" scattering may be closely represented by central p scattering plus a small amount of additional equivalent s wave scattering. Thus if the actual scattering resembles either of these two theoretical predictions, it may not be possible to distinguish any tensor effects in the present experimental results.

Although the square well interactions must represent an oversimplification and the ^3P scattering may be sensitive to a change in well shape, it is not possible to estimate the p wave effects with more reasonable well shapes without complete calculations. This is due to the cancellations of terms just noted.

Comparison of Experimental Results with Tensor Theory Predictions

As shown by reference to Fig. 8, the experimental results are very decidedly in disagreement with the predictions of the "neutral" theory (curve D).

In order to test the agreement of the "symmetrical" and "charged" predictions with experiment, a least squares analysis was made to determine the s phase shift and the fraction c of the theoretical p wave scattering which best fitted our results. The conclusions from this analysis are presented in Table IV with the results of the central analysis.

It will be noted that both the "symmetrical" and "charged" theories give reasonable agreement with experiment, as indicated by c values close to 1. The "charged" theory, however, because of the tensor scattering term appreciable at forty-five degrees, requires a decrease of the s phase shift which increases the discrepancy between the experimental s phase shift and that predicted by extrapolation of the low energy experiments. (53.8° for square well, 54.0° for Gauss error, and 55.6° for meson.)

The combinations of the p wave scattering of the "charged" and "symmetrical" theories, as modified by the c factors with the scattering corresponding to the best s phase shifts, differ at all angles by less than 0.2 percent from the fitted central scattering and are all shown by curve C in Fig. 8. There is no indication for the need of tensor forces, but the strong tensor interaction of the "charged" theory causes wider disagreement with the extrapolated s phase shift because of the appreciable "tensor" term in the scattering.

The determination of the amount of p wave effect depends upon the relative values of the scattering at small angles to that at large angles. The sensitivity of the strength of the p wave scattering to the absolute values of the cross section was indicated by analysis of the data with all experimental cross sections increased by 6 percent. This adjustment of the cross sections fitted the scattering at 45° to that expected from a 10.5-Mev, e^2/mc^2 square well. This analysis showed that an increase of approximately 50

percent in the strength of the p wave scattering was required. The estimated experimental uncertainty in the over-all experimental curve is, however, estimated at less than two percent.

XV. CONCLUSION

The photographic method has been shown to have certain advantages in proton-proton scattering experiments. As used here, the chief disadvantage is the need for a large correction for penetration of slit edges. Experiments by another group at Rochester are nearing completion. Their apparatus has been enlarged and slit construction modified so as to make the correction very small. The further experiments should provide a check of the reliability of our absolute cross sections and a check of the relative cross sections with a new geometry.

Analysis of the results has indicated a somewhat smaller s phase shift than would be predicted from the extrapolation of the low energy data as analyzed with square well, Gauss, and meson potentials. This result depends upon the accuracy of our absolute cross sections at larger angles. This effect may be, of course, due in part to velocity dependence of the potentials, an effect which has not been considered here.

The p wave analysis shows a small repulsive effect which may be fitted with central p wave scattering but which also agrees with the p wave scattering from the square well tensor interaction of Rarita and Schwinger labeled by its exchange properties as "symmetrical." The "charged" exchange of Rarita and Schwinger provides a less satisfactory fit when considered with the s phase shift expected from low energy experiments. The "charged" theory also has no clear connection with actual meson theories.

Experiments at 7 Mev are not sensitive to the large difference in strengths of the ^3P interactions in the "symmetrical" and "charged" theories. As Ashkin and Wu[25] indicate in their analysis of proton scattering at 100 and 200 Mev, experiments in this energy range will be quite sensitive to the strengths of the triplet interactions.

ACKNOWLEDGMENTS

We should like to acknowledge financial aid from the Research Corporation which, through a grant to Professor S. W. Barnes, supported this work in part. One of us (J. E. P.) was recipient during part of this work of a fellowship established by E. I. du Pont de Nemours and Company.

We gratefully acknowledge the continued interest and suggestions of Professor S. W. Barnes who suggested the problem to us and designed the early form of the apparatus. In addition, we received encouragement and help from Professors S. N. Van Voohris, R. E. Marshak, and Julius Ashkin. We also appreciate the aid of Mrs. Oxley who performed many of the numerical calculations. Many members of the laboratory staff generously contributed suggestions, time, and equipment.

Note Added in Proof: Preliminary results of experiments by the second Rochester group indicate larger values of absolute cross sections than those given here.

[25] J. Ashkin and T. Y. Wu, Phys. Rev. **73**, 973 (1948).

Inelastic Scattering of Fast Neutrons by Fe, Pb, and Bi

L. SZILARD, S. BERNSTEIN, B. FELD, AND J. ASHKIN*
Metallurgical Laboratory, University of Chicago, Chicago, Illinois
(Received February 27, 1948)

Measurements of inelastic scattering effects of Ra$-\alpha-$Be and Ra$-\alpha-$B neutrons in Fe, Pb, and Bi have been made. A U^{238} fission threshold detector was used. The method consisted in measuring the fission counting rate in the detector with and without the spherical scatterer surrounding the source. From the decrease in the counting rate caused by the presence of the scatterer, values of the cross section for inelastic scattering to below the U^{238} fission threshold were calculated for several assumed values of the elastic scattering cross section.

I. INTRODUCTION

THIS report describes some experiments performed by the authors in the early part of 1943 at the Metallurgical Laboratory of the University of Chicago under the auspices of the Manhattan District. The purpose of the experiments was to measure the cross sections of Fe, Pb, and Bi for inelastic scattering of fast neutrons. As sources of fast neutrons Ra$-\alpha-$B and Ra$-\alpha-$Be mixtures[1] were used. For detector, the fast fission of U^{238} with a threshold of about one Mev was employed. Because fast fission of U^{238} was used as detector, the experiment dealt only with that part of the neutron source spectrum which is above the threshold energy. More exactly, the inelastic scattering cross section measured is an average for all the energies in the neutron spectrum of the cross section for scattering of these neutrons to below the threshold.

II. EXPERIMENT

The experimental procedure is patterned after that used by Szilard and Zinn.[2] Figure 1 is a schematic diagram showing the experimental arrangement. A source of fast neutrons was placed at a given distance from a spherical uranium-coated ionization chamber. The chamber was connected in the conventional manner to a linear amplifier and scaling circuit for the purpose of counting fission pulses. The chamber was surrounded by Cd so that neutrons which may have been slowed down to thermal energies by collisions with the walls of the room would be prevented from causing fissions in the U^{238}. There were, possibly, some fissions in U^{235} resulting from epi-cadmium neutrons, but the number of these relative to the number of fast fissions in U^{238} must be small, since the relative amount of U^{235} in normal uranium is small, and the source emits no slow neutrons. The fission counting rate is then proportional to the fast neutron flux through the chamber. (A fast neutron in this report is defined to be one whose energy is above the U^{238} fission threshold.) The source is then surrounded by a sphere of scattering material and the measurement of the fission counting rate repeated. The ratio of counting rates, with to without scatterer, is thus determined. From this ratio the inelastic scattering cross section may be derived. Table I gives the measured values of this ratio, called F, for the various scatterers used.

III. INTERPRETATION

The ratio of fast fission counting rates, F, is equal to the ratio of fast fluxes through the fission chamber. From F it is possible to obtain the ratio, F', of the number of fast neutrons emerging from the scattering sphere to the number of fast neutrons emitted by the source. Since the presence of the sphere (and elastic scattering in the sphere) gives the emerging neutrons an angular distribution which no longer corresponds to a point source, F' and F are not precisely equal. An estimate of the upper limit of the difference between F and F' indicated that, for the small spheres and large source to

* Present addresses of the authors: L. Szilard, Institute for Radiobiology, University of Chicago, Chicago, Illinois; S. Bernstein, Clinton National Laboratories, Oak Ridge, Tennessee; B. Feld, Massachusetts Institute of Technology, Cambridge, Massachusetts; J. Ashkin, University of Rochester, Rochester, New York.
[1] H. L. Anderson and B. T. Feld, Rev. Sci. Inst. 18, 186 (1947).
[2] Private communication.

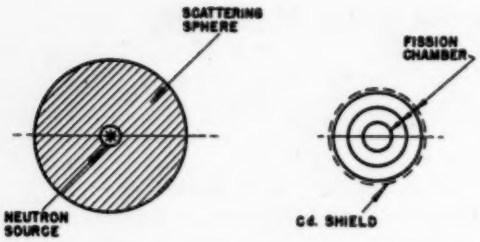

FIG. 1. Schematic diagram of experimental arrangement.

detector distances used in the experiments, the difference was always less than 1 percent. This correction has been applied in the interpretation of the data.

The simplest interpretation of the experiments assumes that the only possible process is one of inelastic scattering. For fast neutrons the capture cross section can be considered negligible in comparison. Thus, if λ_i is the mean free path for inelastic scattering in the sphere, the number of fast neutrons emerging is

$$F=e^{-t/\lambda_i}, \tag{1}$$

where t is the thickness of the sphere (the radius minus the small amount cut out to accommodate the source).

This interpretation is satisfactory if: (1) the thickness of the sphere is small compared to the mean free path for total (elastic plus inelastic) scattering; (2) the elastic scattering cross section is small compared to the inelastic scattering cross section. The values for inelastic scattering cross section found in this approximation are given in column 6 of Table I.

Elastic scattering will cause a decrease in the number of fast neutrons emerging from the scattering sphere. For elastic scattering increases the path of the fast neutrons in the sphere and, thus, gives them a greater opportunity to suffer inelastic collisions. The larger the sphere, the more pronounced will be the effect of elastic scattering on the number of emergent fast neutrons. To calculate this effect we classify the neutrons as primary, first, second, etc., generation fast neutrons. A primary fast neutron is one which emerges from the sphere without having suffered any collisions; a first generation fast neutron has suffered one elastic but no inelastic collision, etc.

For one fast neutron starting out from the source, the number of primary fast neutrons emerging from the sphere is

$$f_0=e^{-t/\lambda}, \tag{2}$$

where t is the thickness of the sphere, λ is now the mean free path corresponding to both elastic and inelastic scattering.

The primary neutrons act as a source of first generation fast neutrons. The number of these produced in the sphere is $(1-f_0)(\sigma_{\text{elastic}}/\sigma_{\text{total}})$. The density of first generations neutron is proportional to

$$1/r^2e^{-r/\lambda},$$

where r is the distance from the center of the source in the sphere. The fraction of these emerging as fast neutrons from the sphere, f_1, can no longer be calculated as simply as though the source were at the center; however, it can be computed in a straightforward fashion by performing numerical integrations. The number of first generation neutrons emerging per primary fast neutron is then

$$F_1=(1-f_0)\frac{\sigma_{\text{el}}}{\sigma_{\text{total}}}f_1\equiv p_0f_1. \tag{3}$$

The number of second generation neutrons produced is $p_0(1-f_1)(\sigma_{\text{el}}/\sigma_{\text{total}})\equiv p_0p_1$. Of these, the fraction f_2 emerges fast from the sphere. f_2 may be calculated if we know the source distribution of second generation neutrons in this sphere. For the second and all further generations, we have assumed a neutron density proportional to $1/r^2$. Using this calculated $f_2=f_3=\cdots=f_n$, the number of second generation neutrons emerging from the sphere, F_2, is $p_0p_1f_2$ and the number of third generation neutrons produced is $p_0p_1p_2$. The number of third generation neutrons emerging from the sphere is $p_0p_1p_2f_2\equiv F_3$.

Calculating in this way the number of fast neutrons escaping for each generation, we have for the nth generation

$$F_n=p_0p_1p_2^{n-2}f_2. \tag{4}$$

The total number of fast neutrons escaping from

TABLE I. Pairs of σ_i and σ_{el} to give measured ratios, F.

Source	Scatterer	Radius of scatterer, cm	Thickness of scatterer, cm	F	$\sigma_{el}=0$	σ_i in Barns 1	2	3	4
RaB	Bi	8.29	7.10	0.79±0.02	1.18	1.12	1.08	1.05	0.97
		12.02	10.86	0.69±0.02	1.21	1.14	1.05	0.97	0.90
	Pb	8.21	7.22	0.80±0.02	0.94	0.88	0.83	0.77	0.72
		10.72	9.55	0.71±0.02	1.12	1.04	1.00	0.88	0.80
	Fe	5.70	4.60	0.73±0.02	0.88	0.78	0.69	0.60	0.49
		8.33	7.14	0.62±0.02	0.82	0.71	0.60	0.47	0.35
Ra-Be	Bi	8.29	7.30	0.73±0.02	1.56	1.48	1.38	1.29	1.20
		12.02	11.10	0.64±0.02	1.44	1.35	1.24	1.14	1.06
	Pb	8.21	7.47	0.74±0.02	1.26	1.19	1.11	1.04	0.95
		10.72	9.79	0.64±0.02	1.42	1.34	1.23	1.12	1.00
	Fe	5.70	4.80	0.68±0.02	1.05	0.92	0.80	0.71	——
		8.33	7.38	0.57±0.02	1.00	0.83	0.72	0.62	——

the sphere is, thus,

$$F=\sum_{n=0}^{\infty} F_n = f_0+f_1p_0+f_2p_0p_1 + f_2p_0p_1p_2+\cdots+f_2p_0p_1p_2^{n-2}, \quad (5)$$

$$F=f_0\left\{1+p_0\left[\frac{f_1}{f_0}+\frac{p_1}{1-p_2}\frac{f_2}{f_0}\right]\right\}. \quad (6)$$

The number which have suffered an elastic collision before escaping is obtained by summing all generations except the primary.

$$\sum_{n=1}^{\infty} F_n = p_0\left[f_1+\frac{p_1}{1-p_2}f_2\right]. \quad (7)$$

It is to these neutrons that the correction for angular distribution must be applied. A series of calculations has been carried out using the above formulae and different values of σ_{el}. From these, the values of σ_i, the inelastic scattering cross section, best fitting the experimental ratio have been found for a number of different values of σ_{el}. These are given in Table I.

IV. CONCLUSIONS

If the only effects taking place in the scattering spheres were those discussed above, and if the above outlined method of calculation of these effects were adequate, then there should be one combination of inelastic and elastic scattering cross sections leading to the measured F for the two different thicknesses of scatterer used for each type of material. A glance at the table serves to show that this is not the case.

One possible reason for the failure of the simple interpretation outlined above is that there is another effect which tends to decrease the inelastic scattering cross section (as measured in this experiment) as the size of the scattering sphere is increased. This effect is in the nature of

TABLE II. Inelastic scattering cross sections (barns).

Neutron source	Detector	Lead	Bismuth	Iron	Reference
Ra-Be	$Fe^{56}(n,p)Mn^{56}$	2.13±0.24	2.32±0.20		(3)
	$Al^{27}(n,p)Mg^{27}$	1.97±0.16	1.98±0.09		(3)
	$Cu(n,n\gamma)$	0.91±0.08	0.63±0.09	0.57±0.05	(3)
	$Pb(n,n\gamma)$	0.73±0.16		0.62±0.07	(3)
Rn-Be	$Si(n,p)$	1.4	1.3		(4)
	$Al(n,p)$	1.8		1.1	(4)
	U^{238} fission	1.34	1.85		(5)
d-d	U^{238} fission	0.55	0.64		(6)

[3] D. C. Graham and G. T. Seaborg, Phys. Rev. **53**, 795 (1938).
[4] C. H. Collie and J. H. E. Griffiths, Proc. Roy. Soc. **A155**, 434 (1936).
[5] J. Marshall and L. Szilard, priv. comm.
[6] W. H. Zinn and L. Szilard, priv. comm.

a "hardening" effect, arising out of the fact that the "cross section for inelastic scattering to below the U^{238} fission threshold" decreases with increasing neutron energy, so that the neutrons with energy close to the threshold are more rapidly removed from the fast neutron beam than those neutrons of energy far above the threshold. The sources emit a spectrum of energies going up (in the case of Ra$-\alpha-$Be) to about 12 Mev.

It should be stressed that what we call, for the purposes of this report, inelastic scattering is really only a special type of inelastic scattering wherein the original fast neutron loses enough energy to drop below the threshold of our detector. Strictly speaking, inelastic scattering is a process in which the scattering nucleus is left in any one of the (energetically) possible excited states; elastic scattering (except for "shadow" scattering) is a special case where the nucleus ends up in its ground state. Of all the possible states in which inelastic scattering can leave a nucleus, our method of measurement picks out only those scatterings in which the neutron loses enough energy to drop below the threshold. For neutrons of energy very much greater than 1 Mev, most inelastic scatterings will not be detected. Our experiment is most sensitive for neutrons close to the threshold. On the other hand, since more levels become available with increasing neutron energy, the true inelastic scattering cross section increases with energy until it reaches the value πR^2 (the cross section for formation of the compound nucleus).

Little is known about the energy spectra emitted by the sources used in this experiment beyond the fact that both emit a rather broad distribution of energies, with both the average and the maximum energy being greater for the Ra$-$Be source.[7] Because we do not know the energy distributions, nor the details of the level schemes of the nuclei involved, none of the effects mentioned above could be calculated or even estimated for our experiment. Hence the uncertainty in the results, as indicated by the values in the table. For all three elements, however, the inelastic scattering is greater for Ra$-$Be than for Ra$-$B neutrons. For the three elements investigated the inelastic scattering increases with atomic weight.

What is really needed for a determination of details of the inelastic scattering process is a series of experiments involving the scattering of monoenergetic neutrons and measurements of the energy distribution of the scattered neutrons. This has been done in one instance.[8] In most cases other observers have also used non-monochromatic neutron sources and threshold detectors. Their results are equally difficult to interpret rigorously. A compilation of values of other observers is given in Table II.[9]

---

[7] B. T. Feld, R. Scalettar, and L. Szilard, Phys. Rev. **71**, 464 (1947).

[8] H. F. Dunlap and R. N. Little, Phys. Rev. **60**, 693 (1941).

[9] Note added in proof: See also the recent work of H. H. Barschall, J. H. Manley, and V. F. Weisskopf, Phys. Rev. **72**, 875 (1947), and H. H. Barschall, M. E. Battat, W. C. Bright, E. R. Graves, T. Jorgensen, and J. H. Manley, Phys. Rev. **72**, 881 (1947).

Photo-Effects in Middle-Weight Nuclei

L. I. SCHIFF
Stanford University, Stanford University, California
(Received February 24, 1948)

The statistical model is applied to (γ,p) and (γ,n) processes induced by Li γ-rays. It is shown that the assumption of a particular regularity for the residual nuclear states that can arise from the compound nucleus gives results that are in good agreement with recent experiments by Hirzel and Wäffler.

THE results of relative measurements of the total cross sections for (γ,p) processes induced by Li γ-rays (17.3 Mev) in several light- and middle-weight nuclei have recently been reported by Hirzel and Wäffler.[1] Although their experimental technique was not adapted to the measurement of (γ,p) and (γ,n) processes for the same parent nucleus, they were able to estimate the cross-section ratio $\sigma(\gamma,p)/\sigma(\gamma,n)$ by interpolation of $\sigma(\gamma,n)$ values for neighboring isotopes. For light nuclei (Mg, Al, Si) they found that the cross sections fluctuate considerably and that the ratios are of order unity. For middle-weight nuclei ($Z=30$ to 50) the fluctuations become less pronounced as Z increases, and the cross-section ratios show a general decrease from about 0.05 at $Z=30$ to about 0.02 at $Z=50$.

The observed ratios are 100 to 1000 times larger than those obtained from a straightforward application of the statistical theory of nuclei,[2] which should provide an adequate description in the range of Z from 30 to 50. The small values of the theoretical ratio arise from a combination of two factors. 1. The Coulomb potential barrier surrounding the compound nucleus formed by absorption of a γ-quantum makes the escape of a proton less probable than the escape of a neutron with the same energy. 2. The rapid increase in the density of energy levels of the two residual nuclei with increasing excitation energy favors the emission of low energy protons and neutrons, for which the barrier effect is most pronounced. It is apparent that any theoretical consideration that increases the number of high energy nucleons that are available for emission also increases the cross-section ratio, and thus reduces the discrepancy between theory and experiment.

It might seem at first that the direct absorption of a quantum by a single proton would give a sufficient number of high energy protons to account for the experimental cross-section ratio.[3] The computed cross section for electric dipole transitions of this type is of the observed order of magnitude if the absorbing proton is weakly coupled to the other nucleons, as is the case with an electron in the corresponding atomic situation. Actually, however, the coupling between particles in a nucleus is so strong that the initial and final wave functions of the other nucleons are different, and the dipole matrix element for a single proton is reduced considerably. This effect accounts for the suppression of dipole with respect to quadrupole transitions in nuclei. Strong coupling implies that radiative transitions involve the nucleus as a whole (liquid drop model), so that the small separation of nuclear charge and mass centers results in small dipole matrix elements.

An alternative explanation of the experimental results, which seems more likely to represent the quite complex processes that actually take place, is based on the statistical model but takes account of the difference in character of the compound nuclei formed by fast nucleon impact and by absorption of a γ-quantum. In the first case the kinetic and binding energy of the incident nucleon is rapidly shared among all particles of the nucleus because of the strong coupling between each particle and its neighbors. This results in a compound nucleus whose state is a superposition of many modes of oscillation of the

[1] O. Hirzel and H. Wäffler, Helv. Phys. Acta **20**, 374 (1947); the writer is indebted to Professor H. H. Staub for informing him of these results prior to publication.
[2] V. F. Weisskopf and D. H. Ewing, Phys. Rev. **57**, 472, 935 (1940).
[3] V. F. Weisskopf, private communication.

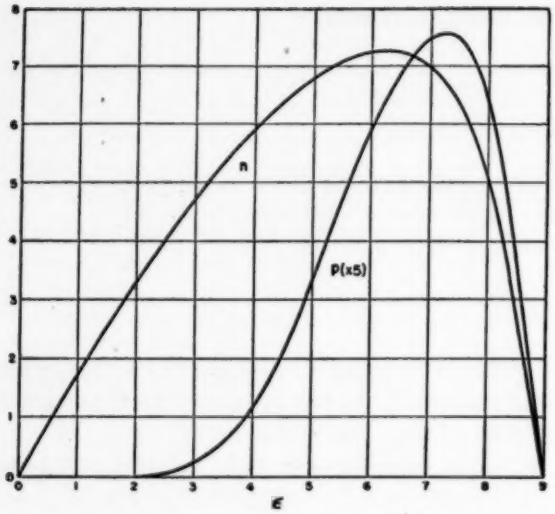

FIG. 1. Relative energy distributions for protons and neutrons when $Z=30$; the ordinates of the proton curve have been multiplied by 5.

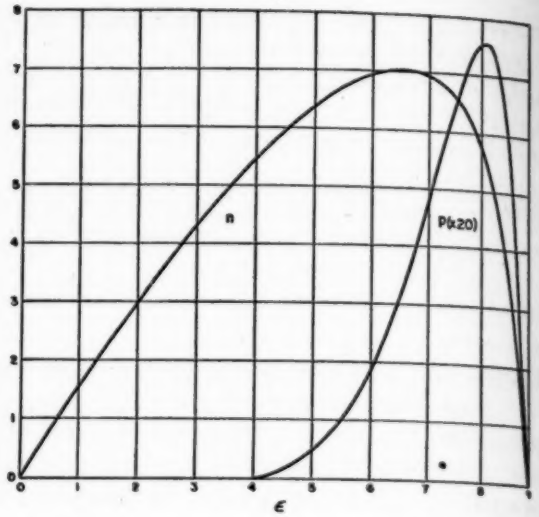

FIG. 2. Relative energy distributions for protons and neutrons when $Z=50$; the ordinates of the proton curve have been multiplied by 20.

nucleus as a whole. In the second case, the electromagnetic field of the incident radiation varies slowly over the nucleus ($\lambda=11\times10^{-13}$ cm for the Li γ-ray), so that all of the protons are acted on by similar forces. This results in a compound nucleus that can be described by a very small number of modes of oscillation.

The high degree of regularity of the compound states formed by γ-ray absorption will be reflected to some extent in the states of the residual nuclei that result from the subsequent emission of a proton or a neutron. This can be seen from a consideration of the reverse process, in which a proton or neutron is absorbed by the residual nucleus to form the compound nucleus. It is clear that only a small fraction of all possible states of the residual nucleus in a given energy range can absorb a proton or a neutron to form such a compound state. If then the density of *regular* energy levels of the residual nuclei (those levels that can result from the compound state by proton or neutron emission) increases less rapidly with increasing excitation energy than the density of all energy levels, relatively more high energy nucleons will be emitted.

The regular level density can be estimated on the basis of the statistical model.[4,5] The total level density is assumed to be proportional to $\exp[2(E/a)^{\frac{1}{2}}]$, where E is the excitation energy of the nucleus in Mev and $a\approx20/A$ Mev for a nucleus of mass number A.[2] This can be shown to be equivalent to the assumption that the frequencies of the modes of oscillation of the nucleus are distributed with constant average spacing a/h.[5] It is plausible to define a regular state as one that can be represented as a superposition of a very small number of modes of oscillation. In particular, if only one mode contributes to each regular level, a simple expression for the regular level density can be obtained. For this purpose, the mode frequencies are assumed to be equally spaced, so that the first mode has energy levels (disregarding the zero point energy) a, $2a$, $3a$, $\cdots$, the second mode has energy levels $2a$, $4a$, $6a$, $\cdots$, and the nth mode has energy levels na, $2na$, $3na$, $\cdots$. Then for an interval E to $E+\Delta E$ of excitation energy, where E and ΔE are large in comparison with a, the number of regular levels is approximately

$$\frac{\Delta E}{a}+\frac{\Delta E}{2a}+\cdots=\sum_{n=1}^{E/a}\frac{\Delta E}{na}\cong\frac{\Delta E}{a}\ln\left(\frac{E+a}{a}\right).$$

Thus the regular level density is proportional to $\ln(E/a)$, and increases much less rapidly with increasing E than the total level density. Similar expressions can easily be obtained for other assumptions concerning the total level density.

[4] H. A. Bethe, Phys. Rev. **50**, 332 (1936).
[5] V. F. Weisskopf, Phys. Rev. **52**, 295 (1937).

The ratio $\sigma(\gamma,p)/\sigma(\gamma,n)$ can now be calculated from Eq. (19) of the paper of Weisskopf and Ewing:[2]

$$\sigma(\gamma,p) \propto \int_0^{\epsilon_0} \epsilon S_p(\epsilon)\xi_p \ln\left(\frac{\epsilon_0-\epsilon+a}{a}\right)d\epsilon,$$

$$\sigma(\gamma,n) \propto \int_0^{\epsilon_0} \epsilon S_n(\epsilon)\xi_n \ln\left(\frac{\epsilon_0-\epsilon+a}{a}\right)d\epsilon.$$

The integrands give the relative numbers of protons and neutrons that are emitted with energy ϵ (in Mev), where the maximum energy ϵ_0 is the difference between the γ-ray energy and the binding energy of a nucleon. For the energy range under consideration, the sticking probabilities, ξ_p and ξ_n, are taken to be unity, and the cross section for neutron capture, $S_n(\epsilon)$, is taken to be the nuclear area. The proton capture cross section, $S_p(\epsilon)$, can be found from Fig. 1 of reference 2. The dependence of ϵ_0 and the residual nuclear level densities on the oddness or evenness of Z and A will be ignored here.

The relative energy distributions computed in this way for the emitted protons and neutrons are shown in Fig. 1 for $Z=30$ ($a=0.30$ Mev) and in Fig. 2 for $Z=50$ ($a=0.17$ Mev); it is assumed that $\epsilon_0=9$ Mev. The cross-section ratios can be found from the areas under the curves:

$$\frac{\sigma(\gamma,p)}{\sigma(\gamma,n)}=\begin{cases}0.124, & Z=30,\\ 0.020, & Z=50.\end{cases}$$

These values are in good agreement with the experimental results,[1] but indicate a somewhat more marked dependence of cross-section ratio on Z than is observed. This suggests that the statistical model is inadequate for the smaller group of Z values covered by the experiments, especially since rather large fluctuations are observed there. Experiments on the energy distributions of protons and neutrons emitted by the same compound nucleus would be helpful in clarifying the nature of the processes that take place.

PHYSICAL REVIEW VOLUME 73, NUMBER 11 JUNE 1, 1948

Note on the Stability of Systems Containing a Light Positive Particle

AADNE ORE*
Palmer Physical Laboratory, Princeton University, Princeton, New Jersey
(Received January 2, 1948)

It is of interest to consider the dynamic stability of atomic or molecular systems which contain a positron, e.g., e^+Cl^-. This paper examines what information about this stability can be obtained without elaborate calculations, (a) from experimental data descriptive of hydrides and of the hydrogen molecule or molecular ion, and (b) from existing calculations of the energy of light polyelectrons. The procedure (a) suffices to guarantee stability only when the positron is replaced by a positive meson which has a mass of the order of twenty-electron masses or more. The second procedure allows a certain lowering of these approximate minimum mass values, in a special case to a few electron masses. The various numerical results are obtained very easily. They indicate that negative atomic ions can have a positive positron affinity.

I. INTRODUCTION

RECENTLY Wheeler[1] envisaged the existence of short-lived atomic or molecular systems which contain a positron, e.g., e^+Cl^-. At present, even the question of the dynamic stability of such systems remains unanswered.

In a quantitative investigation of this stability the approximate methods of atomic or molecular theory do not seem well adapted. In the first place, the electric charge of the positron has the opposite sign of that of an atomic electron. Secondly, the adiabatic approximation, which is justified in the case of ordinary molecules (Born-Oppenheimer), cannot be expected

* Frank B. Jewett Fellow, 1947–48.
[1] J. A. Wheeler, Ann. N. Y. Acad. Sci. **48**, 219 (1946).

to remain valid when the mass of one "nucleus" has been reduced to that of an electron. (If this approximation be valid for a "di-atomic molecule," irrespective of the mass of one "nucleus," and, provided we can consider the zero point energy inversely proportional to the square root of the reduced mass of the "nuclei," one easily finds that the mass of the hydrogen nucleus (e.g., in HCl) can be reduced to the order of a few electron masses before dissociation occurs.)

The simplest system of the kind under consideration is e^+H, which results when one proton is replaced by a positron in the molecular hydrogen ion, H_2^+. Clearly, the same system can be obtained by adding a positron to a hydrogen atom. It is well known that a negative electron can combine with a hydrogen atom to form the stable negative atomic ion H^-, or e^-H. Classically, one would then expect that e^+H would be unstable. That this argument is not valid can be illustrated by the fact that the bi-electron, e^+e^-, can form a stable tri-electron when an electron of *either* sign is added. On the other hand, e^+H results from the stable tri-electron $e_2^+e^-$ when the mass of one of the positive particles is increased. Again, however, increasing the mass of one particle, keeping the charges unchanged, does not necessarily mean that a more stable system results. Thus, when in H^- one of the electrons is replaced by a negative meson (of mass 200m), the second electron will no longer be bound.[2] Hence, we conclude that qualitative arguments can hardly be applied to the problem in question.

It is the purpose of this note to examine what information about the dynamic stability of systems containing a light positive particle can readily be obtained from experimental data descriptive of ordinary molecules and from existing calculations of the energy of light polyelectrons. In an investigation of this stability the Schroedinger equation can be assumed to be valid, that is, we can neglect the finite probability of annihilation and we can apply non-relativistic quantum mechanics (cf. Wheeler, reference 1). Since the results one obtains in this way are not conclusive when the particle in question is a positron, we shall not attempt to discuss the various questions which arise in connection with the formation of such systems.

[2] E. Fermi and E. Teller, Phys. Rev. **72**, 399 (1947).

II. APPLICATION OF MOLECULAR WAVE FUNCTIONS

We shall understand by "system M" an ordinary molecular system which contains at least one hydrogen nucleus (mass M), and by "system μ" the corresponding "molecule" in which a particle of mass μ plays the role of a light isotope of hydrogen. We shall proceed to determine approximate minimum values of μ which are consistent with dynamic stability for system μ in various cases.

In the following it will be understood that we are dealing exclusively with the ground states of the two systems under consideration.

The respective wave equations differ merely in the multiplicative constant of one of the kinetic energy terms. When the part of the Hamiltonians which is common for system M and system μ is denoted by H', the two equations can be written

$$-\frac{h^2}{2M}\nabla^2\psi_M + H'\psi_M = E_M\psi_M, \tag{1}$$

and

$$-\frac{h^2}{2\mu}\nabla^2\psi_\mu + H'\psi_\mu = E_\mu\psi_\mu. \tag{2}$$

We will now let ψ_M approximate ψ_μ in the sense of the variational method. Assuming normalized ψ_M, we obtain

$$E_\mu < -\frac{h^2}{2\mu}\int \psi_M^*\nabla^2\psi_M d\tau + \int \psi_M^* H'\psi_M d\tau, \tag{3}$$

or

$$E_\mu - E_M < \left(\frac{M}{\mu} - 1\right)T \tag{4}$$

where

$$T = -\frac{h^2}{2M}\int \psi_M^*\nabla^2\psi_M d\tau. \tag{5}$$

According to the last equation, T is the mean kinetic energy of the proton in system M. This quantity can be obtained rather accurately from the zero-point energy of that molecule. The lowest vibrational level corresponds closely to that of a harmonic oscillator, that is, one-half of the zero-point energy represents the kinetic energy of the nuclear vibrations.

TABLE I. Approximate lower limit values for the mass μ of a positive particle which can replace a hydrogen nucleus in a molecule (system M).

System M	H_2^+	H_2	HLi^7	HBe^9	HC^{12}	HF^{19}	HNa^{23}	HCl^{35}	HK^{39}	HCa^{40}
μ, (minimum) in units of m	24	24	22	40	38	32	22	33	21	34

The total energy E_M is known only for the lightest hydrides, but since it is only the *difference* $E_\mu - E_M$ that enters the left-hand side of (4), the dissociation energy D_M is all that we need know in order to be able to apply the inequality.

The last statement becomes evident when we write

$$E_M = -R_H h + E_{n-2} - D_M, \tag{6}$$

and

$$E_\mu = -\frac{\mu(M+m)}{M(\mu+m)} R_H h + E_{n-2} - D_\mu. \tag{7}$$

In (6) the term $-R_H h$ is the energy of the hydrogen atom, and E_{n-2} the energy of the partner atom, which consists of all but two of the n particles which form system M.

The reason why we need consider only the type of dissociation indicated in (7) is that the first term in this equation will have a value between -6.77 ev ($\mu = m$) and -13.53 ev ($\mu = M$), while no atom is known to have an electron affinity which exceeds a few electron volts.[3]

It should be understood, however, that in writing down Eqs. (6) and (7) we are assuming that system M is a neutral molecule. When system M is a molecular ion the equations will be somewhat different.

The exact wave function ψ_M is not known explicitly for any molecule. The preceding outline shows, however, that our ignorance as to the form of the function used in the variational calculation is remedied by available spectroscopic data. When we combine the inequality (4) with the proper experimental data, we readily find minimum values of μ consistent with stability ($D_\mu > 0$). Some of the results one finds in this way are given in Table I.**

Small minimum values are favored by low zero-point energy (hydrides of group I in the periodic table) and by large dissociation energy. Since the latter energy is not known to a high degree of accuracy for all hydrides, the values of μ given in Table I may need slight corrections. Such corrections can be of but little significance in the present approximation, however.

According to the variational character of the treatment which has been outlined above, the various systems μ will be dynamically stable when μ has a value exceeding the minimum value, e.g., when the positive particle is a cosmic-ray meson. Furthermore, the possibility is not excluded that the correct lower limits are such as to include a positron.

However, the values given in Table I are still so high that the adiabatic approximation may be essentially valid.

III. MODIFICATION OF ψ_M IN ACCORD WITH THE VIRIAL THEOREM

We shall now proceed to modify the unknown ψ_M in such a way that we obtain a function which will be a better approximation for ψ_μ, at least as far as the energy is concerned. This is possible by what amounts to an application of the virial theorem.†

In the way familiar from variational calculations of binding energies, we introduce a parameter k by writing

$$\psi_M = \psi_M(\mathbf{r}_i) = \varphi(k\mathbf{r}_i), \quad i = 1, 2, \cdots, n. \tag{8}$$

Furthermore, we shall use the following abbreviations:

$$N = \int |\psi_M|^2 d\tau;$$
$$T_{n-1} = -\sum_{n-1} \frac{h^2}{2m_i} \int \psi_M^* \nabla_i^2 \psi_M d\tau, \tag{9}$$

and we denote by V the corresponding matrix element representing the total potential energy. An apostrophe will be used to indicate that

[3] Cf. H. S. W. Massey, *Negative Ions* (Cambridge University Press, Teddington, England, 1938).

** The experimental data have been taken from the book by G. Herzberg, *Molecular Spectra and Molecular Structure* (Prentice-Hall, Inc., New York, 1939).

† Cf. V. Fock, Zeits. f. Physik **63**, 885 (1930).

matrix elements are given in terms of $\varphi(\mathbf{r}_i)$ rather than $\psi_M(\mathbf{r}_i)$, as in (9).

Corresponding to (3) we have

$$E_\mu N < \frac{M}{\mu} T + T_{n-1} + V, \tag{10}$$

whence

$$E_\mu N' < k^2 \left(\frac{M}{\mu} T' + T_{n-1}' \right) + kV'. \tag{11}$$

We minimize the right-hand side of (11) with respect to the parameter k. This minimization actually means that we modify ψ_M, given by (8), in such a way that we obtain an approximate ψ_μ which will be in accord with the virial theorem.

The result can be written as

$$E_\mu < -(V')^2/4N' \left(\frac{M}{\mu} T' + T_{n-1}' \right). \tag{12}$$

(Strictly, we should keep the possibility open that (12) be an equality, since the modification of ψ_M leads to the correct ψ_μ in the case where the system M is the hydrogen atom. This case, however, does not concern us at present.)

We can omit the apostrophes in (12). The omission is equivalent to a multiplication by k^2 of both numerator and denominator in the right-hand side expression.

Similarly, we can write

$$E_M = -V^2/4N(T + T_{n-1}). \tag{13}$$

Again we assume $N=1$. Furthermore, according to the virial theorem we can substitute $2E_M$ for V. From the preceding relations we then obtain the inequality

$$E_\mu < -\frac{E_M}{1 - \left(\frac{M}{\mu} - 1 \right) \frac{T}{E_M}}. \tag{14}$$

This inequality requires for its applicability the value of the total energy E_M and not merely the dissociation energy D_M, as was the case when we applied (4). E_M is not known with accuracy for heavier hydrides. However, even when system M is HLi, and more so for heavier hydrides, the two inequalities (14) and (4) are approximately equivalent.

When system M is either H_2^+ or H_2 one easily finds that the relation (14) guarantees stability for system μ provided the mass μ is greater than about 20-electron masses, as compared to roughly 24-electron masses which was the minimum value resulting from inequality (4) in these cases.

IV. APPLICATION OF APPROXIMATE POLYELECTRONIC WAVE FUNCTIONS

We shall once more consider the two special cases in which system M is either H_2 or H_2^+.

When system M is H_2^+ then system μ consists of a hydrogen atom plus the positive particle of mass μ. This system can be obtained from the positive tri-electron $e_2^+e^-$ when in the latter we replace one positron by a proton and the other positron by the particle μ.

The wave equation for the tri-electron and for the corresponding system μ can be written

$$\left\{ \nabla_1^2 + \nabla_2^2 + \nabla_3^2 + 2\left(\frac{1}{r_1} + \frac{1}{r_2} - \frac{1}{r_{12}} \right) + E_t \right\} \psi_t = 0, \tag{15}$$

and

$$\left\{ \frac{m}{M} \nabla_1^2 + \frac{m}{\mu} \nabla_2^2 + \nabla_3^2 + 2\left(\frac{1}{r_1} + \frac{1}{r_2} - \frac{1}{r_{12}} \right) + E_\mu \right\} \psi_\mu = 0, \tag{16}$$

respectively. In both equations, 1 and 2 refer to the two positive particles and 3 refers to the negative electron. The unit of length is the atomic unit of length, a_H, and we have used $R_\infty h$ as energy unit.

The similarity of the two Eqs. (15) and (16) permits a simple application of Hylleraas' calculations of the energy of the tri-electron[4] to the problem of the dynamic stability of our system μ.

Consider a function φ which is symmetric in r_1 and r_2 and which does not depend upon the third distance (r_{12}) between the particles. Since in this case

$$\int (\nabla_1 \varphi)^2 d\tau = \int (\nabla_2 \varphi)^2 d\tau = \tfrac{1}{2} \int (\nabla_3 \varphi)^2 d\tau, \tag{17}$$

[4] E. A. Hylleraas, Phys. Rev. **71**, 491 (1947).

we readily obtain the following inequality

$$E_\mu < \frac{4E_t'}{\frac{m}{M}+\frac{m}{\mu}+2}. \tag{18}$$

In (18) E_t' is the approximate energy of the tri-electron which results from a variational calculation by means of the function φ. In Hylleraas' calculations φ contains parameters which are given the values which minimize E_t. It follows from (18) that these values are at the same time the best values we can give the parameters when φ is taken to approximate the wave function of system μ.

Hylleraas obtained the approximate value $E_t' = -\frac{1}{2}\times 1.02762 R_\infty h$ when φ had the form

$$\varphi = e^{-\frac{1}{2}s}(1+c_2t^2+c_4t^4+c_6t^6); \qquad s=r_1+r_2, \quad t=r_2-r_1. \tag{19}$$

When this value of E_t' is inserted into (18), one now finds that system μ will be stable provided $\mu > 18m$. Thus, we have obtained a slightly lower value for μ, above which stability is guaranteed, as compared to the values 24 m and 20 m of the preceding sections.

Next, let us consider the case in which system M is the neutral hydrogen molecule, H_2. System μ can then also be obtained from the quadri-electron, $e_2^+e_2^-$, by replacement of the two positrons by one proton and by the particle μ, respectively.

The existing calculations of the energy of the quadri-electron have been made by using variational functions which do not contain the two distances between identical particles and which are symmetric with respect to exchange of electrons, exchange of positrons, and exchange of the two electrons against the two positrons.

Assuming this kind of function, and by a procedure similar to the one above, we arrive at an inequality which differs from (18) merely in that E_t' has been replaced by the approximate energy E_q' of the quadri-electron.

If we take the value $-1.0085R_\infty h$ for E_q', which results from a variational function having the character of a linear combination of somewhat generalized "atomic" functions,[5] we find that the system μ under consideration will be stable for μ greater than about 5 m.

A linear combination of "atomic" and "ionic" functions[6] yielded a slightly lower value for E_q'. The corresponding minimum value of the mass μ, consistent with dynamic stability, is found to be roughly 4.5 m.

V. CONCLUSION

The successive lower limit values which we have obtained in the particular case when system M is the hydrogen molecule, namely, 24-, 20-, and 4.5-electronic masses, show that the choice of variational function is essential for the result. However, not even the function which gave the lowest value, 4.5 m, can be considered to be a very good approximation for the system μ when μ is small compared to the mass of a proton. The symmetry properties mentioned above are not proper in this case. Furthermore, the function does not contain the total number of variables.

For these reasons it seems likely that this system μ will be stable even for $\mu = m$. Furthermore, the values given in Table I then indicate that at least in some cases we can replace the hydrogen nucleus in a hydride molecule by a positron and obtain a dynamically stable system, of the kind envisaged by Wheeler.

ACKNOWLEDGMENTS

The author takes pleasure in expressing his appreciation to Professor J. A. Wheeler for his interest and encouragement. He is also indebted to Professor D. Bohm of Princeton University and to the group of physicists in Yale University with whom he had stimulating discussions.

The author wishes to express his indebtedness to the Trustees of the Frank B. Jewett Fellowships for the award of a fellowship making this investigation possible.

[5] E. A. Hylleraas and A. Ore, Phys. Rev. **71**, 493 (1947).
[6] A. Ore, Phys. Rev. **71**, 913 (1947).

The Rate of Decay of Fission Products

K. WAY AND E. P. WIGNER
Clinton National Laboratories, Oak Ridge, Tennessee

(Received January 28, 1948)

By considering the fission products as a sort of statistical assembly, calculations have been made of the β-disintegrations per second and of the total energy emitted per second at any time after fission has taken place (cf. Fig. 6). The results are in good agreement with experiment. The theoretical work is based on the assumption that the mass of a nucleus of mass number A and charge Z is given by $a(Z_0(A)-Z)^2+b$. Empirical values for a and b are used. Use is also made of an approximate empirical relationship between half-life and disintegration energy. A further basic hypothesis which is important for the results at very short times after fission has taken place is that, in the most probable way of splitting, the chain lengths of the light and heavy fragments are equal and that there is not much deviation from this most probable mode of fission. (See L. E. Glendenin, C. D. Coryell, R. R. Edwards, and M. H. Feldman, CL-LEG-1. A tentative explanation has been given recently by R. D. Present, Phys. Rev. **72**, 7 (1947).) The average number of β-disintegrations per fission is found to be 6; the average energy of all radiations (β, γ, and neutrino) of the fission products is 21.5±3 Mev. Apparently, about half of this energy escapes in the form of neutrinos and a quarter is emitted in the form of β and in the form of γ rays.

A few remarks are made concerning the possible origin of delayed neutrons. It is also pointed out that the spread of the kinetic energy of a given pair of fission fragments cannot be easily explained on the basis of differences of chain length which result in differences in excitation energy of the fragments. It is possible that fluctuations in the production of fission neutrons are at least partly responsible for the kinetic energy spread.

I. INTRODUCTION

THERE are two ways to describe the total β- and γ-radiation emitted by the fission products. The first, more accurate method describes it as the sum of radiations emitted by the different fission products. The second, less accurate method considers the fission products as a sort of statistical assembly and tries to arrive at once at the total radiation from all the fission products together. While this second method is unquestionably less complete than the first one, it is so much simpler that it is much preferable in most practical calculations. Its validity is limited, of course, to times during which the radiation is emitted by many nuclei. At very long times after irradiation, when most of the radiation is caused by a few surviving species of nuclei, the first method is definitely preferable.

A complete description of the radiations would give the energy distribution of the β-rays for all times after irradiation and a similar distribution function for the γ-rays. No experimental data are available which would permit one to obtain this complete information, and it will not be attempted here to obtain it theoretically. Instead, we shall restrict ourselves to the number $\beta(t)$ of β-rays, emitted during unit time, t seconds after a fission has occurred, to the total energy $\mathrm{B}(t)$ of the β-rays which are emitted during the same time element and to the similar quantities $\gamma(t)$ and $\Gamma(t)$ for γ-rays.

If $N(E,t)dE$ be the number of fission products existing at time t after fission has taken place which have disintegration energies between E and $E+dE$ and if $\lambda(E)$ be the decay constant of nuclei with disintegration energy E, then $\beta(t)$ is given by

$$\beta(t)=\int_0^{E_m} N(E,t)\lambda(E)dE, \qquad (1)$$

where E_m is the largest disintegration energy found. Actually, there is no unique relation between disintegration constant and energy, as the function $\lambda(E)$ would imply. However, it will be easy to take care of this point in the course of the calculation.

The total energy emitted at time t following a fission is equal to the sum of the energy of the β-rays, γ-rays, and neutrinos. If one assumes that the energy of the neutrinos is twice greater than the energy of the β-rays (cf. Fig. 1), then this total energy is equal to $3\mathrm{B}(t)+\Gamma(t)$ and is given by

$$3\mathrm{B}(t)+\Gamma(t)=\int_0^{E_m} EN(E,t)\lambda(E)dE. \qquad (2)$$

The functions and quantities which are necessary for the evaluation of the integrals are discussed in the next three sections.

II. RADIOACTIVE NUCLEI FORMED IMMEDIATELY AFTER FISSION

It has been assumed already in the earliest theoretical papers on nuclear physics that the energy difference between the isobars of an odd element can be written in the form $a(Z_0-Z)^2$ where a is a constant (depending on the mass number of the isobars). Z_0 (not necessarily an integer) is another constant which we shall call the charge number of the "most stable isobar" and Z is the charge number of the isobar in question. The value of a has been determined from empirical data[1] (Weizsäcker, 1935; Bethe and Bacher, 1936; Bohr and Wheeler, 1939; Feenberg 1947), and also from theoretical considerations[2] (Wigner, 1937). We attempted to obtain the constant a directly from the data on the disintegration energy of fission chains. We found, however, that the relative energies of isobars are, in most cases, rather irregular functions of Z, showing considerable fluctuations around any smooth function like $a(Z_0-Z)^2$. Thus the a in this formula cannot be determined in any precise fashion. On the whole, we found that $a=0.65$ Mev for the heavy fragment and 1 Mev for the light fragment represent the data as well as we could represent them. These values agree almost exactly with the early values (Weizsäcker, Bethe, and Bacher[1]) given to this constant $(78/A+0.58/A^{\frac{1}{3}})$ and are somewhat larger than the values obtained theoretically[2] $(55/A+0.59/A^{\frac{1}{3}})$. The energy of the radioactive disintegration[3] is given by the difference of the above

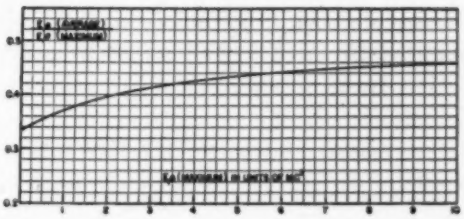

FIG. 1. The ratio of average β-energy to maximum β-energy on the basis of Fermi's formula for the energy distribution in an allowed transition. Effect of Coulomb field is neglected.

expression for two successive values of Z and is, therefore,

$$a(Z_0-Z)^2-a(Z_0-Z-1)^2=2a(Z_0-Z)-a.$$

This decreases as Z increases in the course of successive disintegrations.

The above expression is supposed to hold for isobars with odd mass number A. If A is even, the isobars with odd Z (containing an odd number of protons and also an odd number of neutrons) have, on the whole, higher energy contents than the isobars with even Z (containing an even number of protons and an even number of neutrons). This can be expressed mathematically by using, in case of even n, the expression $a(Z_0-Z)^2$ for the energy of nuclei with even Z and another expression $a(Z_0-Z)^2+b$ for odd Z.

The value given by Bethe and Bacher and by Weizsäcker for the constant b is $40/A+0.6/A^{\frac{1}{3}}$ which is about 0.34 Mev for the light and 0.26 Mev for the heavy fractions. The theoretical values[2] are much higher, *viz.* $92/A$, which gives $b=0.96$ Mev for the light and $b=0.66$ Mev for the heavy fragment. The actual values which will be determined in the third section are even greater than these, *viz.* 2.8 and 1.8 Mev, in agreement with Bohr and Wheeler.[1]

It follows from the above that the energies of successive disintegrations of fission chains with even A will not diminish steadily but that, particularly toward the end of the series, a high energy disintegration will be followed by a low energy disintegration, this again by a high energy disintegration, etc. The energy of transi-

[1] G. Gamow, Int. Conf. on Physics, London, 1934, Vol. I, *Nuclear Physics*, 60–66, Physical Society. W. H. Heisenberg, Rapport du VII me Congress Solvay, Paris, 1934. G. C. Wick, Nuovo Cimento **11**, 227 (1937). C. F. v. Weizsäcker, Zeits. f. Physik **96**, 431 (1935). H. A. Bethe and R. F. Bacher, Rev. Mod. Phys. **8**, 82 (1936), §26, 28, 29, 30, Eq. (185), (185a) ff. N. Bohr and J. A. Wheeler, Phys. Rev. **56**, 426 (1939). E. Feenberg, Rev. Mod. Phys. **19**, 239 (1947).

[2] E. Wigner, Phys. Rev. **51**, 947 (1937). Also Bicentennial Symposium, University of Pennsylvania Press, 1940. W. H. Barkas, Phys. Rev. **55**, 69 (1939), also E. Feenberg, reference 1.

[3] By the energy of disintegration we mean the sum of the energies of all radiations (β, γ, and neutrino) emitted in cascade in a transition from the normal state of the parent to the normal state of the daughter. The energy of transition of a β-disintegration is, on the other hand, the high energy limit of the β-rays emitted in that transition. In the case of a simple β-spectrum, with a succeeding γ-emission, the energy of transition differs by the energy of the γ-rays from the energy of disintegration.

tion from an odd Z to an even $Z+1$ will be represented by $2a(Z_0-Z)-a+b$, the energy of transition from an even Z to an odd $Z+1$ by $2a(Z_0-Z)-a-b$.

The radioactive nuclei to be considered are not all immediately created by fission but are mostly daughters of others. In the series with odd mass numbers, the energy of disintegration decreases. Since the lifetime increases with decreasing energy of disintegration, successive members of the radioactive series will have longer and longer half-lives. (See Fig. 2.) This conclusion is, in general, corroborated by the experimental material,[4] but it is not without exception. If we assume its validity, it is justifiable, for our purpose, to treat all the members of a radioactive series with odd A as immediately created by fission, since the ancestors of any nucleus will have much shorter lives than the nucleus itself, so that the time which elapses before a certain nucleus is formed can be neglected as compared with the lifetime of that nucleus.

If A is even, the situation is only slightly different. In this case, the energies of successive members of a radioactive series will not be steadily diminishing, but, particularly toward the end of the series, a high energy disintegration will be followed by a low energy disintegration, this again by a high energy disintegration, etc. This results in an alternation in the half-lives, such that a long-lived element will be followed by a short-lived element, this again by a long-lived element, etc. As mentioned before, this will be particularly true toward the end of a series while towards the beginning of the series the energies will be successively diminishing and the lifetimes increasing. In the present case (even A) one is not justified any more to consider all nuclei as being immediately formed by the fission. However, if a short-lived nucleus is the daughter of a long-lived nucleus, the lifetime of the short-lived nucleus may be neglected and the life history of the short-lived nucleus will be approximately the same as the life history of its parent. Hence the even-even nuclei (even number of protons and even number of neutrons) may be considered to be immediately formed by fission in the same sense as all odd-mass nuclei were.

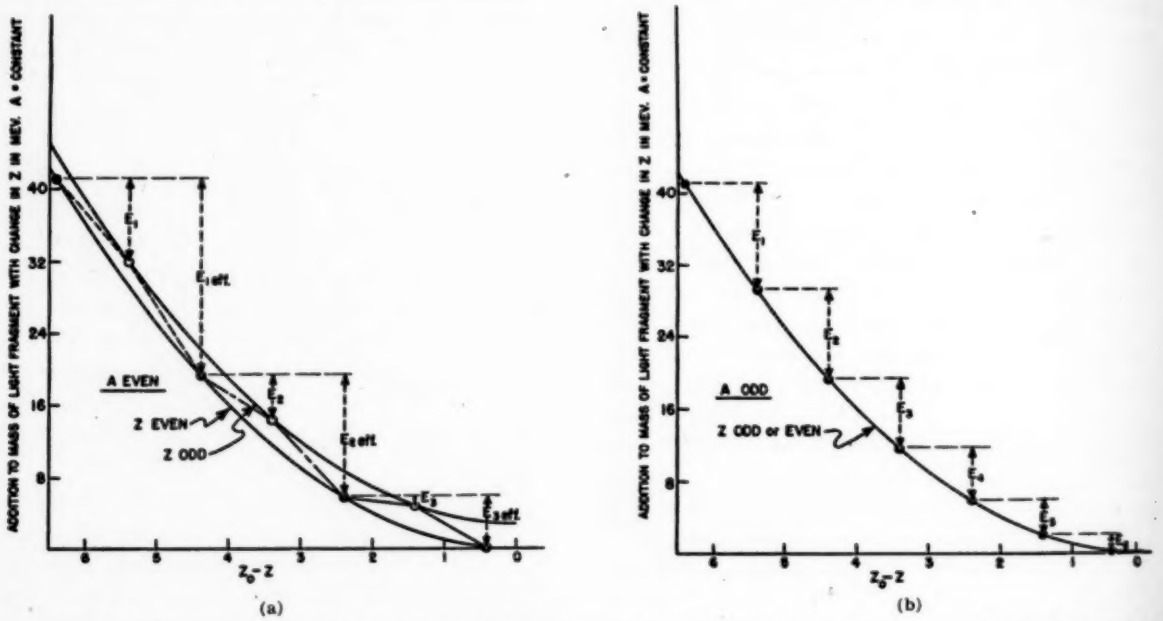

FIG. 2. All fission products with odd masses can be considered to be formed immediately upon fission. Of the fission products with even masses, only those with even charge are considered to have been formed immediately upon fission. The disintegrations of the daughters of these nuclei (which have odd charges) will be considered to occur simultaneously with the disintegrations of the parents. In Fig. 2a ● indicates nuclei "formed immediately in fission." ○ are odd-odd daughters whose half-lives are considered to be those of their even-even parents. In Fig. 2b ● are nuclei "formed immediately in fission."

[4] "Nuclei formed in fission: decay characteristics, fission yields and chain relationships," issued by the Plutonium Project, Rev. Mod. Phys. **18**, 513 (1946).

TABLE I. Number of β-disintegrations per fission.

Mass and yield (percent) of heavy nucleus	130 1.8	131 2.7	132 3.9	133 4.6	134 5.3	135 5.8	136 6.2	137 6.5	138 6.6	139 6.6	140 6.5	141 6.2	142 5.8	143 5.3	144 4.7	145 4.1	146 3.4	147 2.6	148 1.8	149 1.4
Smallest stable Z for this mass	54	54	54	55	54	56	54	56	56	57	58	59	58	60	60	60	60	62	60	62
Most stable Z for this mass ($Z_0(A_H)$)	53.5	54	54.5	55	55.5	56	56	56.5	57	57.5	58	58.5	59	59.5	60	60.5	61	61.5	61.5	62
Masses of corresponding light nuclei	104	103	102	101	100	99	98	97	96	95	94	93	92	91	90	89	88	87	86	85	84
Smallest stable Z for this mass	44	45	44	44	42	44	42	42	40	42	40	41	40	40	40	39	38	37	36	37	36
Most stable Z for this mass ($Z_0(A_L)$)	45.5	45	45	44.5	43.5	43.5	43	42.5	42	41.5	41	41	40.5	40	39.5	39	38.5	38	37.5	37	36.5
Number of β-particles emitted	6	7	7	6	6	6	7	5	4	6	8	6	4	4	6	4	4	6	7	5	6	7	8	7	6	6	8	8	8	7	7	6	6	5	7	6	4	5	7	6
$92-Z_{H0}-Z_{L0}$	7	6*	7	7	7**	7	7	6	7	7	7	7	7	6	7	6	7	6	7	7	7	7	7	7	7	7	7	7	7	7	7	7	7	7	7	7	7	6	7	6

* 6 stands for 6.5.
** 7 stands for 7.5.

Among the odd-odd nuclei (odd number of protons and neutrons) only those will be considered to be formed immediately upon fission which actually are, i.e., the first member of a chain if that first member is odd-odd. On the other hand, all odd-odd nuclei which are daughters of even-even nuclei will be assumed to disintegrate immediately after the disintegration of their parent. These parents will have a relatively long lifetime, corresponding to a relatively low real disintegration energy $E=2a(Z_0-Z)-a-b$ but, for that lifetime, will have an abnormally high effective disintegration energy, namely, the sum of their own and their daughters' disintegration energy:

$$[2a(Z_0-Z)-a-b]+[2a(Z_0-Z+1)-a+b]=2E-2a+2b.$$

III. THE DISTRIBUTION FUNCTION $N(E,t)$: GLENDENIN'S RULE

One would think, offhand, that the most probable way of splitting of a nucleus into two fragments is the one in which the kinetic energy of the fragments can be highest. Therefore, if the splitting occurs into the two masses, A_L and A_H (L and H refer to light and heavy fragment), one would think that the most probable Z for the light fragment would be such that the radioactive energy of the two fragments,

$$E_r=a_L(Z_0(A_L)-Z)^2+a_H(Z_0(A_H)-92+Z)^2, \quad (3)$$

is a minimum. In (3), $Z_0(A)$ is the "most stable nucleus" of mass A in the sense of the preceding section. If $a_L=1$ Mev, $a_H=0.65$ Mev, it would then follow from (3) that the most probable Z of the light fragment is given by

$$[Z_0(A_L)-Z]/[Z_0(A_H)-92+Z]=a_H/a_L=0.65. \quad (4)$$

Since the numerator of the left side of (4) is, crudely speaking, the number of successive disintegrations in the light chain, and the denominator the number of disintegrations in the heavy chain, it would follow that the light chains are about half as long as the heavy chains.

It is important to note that the above picture (which was used in the past by the present writers[5]) is not confirmed experimentally. It has been shown[6] that the light and heavy chains are approximately *equally long* and we shall assume hence that, in the most probable type of disintegration, this is the case.

Since, as demonstrated in Table I, $Z_0(A_L)+Z_0(A_H)$ is, on the average, about 99.0, we can assume that the most probable Z differs by 3.5 from $Z_0(A_L)$ and that, hence, the most probable charge of the heavy fragment is also 3.5 units smaller than the most stable charge $Z_0(A_H)$ for the mass of the heavy fragment.

Knowing the most probable charges, the question arises as to the deviations from these most probable charges. The gas sweeping experi-

[5] E. P. Wigner and K. Way, Phys. Rev. **70**, 115 (1947) and CC-3032.

[6] L. E. Glendenin, C. D. Coryell, R. R. Edwards, and M. H. Feldman, CL-LEG-1. A tenative explanation has been given recently by R. D. Present, Phys. Rev. **72**, 7 (1947).

ments of R. M. Adams, A. Turkevich, and coworkers,[7] and the independent yield determinations of M. H. Feldman, L. E. Glendenin, R. R. Edwards, E. J. Hoagland, N. Sugarman, B. Finkle, and D. W. Engelkemeier[8] provide at least an approximate answer. The probability that the charge of the light fragment be Z is given by the expression

$$P(Z)dZ=(0.7\pi)^{\frac{1}{2}}\times\exp[-0.7(Z_0(A_L)-3.5-Z)^2]dZ. \quad (5)$$

Since Z can assume only integer values, (5) is clearly only an approximate expression. However, it can be expected to give, in a general sort of way, the probability that the charge of the light fragment be Z, that of the heavy fragment $92-Z$. According to (5), the probability for obtaining the charge $Z_0(A_L)-3.5$ is highest, the probability for obtaining either of the charges $Z_0(A_L)-4.5$ and $Z_0(A_L)-2.5$ is only half as high.

We can substitute $Z_p=Z_0(A_L)-3.5$ and, with the aid of $Z_0(A_L)+Z_0(A_H)=99.0$, rewrite (3) to

$$\begin{aligned}E_r&=a_L(Z_p+3.5-Z)^2+a_H(Z_p-3.5-Z)^2\\&=(a_L+a_H)(Z_p-Z)^2\\&\quad+7.0(a_L-a_H)(Z_p-Z)+12(a_L+a_H) \quad (6)\\&=1.65(Z_p-Z)^2+2.5(Z_p-Z)+20.\end{aligned}$$

It follows that the minimum value of E_r is 19.5 Mev. However, the average value of the energy which finally emerges in the form of radiation (γ, β, and neutrino) is

$$E_r=\int[1.65(Z_p-Z)^2+2.5(Z_p-Z)+20]\times(0.7/\pi)^{\frac{1}{2}}\exp(-0.7(Z_p-Z)^2)dZ=21.5 \text{ Mev}.$$

Actually, as has been pointed out by A. Turkevich,[9] 1 Mev has to be subtracted from this. The reason is that the final nucleus is not the most stable nucleus but has, in most cases, a smaller charge. In the case of odd mass, the Z of the final nucleus can differ from Z_0 by as much as $\pm\frac{1}{2}$. Hence, the excess energy is, in this case, the average of aZ^2 for Z between $-\frac{1}{2}$ and $\frac{1}{2}$, i.e., $a/12=0.08a$. The condition, in case of even mass number, that the even-even nucleus with charge Z be stable is a $(Z_0-Z)^2<a(Z_0-Z-1)^2+b$ which gives $Z_0-Z<1.9$. Hence, the excess energy in the even-even end product is the average of a Z^2 for Z between 0 and 1.9 which is $1.2a$. Since half of the final fission products has odd mass, half even mass, the total excess energy in the stable end products is $\frac{1}{2}(a_L+a_H)1.2a=1$ Mev. This correction is, however, compensated by one, due to the fact that one-quarter of all the fission fragments is an odd-odd nucleus with an excess energy of b. This gives an increase in the total radiation of $\frac{1}{4}(b_L+b_H)=\frac{1}{4}(2.8+1.8)=1.15$ Mev which restores the validity of the above figure. The same result can, of course, be obtained also by integrating (14a) over the time t. We estimate that the above figure for the total amount of radiation may be accurate to 15 to 20 percent.

One can calculate, in a way similar to the above, that the root mean square deviation of E_r from its average is 2.7 Mev. This compares with a measured root mean square deviation[10] of the kinetic energy of the fission fragments from their average of 10 Mev. This shows that the variation of E_r from its average forms a not negligible contribution toward the variation of the kinetic energy of the fission fragments from its average, without being able to explain it by itself. Moreover, the observed energy distribution seems quite symmetrical while one would expect the energy variation from this variation in initial Z to be quite unsymmetrical. There would be quite a sharp falling off on the high energy side and a gradual tailing off on the low energy side. One of us (K. W.) has made some preliminary calculations which indicate that the kinetic energy spread may be accounted for by fluctuations in the number of fission neutrons.

The light fragment of charge Z will have, if it has an odd mass, in its first disintegration, a disintegration energy $E=2a_L(Z_0(A_L)-Z)-a_L=2a_L(Z_p+3.0-Z)$. As a result, the probability that the first disintegration energy of the light fragment be E is

$$P_{o1}(E)dE=\tfrac{1}{2}(0.7/\pi)^{\frac{1}{2}}(2a_L)^{-1}\times\exp[-0.7(\tfrac{1}{2}E/a_L-3)^2]dE. \quad (8a)$$

[7] R. M. Adams and H. Finston, cf. Vol. 9B of the forthcoming Plutonium Project Records.

[8] M. H. Feldman, L. E. Glendenin, and R. R. Edwards, PPR, 9B, 7.36, E. J. Hoagland and N. Sugarman, PPR, 9B, 7.7, L. E. Glendenin, PPR, 9B, 7.42.2, B. Finkle, D. W. Engelkemeier, and N. Sugarman, PPR, 9B, 7.42.1.

[9] Personal communication.

[10] W. Jentschke, Zeits. f. Physik **120**, 165 (1943) A. Flammersfeld, P. Jensen, and W. Gentner, Zeits. f. Physik **120**, 450 (1943). M. Deutsch and N. Ramsey, LA-510.

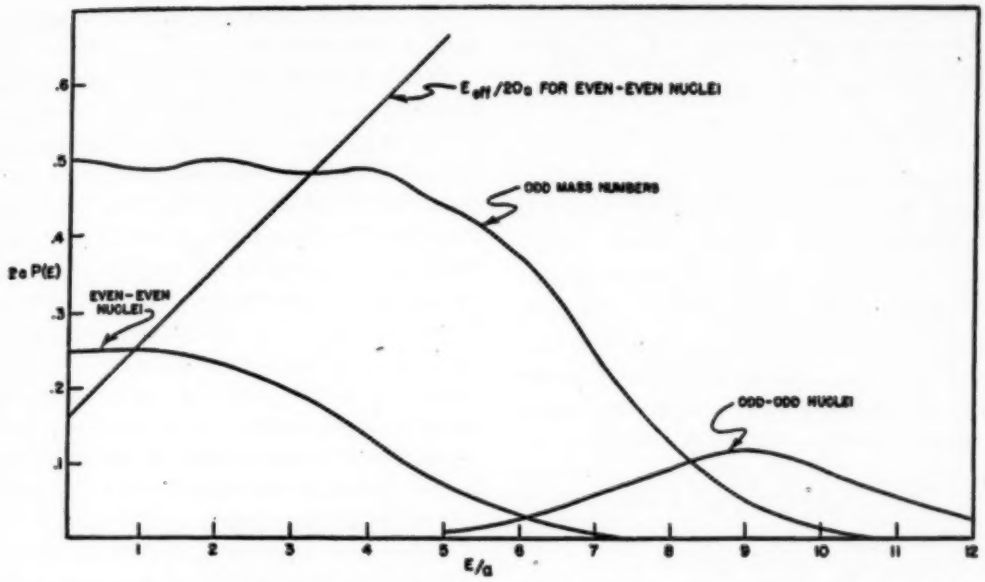

FIG. 3. Distribution of the disintegration energy of the nuclei which are created immediately after fission. This includes all nuclei which are really directly created by the fission, all nuclei with odd mass numbers, and all even-even nuclei. In the last case, the effective energy of disintegration is higher than E and is given, in units of 20a, by the straight line. The curves apply both to the light and the heavy fragment.

The factor $\frac{1}{2}$ has been introduced because only half of the radioactive chains have odd masses. The energy of the second disintegration is

$$E=2a_L(Z(A_L)-Z+1)-a_L=2a_L(Z_p-Z+2.0)$$

so that the probability that the second disintegration yield the energy E becomes

$$P_{o2}(E)dE=\tfrac{1}{2}(0.7/\pi)^{\frac{1}{2}}(2a_L)^{-1}\times\exp[-0.7(\tfrac{1}{2}E/a_L-2)^2]dE, \quad (8b)$$

and so on. By adding the expressions $P_{o1}(E)+P_{o2}(E)+\cdots=P_o(E)$ one obtains the total probability for a disintegration energy E of the light fragment. The same expression, which is shown in Fig. 3, holds for the heavy fragment also, except that a_H must be substituted for a_L.

Needless to say, the wiggles at low E/a are not real but come from our taking too seriously our model of one definite a_L (or a_H) and a definite function (5) for the distribution of the Z. The constancy of $P(E)$ for E well below $2\times3a$ follows from the fact that the energies of successive disintegrations form an equidistant set and that the absolute position of the lines of this set is arbitrary. The absolute value of $P_o(E)$ for low E is simply the reciprocal distance $1/2a_L$ of the lines in this spectrum.

The above picture holds only for odd mass numbers. Since all even-even nuclei are also "immediately created upon fission," we can proceed with them in a similar way, except that the probability is only one-fourth that the nucleus with a given Z be even-even so that the $P_o(E)$ must be multiplied by the further factor $\frac{1}{2}$ in order to obtain $P_{oo}(E)$. In addition, it must be shifted to the left by b because the disintegration energy of an even-even nucleus with given Z_0-Z is smaller by b than the disintegration energy of an odd mass nucleus with the same Z. $P_{ee}(E)$ is also shown in Fig. 3. One has to remember that every disintegrating even-even nucleus gives rise to two β-rays, to its own and to its daughter's, and that the energy emitted during these disintegrations is not E but $2E+2b-2a$.

Finally, there is a chance of one-fourth that the nucleus formed immediately upon fission be odd-odd. If we continue to assume that its Z distribution is given by (5), its energy distribution will be

$$P_{oo}(E)dE=\tfrac{1}{4}(0.7/\pi)^{\frac{1}{2}}(2a_L)^{-1}\times\exp[-0.7(\tfrac{1}{2}(E-b_L)/a_L-3)^2]dE. \quad (9)$$

This function is also shown in Fig. 3.

The distribution function $N(E, t)$ at time $t=0$ can then be written as the sum $P_o+P_{ee}+P_{oo}$ and at any later time

$$N(E, t)=[P_o(E)+P_{ee}(E)+P_{oo}(E)]e^{-\lambda(E)t}.$$

The average number of β-rays emitted by the light chain is the integral of $P_o(E)dE$ (which is $\frac{1}{2}\times 3.5=1.75$) plus the integral of $P_{oo}(E)dE$ (which is $\frac{1}{4}$) plus twice the integral of $P_{ee}(E)dE$. This last quantity is $\frac{1}{4}\times 3.5=0.875$ minus b_L times the ordinate of $P_{ee}(E)$ at $E=0$ which is $0.25/2a_L$. Hence the average number of β-rays in the light chain, which is according to Table I equal to $\frac{1}{2}\times 6.1=3.05$, must be equal to

$$3.05=1.75+0.25+2(0.875-0.25b_L/2a_L). \quad (10)$$

It follows that

$$b_L=2.8a_L. \quad (11)$$

The same holds for the heavy fragment. Hence $b_L=2.8$ Mev, $b_H=1.8$ Mev. This method of determining b is only apparently different from that of Bohr and Wheeler.[1] The average number of odd radioactive nuclei in the light (or heavy) fission chain is 1.75, the average number of even-even and of odd-odd radioactive nuclei in the same chain are 0.52 and 0.78. The same numbers hold for the heavy chain.

Figure 4 shows the energy distribution of the disintegrations of both chains. This should give the energy spectrum of disintegrations in a steadily running chain reacting unit. Of course, the energy spectrum of disintegration is not an immediately observable quantity because a disintegration contains, in general, β-rays, γ-rays, and neutrinos. Nevertheless, this curve may have some interest. For this reason, it also contains the odd-odd nuclei which are daughters and, according to our picture, are not "immediately formed upon fission." For even-even nuclei, it shows the effective energy of disintegration also, i.e., the sum of the energies of even-even parent and odd-odd daughter.

Before leaving this subject we wish to attract attention to one more circumstance.[11] The mass formulae clearly permit one to calculate the binding energy of a neutron, which is an important quantity from the point of view of the so-called "delayed" neutron emission. This is the emission of a neutron by a nucleus, after the nucleus is formed by a β-disintegration. Let us start with a nucleus of mass A and charge Z. Its mass is greater than that of a nucleus of mass A

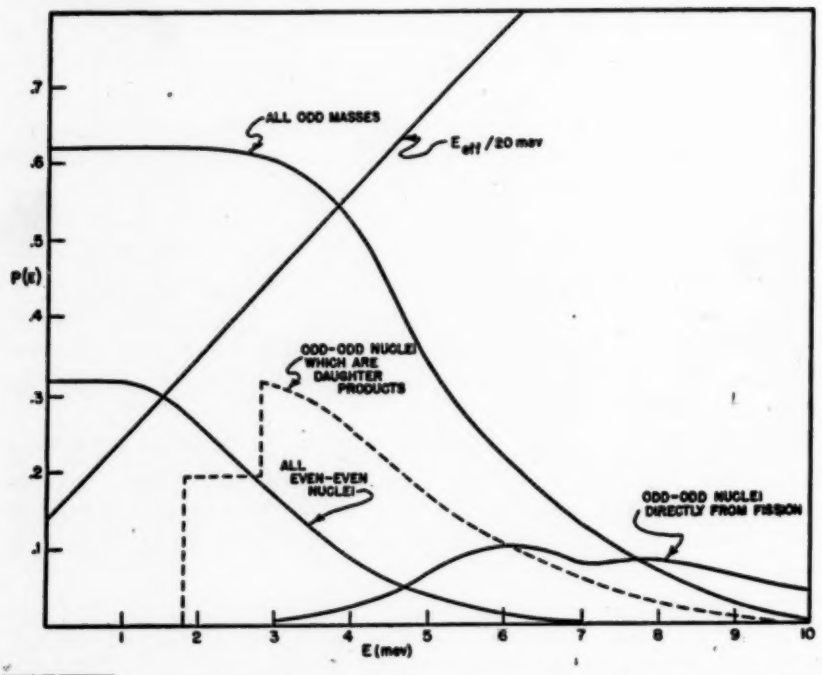

FIG. 4. Distribution of the disintegration energy of all fission products nuclei (both light and heavy fragments): P_o for nuclei with odd masses: P_{ee} for nuclei with even number of protons and of neutrons; P_{oo} for those nuclei with odd neutron and proton number which are fission fragments themselves and not daughters of others; broken line for the other odd-odd nuclei.

[11] We are very much indebted to C. Coryell and to his collaborators for discussions on this subject.

and charge $Z_0(A)$ by the amount $a(Z_0(A)-Z)^2$. The nucleus of mass $A-1$ and charge Z has a mass greater than that of a nucleus of mass $A-1$ and charge $Z_0(A-1)$ by $a(Z_0(A-1)-Z)^2$. $Z_0(A-1)$ is approximately equal to $Z_0(A)-0.45$. The mass difference of these nuclei (A, Z and $A-1$, Z) which is due to the fact that their charges do not have the "most stable" values is then $0.2a-0.9a(Z_0-Z)$. This quantity must then be added to the average energy B required to tear a neutron away from a nucleus of mass A to obtain the correct neutron binding energy. One must also add $+\frac{1}{2}b$ or $-\frac{1}{2}b$, depending on whether the number of neutrons was even or odd in the neutron emitting nucleus. The energy of disintegration which forms the neutron emitting nucleus is $2a(Z_0-Z)+a$ if A is odd. If A is even, $-b$ or $+b$ must be added to this, depending on the odd or even character of Z. Assuming the unlikely condition that all the disintegration energy remains in the nucleus A, Z, then neutron emission will be possible if

$$B+0.2a-0.9a(Z_0-Z)+\tfrac{1}{2}b<2a(Z_0-Z)+a+b\cdots(A \text{ even}, Z \text{ even}),$$
$$B+0.2a-0.9a(Z_0-Z)-\tfrac{1}{2}b<2a(Z_0-Z)+a-b\cdots(A \text{ even}, Z \text{ odd}),$$
$$B+0.2a-0.9a(Z_0-Z)-\tfrac{1}{2}b<2a(Z_0-Z)+a\cdots(A \text{ odd}, Z \text{ even}),$$
$$B+0.2a-0.9a(Z_0-Z)+\tfrac{1}{2}b<2a(Z_0-Z)+a\cdots(A \text{ odd}, Z \text{ odd}).$$

It follows that a delayed neutron is most likely to be emitted from a nucleus with even A, which results from a disintegration of a nucleus with an odd Z. As a condition of a neutron emission we obtain, in this case,

$$B<2.9a(Z_0-Z)+0.8a+\tfrac{1}{2}b.$$

Again, this equation is most likely to be fulfilled for the light fragment. Even in this case and even under the most optimistic assumption which we used (that all the disintegration energy which produced the A,Z nucleus remain in it) we obtain $Z_0-Z>2$. This shows that if a delayed neutron is emitted by a nucleus near the end of a radioactive chain, the fluctuations around the smooth mass formulae must be quite large to make this possible.[12]

[12] Similar deviations of the observed masses from smooth formulae occur in light nuclei also, e.g., at the ends of closed shells. Very strong evidence for similar deviations in heavier nuclei will be given by Maria G. Mayer in a forthcoming paper in the present journal. Her article will also contain references to earlier literature.

IV. RELATION OF ENERGY TO HALF-LIFE. $\lambda(E)$

The next step is the establishment of a rule which connects the half-life $(\ln 2)/\lambda$ with the maximum energy of the β-ray. This is given, according to current theories,[13] by

$$\lambda=M^2/30[(E_\beta/mc^2)^5+5(E_\beta/mc^2)^4+10(E_\beta/mc^2)^3]. \quad (12)$$

In this, M is the matrix element for the nuclear transition, mc^2 the rest energy of the electron, and E_β the maximum β-ray energy of the transition in question. Equation (12) is not immediately useful for two reasons: first, because it contains the unknown quantity M, and second, because it refers to a β-transition to a definite level of the daughter nucleus, instead of referring to transitions to all levels of the daughter nucleus. For this reason, the energy of a transition E_β occurs in it instead of the disintegration energy. In spite of this, Eq. (12) indicates in a general way that for large E_β, the λ is proportional to the fifth power of E_β. For small E_β, the λ does not drop off as rapidly as the fifth-power law would indicate, so that one would be inclined, when giving a global expression for λ as a function of E_β, to use a lower power law and to write, e.g., $\lambda\sim E_\beta^4$. On the other hand, the total probability of the disintegration is the sum of the probabilities of the transitions to all possible levels of the daughter nucleus, and one can expect that there are more final levels available if the energy of disintegration is greater. Also, among the more numerous levels of the daughter nucleus in the case of high E, there is more likelihood to find one with a particularly large M. As a result, one may expect that λ is proportional to E^3 for small E and to an even higher power than E^5 in case of large E. Furthermore, one cannot expect a unique connection between E and λ, but a nucleus with a definite E will have a disintegration constant which may assume any value between a highest and a lowest limit. These expectations are, on the whole, corroborated by the experimental material shown in Fig. 5. This shows that there is a rather definite lower limit

[13] E. Fermi, Zeits. f. Physik **88**, 161 (1938); also E. J. Konopinaski, Rev. Mod. Phys. **15**, 209 (1943).

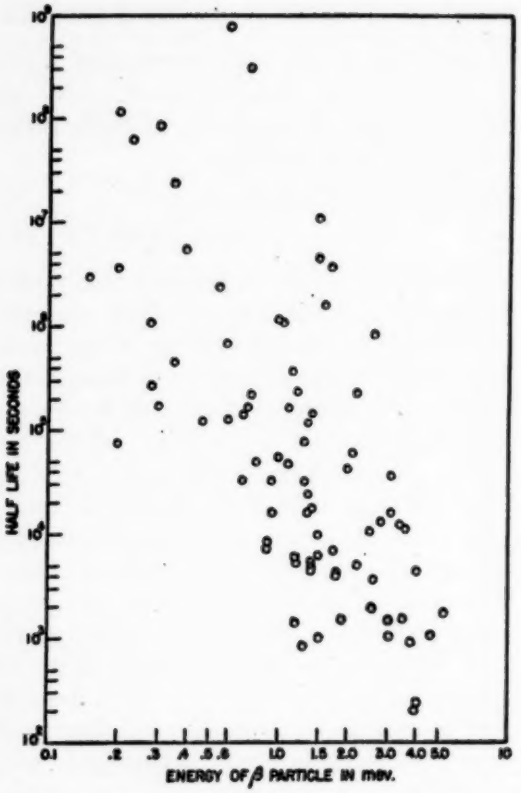

FIG. 5. Half-lives and disintegration energies of fission products.

for the half-life of a nucleus with a definite disintegration energy, corresponding to an upper limit of λ as function of E. (Incidentally, this upper limit of λ lies, as demanded by theory, considerably below the first Sargent curve, so that one obtains an E consistently too low if one tries to estimate it from λ and uses the first Sargent curve.) There is a considerable region of energy, from 0.5 to 1.5 Mev, in which the lower limit of the lifetime is proportional to E^5, and the lower limit behaves as expected outside this region.[14] The upper limit of the half-life, i.e., the lower limit of λ, is less pronounced, corresponding to the fact that there is no theoretical limit as to how forbidden a disintegration may be. In spite of this, one may recognize such an upper limit, running very roughly parallel to the lower. As a result, we can say that, very approximately,

$$\ln\lambda = -C + 5\ln E, \tag{13}$$

where C has, with equal probabilities, values between $C_u = 18.5$ and $C_l = 9$ if λ is measured in sec.$^{-1}$ and E in Mev. Although we realize its limitations, we have adopted (13) for the calculations. We must remember, however, at least the most obvious limitations of Eq. (13): it gives a too low λ for a very low E so that, for very large t when the lifetimes are determined by very low E, the activity will drop more rapidly than our formulae will indicate.

[14] The single exception is Pd^{113}. The data was taken from reference 4.

V. NUMBER OF DISINTEGRATIONS AND RADIOACTIVE ENERGY LIBERATED AS FUNCTION OF TIME AFTER FISSION

If (13) were valid for all nuclei with one single C, the number of β-rays emitted in unit time, at time t after fission, would be given by

$$\beta(t) = \int [P_0(E) + P_{00}(E) + 2P_{ee}(E)] e^{-C} E^5 \times \exp(-e^{-C} E^5 t) dE. \tag{14}$$

Similarly, the total energy (consisting of β-rays, neutrinos, and γ-rays) liberated in the same time interval would become

$$3B(t) + \Gamma(t) = \int [EP_0(E) + EP_{00}(E) + E_{eff} P_{ee}(E)] e^{-C} E^5 \exp(-e^{-C} E^5 t) dE, \tag{14a}$$

where E_{eff} is the function given in Fig. 4. It is the sum of the disintegration energies of an even-even nucleus and of its odd-odd daughter.

Since, however, as explained in the preceding section, C varies from nucleus to nucleus, we have to average the above expressions over C, i.e., integrate them over C from $C_l = 9$ to $C_u = 18.5$ and divide the result by $C_u - C_l = 9.5$. This gives

$$\beta(t) = (9.5t)^{-1} \int [P_0(E) + P_{00}(E) + 2P_{ee}(E)] \times [\exp(-x_u E^5 t) - \exp(-x E^5 t)] dE \tag{15}$$

$$x_u = \exp(-C_u) = 10^{-8.03}; \qquad x_l = \exp(-C_l) = 10^{-3.90}.$$

A similar expression can be obtained for the total disintegration energy liberated in unit time.

$$3B(t) + \Gamma(t) = (9.5t)^{-1} \int [EP_0(E) + EP_{00}(E) + E_{eff} P_{ee}(E)] \times [\exp(-x_u E^5 t) - \exp(-x_l E^5 t)] dE. \tag{15a}$$

In order to obtain $\gamma(t)$ or $B(t)$ and $\Gamma(t)$ separately, it would be necessary to know the fraction of energy that is emitted, on the average, in the form of γ-radiation during a disintegration with a definite disintegration energy. However, there is at present no theoretical foundation for determining this fraction and the quantities (15) and (15a) are the only ones for which a theoretical expression can be obtained with ease.

In general, i.e., for an arbitrary t, the integrals (15) and (15a) have to be evaluated numerically. Both square brackets in (15) as well as in (15a) tend to zero as E increases, but while at low t the first bracket goes to zero more rapidly, at high t the second one becomes very small first. As a result, one can evaluate both integrals more easily if either t is very small (smaller than 1 sec.), or if t is very large (more than one day).

In the former case, i.e., if t is very small, the exponentials in the second bracket can be expanded and the second bracket becomes

$$(x_l-x_u)E^5t-\tfrac{1}{2}(x_l^2-x_u^2)E^{10}t^2 \approx x_lE^5t-\tfrac{1}{2}x_l^2E^{10}t^2, \quad (16)$$

since x_l is so much larger than x_u. Hence, for very small t one has with

$$c_0=9.5^{-1}e^{-9}\int[P_0(E)+P_{00}(E)+2P_{ee}(E)]E^5dE, \quad (17)$$

$$c_1=9.5^{-1}e^{-18}\int[P_0(E)+P_{00}(E)+2P_{ee}(E)]E^{10}dE,$$

$$\beta(t)=c_0-\tfrac{1}{2}c_1t\sim 0.38-2.6t \text{ per sec.} \quad (17a)$$

and with

$$C_0=9.5^{-1}e^{-9}\int[EP_0(E)+EP_{00}(E)+E_{eff}P_{ee}(E)]E^5dE,$$

$$C_1=9.5^{-1}e^{-18}\int[EP_0(E)+EP_{00}(E)+E_{eff}P_{ee}(E)]E^{10}dE, \quad (18)$$

$$3B(t)+\Gamma(t)=C_0-\tfrac{1}{2}C_1t \approx (3.8-0.61t) \text{ Mev/sec.} \quad (18a)$$

Unfortunately, the evaluation of these integrals, c_1 and C_1 in particular, is strongly dependent on the high energy tail of the P. Hence, the value of the constants in (18a) depends greatly on the accuracy of (5) which gives the probability of deviation of the original Z from $Z_0-3.5$. Hence, the relatively good agreement between (18a) and the measured values should rather be taken as an indication that (5) is not too inaccurate for values of $Z_0-3.5-Z$ which are several units great. One must remember that the experimental foundation[6] of (5) comes largely from the region in which $Z_0-3.5-Z$ is negative.

The situation is much more favorable for large t. In this case, the second bracket of (15) and (15a) drops so rapidly that the values of the P for $E=0$ can be used in the first bracket. As was pointed out in Section III, the curves of Figs. 3 and 4 are most accurate in the region of low E where they are essentially constant. We have $P_o=\frac{1}{4}(a_L^{-1}+a_H^{-1})\sim 0.63$ (Mev)$^{-1}$, $P_{oo}\sim 0$, and $P_{ee}=\frac{1}{2}P_o\sim 0.32(Mev)^{-1}$ in this region. As a result, the first bracket of (15) becomes 1.27 and that of (16a), $0.63E+0.32(2E-2a+2b)$. Substituting these expressions for the first brackets, the integrals can be carried out if one introduces a new variable y for x_uE^5t and x_lE^5t. One has, after a day,

$$\beta(t)=1.27\times 9.5^{-1}t^{-6/5}(x_u^{-1/5}-x_l^{-1/5})1/5 \times\int_0^\infty y^{-4/5}e^{-y}dy\approx 5.2\times 10^{-6}d^{-1.2} \quad (19)$$

and

$$3B(t)+\Gamma(t)=(3.9d^{-1.2}+11.7d^{-1.4})\times 10^{-6} \text{ Mev/sec.}, \quad (19a)$$

where d is the time in days. For very large t the first term of (19a) predominates. The origin of this term is the disintegration of an odd-odd nucleus, the formation of which has been long delayed because its even-even parent's disintegration energy was very small.

The variation of the number of β-particles with time as $t^{-1.2}$ depends essentially only on (13), i.e., on the proportionality of the disintegration constant with the fifth power of the disintegration energy. The $t^{-1.2}$ law follows at once from this and the circumstance that the number of radioactive nuclei per unit disintegration energy range is, for small disintegration energies, independent of energy. This last circumstance follows

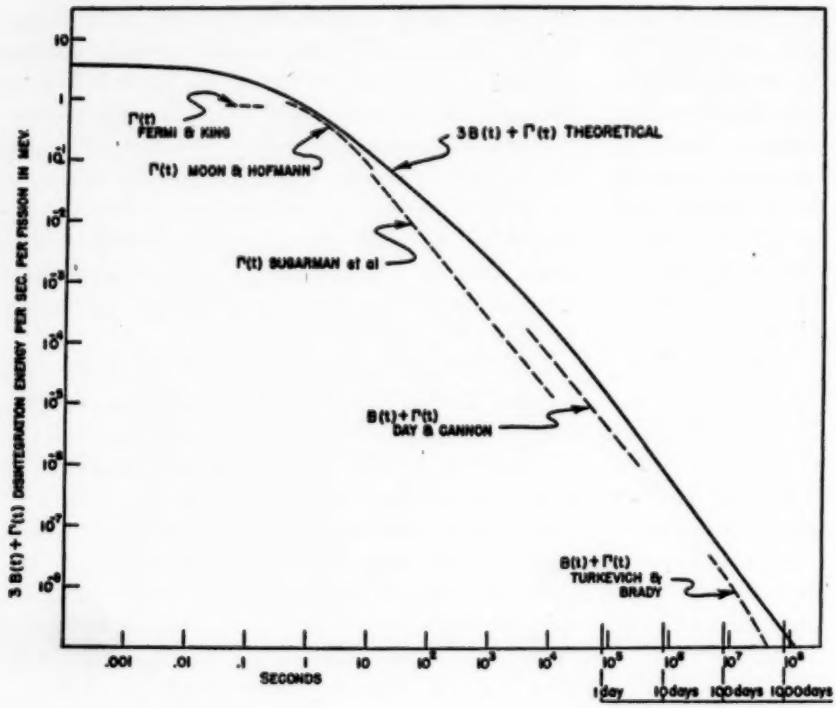

(a)

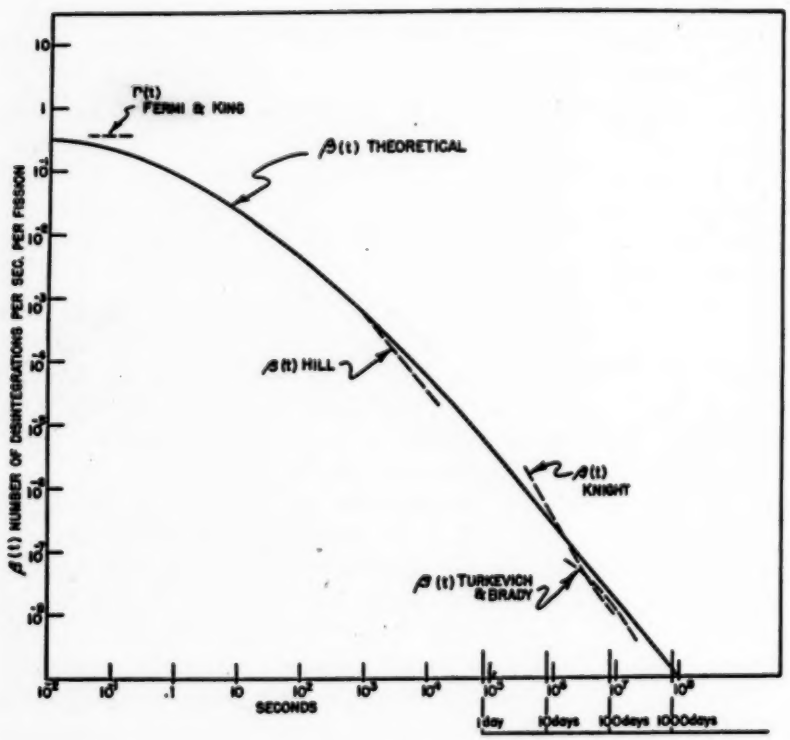

(b)

FIG. 6. Theoretical and experimental results for the radioactivity t seconds after fission. $\beta(t)$ = number of β-particles emitted per second, [$\gamma(t)$ same for γ-rays] $B(t)$ = energy of β-particles in Mev per second, $\Gamma(t)$ = energy of γ-rays in same units. $3B(t)+\Gamma(t)$ is total energy (including neutrino energy) liberated.

TABLE II. Summary of experimental results on rate of decay of fission products.

Quantity	Function of time t after fission	When valid	Reference
$\beta(t)$: Number of β-rays emitted per sec. per fission	$2.54\ t^{-1.23}$	10 min.–4 hrs.	D. L. Hill and L. Lanzl, Metallurgical Laboratory, CP-1827, June 25, 1944.
	$ct^{-1.7}$–$ct^{-1.2}$	1–100 day	J. D. Knight, Clinton Laboratories, CC-3479, May 1, 1946. PPR, 9B, 6.14.
	ct^{-1}–$ct^{-1.5}$	16–240 days	E. L. Brady and A. Turkevich, Metallurgical Laboratory, CL-697, III, D6, March, 1945.
$B(t)+\Gamma(t)$: Total γ-energy and average β-energy emitted per sec. per fission in Mev/sec.	$5.1\ t^{-1.23}$	1–100 hrs.	R. A. Day and C. V. Cannon, Clinton Laboratories, CP-2176, November 9, 1944.
	$5.6\ t^{-1.26}$ $98.0\ t^{-1.61}$	20 m–3 days 50–100 days	L. Borst, Metallurgical Laboratory, CL-697, VIII, C4.
	$29.4\ t^{-1.35}$	16–340 days	E. L. Brady and A. Turkevich. See above.
$\Gamma(t)$: γ-energy emitted per sec. per fission in Mev/sec.	$\sim$ const.	40–140 millisec.	L. D. P. King and E. Fermi, Los Alamos Laboratories, quoted in LA-253A, December 7, 1945.
	See Fig. 6.	0.1–10 sec.	J. A. Hofmann and P. B. Moon, Los Alamos Laboratories, LA-253A, April 7, 1945. I. Halpern, J. A. Hofmann, P. B. Moon, R. Perry, Los Alamos Laboratories, LA-253A, December 7, 1945.
	$0.90\ t^{-1.20}$	10 sec.–1 day	S. Katcoff, B. Finkle, N. Elliott, J. Knight, N. Sugarman, Metallurgical Laboratory, CC-1128, December 11, 1943.
	$4.2\ t^{-1.28}$ $49.0\ t^{-1.61}$	20 m–3 days 50–100 days	L. Borst. See above.
	$ct^{-1.28}$–$ct^{-2.0}$	16–240 days	E. L. Brady and A. Turkevich. See above.

from the assumption that the disintegration energies of successive members of a chain form an equidistant set. The same holds of the possibility of representing the energy liberation as the sum of two terms, proportional to $t^{-1.4}$ and $t^{-1.2}$, respectively. The present paper owes its origin to the recognition of this fact and the experimental confirmation of the $t^{-1.2}$ law.

VI. COMPARISON WITH EXPERIMENT

Figure 6 shows the theoretical curves for $\beta(t)$ and for $3B(t)+\Gamma(t)$ and various experimental results. The experimental work is also listed in Table II where analytical representations are given where possible.

The agreement between the theoretical $\beta(t)$ and the experimental results is seen to be fairly good. No experimental values are available for very short times. The fact that the theoretical curve lies above the experimental ones for the longer times is perhaps due to the approximation made in choosing the relation between λ and E.

The total energy released per second per fission, $3B(t)+\Gamma(t)$, includes the energy carried by neutrinos. The total absorbable energy is only $B(t)+\Gamma(t)$. For times of the order of days after fission, calculations from known β- and γ-energies and fission yields of the different fission products show that $B(t)$ and $\Gamma(t)$ are approximately equal. At these times one would thus expect $3B(t)+\Gamma(t)$ to be twice $B(t)+\Gamma(t)$. Figure 6 shows that it is actually somewhat larger than twice the values of R. A. Day and C. V. Cannon which were obtained by calorimetric measurements. (See Table II for references.[15]) They are also more than twice the values calculated from the lifetimes, decay energies, and yields by A. Turkevich and E. L. Brady. Perhaps this is caused again by the relation between λ and E.

No experimental values of $B(t)+\Gamma(t)$ for very short times after fission are available, but several measurements have been made of $\Gamma(t)$ alone. Figure 6 and Table II give the results. At times of the order of 0.1 sec. after fission the value of $3B(t)+\Gamma(t)$ is about two and one-half

[15] See also articles by J. D. Knight; R. A. Day and C. V. Cannon; L. B. Borst; S. Katcoff, B. Finkle, N. Elliot and J. Knight in the forthcoming Plutonium Project Records, Vol. 9B.

times the experimental value of $\Gamma(t)$, which is certainly very plausible. At these short times, the calculated values depend very sensitively on the values of the disintegration energies and lifetimes of the primary fission products. The agreement with experiment at these times thus lends some support to the assumptions which governed the choice of the initial energies and lifetimes which were (1) that the parabolic mass formula holds for nuclei quite far removed from the region of stability and (2) that the chance of finding a given charge on the primary fission product is given by Eq. (5).

The authors are very much indebted to Mrs. N. Dismuke and Mrs. G. Haines for help in calculating values for the theoretical curves, and to Mrs. A. T. Monk who gave much appreciated assistance with an earlier report on which the present one is based. They are greatly indebted also to members of the Chemistry Divisions of both Argonne and Clinton Laboratories for many helpful discussions and clarification of experimental data. This article is based on work performed under Contract No. W-35-058-eng-71 for the Manhattan Project and the Atomic Energy Commission at Clinton Laboratories.

PHYSICAL REVIEW VOLUME 73, NUMBER 11 JUNE 1, 1948

Dirac's One-Electron Problem in Momentum Representation

A. RUBINOWICZ
Institute of Theoretical Mechanics, University of Warsaw, Warsaw, Poland
(Received June 26, 1947)

In the present note the eigenfunctions of the problem have been transformed into a form suitable for numerical calculations.

I. THE INTEGRAL EQUATION FOR THE PROBLEM

THE non-relativistic one-electron problem for a Coulomb field has been treated in the momentum representation very exhaustively and from several points of view.[1] As far as I know the corresponding relativistic problem for a Dirac electron has, however, not yet been discussed. In the present note we will, therefore, deal with this problem.

In this section we deduce the integral equation for our problem. For this purpose we use the operator[2]

$$T\ldots=\frac{1}{h^3}\int\int\int dxdydze^{-(i/\hbar)(\xi x+\eta y+\zeta z)}\ldots \qquad (1)$$

(ξ, η, ζ = momentum components)

which transforms the space coordinate representation

$$u(x, y, z)=(u_1, u_2, u_3, u_4)$$

of the Dirac wave function into the momentum representation

$$Tu(x, y, z)=v(\xi, \eta, \zeta)=(v_1, v_2, v_3, v_4).$$

Making use of the well-known formula[3]

$$\frac{1}{r}=\frac{1}{2\pi^2}\int\int\int_{-\infty}^{+\infty}\frac{e^{-i(\lambda x+\mu y+\nu z)}}{\lambda^2+\mu^2+\nu^2}d\lambda d\mu d\nu$$

$$=\frac{e^{(i/\hbar)(\xi x+\eta y+\zeta z)}}{\pi h}$$

$$\times\int\int\int_{-\infty}^{+\infty}\frac{e^{-(i/\hbar)(\xi' x+\eta' y+\zeta' z)}}{(\xi'-\xi)^2+(\eta'-\eta)^2+(\zeta'-\zeta)^2}d\xi' d\eta' d\zeta',$$

we get

$$T\frac{u}{r}=\frac{1}{\pi h}\int\int\int_{-\infty}^{+\infty}\frac{v(\xi', \eta', \zeta')}{(\xi'-\xi)^2+(\eta'-\eta)^2+(\zeta'-\zeta)^2}\times d\xi' d\eta' d\zeta'.$$

[1] H. Weyl, Zeits. f. Physik **48**, 1 (1928); E. Podolsky and L. Pauling, Phys. Rev. **34**, 109 (1929); E. A. Hylleraas, Zeits. f. Physik **74**, 216 (1932); W. Elsasser, Zeits. f. Physik **81**, 332 (1931); V. Fock, Zeits. f. Physik **98**, 145 (1936).

[2] Cf. W. Pauli, *Handbuch der Physik* **XXIV**, 227 (1933), second edition.

[3] We can get it using the Fourier integral theorem and the integral relation given by Weyl, see reference 1, p. 41.

Since we also have

$$T[-ih(\partial/\partial x)u]=\xi v,$$

the application of (1) to the Dirac differential equation

$$Hu=\left[E+\frac{Ze^2}{r}+\beta E_0 - ich\left(\alpha_1\frac{\partial}{\partial x}+\alpha_2\frac{\partial}{\partial y}+\alpha_3\frac{\partial}{\partial z}\right)\right]u=0$$

yields the integral equation

$$[E+\beta E_0+c(\alpha_1\xi+\alpha_2\eta+\alpha_3\zeta)]v(\xi,\eta,\zeta) + \frac{Ze^2}{\pi h}\int_{-\infty}^{+\infty}\iint\frac{v(\xi',\eta',\zeta')}{(\xi'-\xi)^2+(\eta'-\eta)^2+(\zeta'-\zeta)^2}\times d\xi' d\eta' d\zeta'=0. \quad (2)$$

This is a system of four linear integral equations for the four functions v_1, v_2, v_3, v_4.

II. THE EIGENFUNCTIONS IN MOMENTUM REPRESENTATION

We obtain a solution of (2) applying the operator T, Eq. (1), to the corresponding eigenfunctions in space coordinate representation. For $j=l+\frac{1}{2}$ they are given by

$$\begin{aligned} u_1&=\left(\frac{l-m+1}{2l+3}\right)^{\frac{1}{2}}Y_{l+1,m}(\Theta,\Phi)iR(r),\\ u_2&=\left(\frac{l+m+2}{2l+3}\right)^{\frac{1}{2}}Y_{l+1,m+1}(\Theta,\Phi)iR(r),\\ u_3&=\left(\frac{l+m+1}{2l+1}\right)^{\frac{1}{2}}Y_{l,m}(\Theta,\Phi)S(r),\\ u_4&=-\left(\frac{l-m}{2l+1}\right)^{\frac{1}{2}}Y_{l,m+1}(\Theta,\Phi)S(r). \end{aligned} \quad (3)$$

Putting

$$\rho=\frac{2p_0}{h}r,\quad \gamma=((l+1)^2-\alpha^2Z^2)^{\frac{1}{2}},$$
$$N=((n'+\gamma)^2+\alpha^2Z^2)^{\frac{1}{2}}$$

(n' = radial quantum number) the functions R and S are expressible in the form

$$R=A(1-\epsilon)^{\frac{1}{2}}e^{-\rho/2}\rho^{\gamma-1}\{n'F(-(n'-1),2\gamma+1,\rho) +(N+l+1)F(-n',2\gamma+1,\rho)\},$$
$$S=A(1+\epsilon)^{\frac{1}{2}}e^{-\rho/2}\rho^{\gamma-1}\{-n'F(-(n'-1),2\gamma+1,\rho) +(N+l+1)F(-n',2\gamma+1,\rho)\},$$

where

$$A=-\frac{(\Gamma(2\gamma+n'+1))^{\frac{1}{2}}}{\Gamma(2\gamma+1)(n'!)^{\frac{1}{2}}}\frac{1}{(4N(N+l+1))^{\frac{1}{2}}}\times\left(\frac{2p_0}{h}\right)^{\frac{1}{2}},\quad \epsilon=\frac{E}{E_0}=\frac{n'+\gamma}{N},$$

and $F(\alpha,\beta,\rho)$ means the confluent hypergeometric function.[4]

To calculate $v(\xi,\eta,\zeta)$ we introduce into T, instead of the Cartesian space and momentum coordinates x,y,z and ξ,η,ζ, the polar coordinates r,Θ,Φ and p,ϑ,φ, respectively, and replace r by $r=(h/2p_0)\rho$ and p by $p=p_0\sigma$, where $p_0=(E_0/c)(1-\epsilon^2)^{\frac{1}{2}}$. Applying the procedure used by Podolsky and Pauling[1] for a non-relativistic hydrogen atom we obtain

$$Th(\rho)Y_{l,m}(\Theta,\Phi) = Y_{l,m}(\vartheta,\varphi)\frac{i^lh^{\frac{1}{2}}}{4\sqrt{2}p_0^{\frac{3}{2}}}\frac{1}{(\sigma)^{\frac{1}{2}}}\int_0^\infty h(\rho)y_{l+\frac{1}{2}}\left(\frac{\rho\sigma}{2}\right)\rho^{\frac{1}{2}}d\rho.$$

The application of T to a function of the form

$$h(\rho)Y_{l,m}(\Theta,\Phi)$$

replaces only the variables Θ,Φ of the spherical harmonic by ϑ,φ, while the radial function $h(\rho)$ goes over into a function $H(\sigma)$ of σ

$$H(\sigma)=i^l\frac{h^{\frac{1}{2}}}{4\sqrt{2}p_0^{\frac{3}{2}}}\frac{1}{(\sigma)^{\frac{1}{2}}}\int_0^\infty h(\rho)J_{l+\frac{1}{2}}\left(\frac{\rho\sigma}{2}\right)\rho^{\frac{1}{2}}d\rho.$$

The factor $i^l(h^{\frac{1}{2}}/4\sqrt{2}p_0^{\frac{3}{2}})$ causes that eigenfunctions normalized in coordinate representation go over in eigenfunctions normalized in momentum representation.

The application of the operator T to (3) gives us, therefore, the eigenfunctions in momentum representation in the form[5]

---

[4] Cp. H. Bethe, *Handbuch der Physik* **XXIV**, 316, second edition.

[5] The fact that $v(\xi,\eta,\zeta)$ has the same form as $u(x,y,z)$ Eq. (3), can be proved also directly. The form (3) of $u(x,y,z)$ follows from the supposition that u is an eigenfunction of the operator corresponding to the z component of the total angular momentum and the operator $\beta((\mathbf{m}\boldsymbol{\sigma})+h)$, where $\mathbf{m}$ and $\boldsymbol{\sigma}$ are the orbital and the spin angular momenta. But both these operators are of the same form in both our representations, because this statement is true for the operator corresponding to the orbital angular momentum $\mathbf{m}$. Therefore, $v(\xi,\eta,\zeta)$, being an eigenfunction of these operators, has the form of $u(x,y,z)$.

$$v_1=\left(\frac{l-m+1}{2l+3}\right)^{\frac{1}{2}} Y_{l+1,m}(\vartheta,\varphi)M(\sigma),$$

$$v_2=\left(\frac{l+m+2}{2l+3}\right)^{\frac{1}{2}} Y_{l+1,m+1}(\vartheta,\varphi)M(\sigma),$$

$$v_3=\left(\frac{l+m+1}{2l+1}\right)^{\frac{1}{2}} Y_{l,m}(\vartheta,\varphi)N(\sigma),$$

$$v_4=-\left(\frac{l-m}{2l+1}\right)^{\frac{1}{2}} Y_{l,m+1}(\vartheta,\varphi)N(\sigma).$$

Using

$$G(\nu,\beta,\delta,l,\sigma)=\frac{1}{(\sigma)^{\frac{1}{2}}}\int_0^\infty e^{-\rho/2}\rho^{\delta+\frac{1}{2}} \times F(-\nu,\beta,\rho)J_{l+\frac{1}{2}}\left(\frac{\rho\sigma}{2}\right)d\rho, \quad (4)$$

the functions $M(\sigma)$ and $N(\sigma)$ are given by

$$M(\sigma)=+B(1-\epsilon)^{\frac{1}{2}} \times\{n'G(n'-1,2\gamma+1,\gamma-1,l+1,\sigma) +(N+l+1)G(n',2\gamma+1,\gamma-1,l+1,\sigma)\},$$

$$N(\sigma)=-B(1+\epsilon)^{\frac{1}{2}} \times\{-n'G(n'-1,2\gamma+1,\gamma-1,l,\sigma) +(N+l+1)G(n',2\gamma+1,\gamma-1,l,\sigma)\},$$

where

$$B=i^l\frac{(\Gamma(2\gamma+n'+1))^{\frac{1}{2}}}{\Gamma(2\gamma+1)(n'!)^{\frac{1}{2}}}\frac{1}{(N(N+l+1))^{\frac{1}{2}}}\frac{1}{4p_0^{\frac{1}{2}}}.$$

Our last task is to give the function G, (4), a form suitable for numerical calculations. To get an expression for $J_{l+\frac{1}{2}}$ applicable for all σ we use the Hankel functions $H^{(1)}_{l+\frac{1}{2}}$ and $H^{(2)}_{l+\frac{1}{2}}$

$$J_{l+\frac{1}{2}}(z)=\tfrac{1}{2}(H^{(1)}_{l+\frac{1}{2}}(z)+H^{(2)}_{l+\frac{1}{2}}(z)),$$

where

$$H^{(1)}_{l+\frac{1}{2}}(z)=\left(\frac{2}{\pi}\right)^{\frac{1}{2}} i^{-(l+1)}e^{iz}\sum_{m=0}^{l}\frac{1}{m!}\frac{(l+m)!}{(l-m)!}\left(\frac{i}{2}\right)^m\frac{1}{z^{m+\frac{1}{2}}}$$

and where for real z the function $H^{(2)}_{l+\frac{1}{2}}(z)$ is equal to the conjugate complex value of $H^{(1)}_{l+\frac{1}{2}}(z)$.

Denoting by G_k the function G in which $J_{l+\frac{1}{2}}$ has been replaced by $H^{(k)}_{l+\frac{1}{2}}$, we get

$$G=\tfrac{1}{2}(G_1+G_2),$$

where, for instance,

$$G_1(\nu,\beta,\delta,l,\sigma)=\frac{1}{(\sigma)^{\frac{1}{2}}}\int_0^\infty e^{-\rho/2}\rho^{\delta+\frac{1}{2}} \times F(-\nu,\beta,\rho)H^{(1)}_{l+\frac{1}{2}}\left(\frac{\rho\sigma}{2}\right)d\rho.$$

Since

$$F(-\nu,\beta,\rho)=\nu!\Gamma(\beta)\sum_{n=0}^{\nu}\frac{(-\rho)^n}{n!\Gamma(\nu-n+1)\Gamma(\beta+n)} \quad (5)$$

and

$$\int_0^\infty e^{-\alpha\rho}\rho^{s-1}d\rho=\frac{\Gamma(s)}{\alpha^s} \text{ for } R(\alpha)>0 \text{ and } R(s)>0,$$

we get

$$G_1(\nu,\beta,\delta,l,\sigma)=i^{-(l+1)}\frac{2}{(\pi)^{\frac{1}{2}}}\nu!\Gamma(\beta)\sum_{n=0}^{\nu} \sum_{m=0}^{l}\frac{\Gamma(n-m+\delta+2)(l+m)!}{n!\Gamma(\nu-n+1)\Gamma(\beta+n)m!(m-l)!}(-1)^n i^m\frac{1}{\sigma^{n+1}}\left(\frac{2}{1-i\sigma}\right)^{n-m+\delta+2}. \quad (6)$$

But using

$$F\left(-l,l+1,-(n+\delta+1),\frac{i+\sigma}{2\sigma}\right) =\frac{1}{\Gamma(n+\delta+2)} \times\sum_{m=0}^{l}\frac{(l+m)!\Gamma(n-m+\delta+2)}{m!(l-m)!}\left(\frac{i+\sigma}{2\sigma}\right)^m$$

or

$$F\left(-\nu,\delta+2-m,\beta,\frac{2}{1-i\sigma}\right)=\frac{\Gamma(\beta)\Gamma(\nu+1)}{\Gamma(\delta+2-m)} \sum_{n=0}^{\nu}\frac{\Gamma(n-m+\delta+2)}{n!\Gamma(\nu-n+1)\Gamma(\beta+n)}\left(-\frac{2}{1-i\sigma}\right)^n,$$

we can write G_1 in the form

$$G_1(\nu,\beta,\delta,l,\sigma)=i^{-(l+1)}\frac{2}{(\pi)^{\frac{1}{2}}}\nu!\Gamma(\beta)\frac{1}{\sigma}$$
$$\times\sum_{n=0}^{\nu}\frac{\Gamma(n+\delta+2)}{n!\Gamma(\nu-n+1)\Gamma(\beta+n)}(-1)^n\left(\frac{2}{1-i\sigma}\right)^{n+\delta+2}$$
$$\times F\left(-l,l+1,-(n+\delta+1),\frac{i+\sigma}{2\sigma}\right)$$
$$\equiv i^{-(l+1)}\frac{2}{(\pi)^{\frac{1}{2}}}\sum_{m=0}^{l}\frac{(l+m)!\Gamma(\delta-m+2)}{m!(l-m)!}\frac{i^m}{\sigma^{m+1}}$$
$$\times\left(\frac{2}{1-i\sigma}\right)^{\delta+2-m}F\left(-\nu,\delta+2-m,\beta,\frac{2}{1-i\sigma}\right). \quad (7)$$

G_2 is given by the conjugate complex value of G_1.

For the calculation of G_1 we can use (6) or (7) for all values of σ. But the practical use of this formula is very tedious, especially for small values of σ, because we must use complex numbers. For $|\sigma|<1$, however, we can obtain for G a real expression. Using

$$\int_0^\infty e^{-\rho/2}\rho^{n+\delta+\frac{1}{2}}J_{l+\frac{1}{2}}\left(\frac{\rho\sigma}{2}\right)d\rho$$
$$=\frac{\Gamma(n+l+\delta+3)}{\Gamma(l+\frac{3}{2})}2^{n+\delta-l+2}\sigma^{l+\frac{1}{2}}$$
$$\times F\left(\frac{n+\delta+l+3}{2},\frac{n+\delta+l+4}{2},l+\tfrac{3}{2},-\sigma^2\right),$$

we get with regard to (5) the function G in the form

$$G(\nu,\beta,\delta,l,\sigma)=\frac{\nu!\Gamma(\beta)}{\Gamma(l+\frac{3}{2})}2^{\delta-l+2}\sigma$$
$$\times\sum_{n=0}^{\nu}\frac{\Gamma(n+l+\delta+3)}{n!\Gamma(\nu-n+1)\Gamma(\beta+n)}(-2)^n$$
$$\times F\left(\frac{n+l+\delta+3}{2},\frac{n+l+\delta+4}{2},l+\tfrac{3}{2},-\sigma^2\right)$$

we wished to obtain.

But this formula can also be further transformed into a form which contains formally only one summation. With the help of well-known relations we get

$$F\left(\frac{n+l+\delta+3}{2},\frac{n+l+\delta+4}{2},l+\tfrac{3}{2},-\sigma^2\right)$$
$$=F\left(\frac{n+\delta-l+1}{2}+l+1,\frac{n+\delta-l+2}{2}\right.$$
$$\left.+l+1,\tfrac{1}{2}+l+1,-\sigma^2\right)$$
$$=\frac{\Gamma\left(\frac{n+\delta-l+1}{2}\right)\Gamma\left(\frac{n+\delta-l+2}{2}\right)}{\Gamma(1/2)}$$
$$\times\frac{\Gamma(l+\frac{3}{2})}{\Gamma\left(\frac{n+\delta+l+3}{2}\right)\Gamma\left(\frac{n+\delta+l+4}{2}\right)}\frac{d^{l+1}}{d(-\sigma^2)^{l+1}}$$
$$\times F\left(\frac{n+\delta-l+1}{2},\frac{n+\delta-l+2}{2},\tfrac{1}{2},-\sigma^2\right)$$
$$=(-1)^{l+1}2^{2l+1}\frac{\Gamma(n+\delta-l+1)\Gamma(l+\frac{3}{2})}{(\pi)^{\frac{1}{2}}\Gamma(n+\delta+l+3)}\frac{d^{l+1}}{d(\sigma^2)^{l+1}}$$
$$\times\{(1-i\sigma)^{-(n+\delta-l+1)}+(1+i\sigma)^{-(n+\delta-l+1)}\}.$$

Therefore, we have

$$G(\nu,\beta,\delta,l,\sigma)$$
$$=(-1)^{l+1}\frac{2^{2l+2}}{(\pi)^{\frac{1}{2}}}\Gamma(\delta-l+1)\sigma^l\frac{d^{l+1}}{d(\sigma^2)^{l+1}}$$
$$\times\left\{\left(\frac{2}{1+i\sigma}\right)^{\delta-l+1}F\left(-\nu,\delta-l+1,\beta,\frac{2}{1+i\sigma}\right)\right.$$
$$\left.+\left(\frac{2}{1-i\sigma}\right)^{\delta-l+1}F\left(-\nu,\delta-l+1,\beta,\frac{2}{1-i\sigma}\right)\right\}.$$

A similar expression for G_1 can be obtained from (7), using

$$F(-l,l+1,\gamma,x)=\frac{\Gamma(\gamma)}{\Gamma(\gamma+l)}x^{1-\gamma}(1-x)^{\gamma-1}\frac{d^l}{dx^l}$$
$$\times(x^{l+\gamma-1}(1-x)^{l-\gamma+1}).$$

The Pure Rotational Spectrum of ICl

C. H. TOWNES,* F. R. MERRITT, AND B. D. WRIGHT**
Bell Telephone Laboratories, Murray Hill, New Jersey

(Received February 6, 1948)

Frequencies and intensities of a number of lines of the $J=3\rightarrow4$ rotational transition of ICl were measured and the spectrum analyzed. Constants obtained for ICl^{35} are (in megacycles) $B_e=3422.300$, $\alpha_e=16.060$, $eq_IQ_I=-2930.0$, $eq_{Cl}Q_{Cl}=-82.5$. The mass ratio $\frac{Cl^{35}}{Cl^{37}}$ obtained from this spectrum is 0.9459801, which appears inconsistent with the most recent mass spectroscopic determination. The molecular dipole moment is approximately 0.65×10^{-18} e.s.u. from intensity measurements.

THE molecule ICl is the first diatomic molecule whose pure rotational spectrum has been investigated by microwave spectroscopy. The value of the molecular constants B_e and α_e are fairly accurately known from measurements in higher frequency regions.[1,2] When the pure rotation spectrum is examined under the high resolution afforder by microwave spectroscopy, it is not as simple as might at first be expected, but is split into a large number of lines by nuclear quadrupole effects. Weidner[3] has detected the $J=0\rightarrow1$ transition of ICl at a wavelength near 4.5 cm, but encountered some difficulties in interpretation because of the quadrupole splitting. Spectrum of the transition $J=3\rightarrow4$ is investigated here and all molecular constants which are involved are evaluated. Both the iodine and chlorine nuclei show electric quadrupole moments, which break up the single transition $J=3\rightarrow4$ for the ground state of a single isotopic species into about 150 lines. Fortunately, most of the intensity is concentrated in a smaller number of these, of which about twenty-five have been measured.

I. EXPERIMENTAL CONSIDERATIONS

Detection of the ICl lines was accomplished by the usual sweeping technique,[4,5] the rectified microwave signal which had traversed an absorption cell of ICl being amplified and arranged to produce pips on an oscilloscope representing a plot of absorption *versus* frequency. The sweep was repeated at the slow rate of about once per second to allow the use of a narrow band (15 cycles/sec.) amplifier to aid in noise elimination. About 5 milliwatts of microwave power was obtained from a 2K50 microwave oscillator which had been accidentally electrically overloaded so that its normal frequency of oscillation was changed to the region of interest near 27,000 mc. Using a 16-ft. absorption cell, the minimum detectable absorption lines had absorption coefficients of about 4×10^{-7} cm^{-1} or 2×10^{-7} nepers/cm.

Because of the reactivity of ICl, the usual silver wave guide could not be used, but was replaced by a 16-ft. stainless steel guide made to standard K-band dimensions by the Superior Tube Company of Norristown, Pennsylvania. This guide had an attenuation of about 10 db at the frequencies used, which proved no great handicap.

The ICl had to be kept from contacting mercury, but greased stopcocks could be used in the gas system because the grease was attacked sufficiently slowly. After opening the absorption cell to the air, there was apparently enough absorption and change in surface conditions to produce reactions with the first few fillings of ICl gas, which reacted and produced very weak lines after standing in the guide a few minutes. Subsequently ICl admitted to the cell appeared to show only very slow reaction.

Since it was desired to measure frequency differences, in particular the isotopic shift, rather

* Now at Columbia University.
** Now at University of Chicago.
[1] W. G. Brown and G. E. Gibson, Phys. Rev. **40**, 529 (1932).
[2] W. E. Curtis and J. Patkowski, Phil. Trans. Roy. Soc. **232**, 395 (1934).
[3] R. T. Weidner, Phys. Rev. **72**, 1268 (1947); Phys. Rev. **73**, 254 (1948).
[4] C. H. Townes, Phys. Rev. **70**, 665 (1946).
[5] W. E. Good, Phys. Rev. **70**, 213 (1946).

accurately, arrangement was made for accurately comparing the signal oscillator frequency with side bands produced by mixing outputs of a stabilized microwave oscillator and a quartz crystal oscillator. Thus the quartz crystal oscillator became the standard for measuring frequency differences. Absolute frequencies were measured only by comparing in the same way some of the ICl lines with a known NH_3 line. Additional details of this technique will be described in a subsequent paper.

II. ANALYSIS OF THE SPECTRUM

Table I lists the ICl^{35} lines due to the $J=3\rightarrow4$ transition which were measured, as well as their identification and frequencies calculated from the molecular constants assumed. The quantity F_1 is the angular momentum in units of $h/2\pi$ resulting from the vector addition of **J** and the angular momentum of the iodine nucleus $\mathbf{I}_1$. F is the total angular momentum in units of $h/2\pi$, which results from the vector addition of **J** and the spins of both nuclei. Since the quadrupole coupling of the iodine nucleus is much stronger than that of the chlorine nucleus, F_1 is, in most cases, a sufficiently good quantum number for identification of the lines. However, in the particular cases $J=3$, $F_1=7/2$ and $J=3$, $F_1=9/2$, the iodine quadrupole energies are almost identical, and this accidental degeneracy is removed by the energies connected with the Cl quadrupole. Under these conditions, F_1 is a poor means of identifying the levels, and it has been given the combination of values 7/2, 9/2.

The frequency difference between each line and the center of gravity of the $F_1=11/2\rightarrow13/2$ group of the ground state of ICl^{35} was measured by the technique described above. Absolute frequencies were then obtained by measuring the interval between the center of this group and the NH_3 7,7 line,[6,7] which was found to be 1621.89 ± 0.15 mc. Incidental to these measurements, the NH_3 8,8 line was found and the interval between it and the NH_3 7,7 line measured as 803.54 ± 0.15 mc.

Table II lists the values of molecular constants required to give the theoretical frequencies listed

[6] D. K. Coles and W. E. Good, Phys. Rev. **71**, 383 (1947).
[7] M. W. P. Strandberg, R. Kyhl, T. Wentink, and R. W. Hillger, Phys. Rev. **71**, 326 (1947).

TABLE I. ICl^{35} lines of the transition $J=3\rightarrow4$.

Designation of line		Measured frequency in megacycles	Theoretical frequency in megacycles	Frequency difference	Theoretical relative intensity
ICl^{35} ground vibrational state					
F_1	F				
3/2→5/2	2→3	27194.75	27195.04	−0.30	.13
3/2→5/2	1→2	27202.64	27202.56	0.08	.07
3/2→5/2	3→4	27204.99	27204.84	0.15	.21
3/2→5/2	0→1	——	27211.74	——	.03
5/2→7/2	3→4	27217.51	27217.36	0.15	.21
5/2→7/2	2→3	27221.02	27221.45	−0.43	.15
5/2→7/2	4→5	27225.32	27225.38	−0.06	.29
5/2→7/2	1→2	27228.34	27228.44	−0.10	.10
1/2→3/2	1→2	27242.59	27242.74	−0.15	.06
1/2→3/2	2→3	27254.90	27255.00	−0.10	.16
7/2, 9/2→9/2		27283.66			
7/2, 9/2→9/2		27286.25			
7/2, 9/2→9/2		27292.63			
7/2, 9/2→9/2		27295.05			
7/2, 9/2→11/2	5→6	27333.85			
11/2→13/2	6→7 5→6	27336.68	27336.51	0.17	.99
11/2→13/2	7→8 4→5	27337.38	27337.53	−0.15	1.00
7/2, 9/2→11/2	3→4	27346.31			
7/2, 9/2→11/2	4→5	27354.71			
9/2→11/2	6→7	27356.58	27356.41	0.17	
7/2, 9/2→11/2	5→6	27357.73			
ICl^{35} excited vibrational state ($v=1$)					
11/2→13/2		27208.54			.31

in Table I. The constants B_e and α_e are in agreement with the values 0.11414 cm^{-1} and 0.00050 cm^{-1}, respectively, given by measurements of Curtis and Patkowski[2] in the visible region. The excited state line at 27,208.49 mc from which α_e was determined was the only line found in the region of lines produced by ICl^{35} which could not be fitted to a line of the ground vibrational state. It was of the correct intensity with respect to the corresponding group of lines of the ground vibrational state, and appeared to have the width to be expected from the fact that it is a group of four lines rather than a single line as are its neighbors. The next most intense group of lines ($F_1=7/2,\ 9/2\rightarrow11/2$) due to ICl^{35} in the excited vibrational state is rather widely split by the chlorine quadrupole and hence weak. Its main intensity should fall at about 27,227 mc, where it would be confused with lines of the ground state.

TABLE II. Molecular constants for ICl^{35} expressed in megacycles.

B_e	3422.300 ± 0.02
α_e	16.060 ± 0.02
$eq_1Q_1=eQ_1\dfrac{\partial^2V_1}{\partial z^2}$	-2930.0 ± 4
$eq_{Cl}Q_{Cl}=eQ_{Cl}\dfrac{\partial^2V_{Cl}}{\partial z^2}$	-82.5 ± 1

In addition, this identification of the line at 27208.49 mc gives a value of α_e which agrees well with that obtained by Curtis and Patkowski. The fact that the iodine quadrupole constant is unusually large and the chlorine constant about the same as in ClCN appears to be consistent with the atomic wave function model.[8] This will be discussed in more detail in a later paper.

The method of Bardeen and Townes[9] was used to analyze the splitting produced by quadrupole moments of iodine and chlorine. The iodine quadrupole coupling is so large, however, that effects of the order $(eq_IQ_I)^2/B_e$ must be taken into account to obtain a satisfactory fit of the experimental data. Thus J is not actually fixed, but in the lower state labeled $J=3$, values $J=1$ and $J=5$ are of some importance, and similarly for the upper state. Expressions for the matrix elements necessary for calculating the shift in energy values produced by these second-order effects are given elsewhere.[10] The magnitude of their contributions to the line positions in this case is of the order of one megacycle.

The lines which involve the degenerate levels ($J=3$, $F_1=7/2$, $9/2$) have not been calculated exactly. A calculation taking into account energies associated with first-order quadrupole interactions for iodine and chlorine and second-order energies $(eq_IQ_I)^2/B_e$ for iodine was made which gave lines agreeing within about two megacycles with those found experimentally. This probably allows a correct identification of the lines in those cases where values of F are given in Table I. Second-order energies of the type $e^2q_{Cl}Q_{Cl}q_IQ_I/B_e$ and $(eq_{Cl}Q_{Cl})^2/B_e$ have not yet been taken into account because their calculation is somewhat involved. Although these energies are not large, final energy values for the degenerate levels are very sensitive to small effects, and perhaps inclusion of these remaining second-order effects will give agreement with the measured frequencies. All lines which do not involve degenerate levels were fitted well by the theory and indicate that fairly accurate values of quadrupole coupling constants for iodine and chlorine are obtained.

No interactions of the form $cI\cdot J$ are in evidence, although small interactions of approximately the magnitude found by Nierenberg and Ramsey[11] in the alkali halides may be present. The upper limit which may be put on $|c|$ from the present measurements is 0.05 mc.

III. THE ISOTOPIC SHIFT

Evaluation of α_e and analysis of the quadrupole coupling energies should allow an accurate prediction of the isotopic shift from the known isotopic mass ratios. The position of the center of the strongest group of lines ($F_1=11/2\rightarrow13/2$) of ICl^{35} is given theoretically by

$$\nu_{35}=8B_e-4\alpha_e-0.0075757eq_IQ_I+0.00029\times[(eq_IQ_I)^2/B_e]+0.0007eq_{Cl}Q_{Cl}.$$

For ICl^{37}, the value of ν should be obtainable from the known ICl^{35} frequency since B_e is inversely proportional to the reduced mass μ of the molecule and α_e is inversely proportional to $\mu^{\frac{1}{2}}$. The effect of the chlorine quadrupole is very small, and its change can be calculated from the known ratio of quadrupole moments[12,13] of the chlorine isotopes. Taking the isotopic masses from Mattauch[14] and using the numerical values of B_e, α_e, q_IQ_I, and $q_{Cl}Q_{Cl}$ obtained here, the isotopic shift should be

$$\nu_{35}-\nu_{37}=8B_e\left(1-\frac{\mu_{35}}{\mu_{37}}\right)-4\alpha_e\left[1-\left(\frac{\mu_{35}}{\mu_{37}}\right)^{\frac{1}{2}}\right]\times0.0029\frac{(eq_IQ_I)^2}{B_e}\left(1-\frac{\mu_{37}}{\mu_{35}}\right)+0.0015eq_{Cl}Q_{Cl}\left(1-\frac{Q_{Cl}^{37}}{Q_{Cl}^{35}}\right)$$

$$=1160.259-4.040-0.031-0.012$$

$$=1156.176 \text{ megacycles.}$$

The measured frequency difference between the center of the group of lines $11/2\rightarrow13/2$ for ICl^{35} and ICl^{37} was 1155.40 ± 0.10 megacycles. This measurement thus appears to give a difference

[8] C. H. Townes, Phys. Rev. **71**, 909 (1947).
[9] J. Bardeen and C. H. Townes, Phys. Rev. **73**, 97 (1948).
[10] J. Bardeen and C. H. Townes, Phys. Rev. **73**, 627 (1948).
[11] W. A. Nierenberg and N. F. Ramsey, Phys. Rev. **72**, 1075 (1947).
[12] C. H. Townes, A. N. Holden, J. Bardeen, and F. R. Merritt, Phys. Rev. **71**, 644 (1947).
[13] W. Gordy, J. W. Simmons, and A. G. Smith, Phys. Rev. **72**, 344 (1947).
[14] J. Mattauch, *Nuclear Physics Tables* (Interscience Publishers, Inc., New York, 1946).

between the two chlorine masses which is about one part in 1500 less than that assumed in making the calculation of isotopic shift. The $F_1=7/2$, $9/2\rightarrow11/2$ group of lines of ICl^{37} was also found, but was not measured because its width and the weakness of single components did not allow accurate measurement of the isotopic shift. The mass ratio calculated from the measured isotopic shift is 0.9459801 ± 0.0000050, as compared with the value 0.9459441 ± 0.0000065 obtained from Mattauch, which is based primarily on the mass spectroscopic measurements of Okuda, Ogata, Aoki, and Sugawara.[15] The ratio obtained here does agree well with the value 0.9459806 ± 0.0000300 obtained from Aston's work,[16] but his quoted errors are rather large. Since microwave spectroscopy should be able to give a number of mass ratios in the future, and possibly with an accuracy ten times that obtained here assuming the theory is complete, it is of considerable interest to know whether the present disagreement with the results of Okuda *et al.* is experimental, or due to some unrecognized source of frequency shift between the two ICl isotopic species.

IV. INTENSITY

The intensity and half-widths of the ICl^{35} group of lines $11/2\rightarrow13/2$ was measured at a pressure high enough that the separation of individual lines was considerably smaller than their width. The half-width, or total width at half maximum intensity, was found to be 13.3 mc. for gas in equilibrium with a trap of temperature -15°C. The pressure measured for this temperature by Cornog and Bauer[17] is 1.2 mm Hg, so that the half-width at a pressure of 1 mm. of mercury would be 11 ± 2 mc. This is comparable with the half-width of the 24,326 mc line of *OCS*, which has approximately the same dipole moment, but almost twice as large as the value found by Weidner[3] for the ICl $0\rightarrow1$ transition. The peak intensity of the $11/2\rightarrow13/2$ lines at pressures high enough to make their peak intensities additive was found to be $1.36\pm0.14\times10^{-5}$ cm^{-1} or $6.8\pm0.7\times10^{-6}$ nepers/cm in free space. Using the half-width quoted above, and assuming a dipole moment of 0.5×10^{-18} e.s.u.,[18] this peak intensity may be calculated to be $0.94\pm0.18\times10^{-5}$ cm^{-1}, considerably less than the measured value. Examination of the intensity and half-width measurements of Weidner[3] shows a similar discrepancy. Interpreting his measured ICl^{35} line as the sum of all quadrupole splitting components, he obtained agreement with the calculated intensity. However, because of quadrupole splitting this line includes only 4/9 the intensity of the entire $J=0\rightarrow1$ transition, so that it is more intense by approximately the factor 9/4 factor than his theoretical expectations. More exactly, he obtained an intensity for the $J=0\rightarrow1$, $F_1=5/2\rightarrow7/2$ line of 1.1×10^{-6} cm^{-1} and a half width 0.168 cm^{-1} at atmospheric pressure or 6.6 mc. at one mm. Hg. pressure.*** Although experimental inaccuracies in intensity and half-width measurements do not allow a determination of the ICl dipole moment to an accuracy better than about 10 percent, they do indicate that the value 0.5 Debye units given by Luft[18] is definitely too small. A value of 0.65 Debye units would better fit the mean of Weidner's and our own experimental results.

[15] T. Okuda, K. Ogata, K. Aoki, and Y. Sugawara, Phys. Rev. **58**, 578 (1940).
[16] F. W. Aston, Proc. Roy. Soc. **163**, 391 (1937).
[17] J. Cornog and E. E. Bauer, J. Am. Chem. Soc. **64**, 2620 (1942).
[18] K. F. Luft, Zeits. f. Physik **84**, 767 (1933).
*** The authors are indebted to Dr. Weidner for a discussion of intensities and for supplying the exact values of his experimental results.

The Directional Intensity of Cosmic Rays at Several Altitudes

MATTHEW SANDS
Laboratory for Nuclear Science and Engineering, Massachusetts Institute of Technology, Cambridge, Massachusetts
(Received February 9, 1948)

The vertical intensity and the intensity at inclined directions of the ionizing cosmic rays which penetrate 5 g-cm^{-2} of brass have been measured with a counter telescope at several altitudes between sea level and 10,700 meters.

I. INTRODUCTION

THE directional intensity of the ionizing cosmic rays has been measured accurately by Greisen[1] at altitudes between sea level and 4300 meters. The vertical intensity at greater altitudes, and at latitudes near 45°, has been measured by Pfotzer[2] and by Millikan, Neher, and Pickering.[3] Measurements have been made at greater latitudes by Johnson[4] and by Carmichael and Dymond.[5] Because of the rapid rate of ascent of the balloons used in these high altitude measurements the statistical errors are relatively large at intermediate altitudes. Also, there is little data available on the intensity at these altitudes for directions away from the vertical. When a B-29 aircraft was made available to this laboratory for other work in cosmic rays, it was thought advisable to make use of the remaining space for some measurements of this kind.

II. THE APPARATUS

The apparatus consisted of a simple counter-telescope and a coincidence circuit. The telescope was composed of seven identical Geiger-Mueller counter tubes held by a light frame in the arrangement indicated in Fig. 1. Two tubes connected in parallel were used for each of the three trays, marked 1, 2, and 3, of the telescope proper. The remaining "tray," the single tube marked 4, was used to determine the effect of side showers on the measurements. The frame held the tubes fixed relative to each other, but the assembly could be tilted about an axis parallel to the axes of the tubes so as to vary the angle θ in the figure. No part of the frame was within the solid angle subtended by the telescope.

Each counter tube was made of a brass cylinder 30 cm long, 2.54 cm in outside diameter, and with an 0.08 cm thick wall. The active part of the central electrode was an 0.008-cm tungsten wire 25.4 cm long. The tubes were filled to a total pressure of 10 cm of mercury with a self-quenching mixture: 90 percent, argon and 10 percent ethanol. The tubes had plateaus longer than 200 volts and were operated between 50 and 75 volts above the thresholds. Under these circumstances the spontaneous time lags were less than 0.7 μsec. for 0.999 of the discharges, and the inoperative time after each discharge was about 1.5×10^{-4} sec.

The four trays of the telescope were connected to a coincidence circuit which recorded simultaneously threefold coincidences (1, 2, 3) and (1, 4, 3), and fourfold coincidences (1, 2, 3, 4). The (1, 2, 3) coincidences were counted by a scale-of-8 and mechanical register; the other two, by registers directly. A scale-of-16 and register could be connected so as to record the discharges of any individual tray or the twofold coincidences between any pair of trays. The resolving time of all the coincidence circuits were 0.7 μsec. The recovery time of the coupling circuits between the tubes and the coincidence circuit, and of the scaling circuits was 20 μsec. and was, therefore, negligible compared with the recovery time of the G-M tubes. The mechanical registers would count successive events which were separated by more than 0.1 sec.[6]

III. THE MEASUREMENTS

The telescope was operated at sea level in Cambridge 3 meters below a 2 cm thick wooden

[1] K. Greisen, Phys. Rev. **61**, 212 (1942).
[2] G. Pfotzer, Zeits. f. Physik. **102**, 23 (1936).
[3] R. A. Millikan, H. V. Neher, and W. H. Pickering, Phys. Rev. **63**, 234 (1943).
[4] T. H. Johnson, Phys. Rev. **54**, 151 (1938).
[5] H. Carmichael and E. G. Dymond, Nature **141**, 910 (1938).

[6] A detailed description of the circuits used will be published elsewhere.

roof. The measurements at all other altitudes were made in the rear pressurized cabin of a B-29 aircraft about 10 cm below the top of the fuselage, at a place where the average thickness of material above the telescope was about 1 g-cm^{-2} of light material. Five flights were made during January and February, 1947. The flights consisted usually of two periods at each of two different pressures. All flights were made at the same latitude (approximately 53° N mag.) and with the axes of the G-M tubes heading east-west. The telescope was inclined either north or south. During each period, at a given altitude, the telescope was operated vertically and at one other angle. For each angle, the counting rate in one tray and the twofold coincidence rates (1, 2), (1, 3) (1, 4), and (2, 4) were obtained as well as the threefold and fourfold coincidence data. The data from the several flights at the same pressure were self-consistent.

The threefold and fourfold coincidence data are given in Table I according to pressure and angle. The first and second columns give the pressure and approximate altitude at which the data were taken, the third, the zenith angle (θ of Fig. 1). In the fifth, sixth, and seventh columns are the data for the number of (1, 2, 3), (1, 4, 3), and (1, 2, 3, 4) coincidences obtained in all corresponding runs, the combined duration of which is given in the fourth column.

IV. THE CORRECTIONS AND RESULTS

The counting rates which one obtains from Table I are somewhat in error because of accidental coincidences and because of losses resulting from the recovery time of the G-M tubes. The correction to the (1, 2, 3) coincidence rate caused by accidental coincidences is given approximately by

$$S=-4\tau[\{1,2\}-I]\cdot[\{1\}-I],$$

where τ is the resolving time of the coincidence

TABLE I. Threefold and fourfold coincidence data.

Pressure (g-cm^{-2})	Approx. alt. (meters)	Zenith angle	Duration (minutes)	Number of coincidences (1, 2, 3)	(1, 4, 3)	(1, 2, 3, 4)
250	10700	0°	62	14888	609	242
		60°	56	4564	240	107
390	9100	0°	45	8560	354	149
		30°	87	13152	452	199
310	7600	0°	171	21928	868	380
		30°	49	4752	185	86
		60°	72	2368	122	45
610	4300	0°	96	3656	133	71
		30°	121	3280	133	68
		60°	153	1288	80	45
1030	0	0°	7955	739120	1325	583
		30°	3445	23304	397	172
		60°	2305	5000	144	72

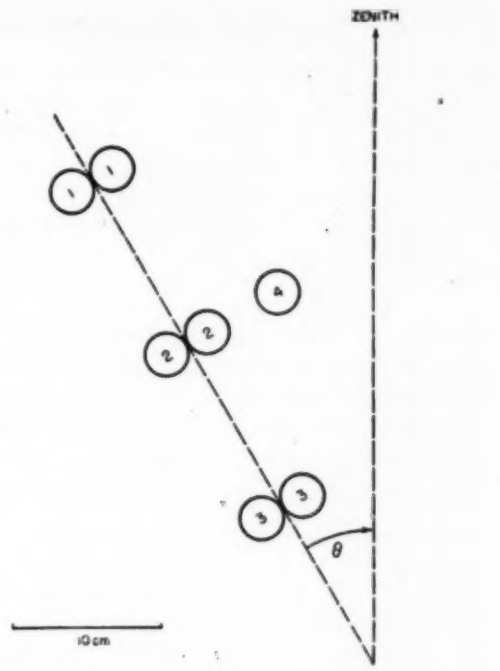

FIG. 1. Arrangement of the counter-telescope.

TABLE II. Corrected counting rates for threefold and fourfold coincidences with $\theta=0$.

Pressure (g-cm^{-2})	Corrected counting rates (min.$^{-1}$) (1, 2, 3)	(1, 4, 3)	(1, 2, 3, 4)
250	244±2	9.9±0.4	4.1±0.3
310	193±2	8.0±0.4	3.4±0.3
390	129±1	5.1±0.2	2.2±0.1
610	38.2±0.6	1.39±0.12	0.74±0.09
1030	9.31±0.03	0.167±0.004	0.073±0.003

TABLE III. Angular dependence of threefold and fourfold coincidence rates; the ratios (counting rate at θ)/(counting rate at 0°) are tabulated.

Pressure (g-cm^{-2})	$\theta=30°$ (1, 2, 3)	(1, 4, 3)	(1, 2, 3, 4)	$\theta=60°$ (1, 2, 3)	(1, 4, 3)	(1, 2, 3, 4)
250	—	—	—	0.40	0.44	0.49
310	0.79	0.67	0.70	—	—	—
390	0.76	0.74	0.82	0.26	0.33	0.28
610	0.71	0.70	0.75	0.22	0.37	0.39
1030	0.73	0.69	0.69	0.23	0.38	0.43

TABLE IV. Vertical intensities of ionizing particles of range greater than 5 g-cm^{-2} of brass.

Pressure (g-cm^{-2})	Relative intensity	Absolute intensity (sec.$^{-1}$-cm^{-2}-steradian^{-1})
250	(26.2±0.21)	(0.280)
310	20.7±0.25	0.222
390	13.9±0.10	0.149
610	4.10±0.07	0.0439
1030	1.00	0.0107

circuit, $\{1\}$ is the counting rate in tray 1 and in tray 3, $\{1, 2\}$ is the rate of (1, 2) and of (2, 3) coincidences, and I is the observed rate for threefold coincidences (1, 2, 3). The correction to the observed (1, 2, 3) coincidence rate due to the counter dead time is given approximately by

$$E=+Ir[\tfrac{3}{2}\{1\}-\tfrac{1}{2}\{1, 2\}-\tfrac{11}{16}I],$$

where r is the dead time of a counter tube and the other symbols are as above. At all altitudes the correction E is much larger than S. At the highest altitude the combined correction, $E+S$, was, for $\theta=0$, +1.7 percent of the observed rate and at sea level +0.1 percent. Similar corrections were made to the rates for $\theta=0$ of threefold coincidences (1, 4, 3) and fourfold coincidences. In all cases these corrections were less than 2 percent. The corrected counting rates for threefold and fourfold coincidences with $\theta=0$ are given in Table II. The errors indicated are the statistical standard deviations.

It will be seen from Table II that the (1, 4, 3) coincidence rate is 2 percent of the (1, 2, 3) rate at sea level and about 4 percent at all other altitudes, and that the (1, 2, 3, 4) rate is 1 percent of the (1, 2, 3) rate at sea level and 2 percent at other altitudes. Part of this difference between the sea level and high altitude ratios may be due to the different location of the solid material above the counters in the two cases (see above). No attempt has been made to correct the (1, 2, 3) coincidence rate for the effect of side showers. Since such a correction would be only a fraction of the (1, 4, 3) coincidence rate, neglecting this correction can cause at most a 2 percent error in the intensities relative to sea level.

Since the instrumental corrections are small and essentially independent of θ, they have not been computed for angles away from the vertical. The ratios of the observed threefold and fourfold coincidence rates for $\theta=30°$ and $\theta=60°$ to those for $\theta=0$ are given in Table III. It is evident that the rate for threefold coincidences (1, 2, 3) exhibits a $\cos^2\theta$ dependence at all altitudes except the highest. The θ-dependence of the side coincidences appears to be only a little less sharp than $\cos^2\theta$. This, and the altitude variation shown in Table II, show that the side coincidence rate is at all altitudes approximately proportional to the soft component in the beam, and is therefore not due to large air showers but probably to small showers of local origin.

Since the angular dependence of the (1, 2, 3) coincident rate is independent of altitude up to 9100 meters, our data for $\theta=0$ represent correctly to that height the altitude variation of vertical intensity of the total ionizing component despite the large solid angle of the apparatus. The vertical intensities relative to the sea level intensity are given in the second column of Table IV. From an analysis of the available data, Rossi[7] concludes that the best value for the absolute intensity at sea level of particles from the vertical which penetrate 5 g-cm^{-2} of brass is 1.07×10^{-2} sec.$^{-1}$ cm^{-2} steradian^{-1}. This absorber thickness corresponds with that of the telescope used in the present experiments.

Using the above figure for the vertical intensity at sea level, one gets the absolute intensities given in the third column of Table IV. It is probable that the figures given in Table IV for a pressure of 250 g-cm^{-2} are a little large if the angular dependence is indeed different at that altitude.

ACKNOWLEDGMENTS

The author is indebted to Professor B. Rossi for suggesting and guiding this research. The work described was supported in part by the Office of Naval Research. The B-29 used for the measurements at high altitudes was provided by the U. S. Army Air Force.

[7] B. Rossi, Rev. Mod. Phys. (to be published).

On the Analysis of Extensive Cosmic-Ray Shower Data

H. W. LEWIS
Institute for Advanced Study, Princeton, New Jersey

(Received February 16, 1948)

Formulae are derived, on the basis of the primary electron hypothesis, which describe the behavior of counters exposed to the large air showers. In particular, expressions for the variation of counting rate with area of the counters, number of counters, and altitude are given, and seem to agree fairly well with experiment, except for the latter at very high altitudes.

I. INTRODUCTION

THERE are at present at least two separate mechanisms which have been suggested for the development of the large air showers. The first of these regards the showers as generated by the ordinary cascade process from extremely energetic primary electrons (tacitly assuming that the ordinary formulae of electrodynamics are valid at such high energies). Here one has a definite picture whose consequences can be worked out in detail. One usually assumes that primary electrons impinge upon the top of the atmosphere with an energy spectrum proportional to $E_0^{-\lambda}dE_0$; λ is adjusted to fit the experiments and usually chosen to be about 2.8. The second mechanism describes the showers as produced by the high energy tail of a primary proton spectrum, and one can choose one of a number of different means of converting a fraction of the primary energy into the soft component (either through the decay of heavy mesons into lighter ones with emission of soft radiation, or other possibilities). Clearly a great deal of flexibility in detail is possible here, so that it does not seem profitable at present to work out the details of any particular version until one knows somewhat more precisely whether there are any real difficulties with the primary electron hypothesis, and, if so, where they are. One might mention, however, one feature which has to do with the penetration of the primaries that is common to all theories that ascribe the air showers to primary protons. Experiments on the penetrating showers, which are probably characteristic of the primary events, both at sea level and at high altitudes have suggested that the primaries have a mean free path of about 125 g/cm^2 in air. Since this distance is roughly equal to three shower units, one might expect that this comparatively high penetrating power would manifest itself in the altitude variation of the properties of a shower deep in the atmosphere. In particular, the asymptotic altitude variation should be characteristic of this distance rather than the distance of one shower unit which describes the decay of individual cascade showers after they have passed their maxima. For these reasons we have decided to make a study of the behavior of the showers near sea level, using the primary electron hypothesis and the cascade theory, to see whether any obvious difficulties are yet apparent and to indicate in which directions experiments might profitably be performed.

In making this study, we have had in mind in particular counter experiments, in which one studies the variation of the counting rate with either the altitude, the number of counters in coincidence, their area, or possibly the zenith angle of the shower axis. We will not consider variations in the geometry of the counter arrangement, since we will always assume that all the counters involved are concentrated at a point. We will discuss this condition in more detail later. For example, experiments have been performed by Hilberry,[1] and by Kraybill and Ovrebo,[2] in which the altitude was varied, and by Cocconi, Loverdo, and Tongiorgi,[3] in which both number of counters and area were varied. In the latter case the information was combined to calculate a density spectrum.

II. GENERAL ASSUMPTIONS

We will use the radial distribution of the shower electrons given by Moliere,[4] and will

[1] N. Hilberry, Phys. Rev. 60, 1 (1941).
[2] H. Kraybill and P. Ovrebo, Phys. Rev. 72, 351 (1947).
[3] G. Cocconi, A. Loverdo, and V. Tongiorgi, Phys. Rev. 70, 846 (1946).
[4] Edited by W. Heisenberg, *Vorträge über Kosmische Strahlung* (Berlin, Germany, 1943).

assume, with him, that the radial distribution does not vary appreciably in the vicinity of the shower maximum. Then the scattering in a shower is measured by a distance r_1 which is equal to R/h where R is the value of r_1 at sea level, about 60 meters, and h the fraction of the atmosphere above the point of observation (assuming an isothermal atmosphere). If the distance from the shower axis measured in units of this characteristic distance is called ρ, then the particle density d is given by $(n/2\pi r_1^2)(w(\rho)/\rho)$, with n the number of particles in the shower, and $w(\rho)$ a function which is plotted by Moliere, and which goes to 3.25 as ρ goes to zero. It is more useful for us to express ρ in terms of d and this has been done empirically, yielding, as an approximate expression good to within about 10 percent for $\rho \leqslant 1$, or $(\beta n/2\pi r_1^2 d) \leqslant 10$

$$\rho \approx (\beta n/2\pi r_1^2 d) \exp[-1.1(\beta n/2\pi r_1^2 d)^{0.35}], \quad (1)$$

where $\beta = w(0) = 3.25$.

We will also need an expression for the number of particles in a shower as a function of the initiating energy and the distance in shower units from the point of origin of the shower. We take, as a basis for this, Heisenberg's[4] approximate expression and simplify it slightly, giving

$$n = (1/4l^{\frac{1}{2}}) \exp[2(yl)^{\frac{1}{2}} - l], \quad (2)$$

where l is the distance in shower units from the point of origin of the shower, and $y = ln(E_0/\epsilon)$, where ϵ, the critical energy for air, is about 10^8 ev. In terms of y, the primary spectrum will be proportional to $e^{-y(\lambda-1)}dy$, and we will make no attempt to conserve constant factors in this work, since we are primarily interested in density spectra and altitude variations.

We will also assume everywhere that all the counters involved are at the same point, and will discuss the range of validity of this assumption later.

III. CALCULATIONS

We are now ready to calculate first the density spectra of the showers at a point of observation l_0 shower units below the top of the atmosphere. The number of primary electrons striking the atmosphere with an "energy" between y and $y+dy$, and an angle with the vertical between ϑ and $\vartheta+d\vartheta$ is proportional to $e^{-y(\lambda-1)}dy \sin\vartheta d\vartheta$, and each of these has to travel through a distance $l = l_0/\cos\vartheta$ to reach the point of observation. Thus the number with l between l and $l+dl$ is $e^{-y(\lambda-1)}dy l_0 dl/l^2$. These showers have a number of particles given by Eq. (2) above, and distance from the shower axis within which the density is larger than Δ is given by

$$\rho \leqslant (\beta n h^2/2\pi R^2\Delta) \exp[-(\alpha\beta n h^2/2\pi R^2\Delta)^{1/\gamma}], \quad (3)$$

where $\alpha = (1.1)^{2.85} = 1.32$, and $1/\gamma = 0.35$. Thus the actual area involved is $\pi(\rho R/h)^2$ which is proportional to

$$f(n, l_0, \Delta) = (n^2h^2/\Delta^2) \times \exp[-2(\alpha\beta n h^2/2\pi R^2\Delta)^{1/\gamma}], \quad (4)$$

and our problem is simply to integrate this over all energies and zenith angles. This is most easily done if one first makes a Mellin transformation on f, with respect to n, obtaining

$$g(\sigma) = \int_0^\infty f(n) n^{\sigma-3} dn \propto (h^2/\Delta^2)(2\pi R^2\Delta/2^\gamma \alpha\beta h^2)^\sigma \Gamma(\gamma\sigma), \quad (5)$$

with Γ the usual Γ-function. As is well known, this can be inverted by means of the contour integration

$$f(n, l_0, \Delta) = (1/2\pi i) \int_C g(\sigma) n^{2-\sigma} d\sigma, \quad (6)$$

where the contour C is taken parallel to the imaginary axis to the right of the singularity of the Γ-function at $\sigma = 0$. We will not invert this until later. We must now evaluate the following expression for the integral density spectrum:

$$N(l_0, \Delta) \propto (1/2\pi i)(h^2/\Delta^2) \int_C d\sigma (8\pi R^2\Delta/2^\gamma \alpha\beta h^2)^\sigma \times \Gamma(\gamma\sigma) \int_{l_0}^\infty (dl/l^{3-(\sigma/2)}) \exp[(\sigma-2)l] \int_0^\infty dy \times \exp[-y(\lambda-1) + 2(2-\sigma)(yl)^{\frac{1}{2}}], \quad (7)$$

where we have used Heisenberg's expression for $n(y,l)$ and the fact that $h \approx l_0/25$, since there are

about 25 shower units in the atmosphere. The last integral can be performed either by setting $y=x^2$, and then setting the lower limit for x equal to $-\infty$, or by the saddle point method; it is assumed in either case that $\Re(2-\sigma)>0$, which restricts the contour to the strip $0<\Re(\sigma)<2$. The result is proportional to

$$(2-\sigma)l^{\frac{1}{2}}\exp[(2-\sigma)^2 l/(\lambda-1)],$$

where it is assumed that $l\gg 1$. We must now integrate

$$\int_{l_0}^{\infty}(dl/l^{(5-\sigma)/2})\exp\left[l\left[\frac{(2-\sigma)^2}{\lambda-1}\cdot-(2-\sigma)\right]\right]$$

$$=\int_{l_0}^{\infty}dl l^{(\sigma-5)/2}\exp\left[\frac{(2-\sigma)(3-\lambda-\sigma)l}{\lambda-1}\right],$$

which is convergent for $3-\lambda\leqslant\Re(\sigma)\leqslant 2$. In this region both factors in the integrand are decreasing, and one has contributions only from values of l near l_0. This is equivalent to the statement that most of the showers recorded will be vertical, and follows from the fact that we are dealing with counters that are close together deep in the atmosphere. In this region, again using the method of steepest descents, the integral is approximately given by

$$l_0^{(\sigma-3)/2}\exp\left[\frac{(2-\sigma)(3-\lambda-\sigma)}{(\lambda-1)}l_0\right]\cdot\frac{1}{[(5-\sigma)/2]+[(2-\sigma)(\lambda+\sigma-3)/(\lambda-1)]l_0}.$$

We have, then, finally

$$N(l_0,\Delta)\propto(1/2\pi i)(l_0^{\frac{1}{2}}/\Delta^2)\int_C d\sigma(490R^2\Delta)^\sigma\Gamma(\gamma\sigma)\cdot\left[l_0^{-(3\sigma/2)}\cdot\exp\left[\frac{(2-\sigma)(3-\lambda-\sigma)}{\lambda-1}l_0\right]\right]\Big/\left[(\lambda+\sigma-3)l_0+\left(\frac{\lambda-1}{2}\right)\left(\frac{5-\sigma}{2-\sigma}\right)\right],\quad(8)$$

where we have used again $h\approx l_0/25$.

We may now consider an experiment in which an N-fold set of coincidence counters, each of area A, is used to record shower counts at a depth l_0. Since the probability of recording a count is $(1-e^{-A\Delta})^N$, we must integrate this over the differential density spectrum at the point of observation. In the integral spectrum (8) Δ enters only as $\Delta^{\sigma-2}$, so that the counting rate is given by

$$C(l_0)\propto\frac{1}{2\pi i}l_0^{\frac{1}{2}}\int_C\frac{(2-\sigma)(490R^2)^\sigma\Gamma(\gamma\sigma)l_0^{-(3\sigma/2)}\exp\left[\frac{(2-\sigma)(3-\lambda-\sigma)l_0}{\lambda-1}\right]}{(\lambda+\sigma-3)l_0+\left(\frac{\lambda-1}{2}\right)\left(\frac{5-\sigma}{2-\sigma}\right)}d\sigma\int_0^\infty d\Delta\cdot\Delta^{\sigma-3}(1-e^{-A\Delta})^N,\quad(9)$$

where the latter integral is proportional to

$$A^{2-\sigma}\int_0^\infty d\delta\cdot\delta^{\sigma-3}(1-e^{-\delta})^N,$$

which is convergent for $N\geqslant 2$. Now, since $\Re(\sigma)<2$ always, and usually <1, the contributions to this integral come from near the origin, and it is sufficient to replace $(1-e^{-\delta})$ by $\delta e^{-\delta/2}[1+(\delta^2/12)+(\delta^3/48)\cdots]$ giving us for the integral

$$(2/N)^N(NA/2)^{2-\sigma}\Gamma(N-2+\sigma)\times[1+[(N-1+\sigma)(N-2+\sigma)/3N]+[(N-1+\sigma)(N+\sigma)(N-2+\sigma)/6N^3]\cdots]=(2/N)^N(NA/2)^{2-\sigma}\Gamma(N-2+\sigma)\cdot S(N,\sigma),$$

yielding, finally,

$$C(l_0)\propto\frac{1}{2\pi i}\left(\frac{2}{N}\right)^N l_0^{\frac{1}{2}}\int_C\frac{(2-\sigma)l_0^{-(3\sigma/2)}d\sigma}{(\lambda+\sigma-3)l_0+[(\lambda-1)/2][(5-\sigma)/(2-\sigma)]}\left(\frac{NA}{980R^2}\right)^{2-\sigma}\Gamma(\gamma\sigma)\Gamma(N-2+\sigma)\times\exp[(2-\sigma)(3-\lambda-\sigma)l_0/\lambda-1]S(N,\sigma).\quad(10)$$

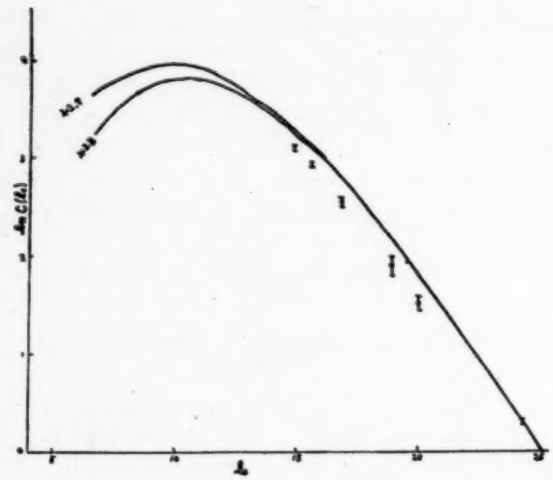

FIG. 1. Variation of counting rate with altitude for $A=200$ cm², and $\lambda=2.8$ and 2.9. Experimental points are those of Hilberry and are normalized so that the sea level point lies on the curve for $\lambda=2.8$.

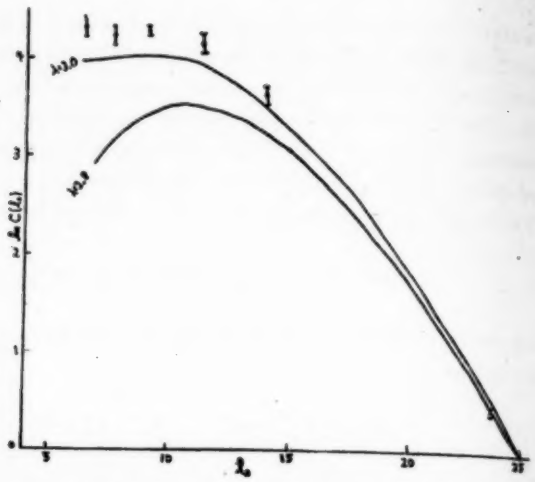

FIG. 2. Variation of counting rate with altitude for $A=100$ cm², and $\lambda=2.8$ and 3.0. Experimental points are those of Kraybill and Ovrebo and are normalized so that the sea level point lies on the curve for $\lambda=2.8$.

We will see that there will, in general, be a saddle on the real axis at $\sigma=\sigma_0(N, l_0, A, \lambda)$. The width of the saddle will be principally determined by the two Γ-functions, and by the term in $\exp[\sigma^2 l_0(\lambda-1)]$, hence proportional to

$$(l_0+[(\lambda-1/2][\gamma^2\psi'(\gamma\sigma_0)+\psi'(N-2+\sigma_0)])^{-\frac{1}{2}}$$

so that we have finally

$$C(l_0)\propto(2/N)^N\frac{(2-\sigma_0)l_0^{\frac{1}{2}(1-\sigma_0)}\Gamma(\gamma\sigma_0)\Gamma(N-2+\sigma_0)S(N,\ \sigma_0)\ \exp[-(2-\sigma_0)(\lambda+\sigma_0-3)l_0/(\lambda-1)]}{\left[(\lambda+\sigma_0-3)l_0+\frac{\lambda-1}{2}\left(\frac{5-\sigma_0}{2-\sigma_0}\right)\right]\left\{l_0+\frac{\lambda-1}{2}[\gamma^2\psi'(\gamma\sigma_0)+\psi'(N-2+\sigma_0)]\right\}^{\frac{1}{2}}}$$

$$\times(NA/980R^2)^{2-\sigma_0},\quad(11)$$

where σ_0 is obtained from

$$\gamma\psi(\gamma\sigma_0)+\psi(N-2+\sigma_0)+[2\sigma_0 l_0/(\lambda-1)]$$
$$-[(5-\lambda)/(\lambda-1)]l_0+\ln(980R^2/NAl_0^{\frac{1}{2}})=0,\quad(12)$$

with the aid of a table of ψ-functions, such as are given by Jahnke and Emde.[5] Here $\psi(z)$ is the logarithmic derivative of the Γ-function, and $\psi'(z)$ is its derivative, and the $\psi(N-2+\sigma_0)$ can usually be neglected in (12).

IV. RESULTS AND COMPARISON WITH EXPERIMENTS

There are now two ways in which the formulae above can be used, of which the more accurate is, of course, the more laborious. This is to solve Eq. (12) for σ_0 for every experimental situation, and then substitute into (11). One has to do this for each point on the curve that is required. This has been done, for example, for the altitude variation of a three counter coincidence arrangement, for counter areas of 100 cm² and 200 cm², respectively, and for two values of λ in each case. The results are shown in Figs. 1 and 2. In the former case the experimental points are those of Kraybill and Ovrebo and in the latter case, Hilberry. It is seen that the agreement leaves something to be desired, especially at high altitudes. The assumption of point geometry breaks down there, but in the wrong direction, as will be discussed later. At sea level the counting rate $\sim e^{-0.3l_0}$, so that one cannot draw any conclusions on the point mentioned in Section I.

If one does not vary the parameters over too large a range, one can obtain a good estimate without much trouble. We notice that the results

[5] E. Jahnke and F. Emde, *Funktionentafeln* (Leipzig, Germany, 1933). In this book $\psi(z)$ is what we call $\psi(1+z)$.

are, to a large extent, characterized by the value of σ_0. For example, if one differentiates Eq. (10) with respect to l_0, the result is multiplied by $(2-\sigma)(3-\lambda-\sigma)/(\lambda-1)$ plus some other terms that are not large if one isn't near the top of the atmosphere. This is a slowly varying factor and will not change the position of the saddle, so that one has, to good approximation

$$dC(l_0)/dl_0 = -[(2-\sigma_0)(\lambda+\sigma_0-3)/(\lambda-1)]C(l_0)$$

or

$$C(l_0) \propto \exp[-[(2-\sigma_0)(\lambda+\sigma_0-3)/(\lambda-1)]l_0] \quad (13)$$

over not too large a range. This fits the curves of Figs. 1 and 2 fairly well near sea level.

By a similar argument, one can find that the variation with A is given by $A^{2-\sigma_0}$. At $l_0=23.5$, around $A=100$ cm^2 and $\lambda=2.8$, one finds that $\sigma_0=0.54$, so that the variation with area should be $A^{1.46}$ in good agreement with the experimental results of Cocconi, Loverdo, and Tongiorgi. One finds similar agreement with their work at $l_0=18.5$, after their correction for effects of the roof. They have performed these analyses by graphical integration and find the same results, combining the effects of changes of A and N.

For the variation with N one finds, in the same way,

$$C(N_1)/C(N_2) = 2^{N_1-N_2}(N_2^{N_2}/N_1^{N_1})(N_1/N_2)^{2-\sigma_0} \times[\Gamma(N_1-2+\sigma_0)/\Gamma(N_2-2+\sigma_0)] \times[S(N_1,\sigma_0)/S(N_2,\sigma_0)], \quad (14)$$

or, in the special case when $N_1=3$, $N_2=4$,

$$C(3)/C(4) = [8/3(1+\sigma_0)](4/3)^{\sigma_0} \times[S(3,\sigma_0)/S(4,\sigma_0)], \quad (14')$$

which again seems to be in fair but not fully satisfactory agreement with the experiments of Cocconi, Loverdo, and Tongiorgi as shown in Table I if one chooses $\lambda=2.8$. Small variations of λ do not essentially change this.

TABLE I.

A	$[C(3)/C(4)]_{\text{theor.}}$, $\lambda=2.8$, $l_0=23.5$	$[C(3)/C(4)]_{\text{exp}}$
27 cm^2	1.66	2.23±0.18
54		2.45±0.25
129		1.65±0.05
258	1.63	1.48±0.06
516		1.70±0.04
774		1.63±0.03
1032	1.61	1.66±0.03

V. SOME LIMITS OF VALIDITY

We wish now to estimate the effective radii of the showers we are considering to find the limitations of the assumption that the counters are at one point. Since we will only be interested in distances of the order of a few meters, it will be sufficient to consider the radial distribution of shower electrons to be following a $1/r$ law. Thus $d\sim\beta nh^2/2\pi R^2\rho=\beta nh/2\pi Rr$. Since the densities we are counting are of order $1/A$, the important distances are $r\sim\beta nhA/2\pi R$, where $n\sim\frac{1}{10}e^{[(5-\lambda-2\sigma_0)/(\lambda-1)]l_0}$, so

$$r\sim(hA/20R)e^{[(5-\lambda-2\sigma_0)/(\lambda-1)]l_0}.$$

For areas of the order of 100 cm^2 and $\lambda\sim2.8$, the coefficient of l_0 in the exponent is close to 1 at high altitudes, so $r\sim(hA/20R)e^{l_0}$. Now for $A=200$ cm^2, $h\sim\frac{1}{2}$, $r\sim e^{l_0}/10^5$ meters, which becomes of order 1 meter at $l_0\sim11$. At sea level one finds $r\sim20$ meters. Thus, below $l_0\sim11$ one can expect our formulae to be valid, and at higher altitudes to be a sort of upper limit to the counting rate (limiting curve as counter separation approaches zero). It is therefore of particular interest that the experimental points in Fig. 2 lie above the theoretical curves.

PHYSICAL REVIEW VOLUME 73, NUMBER 11 JUNE 1, 1948

Transformation Theory Applied to a Radiation Field

José A. Balseiro
Córdoba Observatory, Córdoba, Argentina
(Received December 9, 1947)

Having given a photon distribution described by a field function in terms of an orthogonal system, the question arises as to what will be the photon distribution when the field is given in terms of another orthogonal system of functions. The problem is solved by means of transformation theory.

I. INTRODUCTION

THE complete description of a radiation field requires a photon distribution to be given over the states of an orthogonal system of vibrations, say $\mathbf{A}_r$, satisfying the field equations. If we let the radiation pass through an optical apparatus, it will be, in general, convenient to describe the final state of the radiation field in terms of a new orthogonal system, say $\mathbf{B}_s$, for which the photon distribution remains to be determined.

The underlying physical problem is of interest for the following reason: Up to now only two particular cases have been discussed, the cases of an extremely high number of photons involved (limit of classical electrodynamics) and the case of one single photon present (extreme quantum case). An understanding of the mechanism of quantum field theory requires, however, a more detailed study of the transition between the two mentioned limiting cases, in particular with respect to the fluctuation phenomena to be expected, which in time may become accessible to experiments.

The problem has, for the first time, been mentioned by W. Pauli,[1] and a way for its solution has been indicated by him. We shall show, in the following, that a more general solution of the problem can be given, referring explicitly to the eigenfunctions of the radiation field.

Let there be given the potentials of a quantized radiation field expressed by means of the functions of an orthogonal system:

$$\mathbf{A}=\sum_r a_r\mathbf{A}_r+\text{comp. conj.}, \tag{1.1}$$

where the a_r's are the amplitude operators.

$\mathbf{A}$ can be expressed in terms of another orthogonal system of functions

$$\mathbf{A}=\sum_s b_s\mathbf{B}_s+\text{comp. conj.} \tag{1.2}$$

which is related to the former by the unitary transformation:

$$\mathbf{A}_r=\sum_s c_{rs}\mathbf{B}_s. \tag{1.3}$$

We shall limit ourselves to those cases in which the numbers and frequencies of photons associated with the field are conserved (optical apparatus without absorption).

Let there be given a photon distribution over the states of the system $\mathbf{A}_r$. Let $\Gamma_{n_1n_2\cdots}$ be the eigenfunctions of the initial states $\mathbf{A}_r$. The problem of determining the photon distribution over the states of the system $\mathbf{A}_s$ consists in finding the transformed eigenfunction referred to in this system. This eigenfunction can be expressed by the linear combination

$$\sum_{m_1m_2\cdots} d_{m_1m_2\cdots}^{n_1n_2\cdots}\Delta_{m_1m_2\cdots} \quad (\textstyle\sum_i n_i=\sum_j m_j=N) \tag{1.4}$$

of the eigenfunctions $\Delta_{m_1m_2\cdots}$ which correspond to each one of the individual states of the system $\mathbf{B}_s$.

The amplitude operators are related with those of momentum and coordinate of a linear oscillator by:

$$\begin{aligned} a_r&=\frac{1}{(2h\nu_r)^{\frac{1}{2}}}(p_r-i\omega_r q_r),\\ a_r^*&=\frac{1}{(2h\nu_r)^{\frac{1}{2}}}(p_r+i\omega_r q_r),\\ &\qquad(\omega_r=2\pi\nu_r),\\ b_s&=\frac{1}{(2h\nu_s)^{\frac{1}{2}}}(P_s-i\omega_s Q_s),\\ b_s^*&=\frac{1}{(2h\nu_s)^{\frac{1}{2}}}(P_s+i\omega_s Q_s), \end{aligned} \tag{1.5}$$

where p_r, q_r and P_s, Q_s are canonical variables.

[1] W. Pauli, *Handbuch der Physik Quantentheorie* (Verlag Julius Springer, Berlin, 1933), p. 252.

The operators a_r and b_s are transformed according to

$$b_s=\sum_r c_{rs}a_r, \tag{1.6}$$

and this leads, according to (1.5), to a contact transformation given by:

$$Q_s=\frac{1}{2i}\sum_r\frac{1}{(\omega_s\omega_r)^{\frac{1}{2}}}[(c_{rs}^*-c_{rs})p_r+i\omega_r(c_{rs}^*+c_{rs})q_r], \tag{1.7}$$

$$P_s=\tfrac{1}{2}\sum_r(\omega_s/\omega_r)^{\frac{1}{2}}[(c_{rs}^*+c_{rs})p_r+i\omega_r(c_{rs}^*-c_{rs})q_r].$$

II. THE TRANSFORMATION FUNCTION

Given a transformation between the variables $p\equiv(p_1, p_2\cdots)$, $P\equiv(P_1, P_2\cdots)$, $q\equiv(q_1, q_2\cdots)$, $Q\equiv(Q_1, Q_2\cdots)$ a function $f(q)$ is transformed into a function $F(Q)$ by:

$$F(Q)=\int S(q, Q)f(q)dq, \quad dq=dq_1dq_2\cdots, \tag{2.1}$$

or, reciprocally,

$$f(q)=\int S^*(q, Q)F(Q)\rho(Q)dQ, \tag{2.1}$$

$S(q, Q)$ being the transformation function and $\rho(Q)$ the density function.

If $W(q, Q)$ is the generating function of the contact transformation, it can be shown that, in the present case, in which

$$p_{\mathrm{op},r}=-ih(\partial/\partial q_r), \quad P_{\mathrm{op},s}=-ih(\partial/\partial Q_s),$$

the transformation function is

$$S(q, Q)=e^{-(i/h)W(q,Q)}. \tag{2.2}$$

The generating function is determined by its properties:

$$p_r=(\partial W/\partial q_r), \quad P_s=-(\partial W/\partial Q_s). \tag{2.3}$$

In the particular case of the linear transformation (1.7) the function (2.2) is

$$S(x, X)=\exp(-i\sum_{i,j,r}[\tfrac{1}{2}\gamma_{ri}\beta_{ij}x_jx_r+\tfrac{1}{2}\beta_{jr}\gamma_{ri}X_iX_j-\gamma_{ri}x_rX_i]),$$

$$(x_i=(\omega_i/h)^{\frac{1}{2}}q_i, \quad X_j=(\omega_j/h)^{\frac{1}{2}}Q_j), \tag{2.4}$$

where the coefficients β_{ij}, γ_{ri} are related to those of (1.7) by

$$\beta_{sr}=\tfrac{1}{2}(c_{rs}^*+c_{rs}), \quad \sum_s\gamma_{r's}\alpha_{sr}=\delta_{rr'},$$

$$\alpha_{sr}=\frac{1}{2i}(c_{rs}^*-c_{rs}),$$

and they satisfy the relations

$$\sum_i\gamma_{ri}\beta_{ij}=\sum_i\gamma_{ji}\beta_{ir}, \quad \sum_r\beta_{jr}\gamma_{ri}=\sum_i\beta_{ir}\gamma_{rj}. \tag{2.5}$$

III. THE COORDINATE TRANSFORMATION

When the coefficients c_{rs} of (1.7) are real, the contact transformation degenerates and one is left with a coordinate transformation only. In such a case, the new eigenfunction of argument q can be given by an expansion in terms of the initial eigenfunctions of argument Q.

The eigenfunctions of the radiation field, considering a given configuration defined by numbers of photons n_1, $n_2\cdots n_r$ associated with each of the individual states, are

$$\Gamma_{n_1n_2\cdots n_r}=\exp\left(-\tfrac{1}{2}\sum_{i=1}^{r}x_i^2\right)H_{n_1}(x_1)\times H_{n_2}(x_2)\cdots H_{n_r}(x_r), \tag{3.1}$$

where $H_{n_i}(x_i)$ are normalized Hermitian polynomials.

In the present case, the exponential function remains invariant with respect to the orthogonal transformation between the coordinates, and therefore we have

$$H_{n_1}(x_1)H_{n_2}(x_2)\cdots H_{n_r}(x_r)$$

$$=\sum_{m_1m_2\cdots m_r}d_{m_1m_2\cdots m_r}^{n_1n_2\cdots n_r}H_{m_1}(X_1)H_{m_2}(X_2)\cdots H_{m_r}(X_r),$$

where the coefficients $d_{m_1m_2\cdots m_r}^{n_1n_2\cdots n_r}$ are simply defined by

$$d_{m_1m_2\cdots m_r}^{n_1n_2\cdots n_r}=\int\exp\left(-\sum_{i=1}^{r}X_i^2\right)\times H_{m_1}(X_1)H_{m_2}(X_2)\cdots H_{m_r}(X_r)H_{n_1}(x_1)H_{n_2}(x_2)\cdots\times H_{n_r}(x_r)dX_1dX_2\cdots dX_r.$$

In the case that only one photon is present in the original representation, x_r, according to (1.7) and $c_{rs}^*=c_{rs}$, the distribution of photons over the states defined by the variables X_s is given by

$$H_1(x_r)=\sum_s c_{rs}H_1(X_s),$$

with

$$H_1(x_i)=\left(\frac{2}{\pi^{\frac{1}{2}}}\right)^{\frac{1}{2}}x_i.$$

In this particular case, the coefficients $d_{m_1m_2\cdots}^{1,0,\cdots}$ are directly the c_{rs}.

The transformation referred to here represents a convenient means of studying the fluctuations of the propagation of the radiation through an optical system due to the photon concept and the transition to the classical theory in the case of a great number of photons present.[2]

IV. THE CANONICAL TRANSFORMATION

Let us now consider the general case of the transformation given by (1.7). According to (2.1) and (2.2) the eigenfunction $\Gamma_{n_1n_2\cdots n_r}$ of a given configuration of r states are transformed into the eigenfunction

$$\Delta_{n_1n_2\cdots n_r}(X_1X_2\cdots X_r)$$
$$=\int \exp\left(-\frac{i}{h}W(x_1x_2\cdots x_rX_1X_2\cdots X_r)\right)$$
$$\times\Gamma_{n_1n_2\cdots n_r}(x_1x_2\cdots x_r)dx_1dx_2\cdots dx_r, \quad (4.1)$$

where the transformation function is that of (2.3).

The function $\Gamma_{n_1n_2\cdots n_r}$ is a particular solution of the differential equation

$$\sum_{i=1}^{r}\nu_i\left(\frac{\partial^2}{\partial x_i^2}-x_i^2\right)\Gamma_{n_1n_2\cdots n_r}+\frac{2E}{h}\Gamma_{n_1n_2\cdots n_r}=0, \quad (4.2)$$

with the eigenvalue

$$E=h\sum_{i=1}^{r}(n_i+\tfrac{1}{2})\nu_i.$$

Having, on the other hand,

$$h\sum_{i=1}^{r}(a_i^+a_i+\tfrac{1}{2})\nu_i=\tfrac{1}{2}\sum_{i=1}^{r}(p_i^2+h\nu_ix_i^2),$$
$$h\sum_{j=1}^{r}(b_j^+b_j+\tfrac{1}{2})\nu_j=\tfrac{1}{2}\sum_{j=1}^{r}(P_j^2+h\nu_jX_j^2),$$

one obtains, considering that the total number of photons is conserved

$$\sum_{i=1}^{r}\left(-\nu_i\frac{\partial^2}{\partial x_i^2}+\nu_ix_i^2\right)\exp\left(-\frac{i}{h}W\right)$$
$$=\sum_{j=1}^{r}\left(-\nu_j\frac{\partial^2}{\partial X_j^2}+\nu_jX_j^2\right)\exp\left(-\frac{i}{h}W\right).$$

With the help of this expression and (4.1) one derives that the transformed function of $\Gamma_{n_1n_2\cdots n_r}$ satisfies the differential equation

$$\sum_{j=1}^{r}\nu_j\left(\frac{\partial^2}{\partial X_j^2}-X_j^2\right)\Delta_{n_1n_2\cdots n_r}+\frac{2E}{h}\Delta_{n_1n_2\cdots n_r}=0,$$

which admits, for a given

$$E=h\sum_{j=1}^{r}(m_j+\tfrac{1}{2})\nu_j,$$

the particular solution

$$\exp\left(-\tfrac{1}{2}\sum_{j=1}^{r}X_j^2\right)H_{m_1}(X_1)H_{m_2}(X_2)\cdots H_{m_r}(X_r).$$

The general expression for $\Delta_{n_1n_2\cdots n_r}$, therefore, is:

$$\Delta_{n_1n_2\cdots n_r}=\sum_{m_1m_2\cdots m_r}d_{m_1m_2\cdots m_r}^{n_1n_2\cdots n_r}\exp\left(-\tfrac{1}{2}\sum_{j=1}^{r}X_j^2\right)$$
$$\times H_{m_1}(X_1)H_{m_2}(X_2)\cdots H_{m_r}(X_r),$$

where $d_{m_1m_2\cdots m_r}^{n_1n_2\cdots n_r}$ are coefficients which can be determined by some initial conditions, or by using the expression

$$d_{m_1m_2\cdots m_r}^{n_1n_2\cdots n_r}=\int \exp\left(-\frac{i}{h}W\right)\Gamma_{n_1n_2\cdots n_r}$$
$$\times\exp\left(-\frac{1}{2}\sum_{j=1}^{r}X_j^2\right)H_{m_1}(X_1)H_{m_2}(X_2)\cdots$$
$$\times H_{m_r}(X_r)dxdX.$$

One sees immediately that these coefficients are uniquely determined by those of the transformation (1.7). The modulus

$$\left|d_{m_1m_2\cdots m_r}^{n_1n_2\cdots n_r}\right|^2$$

must be understood to be the probability of the configuration defined by $m_1, m_2\cdots m_r$. When the functions are normalized we must evidently have

$$\sum_{m_1m_2\cdots m_r}\left|d_{m_1m_2\cdots m_r}^{n_1n_2\cdots n_r}\right|^2=1.$$

I am indebted to Professor G. Beck for having suggested this problem and for many helpful discussions and advice.

[2] An application has been made by J. Balseiro and D. Canals Frau, Ciencia e Investigación 2, 444 (1946).

The Application of Onsager's Reciprocal Relations to Thermoelectric, Thermomagnetic, and Galvanomagnetic Effects*

HERBERT B. CALLEN
Laboratory for Insulation Research, Massachusetts Institute of Technology, Cambridge, Massachusetts
(Received January 2, 1948)

Analysis of the thermoelectric, thermomagnetic, and galvanomagnetic effects by means of the reciprocal relations of Onsager leads to a simple and intuitive interpretation of the thermoelectric effects, provides a valid derivation of the Kelvin relations, and answers the long standing question as to the existence of relations among the effects in a magnetic field. It is shown that there exist two independent relations among the eight commonly defined coefficients in a magnetic field—one of these relations having been previously given by Bridgman. The nature of the second relation is discussed. Also, certain general observations on the applicability of the Onsager relations to steady-state processes are discussed.

INTRODUCTION

IN 1854 Lord Kelvin[1] proposed a "quasi-thermodynamic" method of analysis of the thermoelectric effects, leading to the well-known Kelvin relations. Although Kelvin himself carefully pointed out that his method was not completely justifiable, experiment confirmed the validity of the results obtained. The method was subsequently applied to the theory of electrolytic cells by Helmholtz[2] and to the Soret effect by Eastman,[3] and was extended to the galvano- and thermomagnetic effects by Bridgman,[4] in each case yielding important and correct relations. In 1931 Onsager[5] revived the problem and proved a general and powerful set of reciprocal relations treating the symmetry in the mutual interference of two or more irreversible processes occurring simultaneously in a system. On the basis of these relations Onsager has specifically discussed diffusion processes[6] and the flow of heat in anisotropic crystals,[6] and has pointed out that the whole class of results obtained by the quasi-thermodynamic method of Kelvin follows from the reciprocal relations. However, a treatment on this basis of the very important thermoelectric, thermomagnetic, and galvanomagnetic effects has not been given in the literature.**,[7–10] Such a treatment leads to a simple and intuitive interpretation of the thermoelectric effects in terms of an entropy flow per particle, provides a valid derivation of the Kelvin relations, and settles the long standing question as to the existence of relations among the effects in a magnetic field. It is shown that there are two independent relations among the eight commonly defined coefficients in a magnetic field—one of these relations having been previously given by Bridgman.

* This work was sponsored jointly by the Office of Naval Research and the Army Signal Corps, under ONR Contract N5ori-78, T.O.1, and is abstracted from part of a thesis entitled *On the Theory of Irreversible Processes*, submitted to the Department of Physics of the Massachusetts Institute of Technology. Another portion of the work is being extended.

I wish to take this opportunity to thank Professor L. Tisza, the director of the thesis, for extensive discussions and for many helpful suggestions.

[1] Lord Kelvin (Sir W. Thomson) *Collected Papers I* (University Press, Cambridge, 1882), pp. 232–291.
[2] H. v. Helmholtz, Wiss. Abh. **1**, 840 (1877).
[3] E. D. Eastman, J. Am. Chem. Soc. **48**, 1482 (1926); **50**, 283 (1928); **50**, 292 (1928).
[4] P. W. Bridgman, *Thermodynamics of Electrical Phenomena in Metals* (The Macmillan Company, New York, 1934).
[5] L. Onsager, Phys. Rev. **37**, 405 (1931); **38**, 2265 (1931).
[6] L. Onsager, Ann. N. Y. Acad. Sci. **XLVI**, 241 (1945).

** However, Meixner (See reference 7.) has given both a detailed kinetic treatment of these effects, and some discussion of the results in the light of the Onsager relations. The effects have also been treated by the free-electron theory in a classic paper by Sommerfeld and Frank, (See reference 8.) and have recently been treated by Gurevich (See reference 9.) on the basis of an interaction between the electrons and phonons in the lattice. A thesis by DeGroot (See reference 10.) on the Soret effect, has very recently been brought to the author's attention. A part of the formalism of the present paper involving heat and entropy current densities appears also in DeGroot's work.

[7] J. Meixner, Ann. d. Physik (5) **35**, 701 (1939); **36**, 105 (1939); **39**, 333 (1941); **40**, 165 (1941); **41**, 409 (1942); Zeits. f. physik. Chemie **B53**, 235 (1943).
[8] A. Sommerfeld and N. H. Frank, Rev. Mod. Phys. **3**, 1 (1931).
[9] L. Gurevich, J. Phys. U.S.S.R. **9**, 477 (1945); **10**, 67, 174 (1946).
[10] S. R. DeGroot, Thesis, Eindhoven 1945; *L'Effet Soret* (N. V. Noord-Hollandsche Uitgevers Moatschappij, Amsterdam, 1945).

I. ONSAGER'S RECIPROCAL RELATIONS

The reciprocal relations of Onsager express a certain symmetry in the mutual interference of two or more irreversible processes occurring simultaneously in a system. They follow from thermodynamic reasoning, plus the additional fact that, except in the presence of a magnetic or Coriolis force field, the laws of dynamics are symmetric with respect to future and past. The content of the relations may be briefly stated as follows:

Consider a set of irreversible processes, expressible as the rates of change of a set of measurable parameters, α_i, of the system. We shall assume these parameters to be even functions of the momenta of the particles composing the system.***,[11] Assume also that the macroscopic laws which govern the processes (such as Ohm's law of electric conduction, Fick's law of diffusion, etc.) can be expressed in the linear forms

$$\delta\alpha_i/\delta t=\sum_j L_{ij}\gamma_j, \tag{1}$$

where

$$\gamma_j\equiv\delta S/\delta\alpha_j. \tag{2}$$

In equilibrium the entropy S is a maximum and the γ_j are therefore zero. Thus the γ_j are measures of the deviation from the equilibrium state. The L's, or "kinetic coefficients," are functions of the state of the system, depending upon such variables as composition, temperature, and the values of applied magnetic or Coriolis force fields. If the L_{ij} were to be zero for all $i\neq j$, each "current" $\delta\alpha_j/\delta t$ would depend only on its own driving "force" γ_j, and the various processes could be considered as independent. Thus the quantity L_{ij} is a measure of the interference of the jth process on the course of the ith. Onsager's theorem now states that

$$L_{ij}(H)=L_{ji}(-H), \tag{3}$$

where H is the applied magnetic (or Coriolis) field. If no magnetic field is applied, Eq. (3) degenerates into the simple symmetry relation

$$L_{ij}=L_{ji}. \tag{4}$$

The problem involved in the application of Onsager's relations to any particular set of processes is, of course, the identification of the proper "forces" γ_j. To do this directly from the defining equations (Eq. (2)) requires the knowledge of the caloric equation of state (i.e., of the entropy as a function of the variables α_j). It is, however, possible to avoid this by considering the rate of production of entropy rather than the entropy itself. We have, by a first-order Taylor expansion,

$$\delta S=\sum_j(\delta S/\delta\alpha_j)\delta\alpha_j=\sum_j\gamma_j\delta\alpha_j, \tag{5}$$

whence the rate of production of entropy associated with the irreversible process is

$$\delta S/\delta t=\sum_j\gamma_j(\delta\alpha_j/\delta t). \tag{6}$$

This equation provides a more convenient method for identifying the variables γ_j than does Eq. (2).

II. APPLICATION TO THERMOELECTRIC PROCESSES

By utilizing a procedure which might be called the "method of local equilibrium" we may apply the Onsager relations to steady-state processes, such as the thermoelectric processes.

The thermoelectric effects may be viewed as the result of the mutual interference of heat flow and electric current flow in a system, and we must now define appropriate current density vectors. The number of particles, the total internal energy, and the entropy of a system are definable thermodynamic variables. We define a particle current density $\mathbf{J}$, an energy current density $\mathbf{W}$, and an entropy current density $\mathbf{S}$, so that the divergence of each of these current densities is the rate of change per unit volume of the corresponding thermodynamic variable, and so that the current densities vanish in a vacuum.† In accordance with the familiar thermodynamic definition of heat, we are led to define a heat current density by

$$\mathbf{Q}\equiv T\mathbf{S}. \tag{7}$$

A steady-state process is characterized by the

*** Casimir (See reference 11.) has shown that this is not a necessary restriction, and Onsager's theorem can be formulated in other cases. However, most common thermodynamic parameters (such as energy, volume, or number of particles) remain invariant if the directions of motion of all the particles are reversed, and for simplicity of statement we confine ourselves to this case.

[11] H. B. G. Casimir, Rev. Mod. Phys. 17, 343 (1945).

† The condition that the currents vanish in a vacuum is necessary in order to remove the arbitrariness inherent in the definition in terms of a divergence. For a discussion of this matter see Casimir (reference 11).

conditions

$$\nabla\cdot\mathbf{W}=0, \tag{8}$$

$$\nabla\cdot\mathbf{J}=0, \tag{9}$$

and

$$\nabla\cdot\mathbf{S}=\dot{S}, \tag{10}$$

where $\dot{S}$ is the rate of production of entropy per unit volume.

We may now employ the method of local equilibrium to evaluate $\nabla\cdot\mathbf{S}$. Let the actual system be approximated by a collection of small volume elements, each of which is in local equilibrium, and each of which has a distinct value of the temperature T and of the electrochemical potential μ. We shall discuss the validity of this approximation in Section III. Then, since each element is in equilibrium, we may apply to it the usual thermodynamic relations connecting the entropy, internal energy, and number of particles. Assuming no thermal expansion or other mechanical effects in the system (i.e., neglecting terms such as $P\delta V$), we may therefore write for the nth element

$$T_n\delta S_n=\delta U_n-\mu_n\delta N_n, \tag{11}$$

where S is the entropy, U is the total internal energy, and N is the number of particles. In accordance with our definitions of the current density vectors we thus obtain

$$T\mathbf{S}=\mathbf{W}-\mu\mathbf{J}, \tag{12}$$

or

$$\mathbf{Q}=\mathbf{W}-\mu\mathbf{J}. \tag{13}$$

Equation (13) identifies the heat current as the difference between the total energy current and the electrochemical potential energy current, and this agrees with our intuitive notion of heat as a kinetic energy current. Taking the divergence of Eq. (13) and recalling the conditions of a steady state (Eqs. (8) and (9)), we find

$$\nabla\cdot\mathbf{Q}=-\nabla\mu\cdot\mathbf{J}, \tag{14}$$

which states that the rate of increase in heat current is equal to the rate of decrease in the potential energy current.

The rate of production of entropy, $\dot{S}$, follows from Eq. (12) and the conditions for a steady state, Eqs. (8), (9), and (10):

$$\dot{S}=\nabla\cdot\mathbf{S}=\nabla\frac{1}{T}\cdot\mathbf{W}-\nabla\frac{\mu}{T}\cdot\mathbf{J} \tag{15}$$

or, using Eq. (13) to eliminate $\mathbf{W}$ in favor of $\mathbf{Q}$,

$$\dot{S}=\nabla\frac{1}{T}\cdot\mathbf{Q}-\frac{1}{T}\nabla\mu\cdot\mathbf{J}. \tag{16}$$

The interpretation of this equation is best brought out by using Eq. (14) to write

$$\dot{S}=\nabla\frac{1}{T}\cdot\mathbf{Q}+\frac{1}{T}\nabla\cdot\mathbf{Q}, \tag{17}$$

which states that the production of entropy is due to two causes: the first term is the production of entropy due to the flow of heat from high to low temperature, and the second term is the increase in entropy due to the degradation of electrochemical potential energy into heat.

We are now able to identify the proper "forces" for the application of Onsager's reciprocal relations. By comparing Eqs. (15) or (16) with Eq. (6), we find that if we take $-\mathbf{J}$ and $\mathbf{W}$ as currents, the proper forces are $\nabla(\mu/T)$ and $\nabla(1/T)$, whereas if we take $-\mathbf{J}$ and $\mathbf{Q}$ as currents, the proper forces are $(1/T)\nabla\mu$ and $\nabla(1/T)$. Accordingly, we may write the macroscopic laws governing the processes in the form

$$\begin{aligned}-\mathbf{J}&=L_{11}\frac{1}{T}\nabla\mu+L_{12}\nabla\frac{1}{T},\\ \mathbf{Q}&=L_{21}\frac{1}{T}\nabla\mu+L_{22}\nabla\frac{1}{T},\end{aligned} \tag{18}$$

and in the absence of an applied magnetic field, Onsager's theorem states that

$$L_{12}=L_{21}. \tag{19}$$

It is perhaps well to comment here on the nature of the electrochemical potential μ. We may consider μ to be composed of two parts, a chemical portion μ_c and an electrical portion μ_e.

$$\mu=\mu_c+\mu_e. \tag{20}$$

If the charge on a particle is e, then μ_e is simply $e\varphi$, where φ is the ordinary electrostatic potential. The chemical potential μ_c is a function of the temperature and of the particle concentration. In an electrical conductor μ_c plays a minor role, and we fix our attention primarily on the e.m.f. $(1/e)\nabla\mu_e$. However, if we were to consider the diffusion of uncharged particles, $\nabla\mu_c$ would play the part of the driving force.

III. JUSTIFICATION OF THE APPLICATION TO STEADY-STATE PROCESSES

The derivation of the Onsager relations strictly refers only to a specific type of transient irreversible process, and the application of the relations to steady-state processes involves an approximation, the nature and validity of which we shall now examine.

The type of transient process to which the reciprocal relations primarily refer is that which occurs immediately following the lifting of a set of restraints, with respect to which the system is originally in equilibrium. The restriction to this type of process appears implicitly in the derivation given by Onsager in the nature of the averages taken over the statistical ensemble. However, many processes of interest are not of this transient nature, but occur in a steady state.

In Section II we have considered a method of application of the Onsager relations to steady-state processes, and we have seen that the approximation involved lies in the assumption that, for the purpose of calculating the entropy current, the system can be considered as the limiting case of many small sections, each in local equilibrium. In the language of statistical mechanics this is equivalent to the assumption that for the calculation of the entropy current the distribution function may be taken to be in the equilibrium form but with T and μ as functions of position. Actually, it is well known that the distribution function can be expressed as a function of this form plus a small deviation term.[8] It is, of course, the smallness of this deviation term which is responsible for the excellence of the approximation made.

It will be recognized that the calculation of $\mathbf{S}$ on the basis of the local-equilibrium distribution function is very similar to the procedure usually adopted in the application of Boltzmann's kinetic equation. This equation may be written as an equality between certain "flow terms" and certain "collision terms." In the calculation of the flow terms one may use the local-equilibrium value of the distribution function, but since the collision terms vanish in this approximation, it is necessary to include the deviation term in their calculation. Similarly, in our case, $\mathbf{S}$ may be calculated on the basis of the local-equilibrium value of the distribution function, although a direct statistical calculation of $\dot{S}$, which would vanish in this approximation, would require the inclusion of the deviation term.

Finally, we may mention that the kinetic laws governing the processes are themselves linear only in a similar approximation,[12] so that the reciprocal relations for steady-state processes are as valid as Ohm's law, Fick's law, etc.

IV. THERMOELECTRIC EFFECTS

We consider now a system in which a particle (or electric) current and a heat current flow parallel to the x axis, there being no applied magnetic field. Then, by Eqs. (18) and (19),

$$\begin{aligned} -\mathbf{J} &= L_{11}\frac{1}{T}\nabla\mu + L_{12}\nabla\frac{1}{T}, \\ \mathbf{Q} &= L_{12}\frac{1}{T}\nabla\mu + L_{22}\nabla\frac{1}{T}. \end{aligned} \tag{21}$$

The kinetic coefficients (the L's) are properties of the medium considered, and are closely related to such familiar properties as the electric and heat conductivities. We shall see that the knowledge of the set of quantities L_{11}, L_{12}, and L_{22} is equivalent to the knowledge of the electric and heat conductivities and of the thermoelectric power of the medium.

The heat conductivity is defined as the heat current density per unit temperature gradient, for zero particle current.

$$\kappa \equiv -\mathbf{Q}/\nabla T \quad \text{for} \quad \mathbf{J}=0, \tag{22}$$

whence we find from the kinetic equations,

$$\kappa = \frac{1}{T^2 L_{11}}(L_{11}L_{22} - L_{12}^2) = \frac{D}{T^2 L_{11}}, \tag{23}$$

where we introduce the notation

$$D \equiv L_{11}L_{22} - L_{12}^2. \tag{24}$$

Similarly, the electric conductivity is defined as the electric current density ($e\mathbf{J}$) per unit potential gradient $[(1/e)\nabla\mu]$ in an isothermal system. It is easily seen that $(1/e)\nabla\mu$ is actually the e.m.f., for in a homogeneous isothermal system $\nabla\mu_e = 0$ and $\nabla\mu = \nabla\mu_e$. Thus

$$\sigma \equiv -e\mathbf{J}\Big/\frac{1}{e}\nabla\mu \quad \text{for} \quad \nabla T = 0, \tag{25}$$

[12] H. B. Callen, Thesis, M.I.T., 1947.

whence

$$\sigma = e^2 L_{11}/T. \tag{26}$$

In preparation for our application of the kinetic equations to practical experiments, we now note that the variables which can most easily be controlled independently by the experimenter are the particle (or electric) current density and the temperature gradient. We therefore find it convenient to express $\mathbf{S}$ in terms of these variables. We thus obtain

$$\mathbf{S} = -\frac{L_{12}}{TL_{11}}\mathbf{J} + \frac{D}{TL_{11}}\nabla\frac{1}{T}. \tag{27}$$

According to this equation a current flowing in a conductor of a given temperature distribution carries with it an entropy per particle of $-L_{12}/TL_{11}$. This entropy flow is, of course, in addition to the entropy flow $(D/TL_{11})\nabla(1/T)$, which is independent of the particle current. The entropy flow per particle $-L_{12}/TL_{11}$ will prove to be such a useful quantity in the description of the thermoelectric effects that we introduce for it the special symbol S_J.

$$S_J \equiv -\frac{L_{12}}{TL_{11}}. \tag{28}$$

We shall see that $(1/e)S_J$ is equal to the thermoelectric power of the medium, so that, like κ and σ, it has direct physical significance as a property of the substance. The quantities κ, σ, and S_J have been expressed in terms of the kinetic coefficients, and conversely we have

$$\begin{aligned} L_{11} &= \frac{T}{e^2}\sigma, \\ L_{12} &= -\frac{T^2}{e^2}\sigma S_J, \\ L_{22} &= \frac{T^3}{e^2}\sigma S_J^2 + T^2\kappa. \end{aligned} \tag{29}$$

We now consider the various thermoelectric effects in turn.

a—The Peltier Effect

The Peltier effect refers to the evolution of heat accompanying the flow of an electric current across an isothermal junction of two materials. Consider an isothermal junction of two conductors A and B, and consider a current $\mathbf{J}$ to be flowing. Then the total energy flow will be discontinuous across the junction, and the energy difference appears as "Peltier heat" at the junction. (See Fig. 1.) We have $\mathbf{W} = \mathbf{Q} + \mu\mathbf{J}$, and since both μ and $\mathbf{J}$ are continuous across the junction it follows that the discontinuity in $\mathbf{W}$ is equal to the discontinuity in $\mathbf{Q}$.

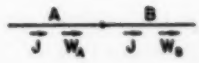

FIG. 1.

$$\mathbf{W}_A - \mathbf{W}_B = \mathbf{Q}_A - \mathbf{Q}_B.$$

Because of the isothermal condition the kinetic equations give, in either conductor,

$$\mathbf{Q} = TS_J \cdot \mathbf{J}, \tag{30}$$

whence

$$\mathbf{Q}_B - \mathbf{Q}_A = T \cdot (S_J^B - S_J^A) \cdot \mathbf{J}. \tag{31}$$

The Peltier coefficient Π_{AB} is defined as the heat which must be supplied to the junction when unit electric current passes from conductor A to conductor B. Thus,

$$\Pi_{AB} \equiv \frac{\mathbf{Q}_B - \mathbf{Q}_A}{e\mathbf{J}} = \frac{T}{e}(S_J^B - S_J^A). \tag{32}$$

The Peltier coefficient has the dimensions of an electromotive force, and is sometimes referred to as the Peltier e.m.f. This terminology must, however, be viewed as a mere figure of speech, for the potential μ is actually continuous at the junction.

We may regard the Peltier heat as supplying the discontinuity in the entropy flow per particle at the junction. For by Eq. (31)

$$\mathbf{S}_B - \mathbf{S}_A = (S_J^B - S_J^A) \cdot \mathbf{J} \tag{33}$$

so that a "Peltier entropy," is equal to $(1/T)$. Peltier heat must be supplied at the junction.

b—The Thomson Effect

The Thomson effect refers to the evolution of heat as an electric current traverses a temperature gradient in a material. Because it is the only one of the three thermoelectric effects which deals with a single material, it is sometimes called the "homogeneous thermoelectric effect."

Consider a conductor carrying a heat current, but no electric current. A temperature distribu-

tion governed by the temperature dependence of the kinetic coefficients (the L's) will be set up. Let the conductor now be placed in contact at each point with a heat reservoir of the same temperature as that point, so that there is no heat interchange between conductor and reservoirs. Now, let an electric current pass through the conductor. Then a heat interchange will take place between conductor and reservoirs, this heat consisting of two parts—the Joule heat and the Thomson heat.

As the electric current passes along the conductor any change in total energy flow must be supplied by an energy interchange with the reservoirs. Thus, we must compute $\nabla\cdot\mathbf{W}$.

$$\nabla\cdot\mathbf{W}=\nabla\cdot(\mathbf{Q}+\mu\mathbf{J})=\nabla\cdot\mathbf{Q}+\nabla\mu\cdot\mathbf{J}, \tag{34}$$

which may be expressed in terms of $\mathbf{J}$ and $\nabla(1/T)$ by using Eqs. (7), (27), and (21):

$$\nabla\cdot\mathbf{W}=-\nabla\left(\frac{L_{12}}{L_{11}}\right)\cdot\mathbf{J}-\nabla\cdot\left(\frac{D}{L_{11}}\nabla\frac{1}{T}\right)-\frac{T}{L_{11}}J^2-\frac{TL_{12}}{L_{11}}\mathbf{J}\cdot\nabla\frac{1}{T}. \tag{35}$$

However, the temperature distribution is that which is determined by the steady state with no electric current. Since $\nabla\cdot\mathbf{W}=0$ in the steady state, Eq. (35) gives, with $\mathbf{J}=0$,

$$\nabla\cdot\mathbf{W}=-\nabla\cdot\left(\frac{D}{L_{11}}\nabla\frac{1}{T}\right)=0. \tag{36}$$

The term $\nabla\cdot[(D/L_{11})\nabla(1/T)]$ must therefore be zero even when $\mathbf{J}\neq 0$, for it depends on the temperature distribution only (it is apparent that the kinetic coefficients depend only on T and not on μ since the zero of μ is arbitrary, whereas the L's are uniquely defined). We thus obtain

$$\nabla\cdot\mathbf{W}=-\nabla\left(\frac{L_{12}}{L_{11}}\right)\cdot\mathbf{J}-\frac{T}{L_{11}}J^2-\frac{TL_{12}}{L_{11}}\mathbf{J}\cdot\nabla\frac{1}{T}, \tag{37}$$

and, writing

$$\nabla\left(\frac{L_{12}}{L_{11}}\right)=\frac{d}{dT}\left(\frac{L_{12}}{L_{11}}\right)\cdot\nabla T,$$

we have

$$\nabla\cdot\mathbf{W}=-\frac{T}{L_{11}}J^2+T\frac{dS_J}{dT}\nabla T\cdot\mathbf{J}. \tag{38}$$

Since by Eq. (26) the electric conductivity is $\sigma=e^2(L_{11}/T)$ we recognize the first term above as the Joule heat. The second term therefore gives the Thomson heat. The Thomson coefficient τ is defined as the ratio of the Thomson heat absorbed to the product $\nabla T\cdot e\mathbf{J}$

$$\tau\equiv\frac{\text{Thomson heat}}{\nabla T\cdot e\mathbf{J}}=\frac{T}{e}\frac{dS_J}{dT}. \tag{39}$$

It will be noted that the form of this equation suggests the analogy of τ to a specific heat $[=T(dS/dT)]$, and, in fact, Thomson referred to τ as the "specific heat of electricity."

The details of the entropy transfer between conductor and reservoirs gives an interesting insight into the Thomson effect. We have

$$\mathbf{S}=S_J\cdot\mathbf{J}+\frac{D}{TL_{11}}\nabla\frac{1}{T}, \tag{27}$$

whence, by Eq. (36), we obtain

$$\nabla\cdot\mathbf{S}=\nabla S_J\cdot\mathbf{J}+\frac{D}{L_{11}}\left(\nabla\frac{1}{T}\right)^2. \tag{40}$$

However, the rate of production of entropy is

$$\dot{S}=-\frac{1}{T}\nabla\mu\cdot\mathbf{J}+\nabla\frac{1}{T}\cdot\mathbf{Q},$$

or, in terms of $\mathbf{J}$ and $\nabla(1/T)$,

$$\dot{S}=\frac{1}{L_{11}}J^2+\frac{D}{L_{11}}\left(\nabla\frac{1}{T}\right)^2. \tag{41}$$

Thus, the reservoirs at each point provide an input of entropy given by

$$\nabla\cdot\mathbf{S}-\dot{S}=-\frac{1}{L_{11}}J^2+\nabla S_J\cdot\mathbf{J}, \tag{42}$$

which represents a Joule and a Thomson contribution. The Joule contribution extracts the entropy produced by the flow of current (Eq. (41)), and the Thomson contribution injects entropy to supply the flow of entropy per particle S_J (Eq. (40)).

c—The Seebeck Effect

The Seebeck effect refers to the production of an electromotive force in a thermocouple, under conditions of zero electric current.

Consider a thermocouple with junctions at temperatures T_1 and T_2 ($T_2>T_1$). Let a voltmeter be inserted in the thermocouple at a point at which the temperature is T'. This voltmeter is to be such that it allows no passage of electricity, but offers no resistance to the flow of heat. We designate the two materials composing the thermocouple by A and B. (See Fig. 2.) With $\mathbf{J}=0$ we obtain from the kinetic equations, for either conductor,

$$\nabla\mu = -S_J\nabla T. \tag{43}$$

Thus,

$$\mu_2-\mu_1 = -\int_{T_1}^{T_2} S_J^A dT, \tag{44}$$

$$\mu_2-\mu_r' = -\int_{T'}^{T_2} S_J^B dT, \tag{45}$$

$$\mu_l'-\mu_1 = -\int_{T_1}^{T'} S_J^B dT. \tag{46}$$

Eliminating μ_1 and μ_2 from these equations,

$$\mu_r'-\mu_l' = \int_{T_1}^{T_2}(S_J^B-S_J^A)dT. \tag{47}$$

But because there is no temperature difference across the voltmeter, the voltage is simply

$$V=\frac{1}{e}(\mu_r'-\mu_l'),$$

or

$$V=\frac{1}{e}\int_{T_1}^{T_2}(S_J^B-S_J^A)dT. \tag{48}$$

The thermoelectric power of the thermocouple, ϵ_{AB}, is defined as the change in voltage per unit change in temperature difference. The sign of ϵ_{AB} is chosen as positive if the voltage increment is such as to drive the current from A to B at the hot junction. Then

$$\epsilon_{AB}\equiv\frac{\partial V}{\partial T_2}=\frac{1}{e}[S_J^B(T_2)-S_J^A(T_2)]. \tag{49}$$

The quantities $(1/e)S_J^A$ and $(1/e)S_J^B$ are referred to as the thermoelectric powers of materials A and B, so that the entropy flow per particle has a direct physical significance as a measurable property of the material.

d—The Kelvin Relations

The Kelvin relations connect the three thermoelectric coefficients. Recalling our values for these coefficients:

Peltier coefficient: $$\Pi_{AB}=\frac{T}{e}(S_J^B-S_J^A), \tag{32}$$

Thomson coefficient: $$\tau=\frac{T}{e}\frac{dS_J}{dT}, \tag{39}$$

Thermoelectric power: $$\epsilon_{AB}=\frac{1}{e}(S_J^B-S_J^A), \tag{49}$$

we immediately obtain the Kelvin relations

$$\Pi_{AB}=T\epsilon_{AB}, \tag{50}$$

$$\tau_B-\tau_A=T\frac{d\epsilon_{AB}}{dT}. \tag{51}$$

V. THERMOMAGNETIC AND GALVANOMAGNETIC EFFECTS

If an external magnetic field is impressed upon a system in which a heat current and electric current simultaneously flow, several new effects appear. These effects have been discussed by Bridgman[4] and by Sommerfeld and Frank,[5] and there has been some speculation as to the existence of relations among the various effects. The application of Onsager's method results in the expression of all effects in terms of a number of independent kinetic coefficients, whence all relations among the effects may be obtained by algebraic elimination. We thus find that among the eight coefficients discussed by Sommerfeld and Frank there are two independent relations, one of which has been previously obtained by Bridgman.

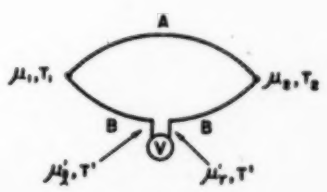

FIG. 2.

If we consider an isotropic system in which a magnetic field is applied parallel to the Z axis and in which the currents and gradients lie in the X-Y plane, we have again the equations

$$\mathbf{S}=\frac{1}{T}\mathbf{W}-\frac{\mu}{T}\mathbf{J}, \tag{52}$$

$$\mathbf{Q}\equiv T\mathbf{S}=\mathbf{W}-\mu\mathbf{J}, \tag{53}$$

$$\dot{S}=\nabla\frac{1}{T}\cdot\mathbf{Q}-\frac{1}{T}\nabla\mu\cdot\mathbf{J}, \tag{54}$$

and Eq. (54) may be written in component form:

$$\dot{S}=\nabla_x\frac{1}{T}\cdot Q_x+\nabla_y\frac{1}{T}\cdot Q_y -\frac{1}{T}\nabla_x\mu\cdot J_x-\frac{1}{T}\nabla_y\mu\cdot J_y. \tag{55}$$

This equation allows us to identify the four proper currents and the four proper forces for the application of Onsager's relations. In terms of these variables the kinetic equations become

$$\begin{aligned}
-J_x&=L_{11}\frac{1}{T}\nabla_x\mu+L_{12}\nabla_x\frac{1}{T}+L_{13}\frac{1}{T}\nabla_y\mu+L_{14}\nabla_y\frac{1}{T},\\
Q_x&=L_{21}\frac{1}{T}\nabla_x\mu+L_{22}\nabla_x\frac{1}{T}+L_{23}\frac{1}{T}\nabla_y\mu+L_{24}\nabla_y\frac{1}{T},\\
-J_y&=L_{31}\frac{1}{T}\nabla_x\mu+L_{32}\nabla_x\frac{1}{T}+L_{33}\frac{1}{T}\nabla_y\mu+L_{34}\nabla_y\frac{1}{T},\\
Q_y&=L_{41}\frac{1}{T}\nabla_x\mu+L_{42}\nabla_x\frac{1}{T}+L_{43}\frac{1}{T}\nabla_y\mu+L_{44}\nabla_y\frac{1}{T}.
\end{aligned} \tag{56}$$

Because of the isotropy†† of the system, however, simple symmetry considerations require certain relations among the kinetic coefficients, and we clearly have

$$\begin{aligned}
-J_x&=L_{11}\frac{1}{T}\nabla_x\mu+L_{12}\nabla_x\frac{1}{T}+L_{13}\frac{1}{T}\nabla_y\mu+L_{14}\nabla_y\frac{1}{T},\\
Q_x&=L_{21}\frac{1}{T}\nabla_x\mu+L_{22}\nabla_x\frac{1}{T}+L_{23}\frac{1}{T}\nabla_y\mu+L_{24}\nabla_y\frac{1}{T},\\
-J_y&=-L_{13}\frac{1}{T}\nabla_x\mu-L_{14}\nabla_x\frac{1}{T}+L_{11}\frac{1}{T}\nabla_y\mu+L_{12}\nabla_y\frac{1}{T},\\
Q_y&=-L_{23}\frac{1}{T}\nabla_x\mu-L_{24}\nabla_x\frac{1}{T}+L_{21}\frac{1}{T}\nabla_y\mu+L_{22}\nabla_y\frac{1}{T},
\end{aligned} \tag{57}$$

where, furthermore, L_{11}, L_{12}, L_{21}, and L_{22} are even functions of the magnetic field and where L_{13}, L_{14}, L_{23}, and L_{24} are odd functions of the magnetic field.

We may now impose the Onsager relation

$$L_{ij}(H)=L_{ji}(-H), \tag{58}$$

and thus obtain

$$\begin{aligned}
-J_x&=L_{11}\frac{1}{T}\nabla_x\mu+L_{12}\nabla_x\frac{1}{T}+L_{13}\frac{1}{T}\nabla_y\mu+L_{14}\nabla_y\frac{1}{T},\\
Q_x&=L_{12}\frac{1}{T}\nabla_x\mu+L_{22}\nabla_x\frac{1}{T}+L_{14}\frac{1}{T}\nabla_y\mu+L_{24}\nabla_y\frac{1}{T},\\
-J_y&=-L_{13}\frac{1}{T}\nabla_x\mu-L_{14}\nabla_x\frac{1}{T}+L_{11}\frac{1}{T}\nabla_y\mu+L_{12}\nabla_y\frac{1}{T},\\
Q_y&=-L_{14}\frac{1}{T}\nabla_x\mu-L_{24}\nabla_x\frac{1}{T}+L_{12}\frac{1}{T}\nabla_y\mu+L_{22}\nabla_y\frac{1}{T}.
\end{aligned} \tag{59}$$

Thus there are just six independent kinetic coefficients. The coefficients L_{11}, L_{12}, and L_{22} are even functions of the magnetic field, while the coefficients L_{13}, L_{14}, and L_{24} are odd functions of the magnetic field.

We may now consider in turn the various coefficients defined by Sommerfeld and Frank. The definitions of the various effects are self-explanatory, and we give the appropriate coefficients in terms of the kinetic coefficients, as obtained by application of the kinetic Eqs. (59).

†† In order that our equations shall hold it is not necessary that the system be strictly isotropic, but only that there be isotropy in the X-Y plane and that the crystal symmetry be such that the currents and forces are coplanar (in the X-Y plane). It is of interest to note that physical isotropy in the X-Y plane is guaranteed by the Onsager relations if the crystallographic symmetry is such that the Z axis is a three-, four-, or six-fold rotation axis (cf. Onsager, reference 5).

a—The Isothermal Electric Conductivity

The isothermal value of the electric conductivity is obtained if the system is constrained to maintain a uniform temperature. Thus

$$\sigma_i \equiv -eJ_x \Big/ \frac{1}{e}\nabla_x \mu \tag{60}$$

under the conditions

$$\nabla_x T = \nabla_y T = J_y = 0, \tag{61}$$

whence

$$\sigma_i = \frac{e^2}{TL_{11}}(L_{11}^2 + L_{12}^2). \tag{62}$$

b—The Adiabatic Electric Conductivity

The adiabatic value of the electric conductivity is obtained if the system is so arranged that no transverse currents can flow, although transverse gradients are allowed to develop. Thus

$$\sigma_a \equiv -eJ_x \Big/ \frac{1}{e}\nabla_x \mu, \tag{63}$$

under the conditions

$$\nabla_x T = Q_y = J_y = 0, \tag{64}$$

whence

$$\sigma_a = \frac{e^2}{TD} \cdot \begin{vmatrix} L_{11} & L_{13} & L_{14} \\ -L_{13} & L_{11} & L_{12} \\ -L_{14} & L_{12} & L_{22} \end{vmatrix}, \tag{65}$$

where

$$D = L_{11}L_{22} - L_{12}^2.$$

c—The Isothermal Heat Conductivity

$$\kappa_i \equiv -Q_x / \nabla_x T, \tag{66}$$

under the conditions

$$J_x = J_y = \nabla_y T = 0, \tag{67}$$

whence

$$\kappa_i = \frac{1}{T^2} \cdot \frac{1}{L_{11}^2 + L_{13}^2} \cdot \begin{vmatrix} L_{11} & L_{13} & L_{14} \\ -L_{13} & L_{11} & L_{12} \\ -L_{14} & L_{12} & L_{22} \end{vmatrix}. \tag{68}$$

d—The Adiabatic Heat Conductivity

$$\kappa_a \equiv -Q_x / \nabla_x T, \tag{69}$$

under the conditions

$$J_x = J_y = Q_y = 0, \tag{70}$$

whence

$$\kappa_a = \frac{1}{T^2} \cdot \begin{vmatrix} L_{11} & L_{12} & L_{13} & L_{14} \\ L_{12} & L_{22} & L_{14} & L_{24} \\ -L_{13} & -L_{14} & L_{11} & L_{12} \\ -L_{14} & -L_{24} & L_{12} & L_{22} \end{vmatrix} \cdot \begin{vmatrix} L_{11} & L_{13} & L_{14} \\ -L_{13} & L_{11} & L_{12} \\ -L_{14} & L_{12} & L_{22} \end{vmatrix}^{-1}. \tag{71}$$

e—The Isothermal Hall Effect

$$(\text{Hall})_i \equiv \frac{1}{e}\nabla_y \mu \Big/ HeJ_x, \tag{72}$$

under the conditions

$$J_y = \nabla_y T = \nabla_x T = 0, \tag{73}$$

whence

$$(\text{Hall})_i = -\frac{T}{e^2 H} \frac{L_{13}}{L_{11}^2 + L_{13}^2}. \tag{74}$$

It should be noted that the adiabatic Hall coefficient, defined as the transverse e.m.f. per unit electric current and per unit magnetic field, cannot be obtained from our equations. For in the adiabatic effect we do not have $\nabla_y T = 0$ and therefore $(1/e)\nabla_y \mu \neq$ e.m.f. The adiabatic Hall coefficient is, however, the more commonly measured of the two Hall coefficients.

f—The Isothermal Nernst Effect

$$(\text{Nernst})_i = -\frac{1}{e}\nabla_y \mu \Big/ H\nabla_x T, \tag{75}$$

under the conditions

$$J_x = J_y = \nabla_y T = 0, \tag{76}$$

whence

$$(\text{Nernst})_i = \frac{1}{eHT} \frac{L_{11}L_{14} - L_{12}L_{13}}{L_{11}^2 + L_{13}^2}. \tag{77}$$

g—The Ettingshausen Effect

$$(\text{Ettingshausen}) \equiv \nabla_y T/HeJ_x \tag{78}$$

under the conditions

$$J_y = Q_y = \nabla_x T = 0, \tag{79}$$

whence

$$(\text{Ettingshausen}) = \frac{T^2}{eH}(L_{11}L_{14} - L_{12}L_{13}) \cdot \begin{vmatrix} L_{11} & L_{13} & L_{14} \\ -L_{13} & L_{11} & L_{12} \\ -L_{14} & L_{12} & L_{22} \end{vmatrix}^{-1}. \tag{80}$$

h—The Leduc-Righi Effect

$$(\text{Leduc-Righi}) \equiv \nabla_y T/H\nabla_x T \tag{81}$$

under the conditions

$$J_x = J_y = Q_y = 0, \tag{82}$$

whence

$$(\text{Leduc-Righi}) = \frac{1}{H} \cdot \begin{vmatrix} L_{11} & L_{13} & -L_{12} \\ -L_{13} & L_{11} & L_{14} \\ -L_{14} & L_{12} & L_{24} \end{vmatrix} \cdot \begin{vmatrix} L_{11} & L_{13} & L_{14} \\ -L_{13} & L_{11} & L_{12} \\ -L_{14} & L_{12} & L_{22} \end{vmatrix}^{-1}. \tag{83}$$

i—Relations Among the Coefficients

We have eight coefficients expressed in terms of six independent kinetic coefficients, and it is apparent, therefore, that there exist two independent relations among these coefficients. One relation, attributable to Bridgman, may be easily verified to be

$$T \cdot (\text{Nernst})_i = \kappa_i \cdot (\text{Ettingshausen}). \tag{84}$$

Because the coefficients of the various effects involve third or fourth powers of the kinetic coefficients, it proves impractical to obtain the second relation in an explicit algebraic form, but the expressions for the coefficients of the effects may be considered to be a parametric statement of this relation. We may see also, by considering the field dependence of the coefficients, that this second relation, unfortunately, is of less practical significance than is Bridgman's relation (84). We have seen that L_{13}, L_{14}, and L_{24} are odd functions of the field, and L_{11}, L_{12}, and L_{22} are even functions. It follows that all the coefficients of the various effects are even functions of the magnetic field, which is also evident physically. If, now, we consider only the field-independent term in the coefficients of the effects, we find the relations

$$\kappa_i{}^0 = \kappa_a{}^0, \tag{85}$$

$$\sigma_i{}^0 = \sigma_a{}^0, \tag{86}$$

$$T \cdot (\text{Nernst})_i{}^0 = \kappa_i{}^0 \cdot (\text{Ettingshausen})^0 \tag{87}$$

and no others. Thus, even for small fields, the Bridgman relation has an independent significance, whereas the second relation degenerates into the comparatively trivial Eqs. (85) and (86). Since measurements are ordinarily made in the range in which no distinction is made between κ_i and κ_a or σ_i and σ_a, we thus see that the second relation introduces no practically significant results for this small-field type of measurement.

PHYSICAL REVIEW VOLUME 73, NUMBER 11 JUNE 1, 1948

Interferometric Studies of Faster than Sound Phenomena. Part I. The Gas Flow around Various Objects in a Free, Homogeneous, Supersonic Air Stream

R. LADENBURG, J. WINCKLER, AND C. C. VAN VOORHIS
Palmer Physical Laboratory, Princeton University, Princeton, New Jersey

(Received December 1, 1947)

A small Mach-Zehnder interferometer is used for analysis of the supersonic air flow in a free homogeneous jet of cylindrical symmetry ("open wind tunnel") at Mach number 1.70 and around various simple objects suspended in it. The interferograms obtained can be evaluated because of the axial symmetry of the phenomena, and this process is carried out by integration of the Abel equation. This "open wind tunnel" does not need any windows; however, the working section is rather restricted, especially by the intersection of the head wave of a suspended body under investigation with the free boundary of the jet. Also the turbulent free jet boundary itself is a source of disturbance. The density, pressure, temperature, velocity, and Mach number throughout the air flow have been determined with reasonable accuracy. For suspended cones of 10° and 30° semi-angle the theory of Taylor-Maccoll has been verified—except near the cone tip where a systematic density increase occurred. For a 45° semi-angle cone and a small sphere where a detached curved shock wave appears, no theoretical results exist at present. However, stream and Mach lines were constructed with the help of the measured density distribution and of the conventional equations for compressible fluids, and pressure coefficients on the surface of the objects were calculated. The results show that the rotational effects are small at the present Mach number. The experience obtained with the small interferometer indicates that it is a very valuable instrument in studying supersonic phenomena, and that it will yield accurate quantitative results not obtainable by other methods. Undoubtedly, it can be applied to a modern supersonic wind tunnel, and such investigations are being undertaken with a larger interferometer and associated equipment.

I. INTRODUCTION

OPTICAL methods for the study of phenomena in fluid mechanics are superior to all other methods as they do not disturb the gas flow in any way. Three such optical methods are known: (1) the shadowgraphic method, which reacts essentially upon the second derivative of the density and is therefore extremely sensitive to sudden changes of density, especially to shocks as they appear in supersonic (that is, "faster than sound") phenomena; (2) the striae or schlieren method, which depends upon the first derivative of the density and reacts, therefore, even to slow changes; (3) and the interferometric method, which gives directly the density itself, and that quantitatively. Once the density of a gas stream is known, it is often possible to compute also its pressure, temperature, and velocity on the basis of well-known hydrodynamic relations for compressible gases.

The most suitable instrument for interferometric work is the Mach[1]-Zehnder[2] interferometer, a modification of the Jamin instrument. It divides the incoming light into two coherent beams widely separated so that phenomena in one of these beams do not disturb the other beam (see Fig. 1). A further advantage of this instrument is that by suitable adjustments of the plates the interference fringes can be produced in any plane, so that the fringes may be focused simultaneously with the gas stream upon a photographic plate and so record the density changes produced by the moving gas. Such an instrument has been used by E. and L. Mach[1] and by C. Cranz and his collaborators and pupils for the study of the supersonic gas flow in jets and for the disturbances produced by projectiles fired with supersonic velocity. We have carried out such interferometric investigations of various supersonic phenomena. The present paper, the first of a series, contains the results obtained on the gas flow around various objects suspended in a free, homogeneous, supersonic air stream,

[1] E. Mach and L. Mach, Wien. Akad. Ber. math.-phys. Klasse 98, 1318 (1889); L. Mach, Zeits. f. Instrumentenk. 12, 89 (1892); *ibid.* 14, 279 (1894); see C. Cranz, *Lehrbuch der Ballistik* (1926), volume II, §23; *ibid.* (1927), volume III, §80–82; *ibid.* (1936), Ergaenzungsband, §69.

[2] L. Zehnder, Zeits. f. Instrumentenk. 11, 275 (1891).

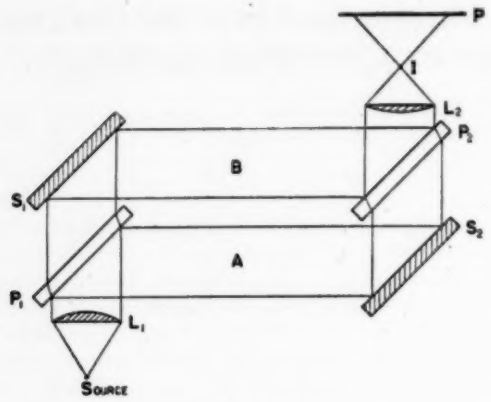

FIG. 1. Mach interferometer.

that is, in a kind of open, intermittent wind tunnel.[3]

The theory of the Mach-Zehnder interferometer has been given by various authors.[4] Details of the instrument used in the present paper, its adjustment and some of its applications are described by one of the present authors (J. W.) in another journal.[5]

II. EXPERIMENTAL METHOD

A. Instrumentation

The interferometer used (Fig. 1) rests on angle irons which, in turn, are supported by concrete pillars and insulated by rubber cushions against vibration. The object of the present investigations is a supersonic air jet, usually located in the light beam B of Fig. 1 between the mirror S_1 and the beam splitting plate, P_2. It produces the displacements of the interference fringes which are straight and equidistant without the jet. The interferometer plates of 6×3 cm size are the property of Dr. R. B. Kennard who was kind enough to lend them for the present experiments, and who, following our request, also directed the construction of the plate holders at the shop of the National Bureau of Standards. Dr. Kennard had used these plates some years ago for the study of temperature distribution and heat flux in air by interferometry.[6] The plates can be rotated by screws around a horizontal and a vertical axis and so adjusted that they give sharp interference fringes of a monochromatic light source, in any direction and in any plane desired. For details of the technique of adjusting the instrument see reference 5.

The air jet for investigation was supplied from a 1½-m³ tank which was filled with dry air at pressures up to 120 lb./in.² fed from high pressure gas cylinders pumped up on a liquid-air machine. The pressure p_0 and temperature t_0 of the air in the tank could be measured accurately. The compressed air escaped from the tank through a streamlined neck, and then passed through a valve which formed a smooth passage when open into a kind of Laval nozzle (see Fig. 2) and emerged as a parallel, homogeneous, supersonic stream at atmospheric pressure. The valve could be opened and closed by hand within one or two seconds. The expanding portion of the nozzle was shaped according to designs of Mr. Alan Puckett of the Guggenheim Aeronautical Laboratory, California Institute of Technology, to give a Mach number of about 1.7. The "throat" is actually the straight portion between D and C of Fig. 2. The ratio between the throat area, A, and the final section area, A_1, determined the final Mach number, M, according to the relation

$$\frac{A}{A_1}=\frac{1}{M}\left(1+\frac{\gamma-1}{2}M^2\right)^{\frac{1}{2}(\gamma+1)/(\gamma-1)}, \qquad (1)$$

where

$$\gamma=C_p/C_v=1.404 \text{ (for air)}.$$

The numerical table in Fig. 2 gives the data from which the nozzle was shaped. No consideration was given to the effect of the boundary layer on effective nozzle diameter, nevertheless the Mach number actually was found to be very close to 1.70. The long throat, in which the Mach number is theoretically unity, is probably an undesirable feature as the gas flows at high speed near the wall for a finite time. The turbulence arising from this, as well as that from the boundary of the free jet in the atmosphere, is

[3] The work described here was started in 1944 under the sponsorship of the Office of Scientific Research and Development, and was taken over in 1945 by the Bureau of Ordance of the Navy Department under Contract NORD 9240. Short abstracts appeared in Phys. Rev. **69**, 251 (1946) and **71**, 464 (1947).

[4] C. Cranz, reference 1; G. Hansen, Zeits. f. tech. Physik **12**, 436 (1931); H. Schardin, Zeits. f. Instrumentenk. **53**, 396, 424 (1933); W. Kinder, Optik **1**, 413 (1946). These papers also contain references to the complete literature.

[5] J. Winckler, Rev. Sci. Inst. **19**, 307 (1948).

[6] R. B. Kennard, J. Research Nat. Bur. Stand. **8**, 787 (1932).

the main limitation on the over-all accuracy of the present results.

The models were supported in a simple way on the end of an axial rod, which was secured to a cross-piece some distance downstream from the working section. The area viewed by the interferometer extends about 25 mm out from the orifice, and is about 40 mm in width, or slightly greater than the width of the air stream. The actual working section is less than this for reasons which will be discussed later (see Section III, A).

In operation, the tank was filled with dry, compressed air to a pressure slightly higher than the working pressure. The valve lever was turned quickly by hand, and when enough air had escaped to drop the pressure to the working value, an automatic switch discharged the spark which made the photograph. The working tank pressure P_0, which is necessary to produce the free jet at atmospheric pressure P, is determined by the Mach number according to the relation

$$P_0/P=[1+\tfrac{1}{2}(\gamma-1)M^2]^{\gamma/\gamma-1}. \qquad (2)$$

This pressure was first calculated and finally established by trial (see Section III, A).

The light source used was a magnesium spark excited by a 0.5-μf capacitor charged to 9000 volts, in connection with a monochromator for isolating the strong violet line 4481A. This line has an intensity about twice that of the underlying continuum and is monochromatic enough to produce about 200 usable fringes, with illumination times of about 1 microsecond and a photographic image of about $1\frac{1}{2}\times 2$ inches. Eastman spectrographic plates, 4 in.$\times$5 in., type 103-0, were used for the interferograms. For taking these pictures a special plate holder was equipped with interchangeable slides, running in grooves as close as possible to the front of the plate. One slide consisted of horizontal slits of $\frac{1}{2}$-mm opening extending across the plate at intervals of 5 mm; the other slide contained $\frac{1}{2}$-mm diameter wires stretched at the exact position necessary to blank out the slits. Thus it was possible, by use of the slits, to photograph the undisplaced fringes, and then to substitute the wires and repeat the exposure with the jet turned on. Since the fringes are customarily oriented vertically, that is, parallel to the streaming gas, this results in a composite photograph in which the undisplaced fringes are available for reference, so that a correction may be made for optical errors in the system, such as lack of plane-parallelism in the plates, etc. Figure 14 shows a composite interferogram using grids. The undisplaced fringes appear in the narrow bands.

Shadowgrams are made in the parallel light from a point source spark of the type designed by Dr. Charters of the Ballistic Research Laboratory, Aberdeen Proving Ground, and a 70-mm focal length telescope objective. Ordinarily the photographic plate was fixed 25 mm from the jet axis. Schlieren photographs were made in an elementary way with a single lens which focused this same spark on a knife edge, and at the same time focused the jet on the photographic plate placed after the knife edge.

B. Measurement of the Interference Patterns

The purpose of the study is to obtain first of all the fringe shifts in various horizontal cross sections through the vertical flow of the gas stream. If one adjusts the interference fringes in a horizontal direction, that is, perpendicular to the gas flow, one obtains pictures like that in Fig. 12 where a conical object of 30° semi-angle

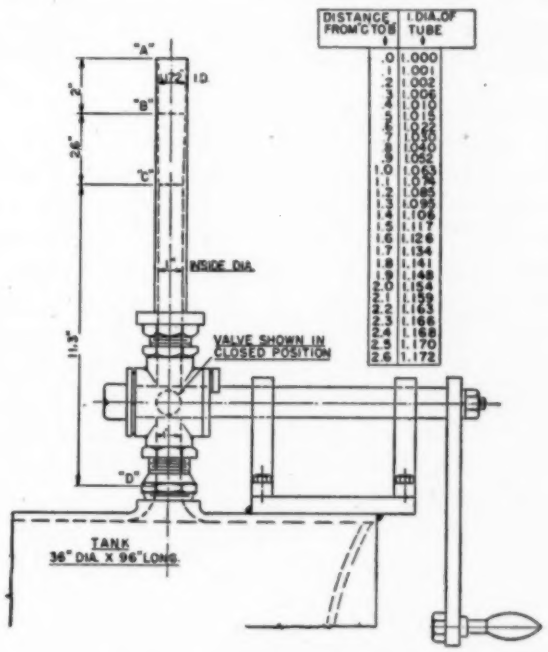

FIG. 2. Orifice and valve assembly.

is supported in the jet. The picture is symmetrical with respect to the vertical axis of the jet as one should expect. In order to get the fringe shifts along a horizontal cross section one has to measure at first the position of each fringe along a series of directions normal to the horizontal fringes and then to transform the shifts of each fringe from its undisplaced position to the various horizontal cross sections. The procedure is simplified if the undisplaced fringes are oriented vertical, that is, parallel to the gas flow (Fig. 14). Now they appear asymmetric with respect to the vertical axis of the jet since they are all shifted to the right or to the left along a horizontal cross section. Therefore they are crowded on one side and widened on the other side. However, if one now measures the shifts of the fringes from their undisplaced positions along a horizontal axis, one obtains without further transformation the desired fringe shifts which are symmetrical with respect to the axis of the jet.

The positions of the undisplaced fringes are obtained on the same photographic plate as the interferograms under measurement, with the help of the horizontal slits and wires described in the previous section. Pictures of the fringes without the jet flowing showed that, due to small inhomogeneities of the interferometer plates, the undisplaced fringes were not quite parallel, uniformly spaced lines, but deviated in some places by as much as 0.4 fringe units from this condition. The correction values were plotted on a map of the area of observation, and this map could then be used to correct, point by point, the fringe shift curves.

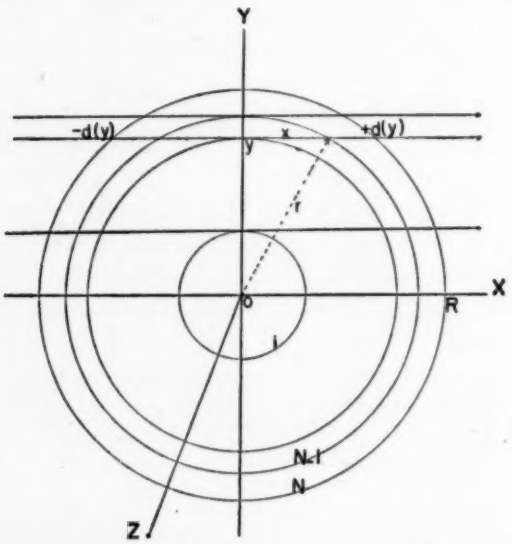

FIG. 3. Horizontal cross section through jet divided into concentric zones of equal width.

The fringe shift values obtained for each cross section were evaluated and plotted completely across the section on transparent paper, producing a nearly symmetrical curve of points. The curve was folded at its axis of symmetry by trial, by use of an illuminated viewing box, and a new curve, representing the average of the two sides, was traced in.

C. Determination of the Density Distribution and its Accuracy

The fringe shifts produced by the streaming gas are due to the differences between its refractive index and that of the air in the other beam of the interferometer. The computation of the density distribution in the streaming gas from the obtained fringe shifts is very simple only in a two-dimensional channel pattern when the density is constant along the light path through the field of view.

Let t be the uniform thickness of the channel along the light path, n_0 and ρ_0 refractive index and density, respectively, of the undisturbed gas in the corresponding light beam of the other arm of the interferometer, and λ the wave-length of the light used. Then the refractive index, n, and density, ρ, at a place where the fringe shift is δ, are given by the simple relations

$$\delta \cdot \lambda = (n-n_0)t = K(\rho-\rho_0)t, \qquad (3)$$

where

$$K = (n-1)/\rho,$$

the Gladstone-Dale constant, depends only on the wave-length and the kind of gas used; therefore,

$$\rho = \rho_0 + (\delta \cdot \lambda)/(K \cdot t).$$

In the present case, the density of the streaming gas is not constant along the light path since the gas escapes through a circular orifice and expands radially as well as in the direction of the jet. Also, various parts of the light beam penetrate different thicknesses of the jet. However, the phenomenon has axial symmetry and can be completely evaluated. Let us assume parallel light and consider a horizontal cross

section through the jet (Fig. 3). Let x again be the direction of the light path, y the other coordinate in this plane, measuring the distance from the axis of the jet, and z the direction of the excaping gas in the jet. Then the fringe shift

$$\delta(y)\cdot\lambda = 2\int_0^{d(y)} [n(y)-n_0]dx$$

$$= 2\int_y^R [n(r)-n_0][rdr/(r^2-y^2)^{\frac{1}{2}}], \quad (4)$$

where $d(y)$ is half the thickness of the jet at a distance y from the axis, $r^2=x^2+y^2$, and R is the radius of the jet in the considered cross section.

A solution of this problem in rough approximation has been given by L. Mach[7] and by H. Schardin.[4] They obtain the values of the refractive index of the jet, $n(r)$, by subdividing the cross section considered into many annular zones of radii r where

$$0=r_0<r_1<\cdots<r_i<r_{i+1}<\cdots<r_N=R,$$

and assuming that $n(r)$ is constant in each zone (Fig. 3). Hence, the value of $n(r_{N-1})$ for the outermost zone between the circles r_N and r_{N-1} is obtained from the fringe shift δ_{N-1} of the beam penetrating this zone in the same way as $n(y)$ is obtained from $\delta(y)$, according to Eq. (3). The next chord traverses only one more zone besides the zone of refractive index $n(r_{N-1})$—that of refractive index $n(r_{N-2})$ which can be obtained in a similar way. Therefore, Eq. (4) reduces to a simple system of linear equations for the unknown values of the refractive index. Let

$$n(r_i)-n_0=\begin{cases} v_i \text{ for } r_i\leqq r\leqq r_{i+1}, \\ 0 \text{ for } r\geqq R, \end{cases}$$

then

$$\lambda\cdot\delta(y)_{y=r_i}=\lambda\cdot\delta_i=\sum_{\kappa=i}^{N-1} 2v_\kappa\int_{r_\kappa}^{r_{\kappa+1}}\frac{rdr}{(r^2-r_i^2)^{\frac{1}{2}}}$$

$$=2\sum_{\kappa=i}^{N-1} v_\kappa\{(r_{\kappa+1}^2-r_i^2)^{\frac{1}{2}}-(r_\kappa^2-r_i^2)^{\frac{1}{2}}\}$$

$$=2l\sum_{\kappa=i}^{N-1} v_\kappa\{[(\kappa+1)^2-i^2]^{\frac{1}{2}}-(\kappa^2-i^2)^{\frac{1}{2}}\}$$

$$=2l\sum_{\kappa=i}^{N-1} v_\kappa\cdot a(\kappa,i), \quad (5)$$

when $0\leqq i\leqq\kappa\leqq N-1$ and if all zones have equal width l so that $r_i=i\cdot l$. A systematic manner of solving this system, provided a master table of the coefficient $a(\kappa,i)$ is available, will be found in the paper by F. J. Weyl "Computational aspects of gas flow interferometry" to appear in this journal. That paper contains also details of a refinement of this procedure suggested by one of the present authors (C.C.V.V.); instead of assuming $n(r)$ constant in each zone one approximates it by a linear function of r:

$$n(r)-n_0=v_i+[(r-r_i)/(r_{i+1}-r_i)](v_{i+1}-v_i) \quad \text{for } r_i\leqq r\leqq r_{i+1},$$

where, as before,

$$v_i=n(r_i)-n_0.$$

This approximation leads again to a number of linear equations

$$\lambda\cdot\delta_i=lv_iA(i,i)$$

$$+l\sum_{\kappa=i+1}^{N-1} v_\kappa\{A(\kappa,i)-A(\kappa-1,i)\}, \quad (6)$$

where

$$A(\kappa,i)=(\kappa+1)[(\kappa+1)^2-i^2]^{\frac{1}{2}}-\kappa(\kappa^2-i^2)^{\frac{1}{2}}$$

$$-i^2\log\frac{\kappa+1+[(\kappa+1)^2-i^2]^{\frac{1}{2}}}{\kappa+(\kappa^2-i^2)^{\frac{1}{2}}}, \quad (6a)$$

and the zones are supposed to be of equal width as before.

A large master table of these coefficients for 50 zones is contained in NAVORD Report 69–46.[8] The use of a larger number of zones in the reduction of a given fringe shift curve, quite apart from the fact that it increases greatly the amount of computational labor involved, does not necessarily entail greater accuracy in the result. It is, therefore, a distinct advantage of this procedure that any particular zone where interesting details exist in the $\delta(y)$ curve can be subdivided. The coefficients to be used for subdivided zones and the procedure for carrying out such computations will be given in Weyl's paper. (More details are contained in NAVORD report 69–46.) Such increase of the resolution is especi-

[7] L. Mach, Wien. Akad. Ber. math.-phys. Klasse **105**, 605 (1896).

[8] A photostatic copy of this table may be obtained on request from Palmer Physical Laboratory. In this table the letter κ is replaced by the letter μ. Copies of the NAVORD reports may be obtained from the Bureau of Ordnance, Navy Department, Washington, D. C.

ally useful at shock fronts. The actual shock front, however, is beyond the resolution of optical methods (a few mean free-paths in thickness).

Dr. Hans Panofsky has suggested another procedure for computing the rapid change of refraction index and density at a shock. It consists in inserting a "Schardin zone" just at the shock position by using suitable coefficients. This eliminates "over-shooting" of the computed values, which is apt to occur whenever the actual rate of change of ν in a zone is greater than the assumed linear rate between zone boundaries, and it produces a smooth behavior of the density curve after a shock. Such a "Schardin zone," being a density plateau with a flat top and square front, approximates closely the density behind an actual shock front. Details will be discussed in the paper by F. J. Weyl mentioned above.

The evaluation of the interferograms of jets is partly done by this approximation of Van Voorhis and Weyl, and partly by a still more exact solution of Eq. (4) suggested by J. Von Neumann. Introduction of the variables

$$v=r^2, \quad u=y^2$$

reduces Eq. (4) to

$$\lambda\cdot\delta(u)=\int_u^\infty \frac{\nu(v)}{(v-u)^{\frac{1}{2}}}dv,$$

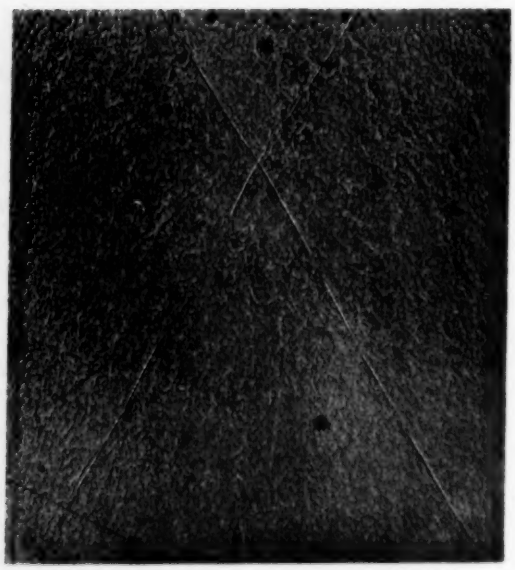

FIG. 4. Shadowgram of the homogeneous jet. $M=1.70$.

where $\nu=n-n_0$ is now a function of v only. Solution of this integral equation is accomplished by applying once more the Abel operator

$$\int_u^\infty [f(v)dv/(v-u)^{\frac{1}{2}}]$$

to both sides of the integral equation. The procedure of this solution has been worked out by F. J. Weyl and will be described in this journal. Also given there is the complete mechanization of the computation with the help of IBM machines, as worked out by H. Polachek, and a discussion of the accuracy obtainable. Coefficients for 100 zones have been worked out for use in this method.

A comparison of the results gained by this method and by the Van Voorhis-Weyl approximation for the same interferogram showed good agreement within the accuracy obtainable, but the use of the IBM machines saves a large amount of labor. It is hoped that the new electronic machines for computation will reduce appreciably the time needed for computation.

From the ν-value sone obtains the corresponding values of the density in the jet

$$\rho=\rho_0+(\nu/K),$$

where K is the Gladstone-Dale constant for the jet of dry air, $K=(n-1)/\rho$, and ρ_0 is the equivalent density of the displaced air, assumed to be half-saturated with water vapor. The zone width l is optional. This calculation is easily carried out on a hand computing machine. For the magnesium line used in the present experiments, $\lambda=4481$A, one obtains, from the best known values of density and refractive index for air,

$$K=0.22823 \text{ cm}^3/\text{g}.$$

The absolute values of the densities obtained in the present paper lie between 1 and 5 mg/cm^3. An estimate of its accuracy is complicated by the stepwise, accumulative method of evaluating the refractive index. The plotted values of the fringe shifts $\delta(y)$ probably represent accurately the optical effect of the jet within about 0.03 of a fringe shift unit at places of small slope, and within 0.07 at places of large slope. In the extreme case of large slope, if the error occurs at the center, and with a zone width of 0.02 cm, the

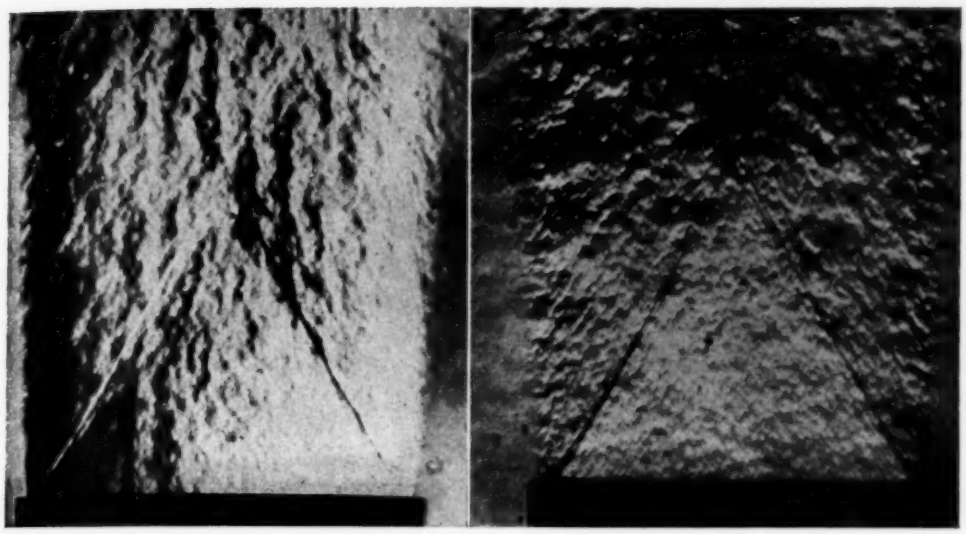

FIG. 5. Schlieren photographs of the homogeneous jet. (a) Schlieren—knife edge parallel to jet axis. (b) Schlieren—knife edge perpendicular to jet axis.

error in ρ will be about 0.8 mg/cm³. If the same error occurs near the edge of the jet, the error in ρ will be only $\frac{1}{10}$ as large. Usually, however, the $\delta(y)$ curve is horizontal at the jet center, so the smaller error in $\delta(y)$, 0.03, should apply, and the error in ρ will be proportionally smaller. Furthermore, the $\delta(y)$ curve is smoothed so that the error is spread over neighboring zones, enters into the sum, and tends to reduce itself.

Probably the major source of error arises from local fluctuations in the jet density, which disturb its cylindrical symmetry, and from random fluctuations in the density of the room air in the interferometer beams (see Section III, A for moving film records of the jet). A safe limit for the absolute error is 10 percent. Density values are probably self-consistent within 5 percent.

III. EXPERIMENTAL RESULTS

A. The Homogeneous Open Jet without Models

The edge of the orifice of the jet represents a region where the bounding medium changes from metal to air. A disturbance always arises at this point, and is propagated into the jet at the local Mach angle (36° to the axis for $M=1.70$). It is desirable to limit the working section to the conical region bounded by the plane of the orifice and this conical Mach wavelet. If the jet emerges at less than atmospheric pressure, it contracts, and a compression shock sets in from the lip at angles greater than the Mach angle, thus further restricting the working section. Higher pressures than atmospheric cause the jet to expand, the expansion region beginning at the Mach wavelet from the lip, but the size of the working section remains unchanged. Thus it is desirable to maintain the jet pressure at atmospheric or slightly higher. Equation (2) gives $P/P_0=0.203$ for $M=1.7$; accordingly, the necessary tank over-pressure is 58 p.s.i. if P is to be one atmosphere (14.7 p.s.i.).

Shadow, schlieren, and interference photographs were taken of the jet over a range of pressures both higher and lower than this. The

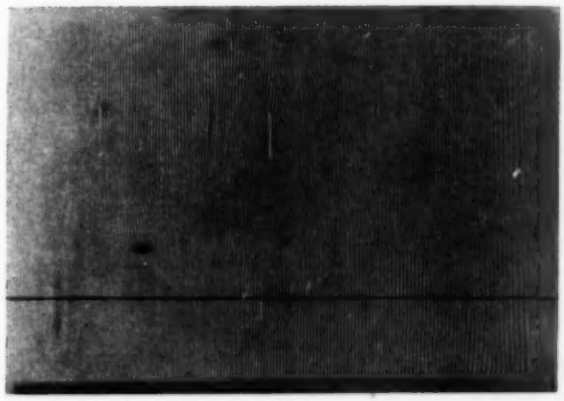

FIG. 6. Interferogram corresponding to the jet of Fig. 4.

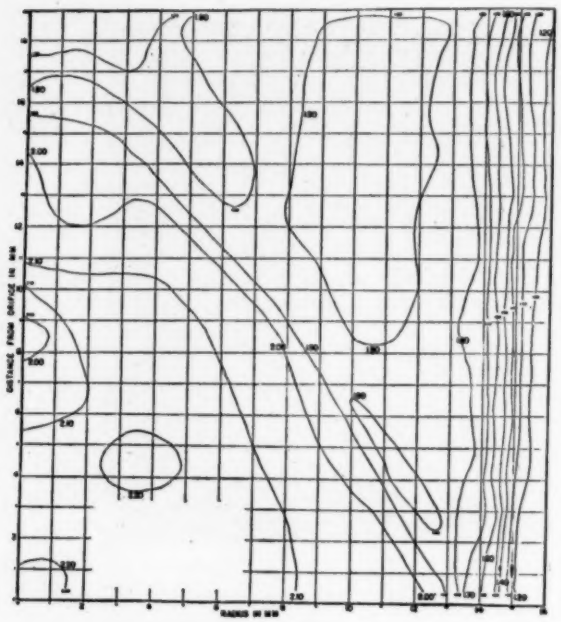

FIG. 7. Isopycnal chart for the homogeneous jet without model.

interferograms were each analyzed at three cross sections, located 1, 12, and 23 mm from the jet orifice. The general result showed that below 60-p.s.i. tank over-pressure a compression shock occurred, and that at 80 p.s.i. very definite expansion regions arose. Accordingly, a working over-pressure of about 69 p.s.i. was selected. This corresponds to an absolute pressure of 5.7 atmos., and at a temperature of 301°K to a density of 6.71 mg/cm³. Shadow, schlieren, and interference photographs of the jet at 69.5 p.s.i. are shown in Figs. 4, 5, and 6. Figure 7 gives a complete density analysis of the jet ("isopycnal chart"), and represents the averaged results of two photographic plates. The averaging was carried out on the fringe shift curves before the reduction process.

The density in the working section was 2.10 ± 0.1 mg/cm³, whereas the undisturbed air had a density of 1.20 at the prevailing pressure and temperature. Since the pressure in the working section was slightly higher than atmospheric, a weak conical expansion wave originated from the edge and reduced the density just outside this conical region from about 2.1 to 1.9 (see Fig. 7). Besides, the 2.2 isopycnic line (contour of density 2.2 mg/cm³) always appears near the center of the orifice. Various other "islands" in the working section do not appear invariably and probably are due to accidental fluctuations.

If the viscosity and the heat conductivity of the gas are neglected, knowledge of the density and the initial conditions enables one to calculate the pressure P, temperature T, Mach number M, and flow velocity U in the jet. When the jet is free of shocks the adiabatic law may be used starting from the tank where U and $M=0$. As long as the density ratio in the shocks is <1.4, as in the case in our homogeneous jet, the use of the adiabatic law does not introduce errors greater than 1 percent. Across stronger shocks, such as occur by inserting objects (see Section III, B, C, D), U, P, T, and M are connected by the Rankine-Hugoniot equations (Eqs. (9) in Section III, B). In the regions downstream from a shock, within a region free of rotational flow, the adiabatic laws may be used again, beginning with the conditions just after the shock. Once the temperature is known, the flow velocity may be calculated from the energy law which holds anywhere in the jet:

$$U^2+2C_pT=\text{constant}=2C_pT_0,$$

where T_0 is the tank temperature and C_p the specific heat at constant pressure (1.00×10^7 erg/g°K). Table I gives pressure, temperature, Mach number, and velocity for each isopycnic line in the adiabatic undisturbed region of the homogeneous jet, together with the exact initial conditions and the equations used. However, this table is valid only inside the 1.80-mg/cm³ contour, because of mixing of the jet with the atmosphere outside this line. It is obvious that in this region of "mixing," viscosity, and heat conductivity cannot be neglected as was assumed at the beginning of this section. Also rotational flow may occur in a turbulent region.

As a check on the validity of the Mach numbers obtained from the density, Mach number values were measured directly with a multiple probe consisting of five 10° semi-angle cones. The head wave angles were measured from shadowgrams of the type shown in Fig. 8, and the Mach number was then obtained from the Taylor-Maccoll curves (see Section III, B). Actually the head wave angle differs but slightly from the Mach angle for this cone size and Mach number.

The Mach numbers obtained with the multiple

probe are considered to be the correct values; those obtained from the measured densities are correct only if the entropy has not changed in the flow of the gas from the pressure tank to the region under consideration. They agree with each other within about 1½ percent, but only in a region limited by the orifice as base and the conical expansion wave mentioned above. In this region the flow is nearly homogeneous within the experimental accuracy. The results show further that the jet is surrounded by a boundary layer in the form of a cylindrical sheath of approximately 4-mm width, where the actual Mach numbers obtained by the probe are appreciably less than the computed values due to the influence of friction and heat conductivity.[9]

In spite of the thick boundary layer, the Mach number calculated from the ratio of the area of the "throat" and the orifice (see Section II, A) agrees within one percent with the Mach numbers measured. This agreement is probably due to the fact that the boundary layer is already developed in the throat so that the ratio of the effective area of the streaming gas is not appreciably different from the ratio of the geometrical areas of the nozzle.

One further examination of the jet was made, namely, that of high speed moving film records. Vertical fringes formed by the intense constant light of a G.E. AH-6, 1-kw mercury arc operated on d.c. (with light filter for singling out the green line 5461A) were focused on a 0.2-mm aperture horizontal slit, placed just before the moving film of a General Radio Type 651-AE recording camera. The points, formed wherever a bright fringe crossed the slit, were drawn out into traces as the film moved, providing a time record of the sidewise motion of the fringes. The camera is adapted for standard 35-mm film and was run at the rate of about 1 cm per millisecond. A typical record is shown in Fig. 9 (cross section near orifice). On this picture the distance between successive perforations is about 500 microseconds. The section at the bottom shows the appearance of the undisplaced fringes before the opening of the valve. The cross section viewed by the slit is about 4 mm from the orifice. The magnification in this figure is about half that of Fig. 6.

[9] For details see NAVORD Report 93–46.

TABLE I. Values of the gas dynamical variables (pressure, etc.) corresponding to density values in the homogeneous jet. (On the basis of the adiabatic law.) (Refers to Fig. 7.) $P/P_0=(\rho/\rho_0)^\gamma$, $T/T_0=(\rho/\rho_0)^{\gamma-1}$, $M^2=U^2/a^2=2[T_0/T-1](\gamma-1)$, $U^2=2C_p(T_0-T)$, $\gamma=C_p/C_v=1.404$, $C_p=1.00\times10^7$ erg/g °K, $\rho_0=6.708$ mg/cm³, $P_0=5.72$ atmos., $T_0=301°K$.

Density ρ (mg/cm³)	Pressure P (atmos.)	Temperature T (°K)	Mach number $M=U/a$	Velocity U (meter/sec.)
1.5	0.698	164	2.03	523
1.6	0.764	169	1.97	514
1.7	0.832	173	1.91	506
1.8	0.902	177	1.86	498
1.9	0.974	181	1.81	490
2.0	1.046	184	1.77	484
2.1	1.120	188	1.72	475
2.2	1.196	192	1.68	467
2.3	1.273	195	1.64	460
2.4	1.351	199	1.59	452
2.5	1.431	202	1.56	445

The principal feature of these records is the revelation of rapid changes in density that appear simultaneously across the entire jet and reoccur irregularly. These density fluctuations produce a fringe shift fluctuation of as much as two units.

A similar photograph made with the jet displaced just out of the interferometer light path showed that the main effect was in the jet itself, and that smaller additional effects were caused probably by the disturbance propagating away from the jet in the direction of the light path. The duration of these disturbances is too long for true turbulence, rather, they are to be associated with sound vibrations, plainly audible

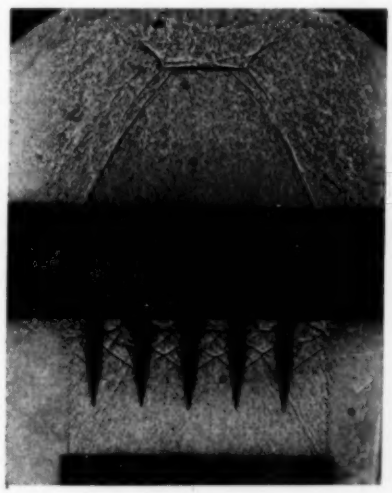

FIG. 8. Direct measurement of Mach number with probes in the homogeneous jet. Probe semi-angle 10°. $M=1.70$.

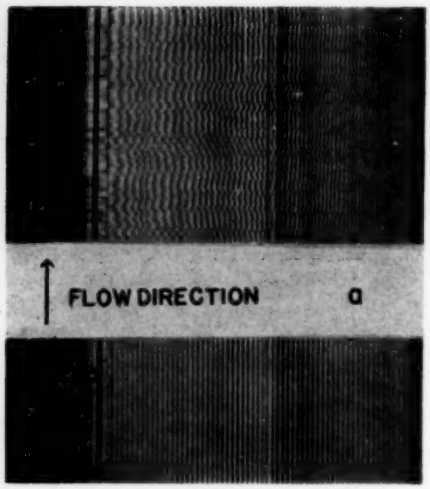

FIG. 9. Moving film records of the homogeneous jet at the cross section marked by the horizontal line in Fig. 6. (a) Jet on—displaced fringes. (b) Jet off—undisplaced fringes.

as the hissing of the discharge, perhaps due to fluctuations of the boundary layer in the nozzle.

Such disturbances are, of course, undesirable, and they explain the need for short exposure times, but their effect on the results of the measurements is probably not serious as the jet is quasi-stationary with respect to their duration time. The spark light source (1–1½ μsec.) used for interferometry, on the other hand, reveals true turbulence as small fluctuations which differ at various parts of the field. The slit aperture used for the moving film records corresponds to about 20 μsec., so that true turbulence would not be resolved.

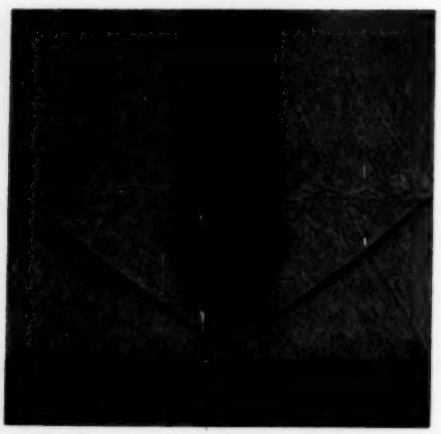

FIG. 10. Shadowgram of air flow about 30° semi-angle cone. Homogeneous jet. $M = 1.70$.

B. The Air Flow about a 30° Semi-Angle Cone in the Homogeneous Open Jet

Shadow, schlieren, and interference photographs were made of three cone sizes, chosen, respectively, to give a weak effect (10° semi-angle), a medium effect (30° semi-angle), and a strong effect with detached head wave (45° semi-angle). The results of Taylor and Maccoll,[10] giving the theoretical flow about the 10° and 30° cones, were available for comparison with the measurements. To date no theoretical calculation has been made of the flow in the case of the detached head wave of a cone. The effect on the 10° semi-angle cone turned out to be so small the accuracy of the results obtained was rather poor. Inasmuch as the essential features are the same as for the 30° semi-angle cone, where the results have appreciably higher accuracy, only these are given here.[11]

Shadow, schlieren, and interference photographs of this cone suspended in the homogeneous open jet are reproduced in Figs. 10–14. Figure 13 has been specially made to trace the course of a single fringe through the interferogram by using the complete spectrum of the spark and, accordingly, only the zero-order or "white light" fringes are visible. The isopycnal chart is given in Fig. 15. It is obtained from two separate interferograms, which were reduced and averaged. In this way accidental fluctuations are largely smoothed out. The chart was drawn from the analysis made at 6 cross sections of each interferogram, spaced every 2 mm between 0.5- and 10.5-mm distance from the orifice.

The general features of the homogeneous jet, shown in Fig. 7, are here exhibited upstream from the oblique conical shock head wave; namely, the general density of about 2 mg/cm³, a decrease through the boundary layer down to the atmospheric density of 1.2 mg/cm³, and the weak expansion region proceeding up from the

[10] (a) G. I. Taylor and J. W. Maccoll, "The air pressure on a cone moving at high speeds," Proc. Roy. Soc. **139**, 278, 298 (1933); (b) J. W. Maccoll, "The conical shock wave formed by a cone moving at high speeds," Proc. Roy. Soc. **159**, 459 (1937).

[11] For the results obtained with the 10° cone see NAVORD Report 93–46.

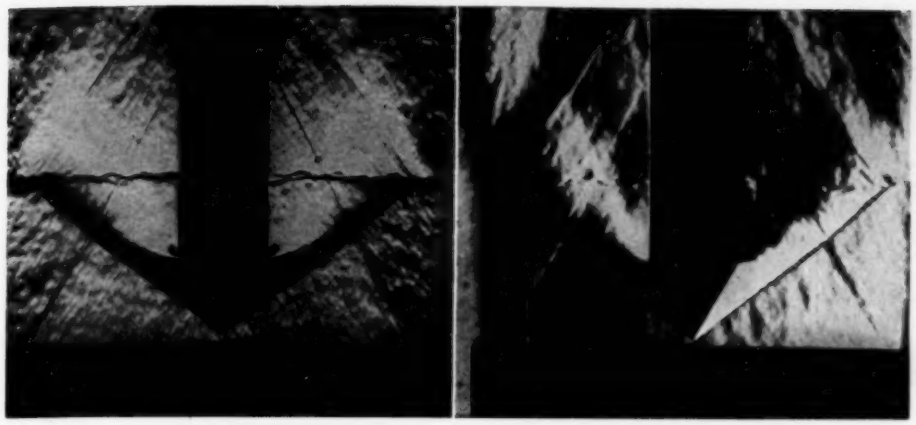

(a) (b)

FIG. 11. Schlieren photograph of air flow about a 30° semi-angle cone. (a) Knife edge normal to axis. (b) Knife edge parallel to axis.

corner of the jet. However, downstream from the strong shock wave the flow pattern is completely changed and shows the characteristic features of a flow about a cone, namely, the large compression of the air before the slant face of the cone starting at its tip, the large expansion around the shoulder, and the more or less conical regions arising from the tip and shoulder. The shock wave is accurately straight over most of its length, and the measured angle ($54.7°\pm0.2°$) agrees well with the theoretical angle (54.66°) as given by Taylor and Maccoll for such a cone at a Mach number of 1.70. The shock angle and its strength decrease after the first expansion wavelet from the shoulder reaches out to the shock. There is also a small increase of strength and angle near the tip (see discussion below).

The values of pressure, temperature, Mach number, and velocity in the conical region between head wave and surface of the cone are listed as functions of the observed density in Table II, which has been derived on the assumption of adiabatic conditions after the shock wave. The equations used and the initial values are given in Table II also. The pressure, P_2, and temperature, T_2, on the downstream side of the head wave are obtained from the corresponding values on the upstream side by use of the Rankine-Hugoniot equations (see below).

The check between the theory of Taylor and Maccoll may be made by comparing—besides the head wave angle—the following factors:

1. The assumption that there is a conical region between the cone and its head wave, i.e.,

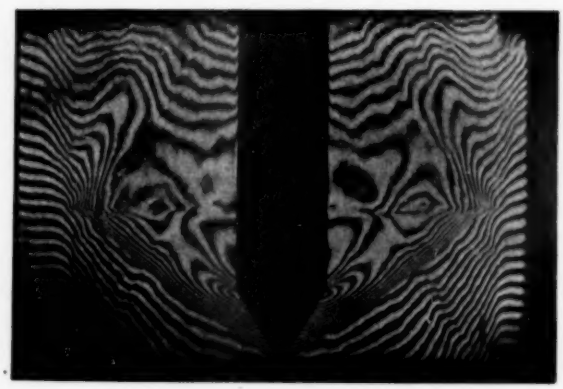

FIG. 12. Interferogram of air flow about 30° semi-angle cone. Fringes perpendicular to flow.

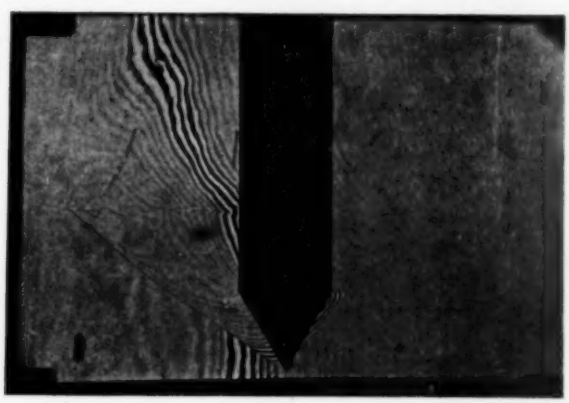

FIG. 13. Interferogram of air flow about 30° cone using "white light fringes."

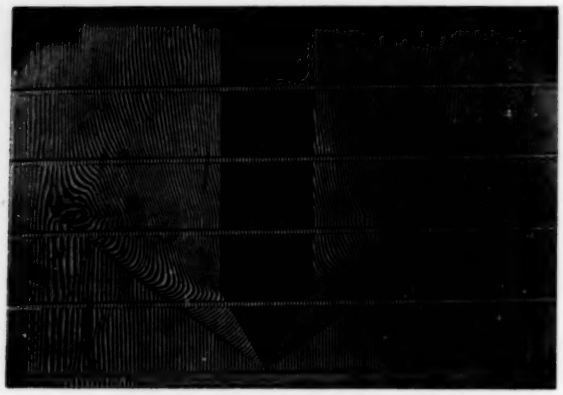

FIG. 14. Interferogram of air flow about 30° cone. Fringes parallel to jet.

that all variables are functions of θ only, where θ is the angle between the axis of the cone and a radius vector starting at the tip of the cone.

2. The actual value of the density ρ at the angle θ.

3. The pressure coefficients, $(P_s-P_1)/\rho_1 U_1^2$, on the conical surface where index 1 refers to the conditions in the undisturbed homogeneous jet.

The check of the factors (1) and (2) is shown in Fig. 16. Here the density is given, for various angles θ, as a function of the distance R from the tip of the cone. The observed values are represented by the solid lines. The theoretical straight lines are dotted and are, of course, parallel to the R axis as the theory assumes this regime to be conical. The notation is the same as that used by Taylor and Maccoll. The theoretical values of the sound velocity, a, and the components of gas velocity along and normal to the radius vector, u and v, were furnished in tabular form for $\frac{1}{2}°$ increments of θ for $M=1.70$, $\theta_s=30°$, through the kindness of Dr. Z. Kopal of the Department of Electrical Engineering, M. I. T. From the initial reservoir conditions $P_0=5.72$ atmos., $\rho_0=6.71$ mg/cm³, and average observed Mach number in the working section, 1.705, the average pressure P_1 and density ρ_1 in the working section upstream from the shock regions were calculated by the relations

$$P_1=P_0(1+\tfrac{1}{2}(\gamma-1)M^2)^{-\gamma/(\gamma-1)}, \qquad (7)$$

$$\rho_1=\rho_0(1+\tfrac{1}{2}(\gamma-1)M^2)^{-1/(\gamma-1)}, \qquad (8)$$

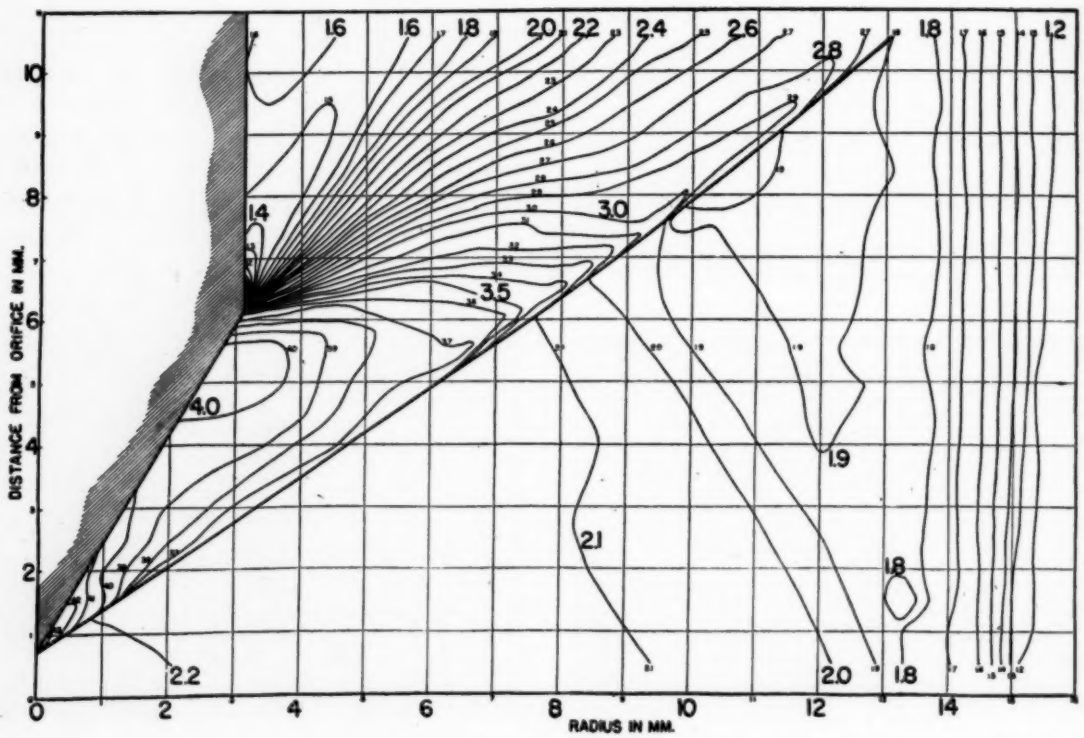

FIG. 15. Isopycnal chart for air flow about a cone of 30° half-angle. Mach No. 1.70. Contours labeled in mg/cm³.

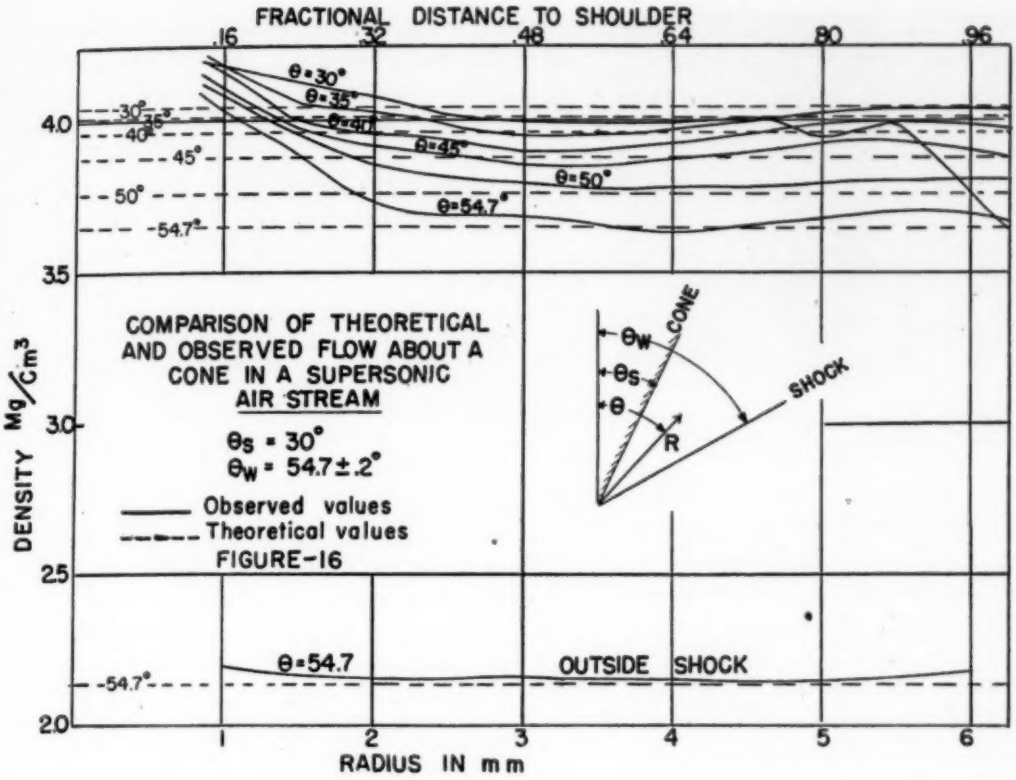

FIG. 16.

which assume isentropic flow through the nozzle (see also Table I). The pressure P_2 and density ρ_2 just after the shock were then calculated from the observed shock angle $\theta_W = 54.7°$ and the Rankine-Hugoniot relations expressed in the form

$$\frac{P_2}{P_1} = \frac{[(\gamma+1)/(\gamma-1)](\rho_2/\rho_1)-1}{[(\gamma+1)/(\gamma-1)]-\rho_2/\rho_1},$$

$$\frac{\rho_2}{\rho_1} = \frac{(\gamma+1)/2}{(1/M_n^2)+[(\gamma-1)/2]}$$

and

$$\frac{T_2}{T_1} = \frac{[(\gamma+1)/(\gamma-1)]-\rho_1/\rho_2}{[(\gamma+1)/(\gamma-1)]-(\rho_2/\rho_1)}, \qquad (9)$$

where $M_n = M \sin\theta_W$. The density in the region bounded by the cone and its head wave was then determined adiabatically, using the theoretical sound velocity at the desired values of θ with the aid of the relation

$$\rho = (\gamma c/a^2)^{1/(1-\gamma)},$$

which may be derived from the relations

$$P/\rho^\gamma = \text{constant} = P_2/\rho_2^\gamma = C, \quad \text{and} \quad a^2 = \gamma P/\rho.$$

In this calculation, the observable quantities

TABLE II. Pressure, etc., in the conical region for supersonic air flow about a 30° semi-angle cone at Mach No. 1.70. (Refers to Fig. 15.) $P/P_2 = (\rho/\rho_2)^\gamma$, $T/T_2 = (\rho/\rho_2)^{\gamma-1}$, $M = [2(T_0/T-1)/\gamma-1]^{\frac{1}{2}}$, $U^2 = 2C_p(T_0-T)$, $\gamma = 1.404$, $C_p = 1.00\times10^7$ erg/g °K, $\rho_2 = 3.58\times10^{-3}$ g/cm³, $P_2 = 2.41$ atmos., $T_0 = 301$°K, $T_2 = 237$°K, $MT_2 = 1.15$.

Density ρ (mg/cm³)	Pressure P (atmos.)	Temperature T (°K)	Mach No. $M = U/a$	Velocity U (meter/sec.)
1.4	0.64	162	2.06	527
1.6	0.78	171	1.94	510
1.8	0.92	179	1.83	493
2.0	1.06	187	1.74	477
2.2	1.22	195	1.64	461
2.4	1.37	202	1.56	446
2.6	1.54	208	1.49	431
2.8	1.70	214	1.41	416
3.0	1.88	221	1.34	401
3.2	2.06	226	1.28	386
3.4	2.24	232	1.21	371
3.6	2.43	237	1.15	357
3.8	2.62	243	1.09	341
4.0	2.81	248	1.03	326
4.2	3.01	253	0.97	311
4.4	3.22	258	0.91	295
4.6	3.42	262	0.86	279

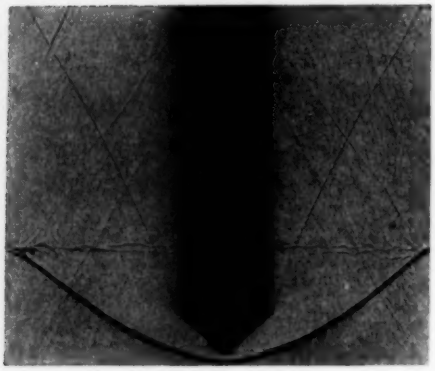

FIG. 17. Shadowgram of the air flow about a 45° semi-angle cone in a homogeneous jet. $M=1.70$.

which must be used to fix the theoretical values in the conical regions (shock angles, Mach number, and reservoir conditions) were chosen so as to involve the smallest experimental error without making use of the interferometer results. The air density values ρ in mg/cm³ are plotted as ordinates in Fig. 16. Both the actual radial distance R in mm and the fractional distance between the cone point and shoulder are plotted as abscissae. The experimental results show slight variations of the density with R; these may at least be partly due to variations of the density in the working section.

For $1<R<6$ mm the deviation from the conical regime outside the cone surface amounts to ± 7 percent maximum. For $2<R<6$ mm the deviation is only ± 1 percent maximum, with the absolute values of density in equally good agreement. On the surface ($\theta=30°$) the density drops rapidly near the shoulder. For $0.8<R<2$ mm there is a systematic rise in density, as has also been found for the 10° cone. (One would expect that the shock angle at this point is also somewhat larger than at a greater distance from the tip of the cone, and this is actually observed (see Fig. 15)). It is reasonable to attritube this effect to the formation of a boundary layer on the cone surface, which is effective in making the cone slightly blunt; besides, the cone point was not ideally sharp. Further, the drop in pressure and density after the shoulder was propagated upstream along the surface in this boundary layer and produced the large drop in density for $\theta=30°$, $R>4.5$ mm for $\theta=54.7°$, completely outside the headwave, the density is quite constant, and agrees closely with the average density for the working section, as shown by the dotted line at $\rho=2.14$ mg/cm³ (Fig. 16). The pressure coefficient $K=(P_s-P_1)/\rho_1 U_1^2$ at the cone surface, calculated from the density $\rho_s=3.98$ mg/cm³, with $P_1=1.164\times 10^6$ dynes/cm², $\rho_1=2.14\times 10^{-3}$ g/cm³, and $U_1=47100$ cm/sec., gives $K=0.351$, whereas we would expect 0.352 from Taylor and Maccoll's results.

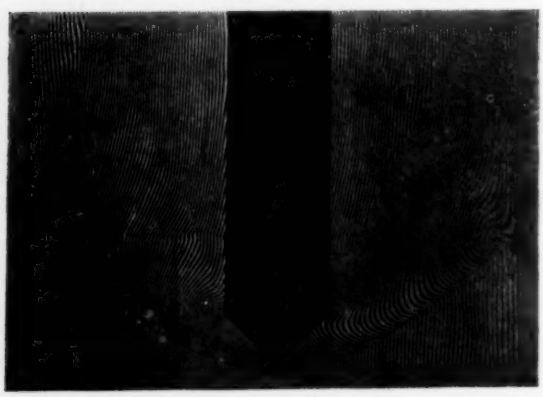

FIG. 18. Interferogram of the air flow about a 45° semi-angle cone in a homogeneous jet. $M=1.70$.

Taylor and Maccoll[12] give a comparison of the theoretical pressure coefficient with values measured in a wind tunnel with pressure holes on the conical surface. It is of interest that their values for hole "A" near the tip of the cone are higher, at least for the 20° and 30° cones, than theory would predict. This is in line with our observation of higher density near the tip. Besides this effect there is no systematic deviation of our results or of those of the wind tunnel experiments reported by Taylor and Maccoll from the theory.

In general, then, we may conclude that our results agree with Taylor and Maccoll's theory within the experimental error.

C. The Air Flow about a 45° Semi-Angle Cone in the Homogeneous Open Jet

(1) *Experimental Results*—Theory predicts that at Mach number 1.7 the head wave of this cone should be detached. This was found to be the case, as shown by the shadowgram of Fig. 17. The corresponding interferogram is given in Fig. 18 and the resultant isopycnal chart in Fig. 19.

One notices in the shadowgram of the 45° cone

[12] Reference 10(a), Fig. 12, p. 294.

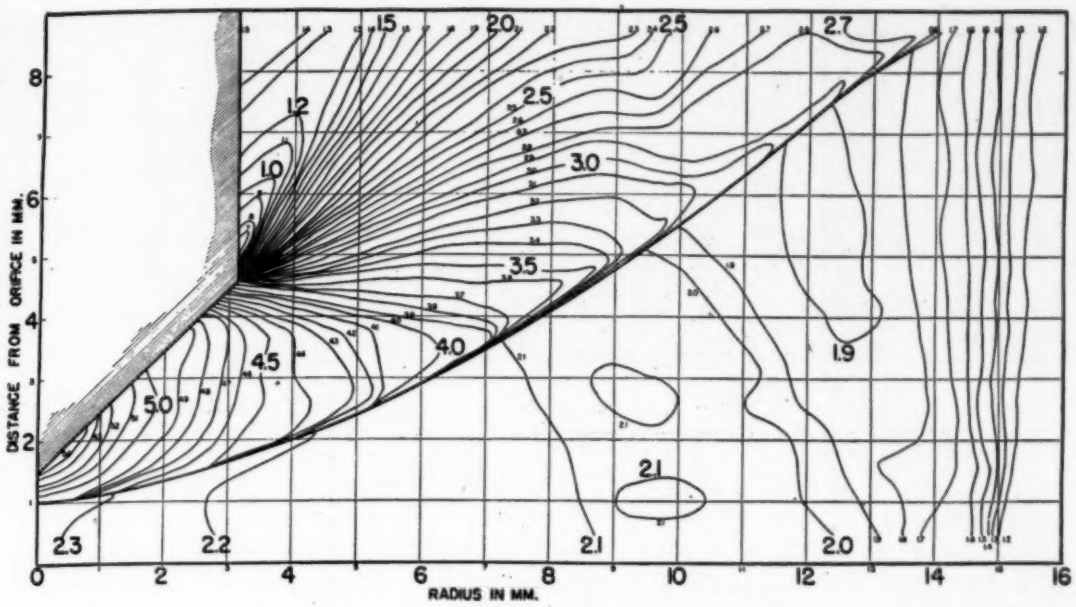

FIG. 19. Isopycnal chart for air flow about a cone of 45° half-angle. Mach. No. 1.70. Contours labeled in mg/cm³.

(Fig. 17) as well as in similar photographs of the 30° cone (Fig. 10) that appreciable distortion results from the strong refraction of the light. The cone shoulders, for example, appear to have projections which are actually not present. The schlieren photograph (Fig. 11) and, of course, the interferometric results (Figs. 15 and 19) reveal the region of very strong expansion at the shoulder which evidently causes the distortion in the shadowgram.

(2) *Calculation of Stream Lines*—In the case of the detached head wave, Taylor and Maccoll's theory breaks down as the regime around the cone is not of the simple conical type. The head wave is curved; consequently, the flow is rotational, and there is no simple way to calculate the pressure coefficient on the surface, or the values of pressure, temperature, and velocity at points in the flow field.

However, the interferometric results give the density at all points in the gas stream, and one is able to calculate the stream lines at each point in a stepwise approximate manner from well-established hydrodynamical relations. The simplest way is to use the equation of continuity, in the form $A\cdot\rho\cdot U=$a constant, where A is the area between adjacent stream lines, corresponding to the density ρ and velocity U. The product $A\cdot\rho\cdot U$ is fixed from known conditions upstream from the shock wave. The stream direction is everywhere parallel to the jet axis in this region. One computes the velocity U_2 on the downstream side of the shock from the usual Hugoniot equations, knowing U_1 on the upstream side and the shock wave angle θ at that point (see Fig. 20). If α is the deflection of the stream

$$U_1\sin\theta=U_2\sin(\theta+\alpha),$$

$$\frac{U_1\cos\theta}{U_2\cos(\theta+\alpha)}=\frac{1+[(\gamma+1)/(\gamma-1)]P_2/P_1}{[(\gamma+1)/(\gamma-1)]+P_2/P_1},$$

$$P_2/P_1=2\gamma M_1^2\cos^2\theta/\gamma+1-[(\gamma-1)/(\gamma+1)].$$

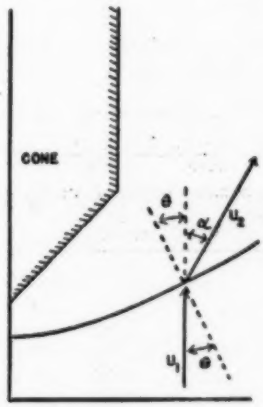

FIG. 20. Deflection of the gas stream in crossing an oblique head wave.

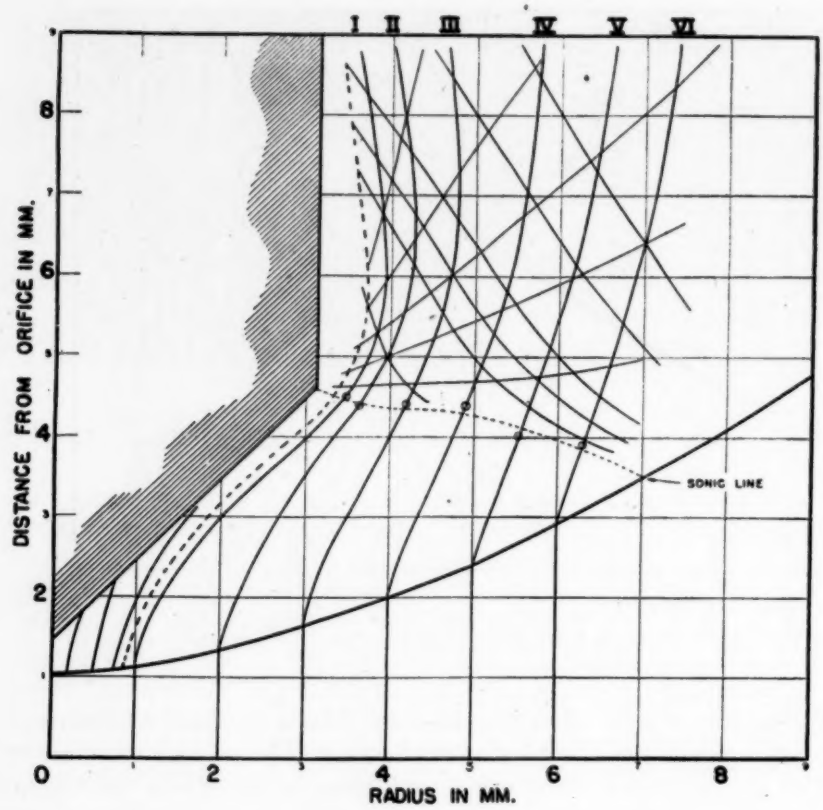

FIG. 21. Stream and Mach lines about a cone of 45° half-angle. Mach No. 1.70.

Therefore

$$U_2 = U_1 \sin\theta \left[\frac{1}{\tan^2\theta} \left[\frac{1}{M_1^2 \cos^2\theta} + \frac{\gamma-1}{2} \right]^2 + 1 \right]^{\frac{1}{2}},$$

$$\alpha = \left\{ \tan^{-1} \left[\frac{\frac{1}{2}(\gamma+1)\tan\theta}{(1/M_1^2\cos^2\theta)+(\gamma-1)/2} \right] \right\} - \theta.$$

TABLE III. Pressure coefficient on the surface of a 45° semi-angle cone. Mach number 1.70. (Refers to Figs. 19 and 21.)

$$K = \frac{P_s - P_1}{\rho_1 U_1^2} = \frac{0.361\rho_s^{1.404} - 1}{408} \times 10^2$$

r—radius in mm, s—distance from orifice in mm

Location of point (r,s)mm	ρ_s mg/cm³	K
(0, 1.5)	5.42	0.704
(0.52, 2.0)	5.44	0.709
(1.53, 3.0)	5.09	0.624
(2.53, 4.0)	4.74	0.541
(3.12, 4.57)	3.72	0.315
(3.12, 5.0)	0.70	−0.191
(3.12, 6.0)	1.00	−0.181
(3.12, 7.0)	1.25	−0.124
(3.12, 8.0)	1.43	−0.099

On the downstream side the values of U of each point are obtained from the measured ρ-values by use of the adiabatic relations and the gas law. Since $A \cdot \rho \cdot U$ is constant also, A may be calculated at each point in a stepwise approximate manner. Knowledge of A serves to fix the stream line position. In flows where the deflection of the stream is large, the approximations involved in this method become poor and the method is difficult to apply. Then another method, developed by one of the present authors (J. W.), may be used. It consists in a stepwise integration

TABLE IV. Pressure coefficient on the surface of a sphere at Mach number 1.70. (Refers to Figs. 24 and 25.)

$$K = \frac{P_s - P_1}{\rho_1 U_1^2} = \frac{0.359\rho_s^{1.404} - 1}{408} \times 10^2$$

r—radius in mm, s—distance from orifice in mm

Location of point (r,s)mm	ρ_s mg/cm³	K
(0, 4.)	6.1	0.869
(1.37, 4.20)	5.37	0.697
(2.66, 5.0)	3.87	0.344
(3.42, 6.0)	2.97	0.160
(3.80, 7.0)	1.90	−0.029
(3.88, 8.0)	1.20	−0.132

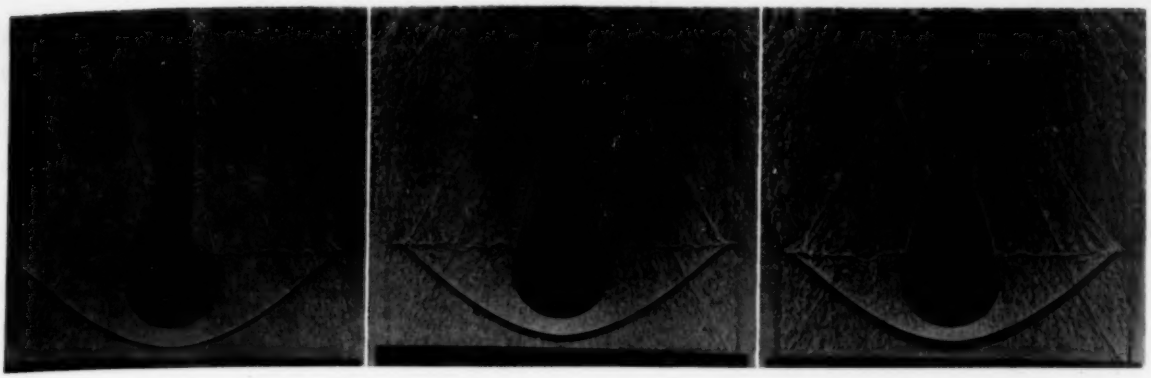

(a) (b) (c)

FIG. 22. Shadowgrams of air flow about a sphere in a homogeneous jet. $M=1.70$. (a) Plate—sphere distance distance = 25 mm. (b) Plate—sphere distance = 50 mm. (c) Plate—sphere distance = 100 mm.

of the equations of motion of the gas

$$\mathbf{dU/dt} = -(\mathbf{grad\ P})/\rho,$$

considering that the measured isopycnals are identical with the isobars in a shock free region, except in cases of very large rotations,[13] and that the stagnation temperature T_0 and pressure P_0 in the tank are known. Figure 21 shows typical stream lines constructed in this way for flow about the 45° semi-angle cone. This figure shows also the Mach lines. The Mach numbers and the local angle $\pm\phi$ between Mach lines and stream lines at any point may be calculated from the equation

$$M = U/a = 1/\sin\phi = \pm\{2/(\gamma-1)[(T_0/T_2)(\rho/\rho_2)^{1-\gamma}-1]\}^{\frac{1}{2}}. \quad (10)$$

The sonic line may be located by setting $M=1$ in this equation and solving for ρ. The calculated points and the best line through them are also shown in Fig. 21 although it is evident that the sonic line does not simultaneously intersect the stream lines at $\phi=90°$ and pass through the sonic points, as it should. This shows that the accuracy of the present results is not high.

Besides the velocity, temperature, and pressure along stream lines may be calculated adiabatically, starting after the shock wave. It turns out that the constants in these equations for the different stream lines are the same within the accuracy of the experiments,[14] showing that the rotational effects due to the curvature of the head wave may be neglected for these calculations. The equations for the pressure P in atmos., the temperature T in °K, the Mach Number M, and the velocity U in meter/sec. are

$$P = 0.414\rho^{1.404}, \quad T = 144\rho^{0.404},$$
$$M = 3.20(\rho^{-0.404}-0.485)^{\frac{1}{2}},$$
$$U = 533(2.063-\rho^{0.404})^{\frac{1}{2}}\text{(meter/sec.)},$$

where ρ is in mg/cm³ and $\gamma = C_p/C_v = 1.404$. For example, for 1 mm from the axis and 2 mm above the orifice one obtains for $\rho = 5.23$ mg/cm³, $P = 4.22$ atmos., $T = 282$°K, $M = 0.526$, and $U = 179$ meter/sec.

The pressure coefficients K at several points on the surface of the 45° cone are given in Table III. They were calculated from the values obtained by inserting the surface density values ρ_s at the indicated places with coordinates (r,z), as given in Fig. 19.

D. Examination of the Air Flow about a Sphere in the Homogeneous Open Jet

(1) *Experimental Results and Comparison of Shadowgraph Theory and Experiment*—Shadowgrams of the air flow about a sphere of $\frac{9}{32}$-in. diameter, made with parallel light from a point

[13] For details see NAVORD Report 93–46.

[14] See NAVORD Report 93–46, Table III, p. 39.

FIG. 23. Interferogram of the air flow about a 9/32-in. sphere in a homogeneous jet. $M=1.70$.

source, are shown in Fig. 22. The three photographs are all of the same phenomena but differ in appearance as the photographic plate was placed at different distances from the jet axis (25, 50, and 100 mm, respectively, for Fig. 22(a), (b), and (c)). The result is that the width of the dark band, representing the effect of the head wave, increases from (a) to (c). Other shadows change correspondingly, giving the appearance of over-all greater contrast. The theory of shadowgrams, as developed by Keenan and Polachek,[15] enables one to determine the shock strength by measuring the width of the dark bands on photographic plates placed at several known distances from the shock wave. For the shadowgrams of Fig. 22 these authors find $\rho_2/\rho_1=2.18$ for the shock strength on the axis as compared with $\rho_2/\rho_1=2.26$ measured by the interferometer. The shadowgraph method also gives the density gradient immediately after the shock; the spacing of the measured cross sections in our interferogram was not made small enough in this case to give a value of the gradient sufficiently accurate for comparison.

(2) *Interferometric Results*—The shadowgrams, as well as the interferogram of the same sphere (Fig. 23), reveal one drawback of the experimental arrangement; namely, that the head wave intersects the jet boundary on a level through the rear portion of the sphere. The disturbance caused by this intersection is in the path of the light beam all the way around the periphery of the circular jet and is severe enough to distort the fringes badly. Accordingly, Fig. 23 was measured only up to a horizontal line through the center of the sphere (the resulting isopycnal chart is given in Fig. 24). In the usual high speed wind tunnel with glass or metal walls, the length of working section is considered to be limited to the place where the reflected head wave intersects the axis. Here, however, the

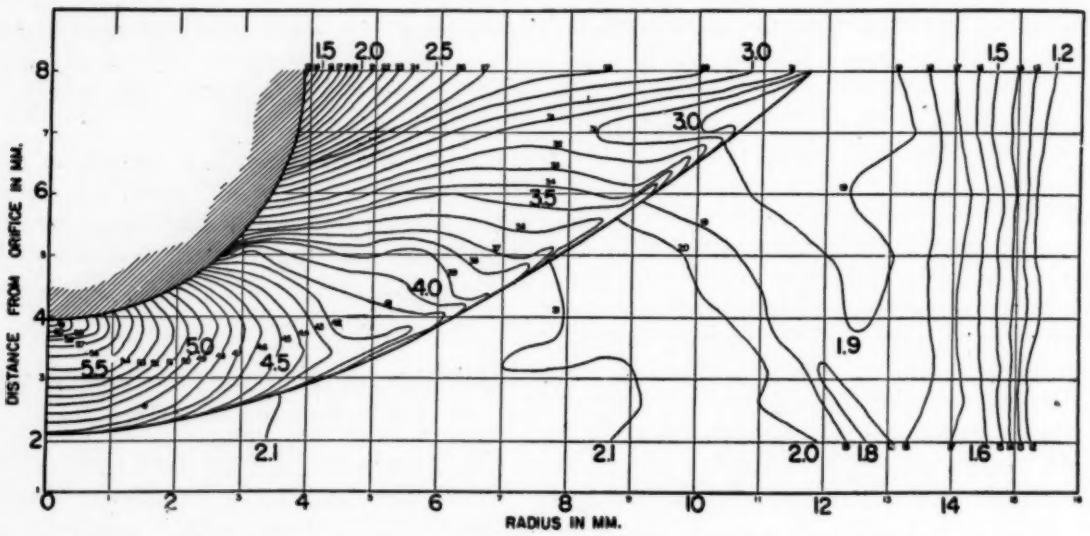

FIG. 24. Isopycnal chart for air flow about a sphere. Mach No. 1.70. Contours labeled in mg/cm³.

[15] See P. C. Keenan and H. Polachek, "Measurement of densities in shock waves by the shadowgraph method," NAVORD Report 86-46.

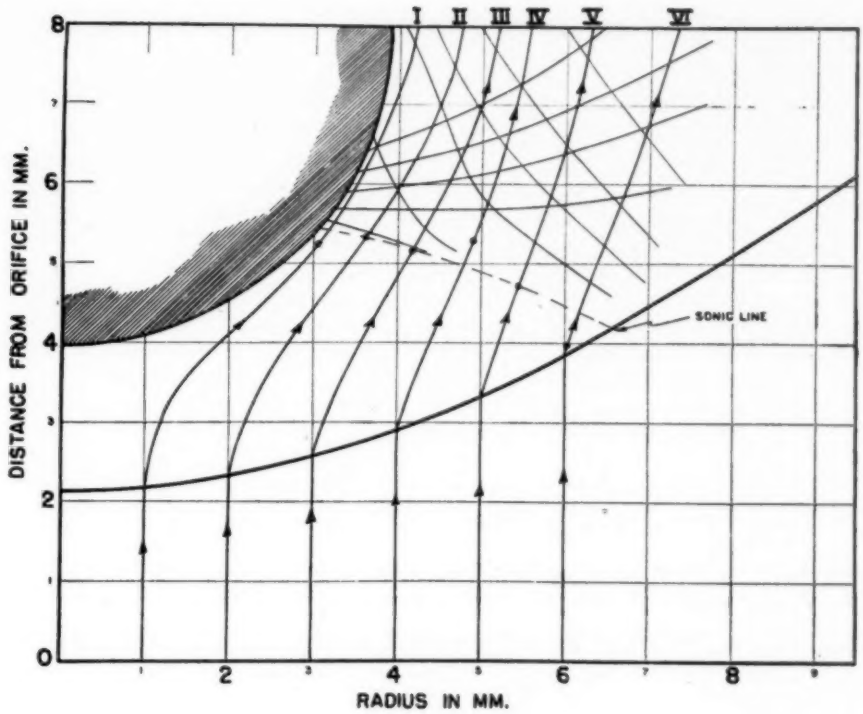

FIG. 25. Stream and Mach lines about a sphere. Mach No. 1.70.

working section cannot extend beyond the point where the head wave intersects the free boundary of the jet. Stream lines, Mach lines, and the sonic line have been calculated in the case of the sphere by the method outlined above for the 45° cone, and the results are given in Fig. 25. If pressure, temperature, Mach number, and velocity in the region between sphere and detached shock wave are calculated in the same way as for the 45° cone, the coefficients for the various stream lines show small differences, just outside the experimental accuracy, due to small rotational effects.[16] Pressure coefficients on the sphere surface are given in Table IV. They were calculated by use of the equation $P=0.412\rho^{1.404}$ for stream line 1.

The results obtained indicate that for axially symmetric slender bodies, such as projectiles, surface pressures could be determined from the analysis of interferograms without exact knowledge of the stream lines, by making a reasonable guess at the path of the gas flowing along the surface.

[16] See Table V in NAVORD Report 93–46.

Domain Structure and Dielectric Response of Barium Titanate Single Crystals*

B. MATTHIAS** AND A. VON HIPPEL
Laboratory for Insulation Research, Massachusetts Institute of Technology, Cambridge, Massachusetts

(Received February 24, 1948)

Single crystals of $BaTiO_3$ have been grown and investigated by means of the polarization microscope, x-ray diffraction, and their dielectric and piezoelectric response. It has become possible to see the domains in the ferroelectric state and to change their number, size, and orientation. Wall displacements and the alignment of such domains, for which well-known indirect evidence exists in the case of ferromagnetics, have been observed in both polarized and unpolarized light, and the influence of temperature and electric fields on the domain structure and orientation of the polar axis have been investigated. In addition to the Curie point near 120°C, there exist two polymorphic transitions near 5°C and −70°C. A tentative explanation for the development of the ferroelectric state is given which brings the new ferroelectric group of the titanates into close relation to those of the tartrates and phosphates.

1. INTRODUCTION

INVESTIGATIONS on titania ceramics have made it seem probable that $BaTiO_3$ and solid solutions of barium-strontium and barium-lead titanates represent a new class of ferroelectric materials.[1–3] Ferroelectrics, the electric analogs of ferromagnetics, were previously discovered among the tartrates and the dihydrogenphosphates.[4] An accurate study of the titanates necessitated proceeding from multicrystalline materials to studies on single crystals.

A first attempt to grow single crystals of $BaTiO_3$ in an arc furnace proved unsuccessful.[1] Crystals of hexagonal, cubic, and monoclinic symmetry, however, were obtained in Switzerland by Blattner, Matthias, Merz, and Scherrer from ternary melts.[5,6] Their method was taken up in this laboratory and further improved. An accurate chemical analysis of the hexagonal modification in Zürich[5] and of the cubic one here[7] established that both correspond to the composition $BaTiO_3$. Only the latter type is ferroelectric and is identical with the cubic modification identified previously in ceramics.[1,8]

Since then these cubic crystals have been investigated in detail. Dielectric constant and

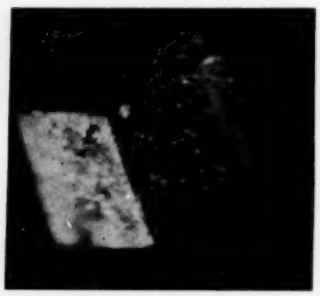

FIG. 1. Cubic $BaTiO_3$ crystal.

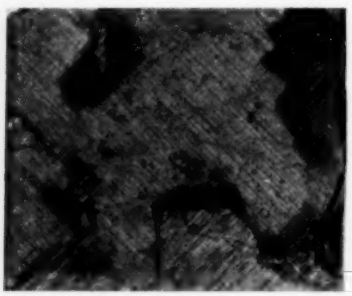

FIG. 2. Crystal type 1 (45° stripes).

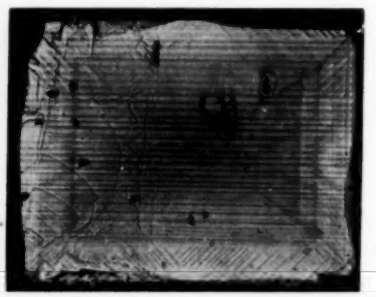

FIG. 3. Crystal type 2 (stripes parallel to one cube edge).

* The work reported in this document was made possible through support extended to the Massachusetts Institute of Technology, Laboratory for Insulation Research, jointly by the Navy Department (Office of Naval Research) and the Army Signal Corps under ONR Contract N5ori-78, T.O.1.

** Present address: Bell Telephone Laboratories, Murray Hill, New Jersey.

[1] A. von Hippel and coworkers, NDRC Reports 14–300 (1944), 14–540 (1945); A. von Hippel, R. G. Breckenridge, F. G. Chesley, and L. Tisza, J. Ind. Eng. Chem. **38**, 1097 (1946).

[2] B. M. Wul, J. Phys. USSR. **10**, 95 (1946); *ibid.*, Nature **157**, 808 (1946).

[3] S. Roberts, Phys. Rev. **71**, 890 (1947).

[4] G. Busch, Helv. Phys. Acta **11**, 269 (1938).

[5] H. Blattner, B. Matthias and W. Merz, Helv. Phys. Acta **20**, 225 (1947).

[6] H. Blattner, B. Matthias, W. Merz, and P. Scherrer, Experientia **3**, 4 (1947).

[7] B. Matthias, R. B. Breckenridge, and D. W. Beaumont Phys. Rev. **72**, 532 (1947).

[8] H. D. Megaw, Proc. Roy. Soc. London **A189**, 261 (1947).

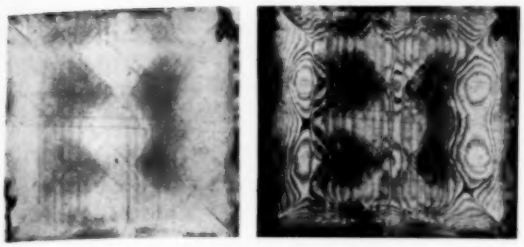

A B

FIG. 4. Crystal type 3. (A) Natural light. (B) Polarized light.

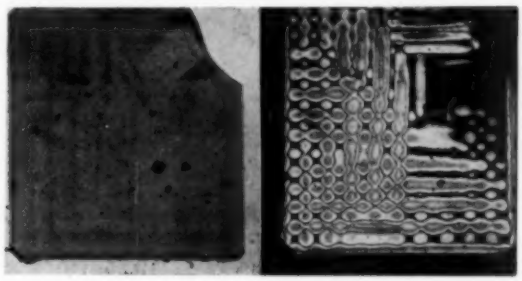

A B

FIG. 5. Crystal type 4. (A) Natural light. (B) Polarized light.

loss, and piezoelectric effect have been measured as a function of temperature, crystallographic orientation, and biasing voltage. It has also become possible to follow the formation of ferroelectric domains and to observe their orientation, growth, and decay under various field and temperature conditions.[9] The present paper summarizes our experiments and draws qualitative conclusions as to the mechanism of ferroelectric polarization and its action in ceramic materials.

2. APPEARANCE OF THE BARIUM TITANATE CRYSTALS

Figure 1 shows a crystal of the cubic modification. The hexagonal and monoclinic ones have not yet been studied in detail. The crystals are usually obtained in the form of flat plates. Growing conditions and discoloration have been discussed previously.[7,9]

A microscopic inspection reveals that the plates exhibit a great variety of structures. To describe them, it will be convenient to refer to four groups of patterns which either alone or combined have been found in all crystals observed thus far.

(1) The crystal may be divided into regions shaded by fine parallel lines, oriented at an angle of 45° to the cube edges (Fig. 2). The lines are sometimes so closely spaced as to blur the transparency of the crystal. Observed between crossed Nicols, the crystal shows parallel extinction except in regions of great strain.

(2) The crystal may have stripes of varying widths parallel to one cube edge. Between crossed Nicols such a crystal shows parallel extinction and is, in intermediate positions, white or faintly colored (Fig. 3).

(3) The crystal appears transparent with a very slight indication of faint lines parallel to the cube edges, spaced rather widely from each other. Between crossed Nicols, strong colors are seen which give the appearance of birefringent or of photo-elastic strain patterns. They are divided by black lines and regions which show a centered uniaxial interference figure. These black regions are free from striation and strains (Fig. 4).

(4) The crystal is transparent in natural light. Between crossed Nicols, however, it shows an extremely regular square net pattern (Fig. 5).

3. EFFECT OF TEMPERATURE

Measurements on the barium titanate ceramics have established that $BaTiO_3$ goes through three transitions between approximately 120°C and liquid-air temperature.[1,2] With decreasing temperature the lattice changes near 120°C from cubic to pseudo-cubic; this is the "Curie point" of the material at which temperature the dipoles seem to line up spontaneously and thus ferroelectricity develops. In addition, there exist

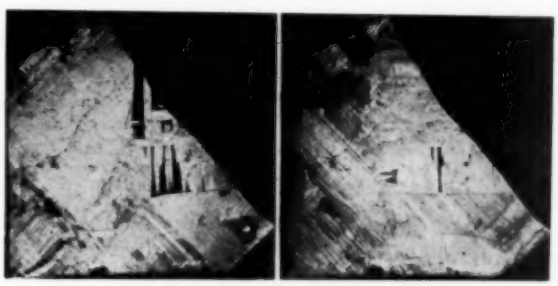

A B

FIG. 6. (A) Initial pattern at 25°C. (B) The same crystal at 25°C after heating above Curie point.

[9] B. Matthias and A. von Hippel, Phys. Rev. **73**, 268 (1948).

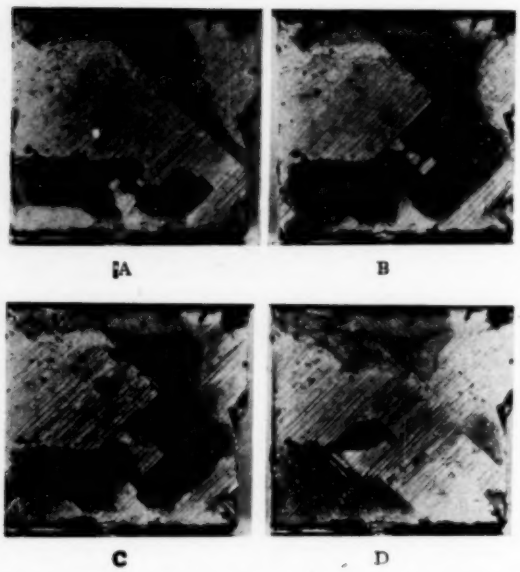

FIG. 7. Effect of electric field on domain structure of $BaTiO_3$ crystal. (A) No field applied. (B) +2000 volts/cm. (C) Field removed. (D) −2000 volts/cm.

regions of anomalous dielectric response near 5°C and −70°C, which become pronounced in the ceramics at higher field strength.

In observing single crystals on a heating stage, it was found that with rising temperature near the Curie point the 45° stripes and the broad parallel bands disappear; the plates become completely clear and isotropic. *Vice versa*, in lowering the temperature into the ferroelectric region, first the widely spaced bands begin to subdivide the field of view, next the shading by 45° stripes develops and a pattern builds up which is more or less different from the original one (Fig. 6).

Lowering the temperature through the second and third transition regions does not affect the ferroelectric state as such, but rather the position of the optical axis. Near 5°C this axis seems to rotate by 90°; simultaneously, crystals consisting of a single domain which previously showed a uniaxial interference figure, become strongly birefringent. This might be due either to a rotation of the optical axis, or to a reduction of crystal symmetry. Passing below the third transition point near −70°C seems partly to reverse this effect. The transitions may proceed rather gradually, starting at one corner and propagating throughout the crystal; sometimes they appear delayed, and sometimes they are extremely sluggish. Returning from any of these transitions to room temperature, one obtains, in general, not exactly the initial pattern, but a similar one.

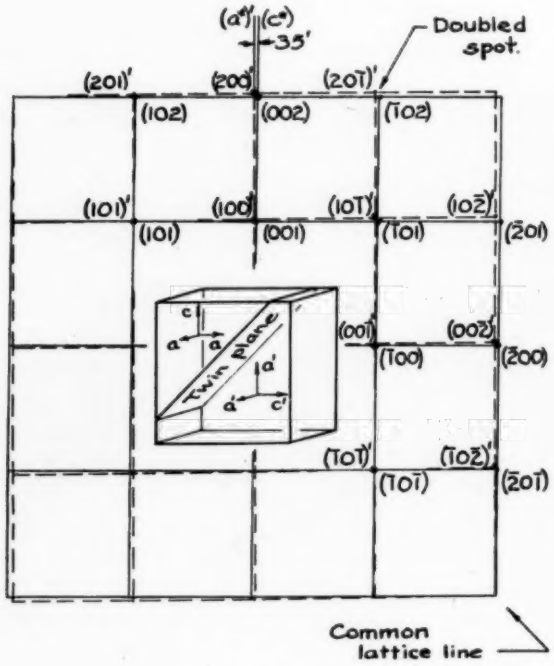

FIG. 8. Precession photograph of a two-domain crystal.

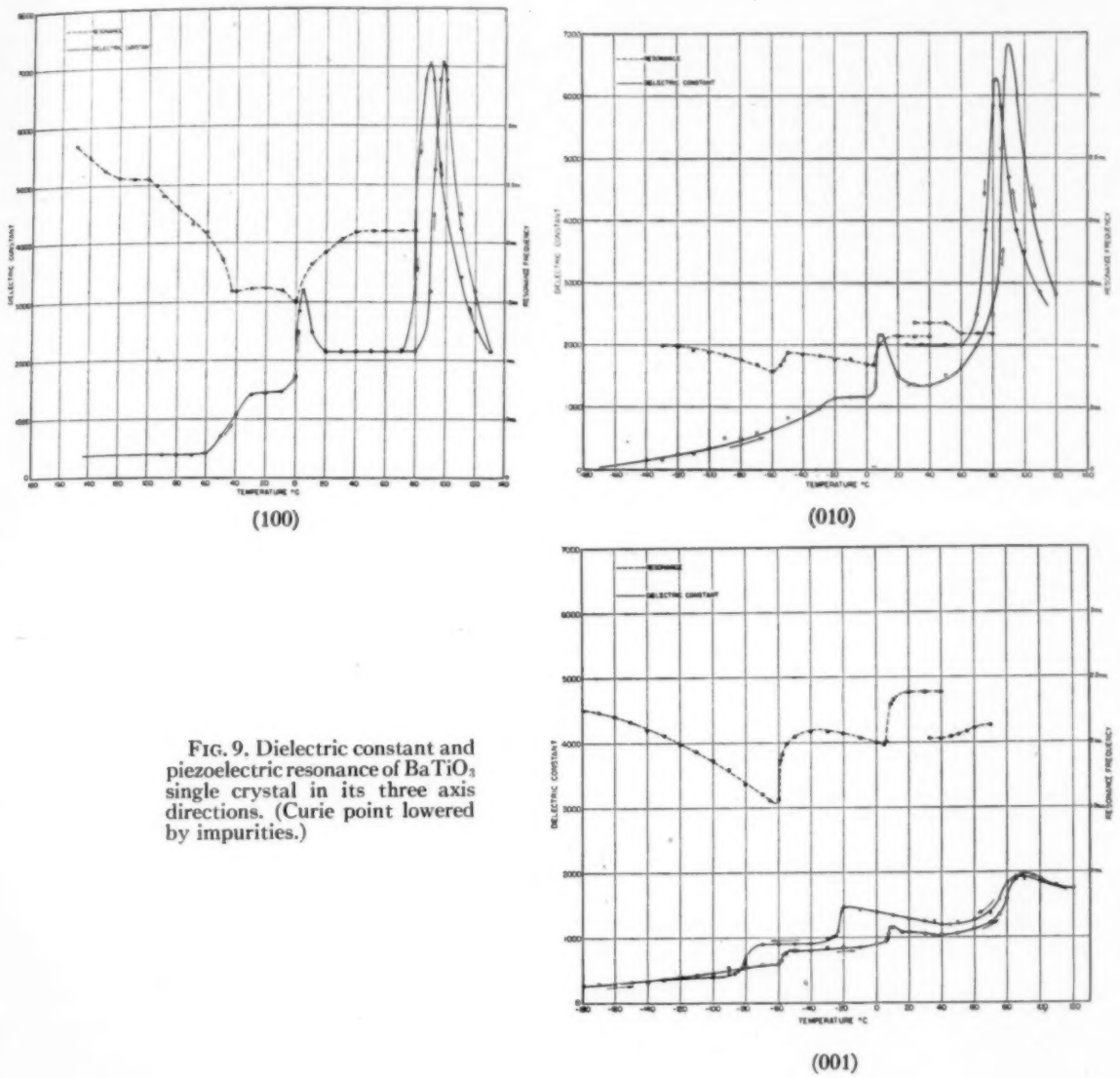

(100) (010) (001)

FIG. 9. Dielectric constant and piezoelectric resonance of $BaTiO_3$ single crystal in its three axis directions. (Curie point lowered by impurities.)

These observations make one already suspect that the patterns are a visual expression of domain structures which develop in the ferroelectric crystals by the aligning of dipole groups in various directions. The action of electric fields on these structures leads to a closer correlation.

4. EFFECT OF ELECTRIC FIELDS

Figure 7 shows in sequence: the initial pattern of a crystal at room temperature, the effect of a d.c. field, the crystal after removal of the field, and finally the structure with the voltage reversed. One observes clearly how areas grow or contract, how sections of new shading suddenly appear, and how disconnecting the voltage leaves a remanent state which requires a counter voltage for removal.

Closer inspection in polarized light with the field parallel or perpendicular to the crystal plate leads to a correlation between the visual structure of a crystal section and the direction of the polar axis. With a moderate electric field parallel to the crystal plate, the areas covered with 45° stripes expand or contract, but are preserved, while the regions initially free of the striation tend to assume it. At very high field strength, the lines disappear, the crystal clears

up, and gives, between crossed Nicols, the picture of a uniaxial crystal observed perpendicularly to the optical axis. If, on the other hand, the field is applied perpendicularly to the crystal plate, and one observes through semitransparent electrodes, the regions without striations are seen to grow at the expense of the 45° line regions; strongly colored bands parallel to the crystal edges appear, and with increasing field, the crystal darkens until the centered uniaxial cross appears showing the optic axis to be parallel to the line of sight.

Below the Curie point, a single crystal breaks up into spontaneously polarized domains oriented with their polar axes in one of the three cube-edge directions. The lattice expands parallel to the axes and contracts perpendicularly to them; hence, the counteracting stresses of different domains produce a complicated stress pattern. An external field of sufficient intensity can turn all axes into the field direction, thus creating a tetragonal crystal with the polar axis identified as the optical axis. The rotation of an axis may be seen in stroboscopic light when a.c. fields are applied by observing the changing pattern of domains. The biaxial pattern disappears when the polar axes become aligned in the field direction.

Further information as to the axis orientation has been obtained from Weissenberg and from Buerger precession x-ray patterns. Figure 8 gives the precession photograph of a small crystal which contained only two domains; it shows the tetragonal lattice of one superimposed on that of the other. These reciprocal lattices have the points (101) in common, thus demonstrating that this plane of the direct lattice is a twin plane. Since the reciprocal lattice is not perfectly square, reflection of the lattice across this plane causes other points to split into double spots, as one lattice deviates from the other. The twin angle shown (35′) corresponds to the c/a ratio of 1.010 reported by Megaw[10] from x-ray studies on powdered ceramics.***

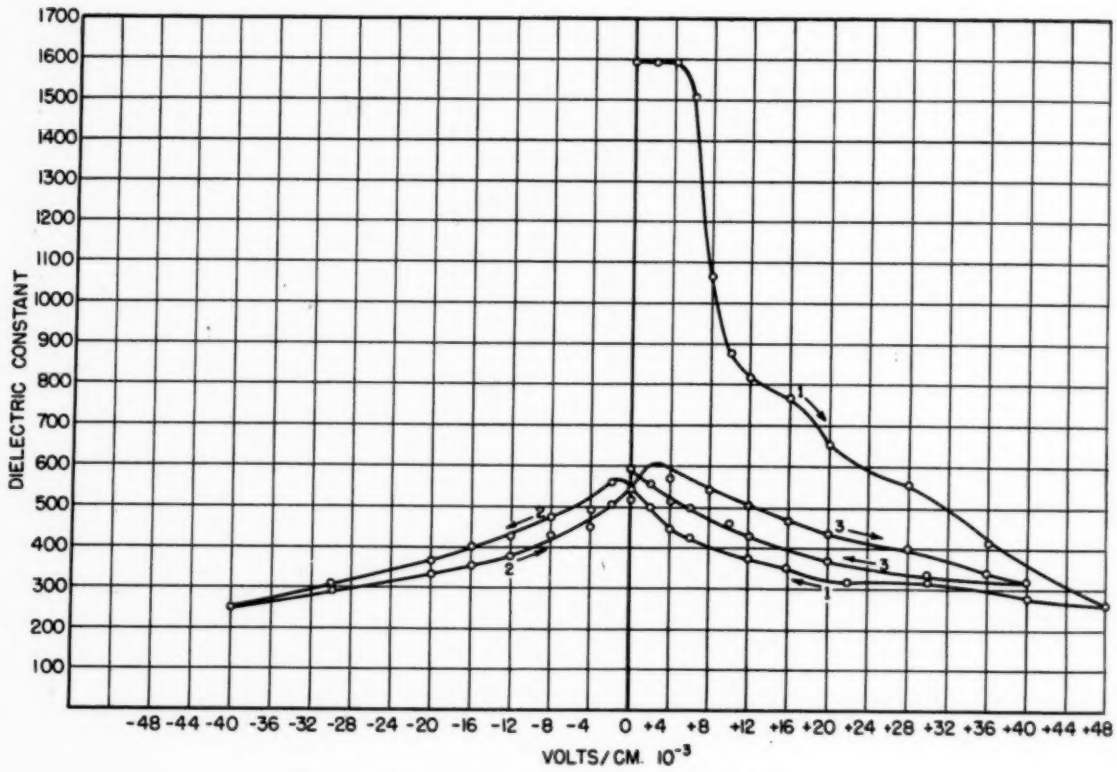

FIG. 10. Dielectric constant as function of biasing field.

[10] H. D. Megaw, Trans. Faraday Soc. **42A**, 224 (1946).

*** Detailed x-ray investigations on single crystals are being made by H. T. Evans, Jr.; the results will be published at a later date.

5. DIELECTRIC AND PIEZOELECTRIC MEASUREMENTS

Figure 9 shows the dielectric constant and piezoelectric resonance frequency measured on the same crystal in the three cube-edge directions as a function of temperature in a small a.c. field of less than 10 volts/cm at 1 kc/sec. The piezoelectric resonance frequency reaches a minimum and the dielectric response a maximum at the two lower transitions because the deformability under electric stress becomes high at these points.[11] When the Curie point is approached, the anisotropy begins to disappear and the piezoelectric response ceases. Two of the three characteristics are nearly identical since most of the domains had their polar axes perpendicular to the major plane of the crystal.

More quantitative information can be obtained by selecting crystals exactly oriented with their polar axes either perpendicular or parallel to the plate surface, i.e., either type 3 or 2. The dielectric constant parallel to the polar axis amounts to about 550 and perpendicular to it about 1600–1800 at room temperature. This anisotropy can be demonstrated by the following experiment (Fig. 10). A small a.c. field is applied perpendicularly to the polar axis and the dielectric constant determined. Then a biasing field is superimposed in the same direction and gradually increased, thus rotating the polar axis by 90° into the parallel position. From here on, a decrease and reversal of the bias voltage changes only the sign of the polar axis but not its angular position. Hence the a.c. field measures now the first derivative of the hysteresis loop for the parallel orientation.

The total charge density bound by a crystal saturated in field direction was about 12×10^{-6} coulomb/cm^2, in relatively good agreement with a value 16×10^{-6} coulomb/cm^2 reported by Hulm.[12]

By attaching small mirrors to the edges of a single crystal, the mechanical deformation under the stress of a d.c. field could be observed. Due to the domain structure, the results cannot be evaluated unambiguously, but show the superposition of a linear and a quadratic piezoeffect. By evaluating the linear effect, which will be largest with the field applied parallel to the optical axis, one obtains a piezomodulus which seems at least one order of magnitude higher than d_{14} of rochelle salt. This large piezoeffect is even audible when one excites a crystal by an alternating field.

[11] B. Matthias, Helv. Phys. Acta **16**, 99 (1943).
[12] J. K. Hulm, Nature **160**, 126 (1947).

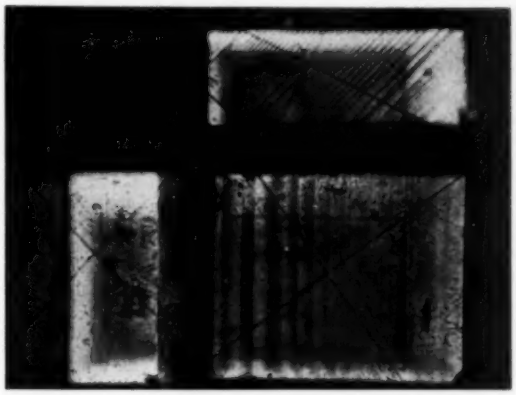

FIG. 11. Striation on a crystal seen from three perpendicular directions.

6. DETAILS OF THE DOMAIN STRUCTURE

Figure 11 shows the same crystal viewed from three perpendicular directions. This picture demonstrates the correlation between the 45° lines and the parallel regions of crystal types 1, 2, and 3. Furthermore the x-ray results indicate that the polar axis turns 90° in crossing each of the 45° lines. These facts lead to the arrangement of domains as shown schematically in Fig. 12.

Increasing field strength reduces the width of the domains that lie with their polar axes perpendicular to the field until they disappear and a completely clear crystal results. At an intermediate stage of domain formation wedge-shaped areas may be observed (Figs. 12 and 13).

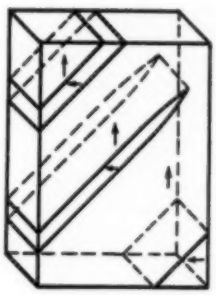

FIG. 12. Correlation between striations and directions of polar axes.

FIG. 13. Wedge-shaped domains.

The pattern of type 4 has a mesh size of the net equal to about twice the thickness of the crystal.†

7. DISCUSSION

The results thus far obtained suggest the following concept: in the cubic structure above the Curie point the Ti^{+4} ions oscillate about the centers of the $Ti-O_6$ octahedra with large induced dipole moments, but without effective mutual coupling. As Eucken and Büchner[13] have pointed out, the Ti ion has a tendency to change from ionic to covalent bonding as its distance to an oxygen atom decreases; hence, we expect the largest induced moments in the direction of the valence vibrations. When the Curie point is approached, the interaction between these induced dipoles overcomes the thermal agitation and the Ti ions are locked in an eccentric position displaced toward one of the six oxygen neighbors. This displacive transformation,[1,14] a case analogous to that of rochelle salt, causes the unstrained crystal to become tetragonal, but generally it subdivides into domains.

In rotating the polar axis, six minimum positions are observed in the cube-edge directions toward the six oxygen neighbors. In a strong external field all intermediate positions may be assumed by the polar axis, and it is not surprising that the high symmetry of the $Ti-O_6$ constellation allows barium titanate ceramic materials to approach the behavior of single crystals.

With decreasing temperature, two polymorphic transitions seem to take place near 5°C and −70°C which change the symmetry of the crystal. Such transitions might be anticipated when one considers that the Ti ion can use the $3d$, $4s$, and $4p$ orbitals for the formation of covalent bonds. The experimental indication is that below the Curie point, first octahedral bond orbitals are preferred, but as the structure contracts, and the thermal vibrations decrease, other hybrid bonds may become dominant.

If the situation is as described, the ferroelectric group of the titanates may bear a true relationship to those of the tartrates and phosphates. The ferroelectric state in the latter two groups is presumably caused by hydrogen bonds, which may be described as covalent in one direction and ionic in the other. This description seems also to apply to the titanium-oxygen bond, hence such dual bond character may be a prerequisite for ferroelectricity. Permanent dipoles in solids cannot ordinarily line up freely because of hindered rotation, but dipoles induced by vibrations may do so. The dual bond character can impart high dipole moments and, by mutual coupling under favorable structure conditions, may overcome the thermal agitation of the lattice even above room temperature.

Investigations are in progress which we hope will lead to a more quantitative treatment of the ferroelectric state of $BaTiO_3$.

† A detailed study of domain structures as equilibrium arrangements is at present being undertaken by P. W. Forsbergh, Jr. The wedge-shaped areas were first observed by him.

[13] A. Eucken and A. Büchner, Zeits. f. physik. Chemie **B27**, 321 (1934).

[14] L. Tisza, Phys. Rev. **72**, 532 (1947).

Crystal Orientation in Al by Slow Neutron Diffraction*

G. ARNOLD AND A. H. WEBER**
Argonne National Laboratory, Chicago, Illinois
(Received February 13, 1948)

Investigations are described of crystal orientation effects in various forms of aluminum by measurement of total cross sections in the neutron energy range 0.003 to 0.05 ev approximately.

1. INTRODUCTION

THE elastic coherent scattering of neutrons has been discussed theoretically by Goldberger and Seitz.[1] Fermi *et al.*[2] have studied, theoretically and experimentally, the transmission of slow neutrons through microcrystalline materials and obtained excellent agreement of theory and experiment for crystal diffraction effects in Be and BeO.

Sachs *et al.*,[3] analyzed by a simple theory the effect on slow neutrons of non-random orientations of the microcrystals in extruded graphite and compared the non-random with the random effect (powdered graphite). Their experimental results were in good agreement with the theory.

The present experiments include neutron diffraction investigations of crystal orientation effects in samples of microcrystalline aluminum prepared in several ways that were designed to influence the orientation of their crystallites.

2. EXPERIMENTAL PROCEDURE

The experiments were carried out by measuring the total cross section in the thermal neutron region of the various aluminum samples by the transmission method.[4] The mechanical slow neutron velocity selector[5] in conjunction with the Argonne heavy-water pile was used. Figures 1 to 4 illustrate typically the results obtained. The following points are noted in addition to the explanatory legends. The Al samples for Figs. 1–3 were machined in the form of rectangular parallelepipedon, presenting a cross-sectional area of $\frac{3}{4}$ in. $\times$ 3 in. to the neutron beam with a depth of $2\frac{3}{4}$ in. in the direction of the beam. The Fig. 4 sample was made of "atomized alumina" [6] pressed with an hydraulic press into a right circular cylinder of $3\frac{1}{2}$-in. diameter and 4-in. length, arranged so that a $\frac{3}{4}$-in. $\times 3\frac{1}{4}$ in. cross-sectional area by a 4-in. depth was presented to the neutron beam.

The curves are either corrected for "dead-time" errors of the counter circuits[7] or were made with the improved circuits of the same instrument which automatically eliminate dead-time errors. Upon each of Figs. 1–4 the absorption cross section, assuming a $1/v$ relation, has been drawn as a dashed line. These absorption curves were located by the point shown circled, 0.23 barn at 0.025 ev.[8] Thus, the total ordinates of the curves of Figs. 1–4 represent total cross sections (coherent elastic scattering cross section plus absorption cross section plus incoherent scattering); the portions of the ordinate distances from the dashed absorption curves up to the solid line are the coherent elastic scattering cross sections plus some small incoherent scattering. The magnitude of the incoherent scattering is shown by the separation between the dashed and solid curves between about 0.002 and 0.0035 ev and is seen to be about 0.25 barn.

* This document is based on work performed under Contract No. W-31-109-eng-38 for the Atomic Energy Project at the Argonne National Laboratory.
** The work reported was done while this author was on leave from St. Louis University, St. Louis, Missouri.
[1] M. L. Goldberger and F. Seitz, Phys. Rev. **71**, 294 (1947).
[2] E. Fermi, W. J. Sturm, and R. G. Sachs, Phys. Rev. **71**, 589 (1947).
[3] R. G. Sachs, V. Myers, and G. Arnold (to be published).
[4] See, for example, W. J. Sturm, Phys. Rev. **71**, 757 (1947).
[5] T. Brill and H. V. Lichtenberger, Phys. Rev. **72**, 585 (1947).
[6] Composed of particles generally spherical in shape (approximately 80 percent processed through No. 325 mesh screen and 20 percent through No. 100 mesh screen), impurities (iron, silicon, copper) less than 1 percent. This material was a gift of the Aluminum Company of America.
[7] Report 4010, Argonne National Laboratory.
[8] L. Seren, W. Sturm, and W. E. Mayer, Report CP1175, Argonne National Laboratory.

The long wave-length cut-off positions[9] of principal Bragg planes for Al (f.c.c.) are shown on Figs. 1–4.

3. RESULTS, DISCUSSION

Figures 1 and 2, for cold-drawn half-hard Al, exhibit the principal orientation effects observed in these experiments. Figure 1 was obtained for the neutron beam incident parallel to the axis of the rod from which the sample was cut, and Fig. 2 was obtained for the neutron beam incident perpendicular to the rod axis. The considerable differences between the two curves establish at once the presence of orientation effects. The main features of the Figs. 1 and 2 cross-section curves can be explained by assuming preferential orientation of the [111] and [100] axes in the direction of the axis of the original aluminum rod. Figure 5 shows diagramatically the effect of the assumed preferential orientation of these axes on the principal Bragg planes[10] and will be found helpful in understanding the cross-section curves.

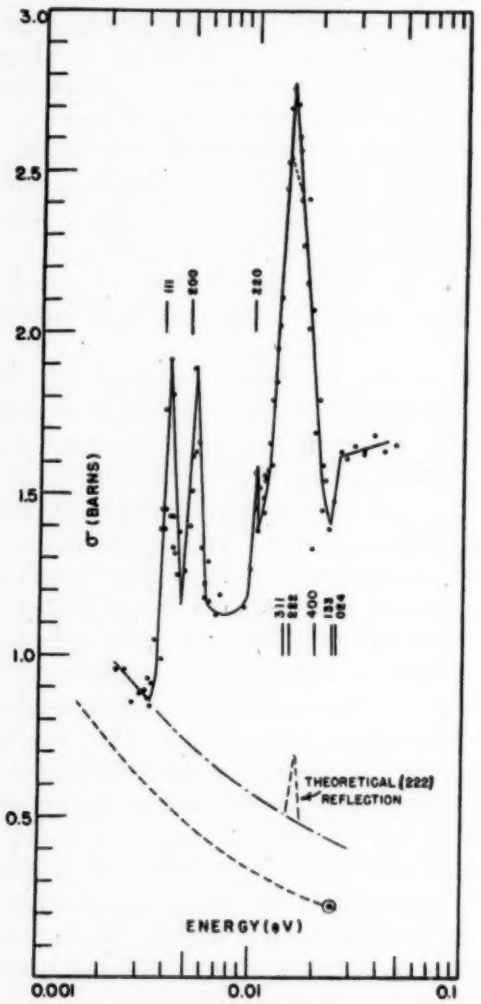

FIG. 1. Total cross section *vs.* neutron energy curve for cold-drawn Al (designated 2S ½-hard) rod with neutron beam incident *parallel* to the Al rod axis.

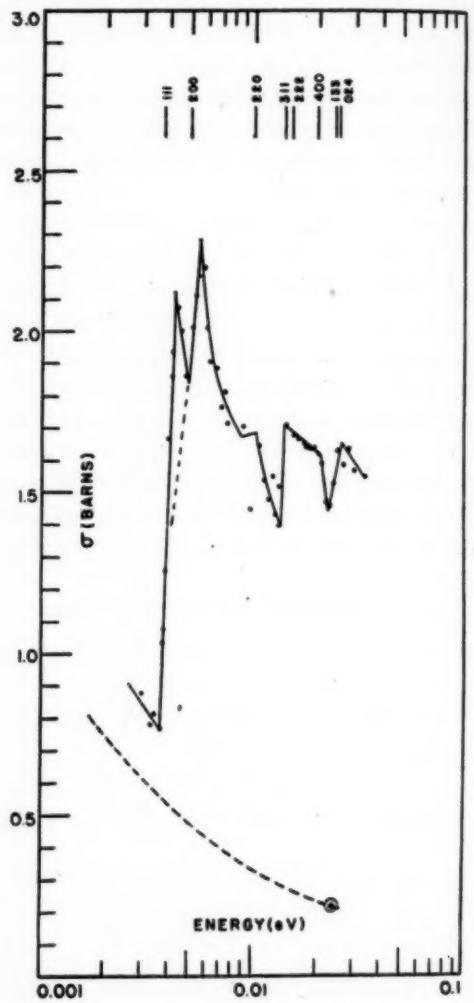

FIG. 2. Total cross section *vs.* neutron energy curve for same specimen as Fig. 1 but with neutron beam incident *perpendicular* to the Al rod axis.

[9] Calculated by $\lambda = 2d$ in conjunction with

$$\lambda_{\text{in A}} = 0.285/(E_{\text{in ev}})^{\frac{1}{2}}$$

where E is the neutron energy and the other symbols have the conventional meaning.

[10] Compare W. T. Sproull, *X-Rays in Practice* (McGraw-Hill Book Company, Inc., New York, 1946), p. 454, Table 20–21.

Consideration of Figs. 1 and 5 shows that for the neutrons incident parallel to the Al rod axis, the [111] and [100] axes alignments in the rod direction produce, respectively, {111} and {200} type planes perpendicular to the incident neutrons. Hence, there should be the observed large coherent scattering at the long wave-length cut-off for these planes.

The large value of the cross section near the (222) cut-off (at about 0.015 ev, Fig. 1) appears at first an anomaly since (222) reflection is merely second-order (111) reflection, and since coherent scattering cross section varies directly as λ^2 (i.e., $1/E$),[11] σ_{111} should be about 4.5 times

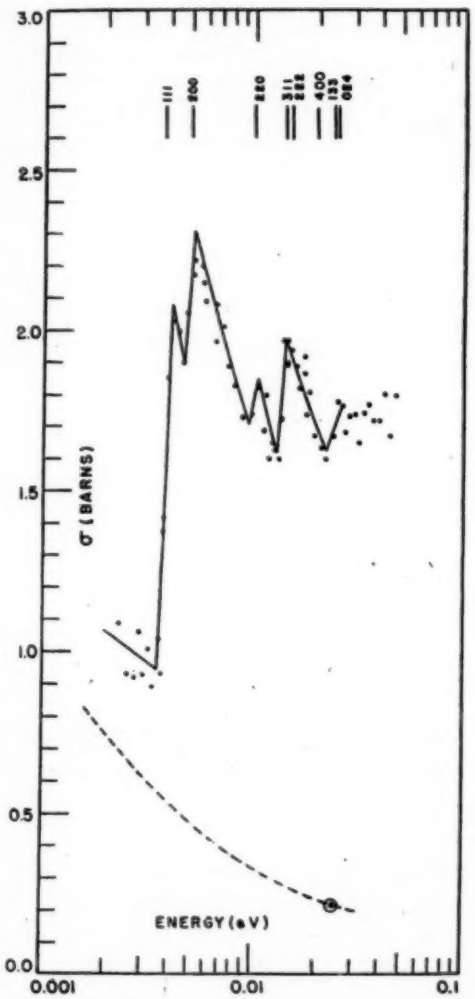

FIG. 3. Total cross section *vs.* neutron energy curve for a pellet pressed from Al powder with neutron beam incident parallel to compression direction.

[11] Reference 2, Eq. (4).

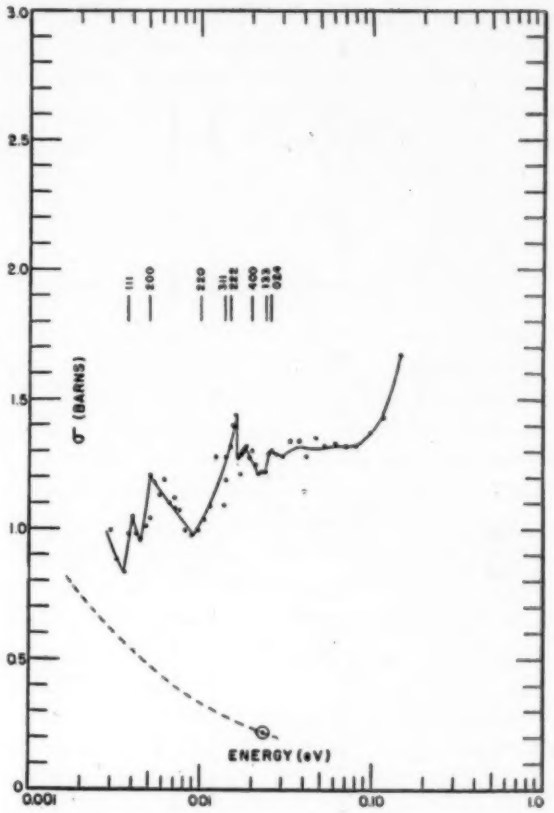

FIG. 4. Total cross section *vs.* neutron energy curve for cast Al.

σ_{222}. It is considered, therefore, that the large observed cross section near the (222) cut-off is due chiefly to the nearby (113) and (220) planes. Figure 5 shows the several possibilities for the required (113) and (220) reflections and the conclusion is seen to be quite reasonable. Following this line of reasoning the theoretical σ_{222} was calculated from the experimental shape of the σ_{111} peak, assuming that the coherent scattering cross section varies directly as λ^2, and appears as the dashed peak labeled "theoretical (222) reflection" drawn from the dot-dashed absorption and incoherent scattering cross-section curve. Separating this experimental curve lowers the prominent peaks near the (222) plane cut-off to approximately the dashed line (at about 2.5 barns).

For neutrons incident perpendicular to the Al rod axis, Fig. 2 shows the importance of the {111} and {200} reflections. Consideration of Fig. 5 establishes the fact that some {200} planes only

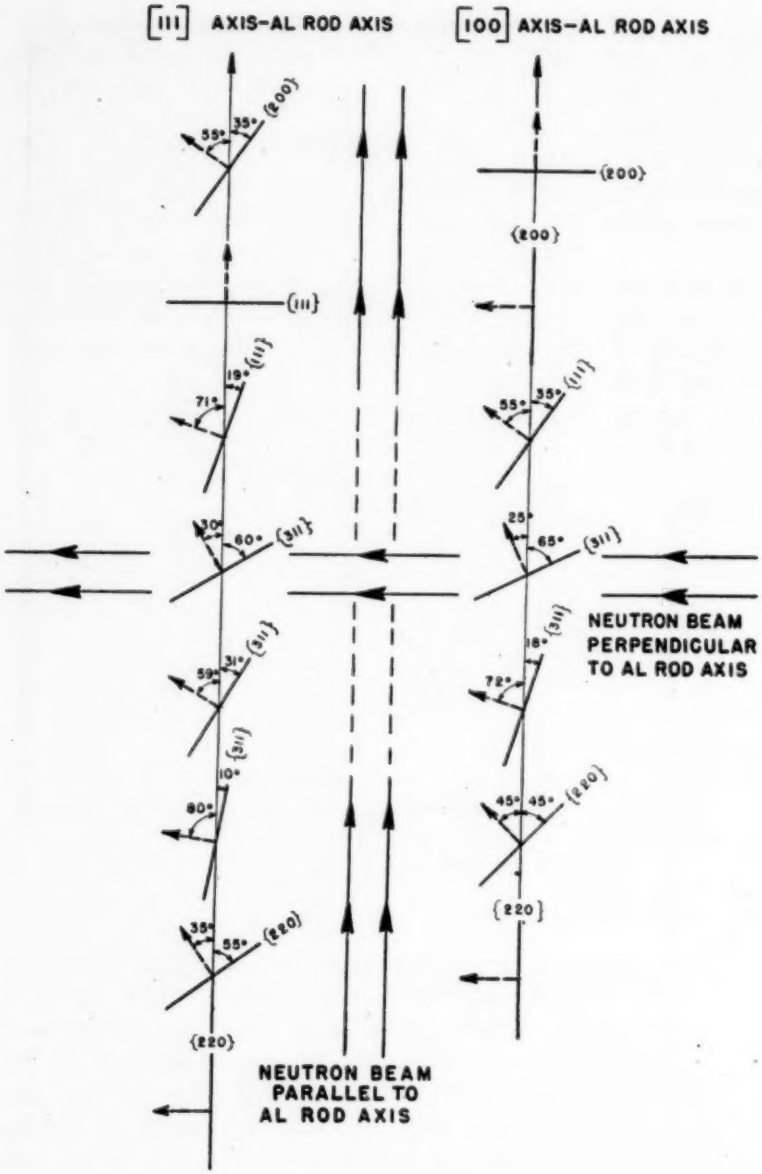

FIG. 5. Orientation of principal Bragg planes relative to [111] and [100] axes assumed in direction of Al rod axis and relative to the two directions of incident neutrons. The dashed arrows represent normals to the Bragg planes.

are presented perpendicular to incoming neutrons with the {111} planes at fairly large Bragg angles. Hence it is concluded that the dominant coherent scattering is by the {200} planes, with at least half of the steep rise associated in position with the nearby {111} planes being actually caused by the {200} reflection.[12] The dashed line located between about 1.4 and 1.85 barns is an approximate attempt to illustrate this conclusion. It is seen that this assumption diminishes considerably the apparently large {111} reflection. This is a likely result.

Inspection of Fig. 5 also should emphasize the possibility of limited preferential orientation of the Bragg planes shown about the two orientation axes, [111] and [100]. For neutrons incident parallel to the orientation axes, any limited orientation of Bragg planes about these axes will have no effect, but for the neutrons incident perpendicular to these axes, orientation of planes

[12] In interpreting the curves shown it must be remembered that the mechanical velocity selector has finite resolution so that the rises in cross section in the vicinity of Bragg cut-offs are not infinitely steep, as is ideally required.

about the [111] and [100] axes would be important. Perhaps it is also obvious that alignment of crystals preferentially orientated is never perfect so that the angles shown by Fig. 5 vary somewhat in the actual samples.

It is seen that the total cross section *vs.* energy curve for the pressed Al powder, Fig. 3, with neutrons incident in the direction of compression, is closely similar to Fig. 2, and therefore the orientations for these two cases must be approximately the same.

The cross-section curve for the cast Al sample, Fig. 4, exhibits relatively weak Bragg scattering, although fairly large crystals could be seen in the specimen by visual inspection. Apparently the crystals are so orientated as to avoid any considerable Bragg reflection.

In addition to the cold-drawn half-hard Al, the pressed Al powder and the cast Al, two other types of Al, 2-SO (soft) aluminum, and a 99.95 percent pure Al casting which had been worked with several passes to reduce grain size, were measured. The soft Al specimen (cut from a drawn rod) yielded total cross section *vs.* neutron energy curves very similar to Figs. 1 and 2 for neutron beams parallel and perpendicular to the soft Al rod. Hence, crystal orientations in the soft Al are about the same as for the cold-drawn half-hard Al. The results for the pure casting established that the small impurities present in the specimens were of little significance in determining the shape of the Figs. 1–4 curves.

4. CONCLUSION

The results show that crystal orientation effects can be investigated conveniently with monoenergetic neutrons as well as with x-rays. It is to be noted that the neutron diffraction experiments yield intensities rather directly since total cross sections are obtained at once, and from these the coherent scattering cross sections can be separated ordinarily without difficulty. The required size of samples, much larger at present for neutron than for x-ray diffraction, has some definite advantages for investigations such as the present one since it is not necessary to work with a small volume of the material being measured.

The authors wish to thank D. J. Hughes and W. H. Zinn of The Argonne National Laboratory for encouragement and material aid in this work.

PHYSICAL REVIEW VOLUME 73, NUMBER 11 JUNE 1, 1948

The Latitude Dependence of Neutron Densities in the Atmosphere as a Function of Altitude

J. A. SIMPSON, JR.
Institute for Nuclear Studies, University of Chicago, Chicago, Illinois
(Received April 2, 1948)

IN order to study nuclear evaporation processes and the origin of neutrons in the atmosphere, a series of experiments was performed in B-29 aircraft which included the measurement of neutron densities for several altitudes at 0°, 19°N, 40°N, and 53°N magnetic latitude. The total vertical intensity of charged particles traversing 5 g/cm² and the vertical intensity of mesons traversing 20 cm of lead were also measured at the same time. The neutron detectors were BF_3 proportional counters surrounded by paraffin cylinders[1] which were covered with cadmium. Two of these detectors containing enriched boron were connected in parallel to a fast amplifier and scaling circuit; a second pair of these detectors containing normal boron was connected with an identical electronic system. These detectors had flat operating characteristic curves of at least 100 volts. They were mounted in the rear pressurized cabin of the plane approximately two feet from any equipment. The detectors respond to neutrons above the cut-off energy for cadmium but are essentially fast neutron detectors. Although they do not have an energy response curve identical with the "long" counters[1]

[1] A. O. Hanson and J. L. McKibben, Phys. Rev. **72**, 673 (1947).

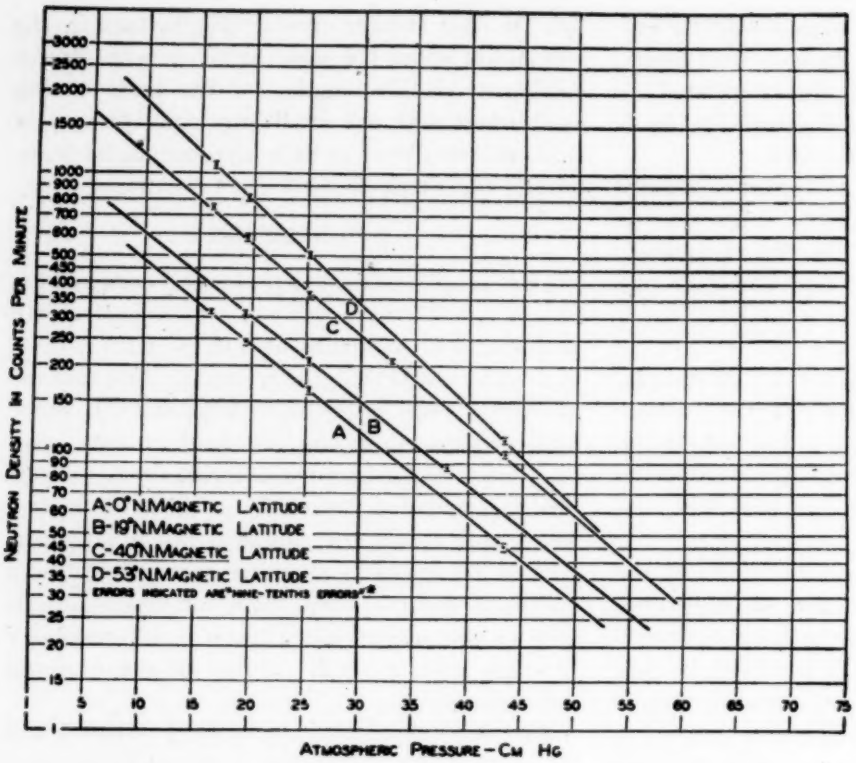

FIG. 1. The relative fast neutron density in the atmosphere.

* The errors shown are such that there is a 0.9 probability that the measured value is within the range of the indicated error.

because the neutrons are incident isotropically, this is not important since these counters are only used to make *relative* measurements. It has been shown that the neutron energy spectrum up to at least 100 ev does not change over the range of atmospheric pressures encountered in this experiment, and that the altitude dependence of the neutron density as measured by these cadmium-paraffin covered detectors is the same as for a bare counter in free space.[2]

In Fig. 1, only measurements were included in which the plane was flown along a course of constant magnetic latitude and pressure altitude. No data were taken under opaque clouds, and it was shown that the measurements were independent of the amount of airplane gasoline and disposition of equipment and personnel in the plane. The constant ratio of counting rates from the enriched boron and normal boron detectors at all altitudes proved that only ionizing events caused by neutron capture were being detected. Data were collected on at least two different days at each latitude, and the flights extended over a period of nine weeks. Points at 16.3 cm Hg and 19.5 cm Hg on the 53°N curve were taken before and after the points on the 0° and 19°N curves.

Each point in Fig. 1 represents from 4000 to 8000 counts, and the error shown is such that there is a 0.9 probability that the measured value is within the range of the indicated error. The atmospheric pressure has been corrected for temperature and instrumental errors. It is seen that the altitude dependence of the neutron density D is adequately represented by $D=D_0 \exp(-bp)$ for the magnetic latitudes between 0° and 53° north. In Table I the values for b are tabulated for p expressed in centimeters Hg. The total exponential absorption in air of the neutron producing radiations is expressed in g/cm² and assumes only vertically incident particles.

There are several independent ways to show that this latitude effect is the same as the latitude effect in free space. For example, the recent free-space measurements of Yuan and Ladenburg[3] at

[2] H. M. Agnew, W. C. Bright, and Darol Froman, Phys. Rev. **72**, 203 (1947); their paper contains references to earlier atmospheric neutron measurements.

[3] L. C. L. Yuan and R. Ladenburg, Bull. Am. Phys. Soc. **23**, 21 (1948).

TABLE I.

Magnetic latitude	b	Exponential absorption g/cm²
0°	0.071±0.003	191±8
19°	0.070±0.003	194±8
40°	0.075±0.003	181±7
53°	0.085±0.004	160±7

53°N mag. lat. and the earlier free-space measurements of Agnew, Bright, and Froman[2] at approximately 43°N magnetic latitude may be compared with Fig. 1 for 53°N and 40°N magnetic latitude after correcting for the differences in latitude. Their measurements are in agreement, within their experimental errors, with the latitude effect shown in Fig. 1 for 40° and 53°.

Measurements of neutron production in lead at 0°, 40°N, and 53°N and in aluminum at 40°N and 53°N mag. latitude were made at a few of the same altitudes at which the neutron densities were measured. These measurements show that the changes of neutron density with latitude correspond to those in free space.

Measurements of neutron density at 25.2 cm Hg between 0° and 56°N at intervals of 2°–5° clearly show characteristic plateau regions near 0° and above 50°N; therefore, a comparison of the results in Fig. 1 may be made with charged particle data in these two latitude regions. Table II gives a preliminary summary of the factor of increase between 0°–3° and 51°–53°N mag. latitude in the vertical intensities of the so-called "soft" component, the meson component as described above, the total ionization,[4] and the neutron densities. These charged particles do not appear to account for the large neutron density latitude effect. However, the slopes of the total ionization curves[4] for 3° and 51° in the pressure range 15–40 cm Hg are in excellent agreement with the 0° and 53° curves in Fig. 1.

It may be concluded that most, if not all, the neutrons in the atmosphere which have been

[4] I. S. Bowen, R. A. Millikan, and H. V. Neher, Phys. Rev. **53**, 855 (1938).

TABLE II. Latitude factor between 0°–3° and 51°–53°N.

Atmospheric pressure cm Hg	Vertical "soft" component	Vertical meson	Total[4] ionization ions/cm³/sec./atmos.	Fast neutron density
45	1.1_4	1.2_2	1.4_5	2.3_2
35	1.1_8	1.2_7	1.6_1	2.6_7
25	1.2_3	1.3_2	1.9_0	3.0_8
15	1.7_7	1.3_6	2.2_2	3.5_2

measured are of secondary origin and arise from processes in which the primary particles are charged particles.

It may be shown from the above data, from $p=15$ to $p=45$ cm Hg, that the ratio of neutron production to ionization production is approximately constant between 0° to 20°N and 20°N to 40°N, but that the ratio has increased by a factor of 3 between 40° and 53°N. An interpretation of the data may be made by assuming that the primary particles, say protons, produce high energy neutrons, protons, and mesons at the top of the atmosphere and that the largest contribution to the neutrons which are measured in the atmosphere arises from the production of high energy nuclear bursts and "stars" by these high energy secondary neutrons and protons along with primary particles. Then, from the change of the neutron-ionization production ratio with latitude it might be concluded tentatively that the magnitudes of the cross sections for nucleon production relative to meson production decreases rapidly with increasing energy of the primary particles. The details and discussion of the experiment along with new data will be published.

The writer particularly wishes to thank Mr. Alex Hoteko for aiding in the construction of apparatus and for assisting in most of the flights and to thank Commander E. Bollay for arranging for these flights. The officers and men of the U. S. Air Force were very cooperative in flying the B-29. A portion of this work was supported by the Office of Naval Research.*

* Contracts N6ori-20, T.O. III and T.O. XVIII.

Precision Wave-Length and Energy Measurement of Gamma-Rays from Au^{198} with a Focusing Quartz Crystal Spectrometer*

JESSE W. M. DUMOND, DAVID A. LIND, AND BERNARD B. WATSON
California Institute of Technology, Pasadena, California

(Received March 29, 1948)

A RECENT paper[1] describes a precision focusing curved crystal x-ray and gamma-ray spectrometer (2-meter focal length) constructed at the California Institute of Technology. This instrument has now been used to study the 0.41-Mev gamma-ray line from a 1-curie source of the artificial radioactive isotope of gold, Au^{198}, of half-life 2.7 days. The source activitated at Oak Ridge by neutron bombardment consisted of a thin flat strip of gold (dimensions: 0.1 mm by 5.0 mm by 30 mm) placed vertically at the focus of the spectrometer and oriented so that with appropriate lead shielding its thin dimension constituted the "slit" which determined the resolution. The gamma-ray spectrum was studied by moving the source along the focal circle with a precision screw[1] which reads directly in x units (calibrated to high precision and also verified by means of several well-known x-ray lines of much longer wave-length) and by plotting the gamma-ray intensity reflected by the (310) planes of the quartz crystal as a function of screw settings. The gamma-ray intensity was measured with our special multicellular gamma-ray Geiger counter (operating with 4 cells and 5 septa) which, in a somewhat earlier form, has already been described.[1] A more detailed description will be given in a later paper. It has a counting efficiency of about 8 percent for lines in the half-million-volt region. Its operation is now satisfactorily stable and reliable. The multicellular counter is shielded from local radioactivity by 2.5 to 3 inches of lead on all sides. It is "shielded" from cosmic-ray background with six auxiliary anticoincidence counters placed immediately above it, and when no radioactive source is in the spectrometer the residual background with all these precautions is 32 counts per minute.

Figure 1 shows four spectral profiles obtained (in the first order) for the 0.41-Mev gamma-ray line by selective reflection, both to right and to left, from the (310) planes of quartz. If the entire wave-length scale were shown to the same scale as the structure of these line profiles, they would be separated by about thirty times the distance shown in this plot. (The Bragg angle for these lines is about 20 minutes for the (310) planes of quartz $d=1.175$A.) The peaks of the lines are about 4.5 times the background intensity and this ratio, as the strength of the source decays, remains substantially constant until the irreducible background of 32 counts per minute is approached. The background on these curves we believe comes chiefly from scattering of the primary transmitted beam on the partitions of the lead collimator or baffle. The full widths of the lines at half-maximum height are about 0.125 x.u. This width is attributable (1) to the geometrical width of the radioactive source on the focal circle and (2) to the slight aberrations of focus of the curved crystal. These two geometrical width factors are of approximately the same order whereas both the "natural" line width and the quartz (310) plane diffraction pattern width for these hard gamma-rays are undoubtedly much narrower.

Repeated measurements yield the precision values listed in Table I for the wave-length and energy in Mev of this gamma-ray line. The precision measures quoted are "probable errors" computed from the consistency of the above data. It seems likely that any possible systematic errors are much smaller than these probable errors. In computing the above energies in Mev the latest conversion factor[2] $(12394.2\pm0.9)\times10^{-8}$ cm (the wave-length associated with 1 ev) has been used. The conversion factor 1.00203 from the Siegbahn scale of x.u. to absolute units was used.

An exploration has been made for two other softer lines at 0.208 Mev and 0.157 Mev (re-

* Work supported since March 1947 by contract with the Office of Naval Research.

[1] Jesse W. M. DuMond, Rev. Sci. Inst. **18**, 626 (1947).

[2] J. W. M. DuMond and E. Richard Cohen, Rev. Mod. Phys. **20**, 82 (1948).

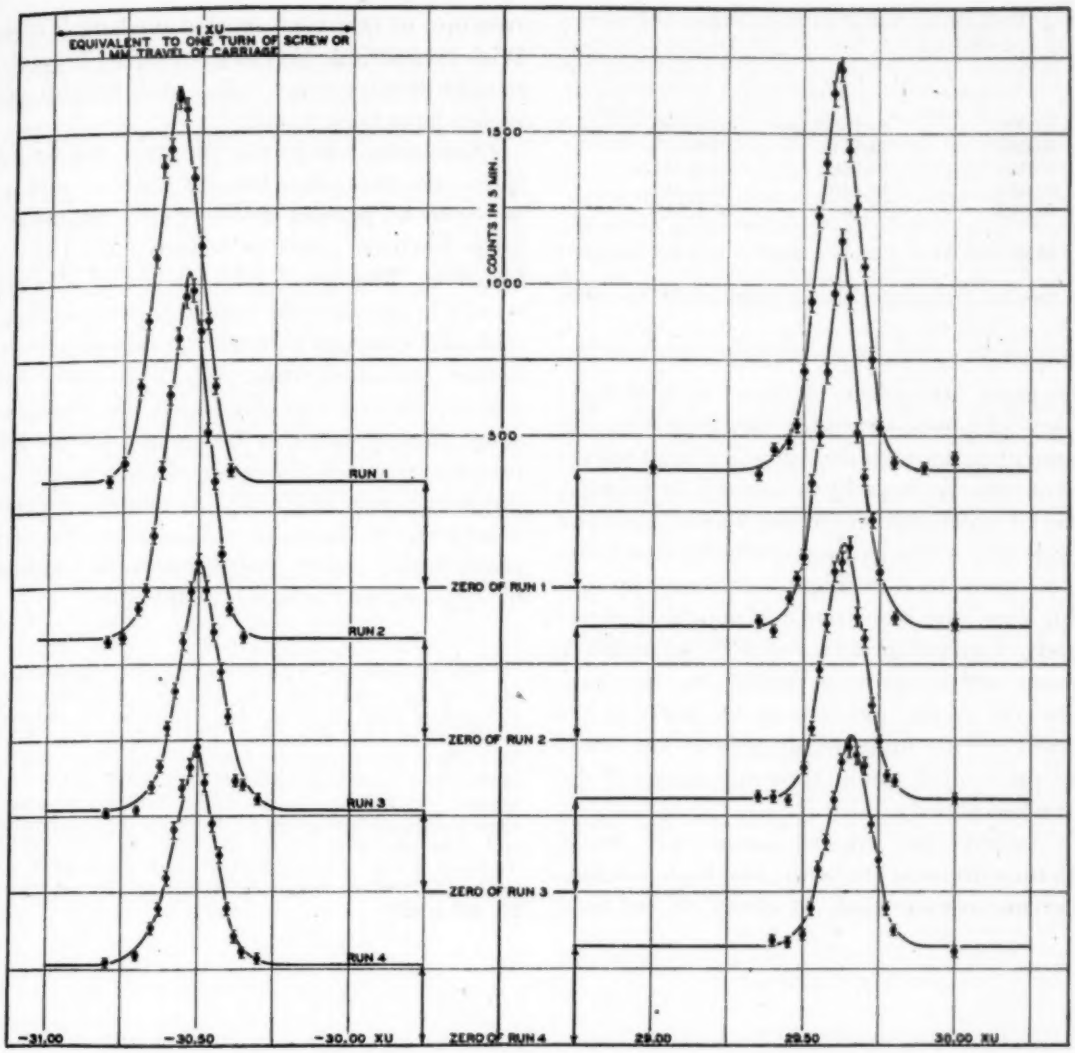

FIG. 1.

ported[3] from this source by β-ray measurements) but these have not been found. These lines, whose intensities were reported to be much lower than the present 0.41-Mev line, would be rendered relatively much weaker still in the present case by self-absorption in our source (thickness, 5 mm), since its specific activity is only about one atom in 10^4. No evidence for heterogeneity of the radiation could be found by absorption measurements with tin in the direct beam but, for the reason stated (self-absorption), this does not conclusively prove the complete absence of the two softer lines.[4]

Careful measurements are being made of the reflection coefficient of the (310) planes of quartz both for the x-ray and gamma-ray region and these results will be published soon. Only about 0.3 percent of the present 0.41-Mev line intensity in the direct beam incident on the crystal is reflected by the crystal planes. This low reflecting power makes the entire method unsuitable for work with weak gamma-ray sources. Sources of the order of 100 mc to 1 curie seem, at present, to be necessary.

[3] P. W. Levy and E. Grueling, Phys. Rev. **73**, 83 (1948).

[4] A. Mitchell, in a private communication, informs us that he has evidence that these softer lines are due to mercury present as an impurity in the gold when it was irradiated. From our failure to detect the 0.208-Mev line we infer that its intensity is surely less than 12 percent of the 0.41-Mev line. Levy and Grueling's estimate of this intensity ratio was 15 percent.

TABLE I. Preliminary values of wave-length and energy.

Run no.	λ_x – x.u.	λ_ϕ cm	$h\nu$ (Mev)
1	30.095	30.156×10^{-11}	0.41100
2	30.080	30.141	0.41121
3	30.065	30.126	0.41141
4	30.085	30.146	0.41114
5	30.083	30.144	0.41116
	30.082 ± 0.004	30.143 ± 0.004	0.41118 ± 0.00005

Recommended preliminary energy value $=0.4112\pm0.0001$ Mev.

The great advantage of direct crystal spectroscopy of gamma-rays as developed in this instrument is the high precision and high resolution it affords. We hope by means of it to establish a series of accurately determined fixed points on the scale of gamma-ray wave-lengths which can then be used as convenient references in calibrating β-ray spectrometers and in other indirect methods. A precision of two or three parts in ten thousand seems easily indicated for the half-million-volt region and four to six parts in ten thousand for the million-volt region. The study of the spectrum of annihilation radiation will also be attacked shortly.

We believe the present gamma-ray wave-length measurements to be the first high precision measurements ever made by direct crystal spectroscopy in this very short wave-length region.[5] With comparable precision in both, it may now be said that the x-ray region and the gamma-ray region have been joined.

(Note added in proof: We have subsequently shown the two softer lines (0.208 Mev and 0.157 Mev) to be present in our source in about the same intensity ratio as reported by Levy and Grueling. This we did by means of absorption curves in tin with the source turned so that the radiation emerged through the thin dimension to reduce self-absorption. We have also subsequently located and eliminated the cause of the small disagreements in the apparent wave-length position at which the spectral lines occur in the different runs (Fig. 1), a minor mechanical trouble in the front pivot. We believe that a precision better than 1/10,000 may now confidently be expected in the region of 0.5 Mev.

[5] The first direct crystal spectra of gamma-rays was made in the remarkable and well-known pioneer work of Rutherford and Andrade. The spectrum of radium was also studied with crystals by J. Thibaud and later by M. Frilley. These workers, however, used flat crystals and necessarily sacrificed radically resolving power for intensity. At 35 x.u., for example, Frilley's photographic spectra indicate line widths of the order of 4 x.u. Rutherford and Andrade, Phil. Mag. **27**, 854; **28**, 262 (1914). J. Thibaud, Thesis, Paris (1925); Ann. de physique **5**, 73–152 (1926). M. Frilley, Thesis, Paris (1928); Ann. de physique **11**, 483 (1929).

Letters to the Editor

PUBLICATION of brief reports of important discoveries in physics may be secured by addressing them to this department. The closing date for this department is five weeks prior to the date of issue. No proof will be sent to the authors. The Board of Editors does not hold itself responsible for the opinions expressed by the correspondents. Communications should not exceed 600 words in length.

The Beta-Spectrum of S^{35} and the Mass of the Neutrino

C. SHARP COOK, LAWRENCE M. LANGER, AND H. CLAY PRICE, JR.
Department of Physics, Indiana University, Bloomington, Indiana
April 23, 1948

USING sources prepared from high specific activity material obtained from Oak Ridge, the momentum distribution of the negatrons emitted by S^{35} has been investigated in a large, high resolution, shaped field magnetic spectrometer employing a 40-cm radius of curvature.[1] Measurements were made on sources of several thicknesses on backings of 0.5 mg/cm² Nylon and 0.03 mg/cm² Zapon. The Zapon counter window transmits electrons down to 2.0 kev.

Figure 1 shows a Fermi plot of the data obtained with three relatively thin sources. The significant fact is that these curves are all straight lines for all energies from $W=1.17$ mc² to the end point.

The deviations from a straight line for energies below 60 kev, which may be partly real[2] and certainly are influenced by source thickness and backing, will be discussed in some detail in a later paper.

The maximum energy of the negatron spectrum obtained by extrapolating the straight line part of the Fermi plot is $W_0=1.331$ mc², corresponding to a kinetic energy of 169.1 ± 0.5 kev.

The enlarged section of the Fermi plot in the immediate neighborhood of the end point shows the theoretical Fermi curves for an allowed transition calculated for assumed neutrino masses of zero, one percent, and two percent the mass of the electron. The equation for these curves includes a relativistic correction factor $1-\nu/WK$ where ν is the mass of the neutrino, W the electron energy, and K the neutrino energy. The sign in this factor conforms with the form of the theory as discussed by Pruett.[3] The inclusion of this factor makes the difference between the extrapolated end point and the theoretical, true end point equal to $\nu/2$. If this relativistic term is neglected as was done by Kofoed-Hansen,[4] this difference would be equal to ν. It is clear that within the limits of experimental error, one can say that the mass of the neutrino is less than one percent that of the electron.

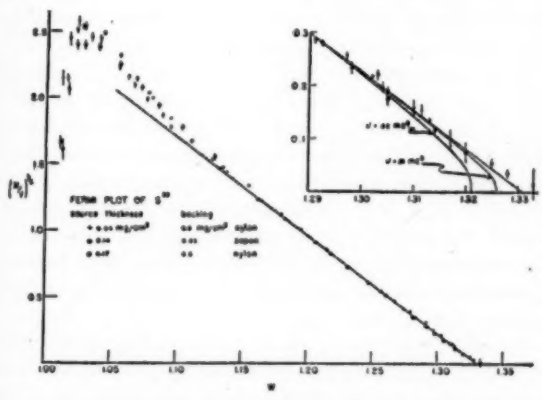

FIG. 1. Fermi plot of momentum distribution of the negatrons of S^{35}. The extrapolated end point is $W_0=1.331$ mc².

The work was supported by a grant from the Frederick Gardner Cottrell Fund of The Research Corporation and by the U. S. Navy under Contract N6-ori-48, T.O. 1.

[1] L. M. Langer and C. S. Cook, Rev. Sci. Inst. 19, 247 (1948).
[2] C. S. Cook and L. M. Langer, Phys. Rev. 73, 601 (1948).
[3] J. R. Pruett, Phys. Rev. 73 (1948).
[4] O. Kofoed-Hansen, Phys. Rev. 71, 451 (1947).

Azimuthal Effect of Cosmic Rays at Bombay (Magnetic Latitude 9.5°N)

P. S. GILL AND G. H. VAZE
Tata Institute of Fundamental Research, Bombay, India
April 8, 1948

IN 1939 Vallarta[1] pointed out that the measurements of the azimuthal effect at intermediate latitudes would determine the sign and the energy spectrum of primary cosmic radiation. One of us[2] undertook the study of the azimuthal effect of cosmic radiation for a fixed zenith angle of 60° at Lahore ($\lambda=22°$N). A similar experiment was carried out at Mexico City ($\lambda=29°$N) by Vallarta, Perusquía, and de Oyarzábal.[3] The results of Mexico City are in agreement with those of Lahore, giving 2.45 as the value of constant C of the primary spectrum K/E^C.

Recently we began to make a study of the azimuthal variation of cosmic-ray intensity at Bombay ($\lambda=9.5°$N) for a fixed zenith angle of 60°. Since for positive primary particles the penumbra bands are prominent in the N–W quadrant, we at first directed our telescopes towards this quadrant and the one opposite to it. Measurements were made for approximately forty hours at each interval of 10 degrees.

The apparatus consisted of twin counter telescopes, pointing in two diametrically opposite directions, mounted on a turntable so as to measure the intensity at the desired azimuth and zenith angle. The solid cone subtended by the telescope is 5.2° in zenith angle and 22° in azimuth.

Taking $C=2.45$, the value calculated[3] from the experiments at Mexico City and at Lahore, we determined the value of K to give the best fit. The energy in millistormers of the main cones were interpolated for each angle from Figs. 5–7 of Lemaitre and Vallarta.[4] Professor Vallarta very kindly gave us an estimate of the penumbra bands at $\lambda=10°$. In Fig. 1 are shown the calculated theoretical curve A and the experimental curve B. A χ^2 test for the

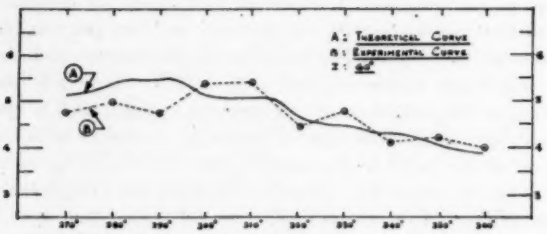

FIG. 1. Azimuthal effect of cosmic radiation in the N-W quadrant at Bombay ($\lambda = 9.5°$N) for zenith angle of 60°.

experimental points shows that though the number of counts at each angle is small, the fit is fairly good, except at azimuth $\alpha = 290°$. On the other hand, the same test shows that the observations are not yet satisfactorily uniform.

It is to be noted that the primary spectrum for energy range from 350 to 640 ms can be represented by K/E^C with $C = 2.45$.

We would like to express our thanks to Professors H. J. Bhabha, M. S. Vallarta, and D. D. Kosambi for their valuable discussion.

[1] M. S. Vallarta, Rev. Mod. Phys. **11**, 239 (1939).
[2] P. S. Gill, Phys. Rev. **67**, 347 (1945).
[3] M. S. Vallarta, M. L. Perusquía, and J. de. Oyarzábal, Phys. Rev. **71**, 393 (1947).
[4] G. Lemaitre and M. S. Vallarta, Phys. Rev. **50**, 493 (1936).

On the Differential Energy Spectrum of Mesons*

M. H. SHAMOS AND M. G. LEVY
Physics Department, New York University, New York, New York
April 13, 1948

THREE points have been obtained in the important low energy region (kinetic energy $<10^9$ ev) of the differential spectrum at sea level by means of a meson detector based upon the instability of mesons. This technique, wherein positive identification of mesons is assured by detection of their decay electrons, has been used by Rossi, Sands, and Sard[1] to investigate the altitude dependence of slow mesons.

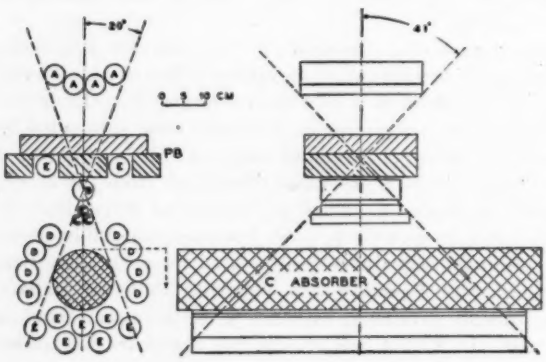

FIG. 1. Counter telescope.

The momentum spectrum of mesons has been investigated with cloud chambers by several workers.[2-5] While the interpretation of such measurements is generally complicated, at low momenta, by the large electron component, Wilson[6] has presented good evidence for a fairly definite maximum in the vicinity of 600 Mev at sea level. However, the usual methods of distinguishing mesons from electrons, such as that based upon the high probability for the production of secondaries by the electrons,[7] are not as reliable as the characteristic decay of the meson.

The counter telescope, shown in Fig. 1, defines a beam (ABC) through the cylindrical carbon absorber, hereafter referred to as "stopper." Counters (E) are connected in anticoincidence and counters (D), effective length 84 cm, detect the decay electrons. The number and distribution in time of the decay events $(ABC-E)(D)$ are recorded by a time circuit somewhat similar to that described by Rossi and Nereson.[8] Because of the time lags in the counters, only those events which are delayed more than 0.95 μsec. are recorded. At this value, the correction for time lags is only ~3 percent.

The meson energies were selected by different thicknesses of absorbing material placed above (A), and between (A) and (B). These thicknesses, taking into account the counter walls (0.5 cm Pb equivalent) and the roof and supporting material in the telescope (0.4 cm Pb equivalent), were: (a) 11.2 cm Pb, (b) 31.6 cm Pb, and (c) 31.6 cm Pb +25.4 cm Fe. The average path length through the absorbing material was evaluated numerically, taking into account the $\cos^2$ distribution of mesons with zenith angle, and found to be 1.1 times the vertical depth. The equivalent cut-off energies, taken from the Rossi-Greisen curves,[9] are then 180 Mev, 465 Mev, and 860 Mev, respectively.

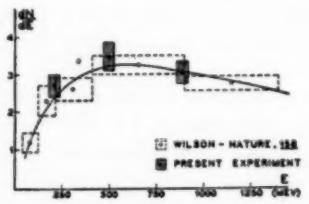

FIG. 2. Differential spectrum.

Runs were taken with and without the carbon stopper under each thickness, and the differences in the numbers of decay electrons were used to determine the differential spectrum. As a check on the experiment, the mean life of the decay process was determined, and was consistent with the value 2.15 μsec. in each case. About 1000 mesons entered the telescope per hour and, of these, some 10 per hour were stopped by the carbon. The pertinent data are tabulated in Table I, where the errors indicated are standard statistical errors.

The differential spectrum is shown in Fig. 2. Here are plotted the relative numbers of decay electrons (in arbitrary units) as a function of the kinetic energy. Since the average path through the carbon stopper is equivalent to about 60 Mev, the points have been located at 210±30

TABLE I.

Absorber thickness	Time (hours) with C	Time (hours) back	Electrons/hour with C	Electrons/hour back	Difference per hour	Corrected for time lags
11.2 cm Pb	150.1	152.5	2.41±0.12	0.96±0.08	1.45±0.14	1.42±0.14
31.6 cm Pb	104.1	186.0	3.24±0.17	1.37±0.09	1.87±0.20	1.81±0.20
31.6 cm Pb+ 25.4 cm Fe	135.3	93.7	2.38±0.13	0.74±0.09	1.64±0.16	1.50±0.16

495±30, and 890±30 Mev.** For the purpose of comparison, the point at 890 Mev has been fitted to the Wilson curve, given here on an energy scale; both experiments were performed at approximately the same geomagnetic latitude.

While the statistical errors in this experiment are about the same, or slightly larger than, the errors in Wilson's points, the resolution is sharper, and indicates the usefulness of this technique in the examination of the differential spectrum.

These results were obtained during the course of an investigation into the energy dependence of the positive meson excess, which will be reported on later, and we are indebted to Professor I. S. Lowen for suggesting the initial problem.

* This work was supported by the Office of Naval Research under Contract No. N6ori-201 Task Order II.

[1] Rossi, Sands, and Sard, Phys. Rev. **72**, 120 (1947).
[2] P. Blackett, Proc. Roy. Soc. **A159**, 1 (1937).
[3] H. Jones, Rev. Mod. Phys. **11**, 235 (1939).
[4] D. Hughes, Phys. Rev. **57**, 592 (1940).
[5] E. Williams, Proc. Roy. Soc. **A172**, 194 (1939).
[6] J. Wilson, Nature **158**, 414 (1946).
[7] V. Sarabhai, Phys. Rev. **65**, 203 (1944); **65**, 250 (1944).
[8] Rossi and Nereson, Rev. Sci. Inst. **17**, 65 (1946).
[9] Rossi and Greisen, Rev. Mod. Phys. **13**, 240 (1941).

** This does not take into account the possible spread in energy resulting from the distribution in path lengths through the upper absorber. If the deviations attributable to this effect are taken to be independent of those due to the stopper, the *maximum* energy spread at each point becomes: 210±40, 495±80, and 890±140 Mev. Inasmuch as qualitative considerations indicate that the true spread is much closer to those shown on the diagram than to the maximum, it was decided to show the former rather than the maximum spread. It should be noted, however, that even with the latter, the conclusion given above concerning the improved resolution remains valid.

On Two Complementary Diffraction Problems

A. STORRUSTE AND H. WERGELAND
Norges Tekniske Högskole, Trondheim, Norway
April 20, 1948

OCCASIONED by a discussion on Babinet's theorem, we have worked out exact solutions for the diffraction of sound waves by a circular disk, and in the corresponding hole, *i*, an infinite plane screen.[1]

Two such complementary obstacles are quite different in topological respect, one being singly connected and the other doubly connected. Therefore the mathematical expressions for the diffracted waves will also be entirely different in the two cases.

So Babinet's theorem does not at all emerge simply from the exact solution. It is a limiting principle, like the Huygens-Kirchhoff method on which it is based, valid at short wave-lengths.

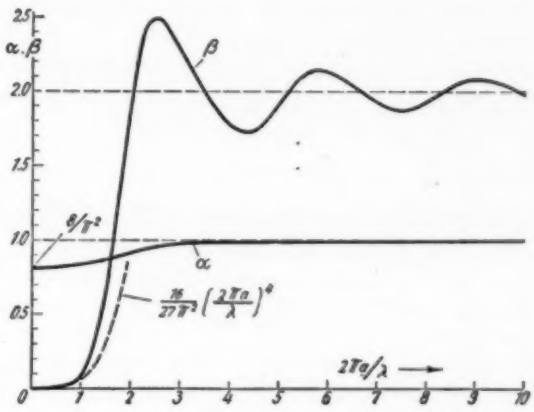

FIG. 1.

The most direct approach to an exact solution is the introduction of spheroidal coordinates. If these—μ, ν, ϕ—are defined by

$$x+iy=a((1+\mu^2)(1-\nu^2))^{\frac{1}{2}}\cdot e^{i\varphi},$$
$$z=a\mu\nu,$$

where

a = radius of the hole,

the disk and the screen, in the xy-plane, will coincide with the coordinate surfaces $\mu=0$ and $\nu=0$, respectively.

Developing the whole sound field ϕ in the corresponding wave functions

$$\phi_\Lambda = M_\Lambda(\mu)N_\Lambda(\nu),$$

where $\mathbf{N}$ and $\mathbf{\Lambda}$ denote eigenfunctions and eigenvalues of the angular differential equation:

$$(d/d\nu)[(1-\nu^2)(dN/d\nu)]+(k^2a^2\nu^2-\Lambda)N=0,$$

and utilizing integral representations of the form (plane waves):

$$M_\Lambda(\mu)=\int \exp(ika\mu\nu)N_\Lambda(\nu)d\nu,$$

it is easy to write down compact expressions for the wave field satisfying the boundary conditions.

In the numerical elaboration of the results use has been made of the tables of Stratton *et al.*[2] and especially of earlier work of Hylleraas.[3]

We shall here give only the result for the total energy scattered by the disk or transmitted through the hole (Fig. 1).

$$\left.\begin{matrix}\alpha\\ \beta\end{matrix}\right\} = \text{total energy}\left\{\begin{matrix}\text{transmitted}\\ \text{scattered}\end{matrix}\right\}\Big/\,\pi a^2\cdot\text{intensity of primary wave};$$

λ = wave-length;
a = radius of hole and disk.

The transmission coefficient, α, starts at a value of 81 percent for long wave-lengths, and the scattering coefficient β increases of course from zero $\sim 1/\lambda^4$ according to Rayleigh's law.

Babinet's theorem applies to the region $\lambda \ll a$, where both curves deviate negligibly from their asymptotes $\alpha=1$, $\beta=2$.

One of us (A.S.) hopes to return to the electromagnetic case.

[1] A. Storruste and H. Wergeland, Kgl. N. V. Selsk. Forh. (1948) (in print).
[2] Stratton, Morse, Chu, and Hutner, *Elliptic Cylinder and Spheroidal Wave Functions* (1941).
[3] E. A. Hylleraas, Zeits. f. Physik **71**, 739 (1931).

Correlation between the States of Polarization of the Two Quanta of Annihilation Radiation*

E. Bleuler and H. L. Bradt**
Purdue University, Lafayette, Indiana
April 13, 1948

It has been pointed out by J. A. Wheeler[1] that according to pair theory the planes of polarization of the two quanta originating in the annihilation of a positron should be perpendicular to each other. This correlation is the equivalent of angular momentum conservation in the process of annihilation of an electron pair with relative velocity zero in the singlet state. The azimuthal variation of intensity of the simultaneous Compton scattering of the two quanta, resulting from this correlation between their respective states of polarization, has been calculated by Pryce and Ward[2] and by Snyder, Pasternack, and Hornbostel.[3] An experimental verification has been attempted with the aid of the arrangement shown in Fig. 1.

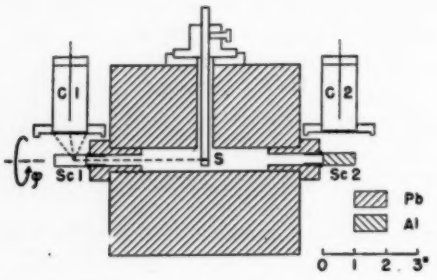

FIG. 1. Coincidence measurement of Compton scattering.

The annihilation radiation of the source S (Cu^{64}, prepared by deuteron irradiation of copper in the Purdue cyclotron) is collimated by a $\frac{3}{8}$-in. channel in the lead block. The quanta are scattered by cylindrical aluminum scatterers *Sc* and detected with bell-shaped Geiger counters with lead cathodes. Coincidences were measured for azimuth differences (φ) of 0°, 90°, 180°, and 270° between the counter axes. In order to eliminate all asymmetries both counters were rotated in turn. As a result of absorption in the scatterer the mean scattering angle is slightly less than 90°, near the theoretical maximum of anisotropy calculated for a scattering angle of 82°. Taking into account the finite solid angle subtended by the counters, a ratio $C_\perp/C_{\parallel}\approx 1.7$ is expected for the coincidence rates at $\varphi=90°$ ($C_\perp$) and $\varphi=180°$ ($C_{\parallel}$). Four different runs were made with different sources consistently showing $C_\perp > C_{\parallel}$. Data for a characteristic run of 16 hours are given in Table I.

TABLE I.

Average single counts without scatterers	3000/min.
Average single counts with scatterers	5370/min.
Chance coincidences ($T=1.2\cdot10^{-7}$ sec.)	0.117/min.
Genuine coincidences $C_\perp$	0.152/min.
Genuine coincidences $C_{\parallel}$	0.073/min.
Asymmetry ratio $C_\perp/C_{\parallel}$	2.1 ± 0.64

The observed average asymmetry ratio for all runs is

$$C_\perp/C_{\parallel}=1.9_4\pm0.3_7.$$

The indicated error is the statistical mean standard deviation. The theoretical prediction is therefore confirmed by this experiment.

* Work done under Navy Contract N6ori-222, Task Order I.
** Now at the University of Rochester, Rochester, New York.
[1] J. A. Wheeler, Ann. N. Y. Acad. Sci. **48**, 219 (1946).
[2] M. H. L. Pryce and J. C. Ward, Nature **160**, 435 (1947).
[3] H. S. Snyder, S. Pasternack, and J. Hornbostel, Phys. Rev. **63**, 440 (1943).

Piezoelectric or Electrostrictive Effect in Barium Titanate Ceramics

W. P. Mason
Bell Telephone Laboratories, Murray Hill, New Jersey
April 13, 1948

In a recent Letter to the Editor,[1] Matthias and Von Hippel have discussed the resonances obtained in a piece of multicrystalline barium titanate ceramic and have called the effect a "quadratic" piezoelectric effect. While the term used is to some extent a matter of definition, it appears worth while to point out that the effect in the titanate ceramic does not conform to the original definition of a "quadratic" piezoelectric effect, but is, on the other hand, the analog of a magnetostrictive effect in a ferromagnetic material.

According to Mueller,[2] a "quadratic" piezoelectric effect is one following the same equations as an electrostrictive effect but depending on a strain caused by a spontaneous polarization or an applied field acting on the piezoelectric constant. The discovery[3] that a shear vibration can be set up when an a.c. field is applied at right angles to a d.c. polarization and the quantitative check between the value of this constant and the radial and thickness constants show that the effect cannot be a "quadratic" piezoelectric effect. This follows from the fact that the only type of symmetry that the ceramic can have in the presence of an applied field is that known as transverse isotropy. For this case the $c=Z$ axis lies along the direction of the field, and the properties in any direction perpendicular to the field are independent of direction. The effect of this symmetry is to reduce the constants to the terms $d_{31}=d_{32}$, d_{33}, $d_{15}=d_{24}$, and there is no necessary relationship between d_{15} and d_{31} and d_{33}.

On the other hand, if the effect is regarded as a second-order electrostrictive effect, it was shown in a previous paper[4] that the stress strain and electric relations are given by the tensor equations (when other second-order effects are neglected)

$$\begin{aligned} S_{ij} &= T_{kl}s_{ijkl}^{D}+\delta_n[g_{ijn}+Q_{ijn0}\delta_0], \\ E_m &= -T_{kl}[g_{mkl}+2Q_{klmn}\delta_n]+\delta_n[4\pi\beta_{mn}{}^{T}], \end{aligned} \tag{1}$$

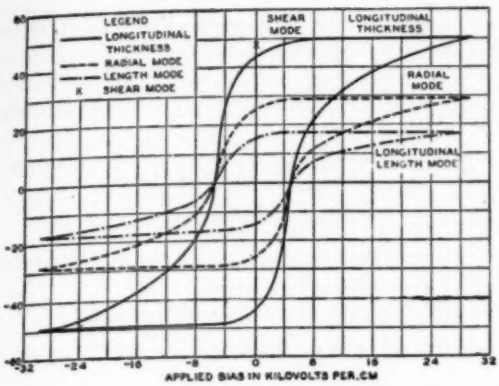

FIG. 1. Measured values of electromechanical coupling as a function of the voltage bias for 4 modes of motion in barium titanate ceramics.

where S_{ij} and T_{kl} are, respectively, the strains and stresses, $\delta_n = D_n/4\pi$ where D_n are the electric displacements, $s_{ijkl}{}^D$ are the constant displacement elastic compliances, g_{ijn} the piezoelectric constants, Q_{ijn0} the electrostrictive constants, and $\beta_{mn}{}^T$ the impermeability constants (i.e., inverse of dielectric constants).

On the assumption that the material is isotropic and non-piezoelectric, these equations reduce to the forms expressed in terms of the usual two index symbols:

$$
\begin{aligned}
&S_1 = s_{11}{}^D T_1 + s_{12}{}^D[T_2+T_3] + Q_{11}\delta_1{}^2 + Q_{12}[\delta_2{}^2+\delta_3{}^2],\\
&\cdots\cdots\cdots\cdots\cdots\cdots\\
&S_{12} = \frac{S_6}{2} = [s_{11}{}^D - s_{12}{}^D]T_6 + [Q_{11}-Q_{12}]\delta_1\delta_2,\\
&E_1 = \delta_1[4\pi\beta_{11}{}^T] - 2[Q_{11}[\delta_1 T_1 + \delta_2 T_6 + \delta_3 T_5] \\
&\qquad + Q_{12}[\delta_1[T_2+T_3] - [T_6\delta_2 + T_5\delta_3]]],\\
&\cdots\cdots\cdots\cdots\cdots\cdots\\
&E_3 = \delta_3[4\pi\beta_{11}{}^T] - 2[Q_{11}[\delta_3 T_3 + \delta_1 T_5 + \delta_2 T_4] \\
&\qquad + Q_{12}[\delta_3[T_1+T_2] - [\delta_1 T_5 + \delta_2 T_4]]].
\end{aligned}
\tag{2}
$$

Hence as shown by the equation for the shear strain S_6, a shear mode is excited when two electric displacements occur at right angles.

Using these equations, the electromechanical coupling factors have been calculated for the longitudinal length mode, the radial mode, the thickness longitudinal mode, and the thickness shear mode. These are given, respectively, by the formulae

$$
k_l = \frac{2Q_{12}\delta_{3_0}}{(s_{11}{}^E(4\pi\beta_{11}{}^T))^{\frac{1}{2}}}; \quad k_r = \left(\frac{2}{1-\sigma}\right)^{\frac{1}{2}} k_l,
$$

$$
k_t = \frac{2\delta_{3_0}\left[Q_{11} - \dfrac{2s_{12}{}^D}{s_{11}D + s_{12}D}Q_{12}\right]}{\left(\dfrac{4\pi\beta_{11}{}^T}{c_{11}{}^E}\right)^{\frac{1}{2}}}; \quad k_s = \frac{2(Q_{11}-Q_{12})\delta_{3_0}}{\left(\dfrac{4\pi\beta_{11}{}^T}{\mu^E}\right)^{\frac{1}{2}}}.
$$

Measurements for the coupling of these four modes as a function of the applied voltage are shown by Fig. 1. The fact that the coupling follows a hysteresis loop shows conclusively that the electrostrictive effect is a function of the electric displacement rather than the applied field. The longitudinal and thickness couplings determine the electrostrictive constants to be

$$
Q_{12} = -2.15\times10^{-12}\left(\frac{\text{cm}^2}{\text{stat. coulombs}}\right)^2;
$$

$$
Q_{11} = +6.9\times10^{-12}\left(\frac{\text{cm}^2}{\text{stat. coulombs}}\right)^2.
$$

Using these constants, the shear mode for a remanent displacement due to the application of 30,000 volts/cm has a calculated coupling agreeing well with the experimental value, which shows conclusively that the effect follows the second-order electrostrictive equations and not the "quadratic" piezoelectric relations. Since a ferromagnetic magnetostrictive material follows a similar set of equations, it appears more logical to call the effect electrostrictive.

[1] B. Matthais and A. Von Hipple, "Structure, electrical and optical properties of barium titanate," Phys. Rev. **73**, 268 (1948).
[2] H. Mueller, "Properties of rochelle salt IV," Phys. Rev. **58**, 805 (1940).
[3] W. L. Cherry and Robert Adler, "Piezoelectric effect in barium titanate," Phys. Rev. **72**, 981 (1947).
[4] W. P. Mason, "First and second order equations for piezoelectric crystals expressed in tensor form," Bell Sys. Tech. J. **26**, 80 (1947).

Slow Neutron Spectrometer Studies of Oxygen, Nitrogen, and Argon*

E. MELKONIAN, L. J. RAINWATER, W. W. HAVENS, JR., AND J. R. DUNNING
Columbia University, New York, New York
April 18, 1948

THE Columbia University slow neutron velocity spectrometer[1] is being used to investigate materials in the gaseous phase. Preliminary measurements on several elements are presented in this letter (Figs. 1–3). Following the usual convention, all cross sections are in units of 10^{-24} cm²/atom.

The samples were contained in aluminum alloy cylinders 1 meter long and having 10-cm inside diameters. Pressures up to 75 atmospheres can be used.

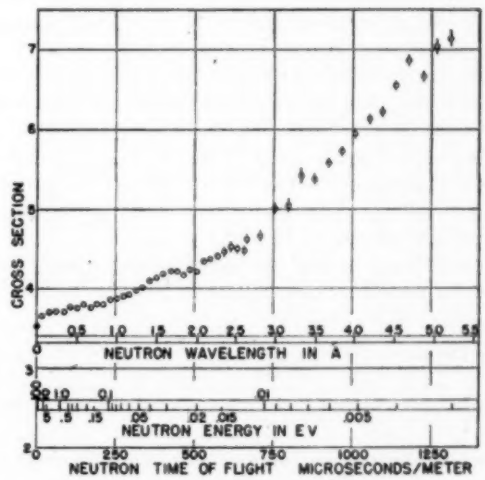

FIG. 1. The slow neutron cross section of oxygen. In each of several runs the sample contained about 8 g/cm², but the exact amount was different for each run. The average of these results is shown.

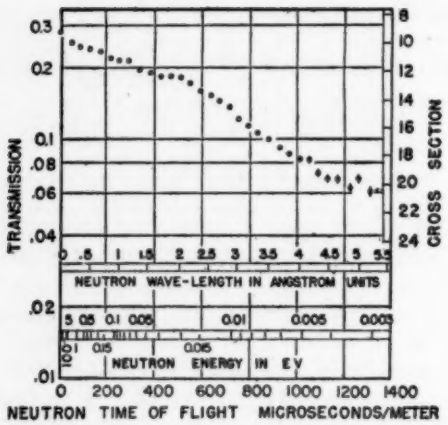

FIG. 2. The slow neutron transmission of 3.168 g/cm² of nitrogen.

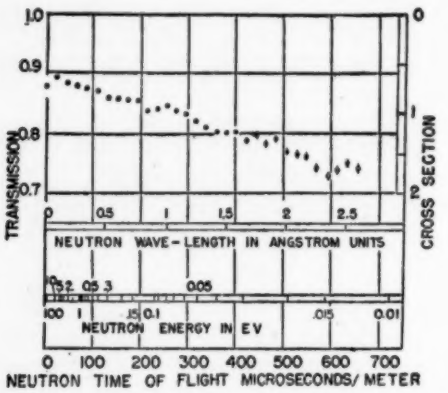

FIG. 3. The slow neutron transmission of 11.71 g/cm² of argon.

In the case of O_2, a beryllium filter (which discriminates against neutrons having energy greater than 0.01 ev) was used at timings greater than 665 microseconds per meter to reduce the small background of faster thermal neutrons. The investigation of nitrogen in this region will be repeated using this filter.

The statistical accuracy is indicated by vertical bars. Where no bars are shown, the statistical accuracy is of the same order as or less than the size of the circles.

The rapid changes in transmission near zero time of flight are due to the resolution width of the instrument which integrates the transmission of the sample over all neutron energies up to 14 Mev.

In addition to nuclear interactions with the neutrons, the following phenomena contribute to the cross section when a gaseous sample is used:

(a) Thermal motion of the gas molecules which causes an increase in cross section with decreasing neutron energy.
(b) Coherent scattering from the atoms in the molecule.
(c) Inelastic collisions (i.e., changes in vibrational and rotational levels of the molecule).

In addition to these effects, part of the increase of the oxygen cross section with decreasing neutron energy is believed to be due to the paramagnetism of oxygen, i.e., to an interaction between the magnetic moments of the oxygen molecules and the neutrons. Professor O. Halpern has separated by theoretical analysis the parts of the cross section corresponding to magnetic and non-magnetic interactions.[2] Oxygen has negligible capture in the thermal region.

The nitrogen cross section for neutron energies greater than 0.025 ev can be represented by

$$\sigma_{\text{thermal}} = [9.60 + 0.48E^{-\frac{1}{2}}] \times 10^{-24} \text{ cm}^2 \text{ per atom},$$

where E is the neutron energy in ev. At least a portion of this slope is attributed to capture.

The argon cross section can be represented by

$$\sigma_{\text{thermal}} = [0.640 + 0.123E^{-\frac{1}{2}}] \times 10^{-24} \text{ cm}^2 \text{ per atom}.$$

Since argon is monatomic so that molecular effects (b) and (c) cannot occur, and since (a) is not appreciable in the region studied, this slope is attributed almost entirely to capture.

Measurements at higher energies with better resolution give the following cross sections per atom for the energy range 15 to 200 ev: O_2, 3.68; N_2, 9.74; A, 0.67.

Fermi and Marshall[3] have reported measurements on the cross section of O_2 and N_2 using BeO filtered pile neutrons having an average wave-length of 5.1A. Their values (O_2, 8.1 per atom and N_2, 23.7 per atom) are about 14 percent higher than those reported here for the same wave-length. The use of a Be filter in the case of N_2 will increase the measured cross section and should decrease considerably or even eliminate the discrepancy between the two results. However, the discrepancy in the case of O_2, presumably outside of experimental error for both measurements, remains unexplained.

* This letter is based on work performed under Contract AT-30-1-Gen-72, and the information covered therein will appear in the Manhattan Project Technical Series as part of the contribution of Columbia University.

[1] Rainwater, Havens, Wu, and Dunning, Phys. Rev. 71, 65 (1947).
[2] O. Halpern, Phys. Rev. 72, 746 (1947).
[3] E. Fermi and L. Marshall, Phys. Rev. 71, 666 (1947).

A Rapid Method for the Determination of the Maximum Energies of β-Emitters with Simple Spectra

L. YAFFE AND KATHARINE M. JUSTUS
Chemistry Branch, Division of Atomic Energy, National Research Council of Canada, Chalk River, Ontario, Canada

April 21, 1948

DURING the course of work on the back-scattering of electrons it became apparent that the back-scattering is a sensitive function of the maximum energy of the β-emitter, especially in the lower energy range.

Samples were mounted on Formvar films (50 mg/cm²) and had such specific activity that no solid deposit was visible after the solution was evaporated on the film. Measurements were made using an "end-on" Geiger counter with mica window 2.8 mg/cm². The sample was placed in position about 1 cm from the counter window and counted first without any back-scattering, save for air, and

secondly by placing a piece of metal directly beneath the film (Pb or Ag, 55 mg/cm² in this case).

β-emitters used in this case were C^{14}, S^{35}, P^{32}, I^{131}, Co^{60}, Rh^{106}.

The values of the maximum energy obtainable from the literature were

	Mev
C^{14}	0.154[1,2]
S^{35}	0.107 to 0.120[3] or 0.167[2]
Co^{60}	0.30[4]
I^{131}	0.60[5]
Rh^{106}	2.8 (20 percent), 3.9 (80 percent)[5]
P^{32}	1.70[6]

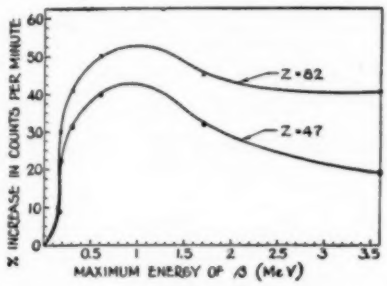

FIG. 1. Variation of the percentage increase in the number of counts per minute due to back-scattering with the maximum energy of the β-emitter. Mass thickness of back-scatterer: 55 mg/cm².

All of these, with the exception of Rh^{106} have simple spectra, and Rh^{106} was used merely to give a value around 3 Mev since no β-emitter with simple spectrum was readily available in that energy range. The results are shown in Fig. 1.

Once this empirical curve is obtained for a certain geometry, then it can be used to determine maximum energies of β-emitters with simple spectra, merely by two measurements, one with and the other without the back-scattering material. When this work commenced, the value for the maximum energy of S^{35} was said to be 0.12 Mev,[3] and that for C^{14} 0.154.[1] The increase in counts for the two radiations due to back-scattering compared to the count without back-scattering was 30 percent and 10 percent, respectively, using lead. This led us to believe, by comparison with Fig. 1, that either the energy value quoted for the S^{35} was too low or the value quoted for C^{14} was too high. More recent work[2] gives a value of 0.167 Mev for S^{35} and this fits well on the curve. This new value has been corroborated by the authors using absorption techniques with very active samples.

This method, although only suitable for β-emitters with simple spectra, is useful for rapidly determining radioactive purity after chemical separation. It can also be used for a swift determination of the maximum energy value of emitters with half-lives too short for absorption measurements and can be done with only several hundred disintegrations per minute. A double value will be obtained in a few cases. This can be resolved by one absorption measurement.

A full report on this work is being submitted to the Canadian Journal of Research.

[1] P. W. Levy, Phys. Rev. **72**, 248 (1947).
[2] A. K. Solomon, R. G. Gould, and C. B. Anfinsen, Phys. Rev. **72**, 1097 (1947).
[3] W. F. Libby, Anal. Chem. **19**, 2 (1947).
[4] M. Deutsch and L. G. Elliott, Phys. Rev. **62**, 558 (1942).
[5] Plutonium Project release, Rev. Mod. Phys. **18**, 513 (1946).
[6] Glenn T. Seaborg, Rev. Mod. Phys. **16**, 1 (1944).

Internal Conversion in Tungsten and Platinum*

M. V. SCHERB AND C. E. MANDEVILLE
Bartol Research Foundation of the Franklin Institute, Swarthmore, Pennsylvania
April 21, 1948

CONTINUING the investigation[1] of the characteristic radiations of the simple beta-ray emitter, tantalum (182), beta-beta coincidences have been observed between the nuclear beta-rays and conversion electrons. The beta-beta coincidence rate, shown in Fig. 1, is seen to follow a

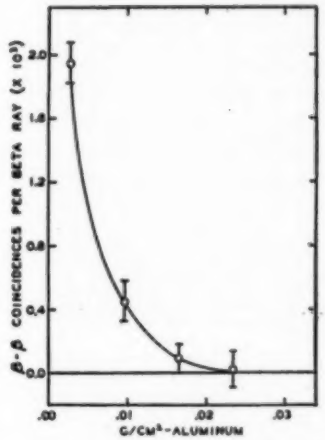

FIG. 1. Beta-beta coincidences in the disintegration of tantalum (182).

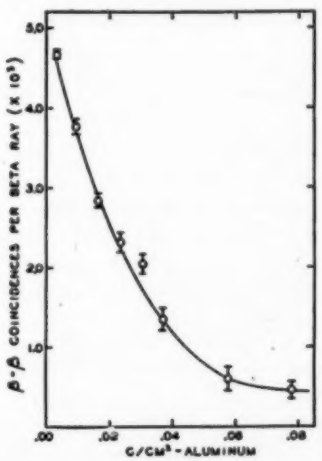

FIG. 2. Beta-beta coincidences in the disintegration of iridium (192).

curve which is roughly exponential in form when plotted as a function of the aluminum absorber thickness. The coincidence rate reaches zero at 0.0235 g/cm², suggesting a maximum conversion electron energy of 0.135 Mev. It has been shown that tantalum (182) emits about sixteen converted gamma-rays.[2] $(N_{\beta\beta}/N_{\beta})/(N_{\beta\gamma}/N_{\gamma})$ at zero absorber thickness was found to be correspondingly large, about 0.7, and since the relative values of the individual conversion coefficients are not known, the total conversion coefficient could not be calculated.[3]

Beta-beta coincidences in the disintegration of Ir^{192} have been reinvestigated.[3] The beta-beta coincidences per beta-ray are shown in Fig. 2 as a function of aluminum absorber thickness. The beta-beta and beta-gamma coincidence rates were extrapolated to zero absorber thickness on a semilogarithmic plot, and the total conversion coefficient was found to be 32±3 percent, in agreement with the previous estimate.[3] Several different geometric arrangements were employed with extremely thin sources of radioactive iridium, and all of the curves were similar in form to that of Fig. 2. The maximum obtained in the region of low energy by Wiedenbeck and Chu[3] was not observed. Thus far, beta-beta coincidences have been measured in Ta^{182}, Ir^{192}, Os^{191}, and Au^{199}, and in every case an exponential curve has been obtained. Curves of this appearance have also been reported by Mitchell.[4]

No beta-beta coincidences were observed in Sc^{46}. This agrees with a previous report[5] that few or no conversion electrons are emitted by Sc^{46}, and demonstrates that there are no spurious beta-beta coincidences arising from scattering effects in the geometries employed.

* Assisted by the Office of Naval Research.
[1] C. E. Mandeville and M. V. Scherb, Phys. Rev. **73**, 340 (1948).
[2] J. M. Cork, Phys. Rev. **72**, 581 (1947).
[3] M. L. Wiedenbeck and K. Y. Chu, Phys. Rev. **72**, 1171 (1947).
[4] A. C. G. Mitchell, Rev. Mod. Phys. **20**, 296 (1948).
[5] J. M. Cork, R. G. Shreffler, and C. M. Fowler, Bull. Am. Phys. Soc. 2, 6 (1947).

Search for Electrons in the Primary Cosmic Radiation*

ROBERT I. HULSIZER AND BRUNO ROSSI
Physics Department and Laboratory for Nuclear Science and Engineering, Massachusetts Institute of Technology, Cambridge, Massachusetts
April 13, 1948

PRELIMINARY results have been obtained from an experiment designed to determine whether or not high energy electrons or photons are present in the primary cosmic radiation. The detector consisted of a cylindrical ionization chamber with a sensitive volume 5 cm in diameter and 15 cm long. Its collecting electrode was a wire 0.63 mm in diameter stretched along the axis of the chamber. The wire was grounded through a 10-megohm resistor, and the outer wall was maintained at −600 volts. Purified argon was used to fill the chamber to a pressure of six atmospheres. The voltage pulse resulting from each ionization burst was amplified and its size transmitted via radio to a receiving station on the ground. The amplifier used in these experiments was designed with a rise time of 2 μsec. and a decay time of 12 μsec.

The apparatus was borne aloft by balloons to a minimum atmospheric depth of 20 g cm⁻², data regarding temperature and pressure being transmitted intermittently during each flight. Two flights were made with half of a cylindrical shell of lead 10 cm long and 2.5 cm thick placed over the chamber, and two more were made with the chamber unshielded. In the latter arrangement the observed bursts were attributed to nuclear disintegrations in the walls or in the gas of the chamber. Of these four flights, only one of each kind stayed at high altitude long enough to give data with good statistics. One additional flight at 306 g cm⁻² was made in a B-29. In this flight, measurements with and without lead were taken.

Calibrating pulses were obtained throughout the experiments from α-particles emitted from a thin polonium source on the inside wall of the chamber.

The experimental results are shown in Table I. A reasonable extrapolation of the unshielded chamber data indicates that at 20 g cm⁻² the burst rate under lead is approximately 1.5 times the burst rate without lead. Since the absorption in 2.5 cm lead of the star producing radiation is negligible,[1] the increase in burst rate caused by the lead represents the effect of electronic showers produced in the lead and possibly of stars produced in the part of the lead adjacent to the chamber.

TABLE I. Rates of occurrence of pulses larger than 1.1 times the α-particle pulse.

Pressure (g cm⁻²)	Burst rate (hour⁻¹)	Period of observations (hour)	Conditions of experiment
20	313	1.2	Lead shield
306	53	1.9	over chamber
45	183	0.6	Unshielded
306	36	2.7	chamber

It can be estimated that any electron or photon of energy larger than 4.5 Bev, traveling on a trajectory which crosses the chamber more than 1 cm inside the boundary of the sensitive volume and which forms an angle of less than 60° with the vertical, produces in the lead a shower of sufficient magnitude to give a pulse larger than 1.1 times the α-particle pulse.[2] Thus this chamber, acting as a detector of electrons or photons of energies greater than 4.5 Bev, has at least a sensitive area of 19 cm² over π-steradians of solid angle. The increase of burst rate caused by the lead, if attributed entirely to electron or photon initiated showers, yields therefore an upper limit of 5×10^{-4} cm⁻² sec.⁻¹ sterad⁻¹ for the intensity of electrons or photons of energies larger than 4.5 Bev. This intensity cannot be much greater at the top of the atmosphere since 20 g cm⁻² is less than one-half of one radiation length in air. On the other hand, the primary cosmic-ray intensity has been estimated to be 7×10^{-2} cm⁻² sec.⁻¹ sterad⁻¹.[3] Consequently it is safe to conclude that the ratio of electrons or photons of energies greater than 4.5 Bev to the total number of primary cosmic rays is less than 1 percent. This also represents an upper limit for the total number of

electrons in the primary radiation, since the latitude effect[4] shows that no singly charged particles with momentum larger than 4.5 Bev/c are present.

We wish to emphasize that it is not necessary to postulate the existence of any electrons or photons in the primary radiation since cascade showers have been observed to be produced in lead by penetrating particles believed to be high energy protons.[5]

* This work was supported in part by the Office of Naval Research. The B-29 used for the measurements of 306 g cm^{-2} was provided by the U. S. Army Air Force.

[1] R. W. Williams and B. Rossi, unpublished results.
[2] Bruno Rossi and Kenneth Greisen, Rev. Mod. Phys. 13, 240 (1941).
[3] Bruno Rossi, Tech. Rep. No. 7, Lab. for Nucl. Sc. and Eng., M.I.T. (1948).
[4] Millikan, Neher, and Pickering, Phys. Rev. 63, 234 (1943).
[5] H. Bridge, W. E. Hazen, and Bruno Rossi, Phys. Rev. 73, 179 (1948).

The Effect of Non-Central Forces on the Collisions of High Energy Neutrons with Protons

H. S. W. Massey, E. H. S. Burhop, and Tsi-Ming Hu
University College, London, England
April 13, 1948

As it is now possible to investigate experimentally[1] the collisions of high energy (~100 Mev) neutrons with protons, it is important to have detailed information about the effects to be expected on the assumption of different types of interaction between neutron and proton. Camac and Bethe[2] have already taken the first step in this direction by calculating the angular distributions of projected protons for various incident neutron energies, assuming central interactions of spherical well type. As, however, the quadrupole moment of the deuteron shows that a strong non-central component of the interaction exists, it is necessary to carry out such calculations with this component included. This is particularly important because for neutrons with energies of 50–100 Mev the scattering of the d component of the incident waves is quite strong. The non-central admixture is therefore likely to have a much greater influence than in phenomena involving neutrons of lower energy. In this note we wish to report the results of the first cases investigated in pursuance of this program.

Following Rarita and Schwinger[3] three forms of the neutron-proton interaction $V(r)$ were assumed:

$$I.\quad V(r)=\tfrac{1}{2}\tau_1\cdot\tau_2\left\{1+\tfrac{1}{2}g(\sigma_1\cdot\sigma_2-1)+\gamma\left(\frac{3\sigma_1\cdot r\sigma_2\cdot r}{r^2}-\sigma_1\cdot\sigma_2\right)\right\}D\cdots r<a$$
$$=0\qquad\cdots r>a.$$

σ_1, σ_2 are the spin and τ_1, τ_2 the isotopic spin operators of the two nucleons, r their relative position vector. In the present calculation the constants a, g, γ, and D were taken the same as those used by Rarita and Schwinger, namely, $a=2.8\times10^{-13}$ cm, $g=0.0715$, $\gamma=0.775$, and $D=13.8$ Mev.

TABLE I.

Type of interaction	Central forces ratio $I_{180°}/I_{90°}$	Non-central forces ratio $I_{180°}/I_{90°}$
I	159*	9.56
II	234	3.80
III	9.7**	0.58

* We have calculated the angular distribution for central forces only in the case of interactions *II* and *III*. For interaction *I* the value quoted is that given by Camac and Bethe (see reference 2).
** The value for $I_{180°}/I_{90°}$ obtained by us with central forces and interaction *III* is almost exactly one-tenth of that given in Table III of Camac and Bethe's paper. Our value appears to follow from the constants given in Table II of their paper, however.

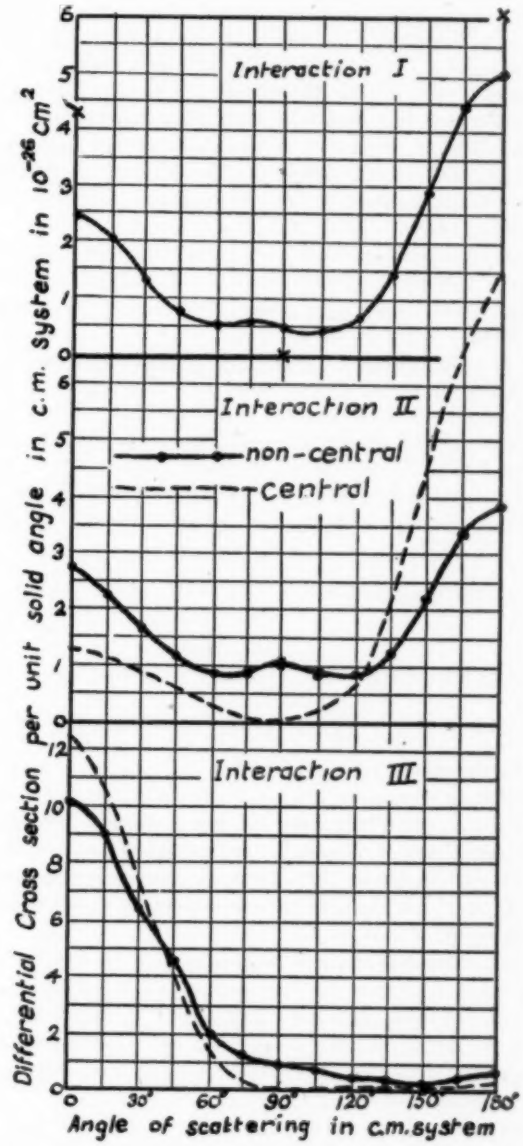

FIG. 1. Comparison of angular distribution of scattered neutrons in the c.m. system for non-central and central forces, and for the three interaction types. The total incident neutron energy assumed is 83 Mev. The circles shown on the curves represent actual calculated values.
In the case of central forces, interaction *I*, the crosses represent points calculated by Camac and Bethe.

This is an interaction of the same exchange type as that given by symmetrical meson theory.

II. As for *I* but with $\frac{1}{2}\tau_1\cdot\tau_2$ replaced by $\frac{1}{2}(1+\tau_1\cdot\tau_2)$. In this case the exchange operator is of the same form as that given by charged meson theory.

III. As for *I* but with $\frac{1}{2}\tau_1\cdot\tau_2$ replaced by -1. This is an interaction without exchange characteristics.

Angular distributions per unit solid angle, in the center of gravity system, for the scattering of 83 Mev-neutrons by protons initially at rest were calculated for each of the three assumed interactions and are illustrated in Fig. 1. The corresponding distributions for central interactions with the same exchange operators and range of the spherical well are also given for comparison.

Apart from the usual feature that the scattering maximum occurs at 180° for the exchange interactions *I* and *II* instead of at 0° as for the ordinary interaction *III*, it will be seen that the variation with angle, particularly for interaction *II*, is much less rapid for the exchange interactions. This is a marked feature only of non-central interactions, as may be seen from Fig. 1 and from the following table which gives the ratio $I_{180°}/I_{90°}$ of the differential cross section at 180° and 90° in the center of gravity system for the three types of interaction in the central and non-central cases for neutrons of energy 83 Mev.

From the preliminary reports of measurements made at Berkeley[1] it would appear that they already rule out a non-central force of type *III* but are not in marked contradiction with predictions based on a non-central force of type *II* with range near 2.8×10^{-13} cm.

The total elastic collision cross sections for collisions of 83-Mev neutrons with protons are found to be in units of 10^{-26} cm^2:

non-central interaction	*I*	14.10
	II	15.77
	III	23.38
central interaction	*I*	11.1 (Camac and Bethe)
	II	13.2 (Authors)
	III	19.5 (Authors)

In the case of central forces we have not calculated the total cross section for interaction *I*. The value 11.1×10^{-26} cm^2 is that given by Camac and Bethe. Actually the calculations of these writers is for a neutron energy of 80 Mev, while our calculations have been made for a neutron energy of 83 Mev, but the difference would not be expected to be significant.

Measurements of the total cross section for 90 ± 13 Mev neutrons scattered by protons, reported recently from Berkeley,[4] have given the value $(8.3\pm0.4)\times10^{-26}$ cm^2.

Calculations are now in progress for non-central forces of other ranges and also with radial variation other than of spherical well form.

We are indebted to Miss K. Blunt for assistance in certain of the numerical calculations.

[1] Hadley, Leith, York, Kelly, and Wiegand, Phys. Rev. **73**, 541 (1948).
[2] M. Camac and H. A. Bethe, Phys. Rev. **73**, 191 (1948).
[3] W. Rarita and J. Schwinger, Phys. Rev. **59**, 436 (1941).
[4] Cork, McMillan, Paterson, and Sewell, Phys. Rev. **72**, 1264 (1947).

Self-Delayed Coincidences with Scintillation Counters*

S. DeBenedetti, F. K. McGowan, and J. E. Francis, Jr.
Oak Ridge National Laboratory, Oak Ridge, Tennessee
April 19, 1948

IT is possible to measure time intervals between two ionizing events by studying the distribution of pulses from a single detector provided the dead time of the detector is smaller than the interval to be measured. A possible method consists in recording the coincidences between the signals from two separate channels, both activated by the same detector pulse, but designed so that the first produces an immediate signal of duration τ_1 and the second gives a signal of delay T and duration τ_2 (*self-delayed coincidences*). Provided $T>2\tau_1$, we obtain a count for detector pulses whose interval in time is between $T-\tau_1$ and $T+\tau_2$. The smallest time intervals which can be measured with this method is $\sim10^{-4}$ sec. for Geiger counters. However, with scintillation counters[1] which supposedly have a very short dead time, the method of self-delayed coincidences should be capable of measuring very short intervals, and has the advantage of requiring only one amplifier.

To test this point a source of Hf^{181} (known to decay into Ta^{181*} of 22-μsec. half-life[2]) was located close to a clear anthracene[3] sample ($\sim0.5\times1\times2$ cm); on the opposite side, at a distance of 0.3 cm, was the glass wall of a 1P21 photo-multiplier tube, operating at 60 volts per stage. The pulses from this tube, after amplification, were fed to a self-delayed coincidence circuit as described above. With this arrangement it was possible to measure the half-life of Ta^{181*}, obtaining a value in good agreement with previous determinations.

Though no special effort was made to realize maximum efficiency (the efficiency can be increased by moving the anthracene closer to the tube and by placing the source between the tube and the anthracene sample), the efficiency of the present arrangement is almost equal to that of the old instrument involving two thin mica window Geiger counters at $\sim$50 percent geometry.

In the following table counting rates (counts/min.) of single counts and delayed coincidences (for the same source and with same delay and resolving times) are shown. This indicates that anthracene scintillation counters are highly efficient, not only for the main radiation from Hf^{181}, but also for the radiation of Ta^{181*}, which consists of electrons and gammas of around 100 kev. Despite the fact that the photo-multiplier was used at room temperature, the background corresponding to this efficiency is not too high.

Table I.

	Geiger counters	Anthracene counters
Background (single counts)	20	150
Single counts from source	9600	7200
Delayed coincidences	230	130

Even in the time range where Geiger counters can be used the scintillation counters present the advantage of a higher efficiency for gamma-rays, and may permit the detection of slightly converted short-lived isomers which are difficult to observe with other techniques. Furthermore, one should not overlook the possibility of measuring much shorter times.

* This document is based on work performed under Contract No. W-35-058 eng-71 for the Atomic Energy Project at Oak Ridge National Laboratory.
[1] H. Kallmann, Natur und Technik (July 1947).
[2] S. DeBenedetti and F. K. McGowan, Phys. Rev. **70**, 569 (1946).
[3] See preceding letter.

Rotational Spectrum of $OC^{14}S$, and the Nuclear Spin of C^{14}

ARTHUR ROBERTS
Physics Department, State University of Iowa, Iowa City, Iowa
April 13, 1948

THE pure rotational transition $J=1\rightarrow 2$ of carbon oxysulphide, OCS, made with C^{14}, has been observed at 24, 173.0±1 mc, which agrees with the value predicted from the frequencies observed for isotopic molecules.[1] No hyperfine structure as great as 0.5 mc is observable. In addition, the Stark effect pattern is visually identical with that of the C^{13} isotopic molecule, showing no sign of hyperfine structure. Furthermore, the *l*-type doublet due to molecules excited to the first vibrational bending mode ($v_2=1$) has been observed; these lines also show no hyperfine structure. With Townes'[2] estimate of $\partial^2V/\partial z^2$ in this molecule, this means that the quadrupole moment of the C^{14} nucleus is probably less than 10^{-27} cm^2. One can therefore conclude that the spin of C^{14} is most probably zero, in accord with the findings of Jenkins[3] from band spectra (published after these measurements were made) and the as yet unbroken rule that even-even nuclei have zero spin.

Well-known and serious difficulties are encountered by current beta-ray theory[4] in attempting to explain the homologous $4n+2$ series of beta-ray transitions $He^6\rightarrow Li^6$, $C^{10}\rightarrow B^{10}$, $Be^{10}\rightarrow B^{10}$, and $C^{14}\rightarrow N^{14}$. Of these the first two are apparently allowed, the last two highly forbidden, although all are expected to follow the same selection rules $I=0\rightarrow 1$ (no), and are in addition favored transitions by Wigner rules. It is perhaps worth pointing out that the polar vector interaction, obeying Fermi selection rules, makes the $C^{14}\rightarrow N^{14}$ transition second forbidden, as the *ft* value seems to require. In this case only the matrix element $\int\boldsymbol{\alpha}\times\mathbf{r}$ survives, giving a definite predicted shape to the beta-spectrum which differs, albeit slightly, from the allowed shape. Thus, a sufficiently precise experimental determination of the beta-ray spectrum of C^{14} may serve to show either (a) that the polar-vector interaction can explain the C^{14} disintegration, in which case spin determinations in the other members of the series will assume even greater interest, or (b) that, as seems more likely, no single interaction can explain the series, and a new theoretical approach is necessary.

The *l*-type doublet of $O^{16}C^{14}S^{32}$ has the spacing 26.8 ±0.4 mc, as compared with 24.9±0.4 mc for $O^{16}C^{13}S^{32}$. The parameter α_2 of the bending vibration is -9.4 ± 0.3 mc as compared with -10.6 ± 0.3 mc for $O^{16}C^{13}S^{32}$ (assuming symmetrical doubling of the rotational levels). The frequency of the C^{14} line was not determined with sufficient precision to check the accepted nuclear mass of C^{14}; because of the central position of the carbon atom, OCS is an unsuitable molecule for this purpose. The $OC^{14}S$ was prepared by G. Matlack and John F. Haskin of the Department of Chemistry and Chemical Engineering under the direction of Professor G. Glockler, from high specific activity[5], C^{14} obtained from the Isotopes Branch of the Atomic Energy Commission.

[1] T. W. Dakin, W. E. Good, and D. K. Coles, Phys. Rev. **71**, 640 (1947).
[2] C. H. Townes, A. N. Holden, and F. R. Merritt, Phys. Rev. **72**, 513 (1947).
[3] F. A. Jenkins, Phys. Rev. **73**, 639 (1948).
[4] E. J. Konopinski, Rev. Mod. Phys. **15**, 209 (1943); J. R. Oppenheimer, Phys. Rev. **59**, 908 (1941).
[5] L. D. Norris and A. H. Snell, Phys. Rev. **73**, 254 (1948).

The Use of Anthracene as a Scintillation Counter*

P. R. BELL
Oak Ridge National Laboratory, Oak Ridge, Tennessee
April 19, 1948

THE method of counting ionizing radiations by photoelectric measurement of the fluorescent light pulses emitted by certain organic substances was first

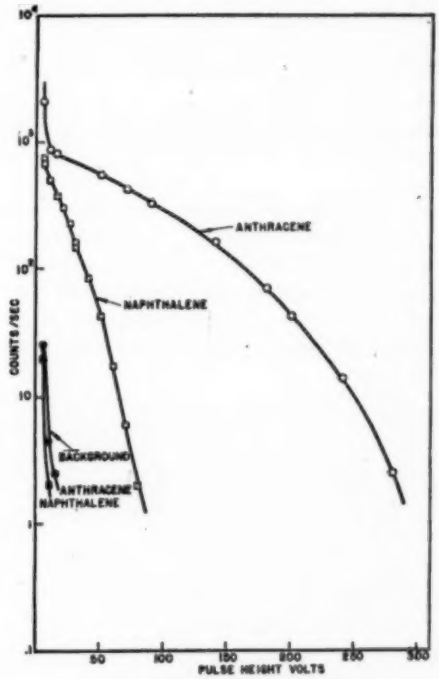

FIG. 1. CO^{60} gamma-rays.

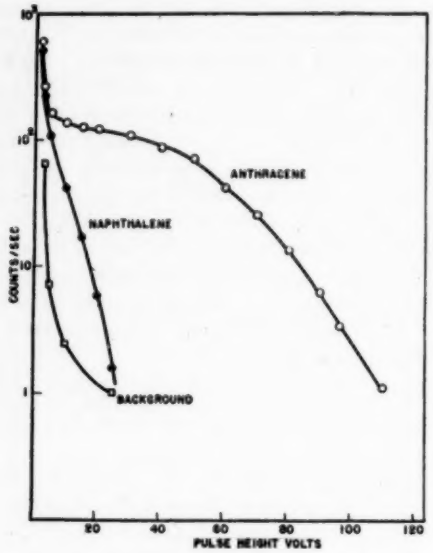

FIG. 2. Alpha-particles of Po.

pointed out by H. Kallman[1] and verified by M. Deutsch.[2] The substance most used by these authors is naphthalene, but both authors have suggested anthracene as a possible alternative.

In this laboratory we have prepared some transparent crystalline slabs of both materials, and their behavior as scintillation counters has been compared. It was found that it was more difficult to prepare satisfactory anthracene samples, but that these performed much better than naphthalene. Both kinds of samples were prepared by slow cooling of the melted materials. Anthracene had to be previously purified by sublimation and crystallization from hot benzene, and had to be melted in an atmosphere of nitrogen or argon. In this way clear pieces which appeared to be single crystals as large as 4×5×1 cm could be obtained.

For the comparison the samples were placed as close as possible to the window of a 1P21 photo-multiplier tube operating at about 60 volts per stage. The tube and crystal were kept at room temperature. The pulses were amplified by a wide band linear amplifier[3] equipped with a pulse height selector with which one could conveniently study the size of the pulses.

Using samples of roughly the same size, it was found that gamma-rays from Co^{60} produced pulses about three times larger in anthracene than in naphthalene. The counting rate against pulse height selector setting is shown in Fig. 1. Extrapolating the counting rate to zero pulse height, the two materials give nearly the same number of counts, which is in agreement with Deutsch's finding that in these conditions we have 100 percent efficiency for the secondary electrons. However, if one sets the pulse height selector to admit only 10 background counts/sec., the anthracene is 93 percent efficient and the naphthalene only 63 percent. Raising still more the pulse height selector setting, it is possible to have both a high efficiency and a low background when anthracene is used.

Some experiments with C^{14}, emitting beta-rays of 154-kev maximum energy, proved that anthracene responds to electrons of this energy with about the same efficiency as a thin mica window Geiger counter.

Although Kallmann states that he was unable to count alpha-particles with his equipment when using scintillations from naphthalene, we could detect Po alpha-particles both with naphthalene and anthracene. Figure 2 shows the pulse height distribution for the two materials; it is evident that the pulses from anthracene are about five times larger. The extrapolated counting rate was the same as that found with the same source in an argon ionization chamber.

It seemed reasonable to expect that this system would count the recoil protons produced by fast neutrons, and some absorption experiments in Pb were carried out using a Po-α-Be neutron source. The absorption coefficient of Pb for the radiation responsible for most of the counts was 0.118 cm^{-1}. This value is much too small for gamma-rays of any energy and is in fairly good agreement with what could be expected for fast neutrons.

The neutrons produce very large pulses, some of which are two times as large as the largest pulses produced by Co^{60} gamma-rays. For an anthracene sample 1 cm thick a rough calculation shows that about 10 percent of the fast neutrons striking the anthracene are counted.

* This document is based on work performed under Contract Number W-35-058 eng-71 for the Atomic Energy Project at Oak Ridge National Laboratory.

[1] H. Kallmann, Natur and Technik (July 1947).
[2] Martin Deutsch, M.I.T. Tech. Rep. No. 3.
[3] W. H. Jordan and P. R. Bell, Rev. Sci. Inst. 15, 703 (1947).

Nuclear Reactions of Arsenic with 190-Mev Deuterons

H. H. HOPKINS, JR. AND B. B. CUNNINGHAM
Department of Chemistry and Radiation Laboratory, University of California, Berkeley, California

April 16, 1948

BOMBARDMENT of thin targets of pure arsenic ($_{33}As^{75}$) with 190-Mev deuterons has led to the observation of nuclear reactions in which some of the product nuclei are more than 20 mass units lighter than the target nucleus. Identification of these and of other reaction products was made by chemical separation of the various radio-isotopes into elemental fractions, followed by an investigation of the radiations associated with each fraction.

The gross rate of decay of the radio-isotopes in each elemental fraction was determined with argon-filled (10 cm pressure) Geiger-Müller counting tubes of the thin window type (*ca.* 3 mg/cm^2 of mica). The half-lives obtained from the resolved decay curves formed the chief basis for identification of known isotopes. In those cases in which sufficient activity was available, samples were placed in a crude beta-ray spectrometer and tested for positive or negative beta-particles.

Most of the radiations observed could be assigned to known isotopes; these isotopes are listed in Table I. The identifications of Zn^{72}, Cu^{60}, Ni^{57}, and Co^{55} are uncertain as they are based on half-lives obtained with low accuracy as a result of the high level of accompanying activities. The assignments of Mn^{52} and Cr^{51} are based on reliable half-life determinations from measurements of a small amount of activity in the manganese and chromium fractions. The identification of the remaining isotopes is beyond doubt.

Several new radioactivities have been observed. Mass assignments have been made by demonstration of the following decay chains.

(a) $\underset{\text{(new) 9.5 d}}{\text{Se}^{72}} \xrightarrow{K} \underset{\text{(known) 26 hr.}}{\text{As}^{72}} \xrightarrow{\beta^+} \text{Ge}^{72}$,

(b) $\underset{\text{(new) 44 m}}{\text{Se}^{71}} \xrightarrow{\beta^+} \underset{\text{(new) 52 m}}{\text{As}^{71}} \xrightarrow{\beta^+} \underset{\text{(known) 40 hr.}}{\text{Ge}^{71}} \xrightarrow{\beta^+} \text{Ga}^{71}$,

(c) $\underset{\text{(unassigned) (1) 250 d}}{\text{Ge}^{68}} \xrightarrow{K} \underset{\text{(known) 68 m}}{\text{Ga}^{68}} \xrightarrow{\beta^+} \text{Zn}^{68}$.

"Milkings" of As^{73} from Se^{73} (β^+, 6.7 hour) have failed to produce measurable activity. This behavior is consistent with the assignment of the 100-day activity[2] to As^{73}.

Rough values for the yields of the isotopes have been determined. The figures presented in the table are ratios relative to the yield of As^{72}, and are average figures for several bombardments. The calculations are only approximate because of errors due to (a) self-absorption and absorption in air, (b) scattering, and (c) unknown counting efficiencies for orbital electron capturing isotopes.

In the column "reaction Δ" are given the differences in mass and charge between the product isotopes and the target nucleus, $_{33}As^{75}$. Because of the time required for chemical separations, no activities of less than about 15 minutes half-life would have been seen. Isotopes of half-life greater than about 200 days formed in yield less than 0.05 that of As^{72} would not have been detected.

Salient features of the data are: (a) the low yield of selenium isotopes as compared with arsenic isotopes, (b) the predominance of neutron deficient isotopes from selenium to gallium, and (c) the presence of isotopes containing an excess of neutrons, of the elements below zinc in yields comparable to those of the neutron deficient isotopes.

It will be noted that over 80 percent of the reactions observed produce isotopes within 8 mass units of As^{75}. Since these reactions require excitation of less than ~75 Mev, it appears that the high energy deuteron gives up only part of its energy in most of the reactions. This behavior is consistent with the picture of high energy nuclear reactions recently proposed by Serber.[3]

This work was performed under Contract No. W-7405-eng-48, with the Atomic Energy Commission in connection with the Radiation Laboratory of the University of California, Berkeley, California. The bombardments were conducted by Dr. Duane Sewell and the 184-inch cyclotron group.

TABLE I. Isotopes produced by $_{33}As^{75}$ + 200 Mev D^+.

Isotope	Type of radiation[a]	Half-life Observed	Half-life Literature[b]	Yield[c] Rel As^{72} [d]	Reaction Δ ΔZ	Reaction Δ ΔA
$_{34}Se^{75}$	(K, γ, e^-)	120 d	115 d[e]	0.11 (5%)	+1	+0
$_{34}Se^{73}$	β^+	6.7 h	—	0.09	+1	−2
$_{34}Se^{72}$	K	9.5 d	—	0.1 (100%)	+1	−3
$_{34}Se^{71}$	β^+	44 m	—	0.01	+1	−4
$_{33}As^{74}$	β^-, β^+, γ	19.0 d	16 d	1.1	0	−1
$_{33}As^{72}$	β^+	26 h	26 h	1.00	0	−3
$_{33}As^{71}$	β^+	52 m	—	0.3	0	−4
$_{32}Ge^{71}$	β^+, K	{38 h {11.4 d	40 h 11 d	2 ~2 (3%)	−1	−4
$_{32}Ge^{68}$	K	250 d	195 d	≈5 (100%)	−1	−6
$_{31}Ga^{68}$	β^+	68 m	68 m	0.2	−2	−7
$_{31}Ga^{67}$	K, γ, e^-	83 h	83 h	~3 (5%)	−2	−8
$_{31}Ga^{66}$	β^+	10 h	9.4 h	~0.1	−2	−9
$_{30}Zn^{72}$	(β^-, γ)	~50 h	49 h[f]	≤0.001	−3	−3
$_{30}Zn^{69}$	$(\beta^-, \text{I. T.}, \gamma)$	{51 m {14 h	57 m 13.8 h	0.07 0.05	−3	−6
$_{29}Cu^{67}$	β^-	61 h	56 h[g]	0.02	−4	−8
$_{29}Cu^{64}$	$(\beta^-, \beta^+, K, \gamma)$	13 h	12.8 h	0.1	−4	−11
$_{29}Cu^{61}$	(β^+, K)	3.3 h	3.4 h	0.1 (100%)	−4	−14
$_{29}Cu^{60}$	(β^+)	~20 m	24.5 m[h]	0.06	−4	−15
$_{28}Ni^{56}$	β^-	56 h	56 h[g]	0.002	−5	−9
$_{28}Ni^{65}$	(β^-, γ)	2.6 h	2.6 h	0.001	−5	−10
$_{28}Ni^{57}$	β^+	34 h	36 h	0.0002	−5	−18
$_{27}Co^{61}$	(β^-)	1.8 h	1.75 h[i]	0.003	−6	−14
$_{27}Co^{58-56}$	(β^+, γ, K)	~80 d	72 d	0.06 (35%)	−6	{−19 −17
$_{27}Co^{55}$	β^+, γ	~16 h	18.2 h	0.003	−6	−20
$_{26}Fe^{59}$	(β^-, γ)	43 d	47 d	0.005	−7	−16
$_{25}Mn^{56}$	(β^-, γ)	2.6 h	2.59 h	0.002	−8	−19
$_{25}Mn^{52}$	(β^+, γ, K)	6 d	6.5 d	0.0002 (40%)	−8	−23
$_{24}Cr^{51}$	(K, γ, e^-)	26 d	26.5 d	0.005 (5%)	−9	−24

[a] Parentheses signify identification based on half-life determination only.
[b] G. T. Seaborg, Rev. Mod. Phys. 16, 1 (1944).
[c] The yield of As^{72} corresponds to a cross section of about 0.02×10^{-24} cm².
[d] Parenthesized figures signify assumed counting efficiencies.
[e] H. N. Friedlander, L. Seren, and S. H. Turkel, Phys. Rev. 72, 23 (1947).
[f] Plutonium Project compilation, "Nuclei formed in fission," J. Am. Chem. Soc. 68, 2411 (1946).
[g] R. H. Goeckermann and I. Perlman, private communication (January, 1948).
[h] C. E. Leith, A. Bratenahl, and B. J. Moyer, Phys. Rev. 72, 732 (1947).
[i] T. J. Parmley and B. J. Moyer, Phys. Rev. 72, 82 (1947).

[1] W. B. Mann, Phys. Rev. 54, 649 (1938).
[2] L. G. Elliot and M. Deutsch, Phys. Rev. 63, 457 (1943).
[3] R. Serber, Phys. Rev. 72, 1114 (1947).

The Neutron-Proton Scattering Formula*

L. EISENBUD
Brookhaven National Laboratory, Upton, New York
April 13, 1948

IN the letter of Flügge and Hückel[1] it was pointed out that the neutron-proton scattering cross sections may be obtained for low energies of the incident neutron from an expression similar to the Breit-Wigner formula. It was stated that the "energy of the singlet level"—the E' ($=\hbar^2\kappa'^2/M$) of their formula—required to provide a fit to observed low energy neutron-proton cross sections is about 1.5 Mev. In the concluding remarks of their letter, Flügge and Hückel imply that the deviation of this value of E' from the "energy of the singlet level" as usually given, $\epsilon' \sim 0.1$ Mev, has important consequences for other problems.

The formalism developed by Wigner and Eisenbud[2] provides a one-level resonance formula for the neutron-proton scattering cross section. The various constants which appear in the formula may be calculated explicitly if the form of the neutron-proton interaction law is known. If we use for the $n-p$ interaction in the singlet state a "square well" with range $a=e^2/mc^2$ and depth adjusted to fit the thermal neutron cross sections, the "energy of resonance" $E_r=E_\lambda+\Delta_\lambda$ (Eq. (56) of reference 2) is 1.9 Mev. This is approximately the value of E' given by Flügge and Hückel.

It should be stated, however, that this "resonance energy" has no direct relationship with the ϵ' as defined by Bethe.[3] The interaction law which was used to obtain 1.9 Mev for the "resonance energy" may also be used to calculate ϵ'; the value which results is $\leqq 0.1$ Mev. Since the same interaction law provides these different numbers, it is clear that the numbers have only a formal significance, and their difference cannot have physical consequences.

* Research carried out at the Brookhaven National Laboratory under the auspices of the Atomic Energy Commission.

[1] S. Flügge and E. Hückel, Phys. Rev. **73**, 520 (1948).
[2] E. P. Wigner and L. Eisenbud, Phys. Rev. **72**, 29 (1947).
[3] H. A. Bethe and R. F. Bacher, Rev. Mod. Phys. **8**, 114 (1936).

On the Lifetime of Negative Mesons

W. L. KRAUSHAAR
Cornell University, Ithaca, New York
April 16, 1948

WHILE it is highly improbable that the proper mean life of the negative meson is different from that of the positive meson, the published experimental evidence for this appears to be scanty.

There are several experiments which show that the mean life of the negative meson cannot be an order of magnitude different from 2 microseconds: (1) The mean life of negative mesons stopped in aluminum was shown by Valley and Rossi[1] to be about 0.74 microsecond, hence the proper mean life cannot be less than that value since capture can only serve to decrease the apparent lifetime; (2) mean life determinations by measurement of the relative meson intensity as a function of depth in the atmosphere are sensitive to mesons of both signs, and the lifetime values so obtained are not in violent disagreement with the accepted positive meson lifetime; and (3) Sigurgierson and Yamakawa[2] found no definite disagreement with a lifetime of 2.2 microseconds for mesons of both signs stopped in light materials, although they had a very small number of counts.

In the course of another experiment we have accumulated some 1500 delayed counts for mesons of either sign stopped in carbon. Details of the experiment will be published at some later date; it is sufficient to note here that the detecting equipment is similar to that used by Rossi, Sands, and Sard.[3] Delayed events in the intervals 1 to 3, 3 to 5, and 5 to 7 microseconds are recorded at an average rate of about 1.5 per hour. The mean life that has been observed from this measurement is 2.21 ± 0.15 microseconds, well within the value obtained by Rossi and Nereson[4] for positive mesons stopped in heavy materials (2.15 ± 0.07 microseconds). A short run using iron in the same apparatus has given 2.21 ± 0.4 microseconds.

The measurements of Valley[5] have shown that a normal positive excess is obtained for mesons stopping in carbon, thus indicating that the mean life of the negative meson is not long and made to appear normal in carbon because of a competitive capture process. Assuming a positive excess of 20 percent and a mean life of 2.15 ± 0.07 microseconds for the positive meson, it is possible to estimate the proper mean life of the negative meson to be 2.28 ± 0.34 microseconds from our data.

This work was supported in part by the Office of Naval Research.

[1] G. E. Valley and B. Rossi, Phys. Rev. **73**, 177 (1948).
[2] T. Sigurgierson and A. Yamakawa, Phys. Rev. **71**, 319 (1947).
[3] B. Rossi, M. Sands, and R. F. Sard, Phys. Rev. **72**, 120 (1947).
[4] B. Rossi and N. Nereson, Phys. Rev. **62**, 417 (1942).
[5] G. E. Valley, Phys. Rev. **72**, 772 (1947).

Stability of Os^{187} against K Capture*

H. H. SELIGER AND H. L. BRADT**
Purdue University, Lafayette, Indiana
April 19, 1948

NALDRETT and Libby[1] have recently described experiments regarding the stability of the isobars $Os^{187}-Re^{187}$. We have investigated the problem some time ago and, since our method was somewhat different, a brief description of our results may be of interest.

The small relative abundance of Os^{187} at first would lead to the expectation that, in the case of the $Re^{187}-Os^{187}$ pair, the Os^{187} isotope should be unstable and transform by K capture into Re^{187}. Zingg[2] tried to detect the rhenium x-rays following the expected K capture of Os^{187} without success. Since air was used as a counter gas, the efficiency for detection of the x-rays was extremely low. Lougher and Rowlands[3] placed osmium powder in a cloud chamber and observed tracks of photoelectrons. Assuming that these electrons were produced in the chamber gas by the rhenium K_α x-rays emitted upon K capture by Os^{187}, a value of 3×10^8 years was estimated for the half-life of Os^{187}.

In our experiment two identical thin-walled aluminum counters filled, respectively, with 29-cm Hg xenon and 10-cm Hg argon (plus 1-cm Hg alcohol) were used to attempt to detect the rhenium x-rays. These counters were alternately surrounded by a cylinder of 19 grams of metallic osmium powder. Since the efficiency for the detection of rhenium x-rays of the counter filled with the 29-cm xenon is very much greater than that of the counter filled with the 10-cm argon, presence of x-rays following K capture of Os^{187} should give rise to a difference in the counting rates of the xenon- and the argon-filled counters.

The cosmic-ray background was reduced to less than seven counts per minute with the aid of an anticoincidence

counter shield. A counting rate of several thousand counts per minute was to be expected from the value of the half-life given by Lougher and Rowlands. The actual counting rate after subtraction of background was 2.9 ± 0.2 counts per minute for the xenon counter and 2.6 ± 0.2 counts per minute for the argon-filled counter. These very small counting rates are equal within the limits of statistical accuracy and are due to beta-rays of approximately 1.7-Mev energy, from a trace of radioactive contamination. Hence, no activity caused by K capture of Os^{187} is indicated. This negative result leads to an estimated minimum value of 4×10^{12} years for the half-life of Os^{187} so far as possible K capture is concerned. Taking into account the counter efficiencies for rhenium L x-rays and the absorption in the counter walls, a minimum value for the half-life in the case of L capture is estimated at 0.6×10^{12} years.

The above result, showing the absence of x-rays due to an orbital electron capture of Os^{187}, is in agreement with the results of Naldrett and Libby, who, using counters filled with argon and OsO_4, respectively, showed that no Auger electrons are emitted by Os^{187}. They showed, moreover, that the other member of the pair, Re^{187}, is β^--unstable.

This experiment was completed in January 1948.

* Work performed under Navy Contract N6ori-222, Task Order I.
** Now at the University of Rochester.
[1] Naldrett and Libby, Phys. Rev. **73**, 487 (1948).
[2] Scherrer and Zingg, Helv. Phys. Acta **12**, 283 (1939); Zingg, Helv. Phys. Acta **13**, 219 (1940).
[3] Lougher and Rowlands, Nature **153**, 374 (1944).

High Energy Neutron-Proton Scattering

G. F. CHEW* AND M. L. GOLDBERGER
Institute for Nuclear Studies, University of Chicago, Chicago, Illinois
April 13, 1948

WE have investigated the scattering of high energy neutrons by protons with the interaction potential given by the symmetrical meson theory with the tensor force omitted:

$$V=\tfrac{1}{3}[1-\tfrac{1}{2}g+\tfrac{1}{2}g\sigma_1\cdot\sigma_2]\tau_1\cdot\tau_2\sigma_1\cdot\sigma_2(\mu B)(e^{-\mu r}/\mu r)$$

σ_1, σ_2, τ_1, τ_2 are the usual spin and isotopic spin operators. The constants B, g, and μ were chosen to give the correct binding energy of the deuteron and low energy neutron-proton scattering.[1] The values taken were $B\mu=67.8$ Mev, $1/\mu=1.18\times10^{-13}$ cm, $g=0.157$. [In order to fit the low energy proton-proton cross section, g should be taken as 0.162.]

The method of phase shifts was used throughout since it was found that the Born approximation gives unreliable results especially with respect to the angular distribution, as has been stressed by Camac and Bethe.[2] At 2.2 Mev and 20 Mev the results are substantially the same as those obtained from the corresponding square well potential. The results at 80 Mev are cited in Table I, with the square well and Born approximation figures given for comparison.

One sees that the Yukawa potential gives an appreciably higher cross section than the square well, but a much more reasonable ratio R, which is found experimentally to be ~3 in the 100-Mev region.[3] Inclusion of the tensor force will modify these results. A preliminary estimate, based on the Born approximation, predicts that R will be reduced by about a factor of 2, while the total cross section is increased slightly.

TABLE I.

	σ Total cross section $\times10^{24}$ cm^2	R Ratio of intensity at 180° to that at 90° in the c.g. system
Yukawa-exact	0.140	6.81
Yukawa-born approximation	0.150	12.5
Square well (range 2.8×10^{-13} cm)[1]	0.111	159

The constants for the tensor force case with a Yukawa potential have been calculated and tentative values are: $\gamma B\mu=85\pm2$ Mev, $(1-2g)B\mu=46.5$ Mev, $B\mu=0\pm3$ Mev, in the Rarita-Schwinger notation. The exact calculation of the high energy cross section for the tensor force case is being carried out.

* National Research Council Predoctoral Fellow.
[1] R. G. Sachs and M. Goeppert-Mayer, Phys. Rev. **53**, 991 (1938); L. E. Hoisington, S. S. Share, and G. Breit, Phys. Rev. **56**, 884 (1939).
[2] M. Camac and H. Bethe, Phys. Rev. **73**, 191 (1948).
[3] J. Hadley, C. Leith, H. York, E. Kelly, and C. Wiegand, Bull. Am. Phys. Soc. **23**, 15 (1948).

Einstein's Equivalence Principle and the Problem of Blind Navigation

JOHN J. GILVARRY
North American Aviation, Inc., Los Angeles, California
April 13, 1948

THE importance of Einstein's equivalence principle[1] in the problem of blind navigation of aerial or space vehicles has been appreciated[2] for a long time. A formulation of the limitations this principle imposes in the practical solution of the problem has, however, never been published. The following discussion assumes a vehicle having no radiation connection with the earth and confining an observer who is posed with the problem of determining the vehicle's position with respect to the earth purely by dynamic measurements. A dynamic measurement is defined as a force measurement on a proof body, or a measurement of acceleration, velocity, or displacement on such a body. The gravitational field in the neighborhood of the vehicle is assumed locally uniform, and Newtonian mechanics is assumed.

The forces acting on the vehicle can be analyzed into three sets: forces, whose sum is **F**, due to external, non-gravitational forces on the vehicle; forces, whose sum is **L**, due to the reaction on the vehicle of the internal forces exerted on a proof body; and forces, whose sum (per unit mass) is **g**, due to the gravitational attraction of all other

mass in the universe. The equation of motion of the center of mass (position vector $\mathbf{R}_i$) of the vehicle and proof body in an inertial reference frame is

$$d^2\mathbf{R}_i/dt^2=\mathbf{F}/(M+m)+\mathbf{g}, \tag{1}$$

where M is the mass of the vehicle and m that of the proof body. The equation of motion of the proof body in a non-rotating reference frame is

$$(\mu/m)(d^2\mathbf{r}/dt^2)+(\mathbf{L}/m)=-\mathbf{F}/(M+m), \tag{2}$$

where $\mathbf{r}$ is the radius vector of the proof body relative to an origin fixed in the vehicle and μ is the reduced mass of the proof body relative to the vehicle. The quantity $\mathbf{b}_{obs}$, defined by

$$\mathbf{b}_{obs}=(\mu/m)(d^2\mathbf{r}/dt^2)+(\mathbf{L}/m), \tag{3}$$

is dynamically measurable within the vehicle (assuming m and μ known), and an instrument designed to measure it is usually termed an accelerometer. The quantity $\mathbf{b}$, defined by

$$\mathbf{b}=\mathbf{F}/(M+m), \tag{4}$$

is the acceleration of the vehicle (and proof body) due to external non-gravitational forces. Equation (2) states:

$$\mathbf{b}_{obs}=-\mathbf{b}, \tag{5}$$

or, in words: A vehicle-borne accelerometer measures the negative of the acceleration due to external non-gravitational forces. From the fact that Eq. (2) does not contain $\mathbf{g}$, it is clear that an accelerometer can never measure $\mathbf{g}$ directly. Equation (6) below shows that an accelerometer (or gravimeter) can determine $\mathbf{g}$ indirectly by measuring the negative of the equilibrant non-gravitational forces per unit mass when the vehicle is unaccelerated (but cannot determine the existence of the equilibrium).

Returning to Eq. (1), one obtains

$$(d^2\mathbf{R}_i/dt^2)-\mathbf{g}=\mathbf{b}(t) \tag{6}$$

as the equation of motion of the vehicle. In this equation, only the term $\mathbf{b}$ (a function of time if a clock is carried) is an observable from the standpoint of the observer within the vehicle. To solve Eq. (6) for $\mathbf{R}_i$, the observer must know the mathematical form of the point function $\mathbf{g}$, and likewise that of the centrifugal and Coriolis accelerations corresponding to the earth's rotation, in their dependence on position (and velocity) coordinates in space. In a geocentric reference frame fixed in the earth (an approximately inertial frame), Eq. (6) becomes

$$(d^2\mathbf{R}/dt^2)+g_0(R_0^2/R^3)\mathbf{R}=\mathbf{b}(t), \tag{7}$$

where $\mathbf{R}$ is the position vector of the vehicle and only the most significant term in the gravitational acceleration (that due to the earth considered as an equivalent sphere of radius R_0 and gravitational acceleration on its surface of g_0) has been retained. To determine $\mathbf{R}$, the vehicle-borne observer must solve the differential equation (7) subject to the appropriate initial conditions on vehicle position and velocity.

The fundamental equation (7) is non-linear, and, except in special cases, can be solved only approximately or numerically. If $\mathbf{b}$ is zero, for example, it becomes the (soluble) differential equation of a rocket in an elliptic trajectory. For a vehicle initially launched vertically from the earth's surface, the linearized solutions in a reference frame with the y axis vertical, the x axis horizontal, and origin on the earth's surface are

$$x=(v_{x,0}/\omega_x)\sin\omega_x t+(1/\omega_x)\int_0^t b_x(\tau)\sin\omega_x(t-\tau)d\tau, \tag{8a}$$

$$y=(v_{y,0}/\omega_y)\sinh\omega_y t-(2g_0/\omega_y^2)\sinh^2(\omega_y t/2)+(1/\omega_y)\int_0^t b_y(\tau)\sinh\omega_y(t-\tau)d\tau, \tag{8b}$$

where $v_{x,0}$ and $v_{y,0}$ are initial velocities, b_x and b_y are components of $\mathbf{b}$, $\omega_x=(g_0/R_0)^{\frac{1}{2}}$ and $\omega_y=(2g_0/R_0)^{\frac{1}{2}}$. The zero-order solutions corresponding to a flat earth are obtained from Eqs. (8a) and (8b) by letting $R_0\to\infty$, which yields the familiar

$$x=v_{x,0}t+\int_0^t\int_0^\tau b_x(\lambda)d\lambda d\tau, \tag{9a}$$

$$y=v_{y,0}t-\tfrac{1}{2}g_0t^2+\int_0^t\int_0^\tau b_y(\lambda)d\lambda d\tau. \tag{9b}$$

A correction factor of type corresponding to Eqs. (9a) and (9b) was used in connection with the accelerometer which fixed the fuel cut-off point of the German V-2 rocket.[3,4]

If Einstein's equivalence principle is formulated analytically[5] as

$$\mathbf{g}_{obs}=\mathbf{g}-(d^2\mathbf{R}_i/dt^2), \tag{10}$$

where $\mathbf{g}_{obs}$ is the apparent gravitation and $(\partial^2R_i/\partial t^2)$ is the acceleration of the observer's reference frame, this formulation is the same as Eq. (7) with the identifications

$$\mathbf{g}_{obs}=\mathbf{b}_{obs}=-\mathbf{b}, \tag{11}$$

and

$$\mathbf{g}=-g_0(R_0^2/R^3)\mathbf{R}. \tag{12}$$

The equivalence principle is frequently interpreted[2] to imply that no dynamic experiment made by an observer within a windowless box can discriminate between a gravitational field due to attracting matter and the apparent field due to an acceleration of the box. This categorical interpretation is obviously too restrictive, since the procedure outlined above of solving Eq. (7) for $\mathbf{R}$, which yields $\mathbf{g}$, is always possible unless the proviso be made that the hypothetical observer is confined to the windowless box *throughout all time.*

[1] A. Einstein, Ann. d. Physik **35**, 898 (1911).
[2] F. K. Richtmyer and E. H. Kennard, *Introduction to Modern Physics* (McGraw-Hill Book Company, Inc., New York, 1942), third edition, p. 151.
[3] W. G. A. Perring, J. Roy. Aero. Soc. **50**, 483 (1946).
[4] T. M. Moore, Elec. Eng. **65**, 303 (1946).
[5] M. Born, *Die Relativitaetstheorie Einsteins* (Verlag Julius Springer, Berlin, 1920), p. 208.

Erratum: Does the Electron Have an Intrinsic Magnetic Moment?

[Phys. Rev. **72**, 984 (1947)]

G. BREIT
Yale University, New Haven, Connecticut

A LETTER to the Editor with above title has been published.[1] It has been stated by Schwinger[2] that the writer's conclusions regarding the magnitude of the ex-

pected effect for s terms disagree with Schwinger's, which were based on a development of quantum electrodynamics. A re-examination of the writer's calculations showed that an error was made in a mathematical transformation. The corrected result is in agreement with Schwinger's as well as with the now established connection of the anomalously large hyperfine structure of the ground state of hydrogen and deuterium[2] with the anomalous magnetic moment of the electron spin.[4]

[1] G. Breit, Phys. Rev. **72**, 984 (1947).
[2] Julian Schwinger, Phys. Rev. **73**, 415 (1948).
[3] J. E. Nafe, E. B. Nelson, and I. I. Rabi, Phys. Rev. **71**, 914 (1947); D. E. Nagel, R. S. Julian, and J. R. Zacharias, Phys. Rev. **72**, 971 (1947).
[4] P. Kusch and H. M. Foley, Phys. Rev. **72**, 1256 (1947); H. M. Foley and P. Kusch, Phys. Rev. **73**, 412 (1948).

Erratum: Neutron-Proton Scattering at 100 Mev

[Phys. Rev. **73**, 641 (1948)]

JULIAN EISENSTEIN AND FRITZ ROHRLICH
Lyman Laboratory of Physics, Harvard University, Cambridge, Massachusetts

WE are sorry to report two misprints which occurred in our Letter to the Editor under the above title.

For the Yukawa potential the singlet range should read 1.18×10^{-13} cm instead of 1.8×10^{-13} cm and is, as stated, the same as the triplet range. The cross section at 100 Mev in the Born approximation is 0.101×10^{-24} cm^2 and not 0.111×10^{-24} cm^2.

Note on the "Natural Radioactivity of Rhenium"

NATHAN SUGARMAN
Argonne National Laboratory and Institute for Nuclear Studies, University of Chicago, Chicago, Illinois
AND
HAROLD RICHTER
Argonne National Laboratory, Chicago, Illinois

April 13, 1948

IN examining the isobaric pair $Re^{187}-Os^{187}$ for radioactivity, Naldrett and Libby[1] found an activity in Re which they attributed to β^--radiations from Re^{187}. The range of the particles was 3.5 mg Al/cm^2 with a corresponding upper energy limit of 43 kev. The samples were purified sufficiently to separate other elements with the exception of the chemically similar Tc (element 43). Since it appeared possible to the authors that the radiations observed might originate in a natural isotope of Tc present in the Re, the Re was subjected to chemical operations which were shown in tracer studies to free it of Tc, and then measured. The activity was essentially unchanged. The details of the chemical separation of Re from Tc and the results of the activity measurements follow.

The Tc tracer used was prepared by irradiation of ammonium molybdate in the "thimble" of the Argonne heavy water pile. The 5.9-hr. Tc^{99} was isolated by using a modification of the radiochemical procedure of Glendenin.[2] The Tc activity is distilled from fuming H_2SO_4 in an air stream. Re carrier is added to the distillate and Re_2S_7 precipitated. After solution of the precipitate in conc. HNO_3 and two evaporations with 3 ml conc. HCl, the solution is diluted to 20 ml with H_2O. The solution is neutralized with NH_4OH and four precipitations of $Fe(OH)_3$ are performed. The level of Tc activity in the tracer solution is determined in an aliquot, more Re carrier is added, and tetraphenylarsonium perrhenate precipitated. The radiochemical purity of the samples was shown to be very high (>99 percent Tc activity) by decay and absorption measurements.

TABLE I. Activity measurements on Re and purified Re_2S_7.

Sample	Area (cm^2)	Sample thickness (mg/cm^2)	Activity (c/m)	Half-life Re^{187} (yrs.)
Re No. 1	260	4.2	38.5±1.5	6.2×10^{12}
Re No. 2	170	5.0	39.3±1.6	4.0×10^{12}
Re_2S_7 (Nos 1a)	240	2.9	21.5±1.4	6.3×10^{12}
Re_2S_7 (No. 1b)	250	2.9	20.4±1.5	6.9×10^{12}

Two methods of separating Re from Tc are given by Perrier and Segré.[3] These consist of distilling Re but not Tc from H_2SO_4 solution in a stream of moist HCl, and precipitating the sulfide of Re alone from 10N HCl. In studying the separation of Re from Tc tracer by sulfide precipitation, another method was found in which Tc is volatilized from a solution by alternate evaporations with HNO_3 and HCl. After five HNO_3-HCl cycles less than 2 percent of the Tc remained while the loss of Re was negligible.

The separation was tested by adding an aliquot of the Tc tracer to two HNO_3 solutions, each containing ~0.6 g Re. The solutions were evaporated almost to dryness. Two successive evaporations were then performed with 15 ml conc. HCl. Alternate evaporations of one addition of 10 ml conc. HNO_3 and two of 15 ml conc. HCl were performed until five such cycles had been completed. Finally, the solutions were diluted to 125 ml, aliquots removed, neutralized, and tetraphenylarsonium perrhenate precipitated. A comparison of the activity in the precipitates to that of the activity added, after correction for the fraction of Re counted, showed that more than 98 percent of the Tc had been removed.

Two one-gram samples of metallic Re (British Drug Houses, Ltd.) were dissolved in conc. HNO_3 and subjected to the separation procedure described above. Although macro-Tc might be expected to behave differently from tracer Tc in some chemical operations, it is probable that Tc, if present, would have been separated from Re. The two Re samples were converted to Re_2S_7, counted, and the activity compared to that of untreated Re metal.

Activity measurements were made in the "screen-wall" counter used by Naldrett and Libby. Anticoincidence shielding added to the counter by Mr. E. C. Anderson reduced the background from 160 c/m to 50 c/m and greatly shortened the counting procedure. Samples of metallic Re (Re No. 1, British Drug Houses, Ltd.; Re No. 2,

Johnson Matthey and Company, Ltd.) and of Re_2S_7 prepared as described were counted. The results are summarized in Table I. The half-life values were calculated from the counting data in the manner described by Naldrett and Libby.

The agreement in half-lives found from Re No. 1 and the Re_2S_7 samples shows that the activity in the samples cannot be attributed to an isotope of Tc. The sulfide samples were also counted through 3.7 mg Al/cm^2 and no activity was observed. This result is in agreement with the observed radiation characteristics of Re and lessens the possibility that the activity in these samples could arise from contamination introduced during the preparation of the samples.

The half-life values found for Re^{187} cluster into two groups, 4×10^{12} yrs. and 6.5×10^{12} yrs. The difference appears to arise from a loss in sensitivity of the counter for the samples of larger area. The Re No. 2 sample of 170-cm^2 area yielded a half-life of 4.0×10^{12} yrs. in good agreement with that found by Naldrett and Libby of 3.8×10^{12} yrs. for samples of the same area.

Some of the work on which this document is based was performed at the Institute for Nuclear Studies, University of Chicago.

The authors take this opportunity in expressing their gratitude to Dr. H. Levi for her generous assistance and to Professor W. F. Libby for his advice and encouragement.

[1] S. N. Naldrett and W. F. Libby, Phys. Rev. **73**, 487 (1948).
[2] L. E. Glendenin, Plutonium Project Record **9B**, 8.11.2 and 12.9 (1946).
[3] C. Perrier and E. Segré, J. Chem. Phys. **5**, 712 (1937); **7**, 155 (1939).